Control of ion and neurotransmitter homeostasis by hippocampal astroglial networks

Dissertation

zur Erlangung des Doktorgrades (Dr. rer. nat.)

der

Mathematisch-Naturwissenschaftlichen Fakultät

der

Rheinischen Friedrich-Wilhelms-Universität Bonn

vorgelegt von

Björn Breithausen

aus

Waldbröl

Bonn, Juni 2020

Angefertigt mit Genehmigung der Mathematisch-Naturwissenschaftlichen Fakultät

der Rheinischen Friedrich-Wilhelms-Universität Bonn

1. Gutachter: **Professor Dr. Christian Henneberger**

Institut für Zelluläre Neurowissenschaften

Universität Bonn

2. Gutachter: **Professor Dr. Walter Witke**

Institut für Genetik

Universität Bonn

Tag der Promotion: 13.11.2020

Erscheinungsjahr: 2020

Table of contents

1 Introduction

Neuroscience is defined as 'the scientific study of the nervous system and the brain' (Cambridge Dictionary[1]). This term highlights the neuron as the pivotal element for brain function, but the knowledge about the importance of other cell types is continuously increasing. These other cell types comprise endothelial cells forming the blood brain barrier and glial cells that are involved in a plethora of important brain functions. Glia cells in the central nervous system (CNS) can be divided into microglia as the main immune cell in the CNS, oligodendrocytes that wrap around axons in order to form myelin sheets, NG2-cells as an oligodendrocyte precursor and astrocytes (Jäkel and Dimou, 2017). From being considered as merely 'Nervenkitt' ('nerve glue') in the 19th century (Virchow, 1859), astrocytes emerged to be active contributors to brain function (Sofroniew and Vinters, 2010). A common model structure in neurophysiology to examine such functions is the hippocampus.

1.1 The hippocampus

The hippocampus is one of the most extensively studied brain regions since it is involved in many physiological and pathophysiological conditions. The human hippocampus is located in the temporal lobe and comprises a highly organized and layered structure (Figure 1). Since this structure is largely conserved between human and rodents, it is commonly used as a model structure to study hippocampus-dependent brain functions (Andersen et al., 2007).

As summarized in 'The Hippocampus Book' by Per Anderson et al. (2007), the hippocampus is subdivided into three Cornu Ammonis (CA) regions, CA1-3. This denomination originates from the shape of the hippocampus that resembles not only the seahorse ('Hippocampus', Latin) but also the coiled ram's horn of the Egyptian deity Amun ('Cornu Ammonis'). The hippocampus and the adjacent brain regions of the dentate gyrus (DG), the subiculum and the entorhinal cortex (EC) form the hippocampal formation. These regions are interconnected by a mainly unidirectional neuronal pathway. This trisynaptic circuit comprises neuronal input from the EC to granule cells in the DG, which then project their axons ('mossy fibers') to the pyramidal cells in the CA3 region. The CA3 pyramidal cells are interconnected but also send their axons ('Schaffer collaterals', SC) to CA1 pyramidal neurons that, in turn, project back to the EC. In addition, the CA3 and CA1 pyramidal neurons also receive direct input from the EC. The hippocampal CA sub regions are organized in different layers.

[1]https://dictionary.cambridge.org/dictionary/english/neuroscience (5.6.2020)

The most prominent layer comprises the cell bodies of the excitatory pyramidal neurons predominantly and is called stratum (str.) pyramidale. The basal and apical dendrites of the pyramidal neurons can be found in the adjacent str. oriens and radiatum, respectively. The str. radiatum contains interconnections between CA3 neurons and connections between CA3 and CA1 neurons ('Schaffer collaterals'). Most of the corresponding CA3/1 synapses are formed on the apical dendrites of the pyramidal neurons in the str. radiatum, but some can also be found on the basal dendrites. The apical pyramidal neuron dendrites extend towards str. lacunosum moleculare where afferents from the EC and other brain regions terminate (Andersen et al., 2007; Deng et al., 2010; Ishizuka et al., 1995). While the cell body of excitatory pyramidal neurons are tightly packed in the str. pyramidale, several types of inhibitory interneurons can be found throughout the different layers (Freund and Buzsáki, 1996). Astrocytes are also numerously found throughout the hippocampus, but their density can differ between the layers (Ogata and Kosaka, 2002).

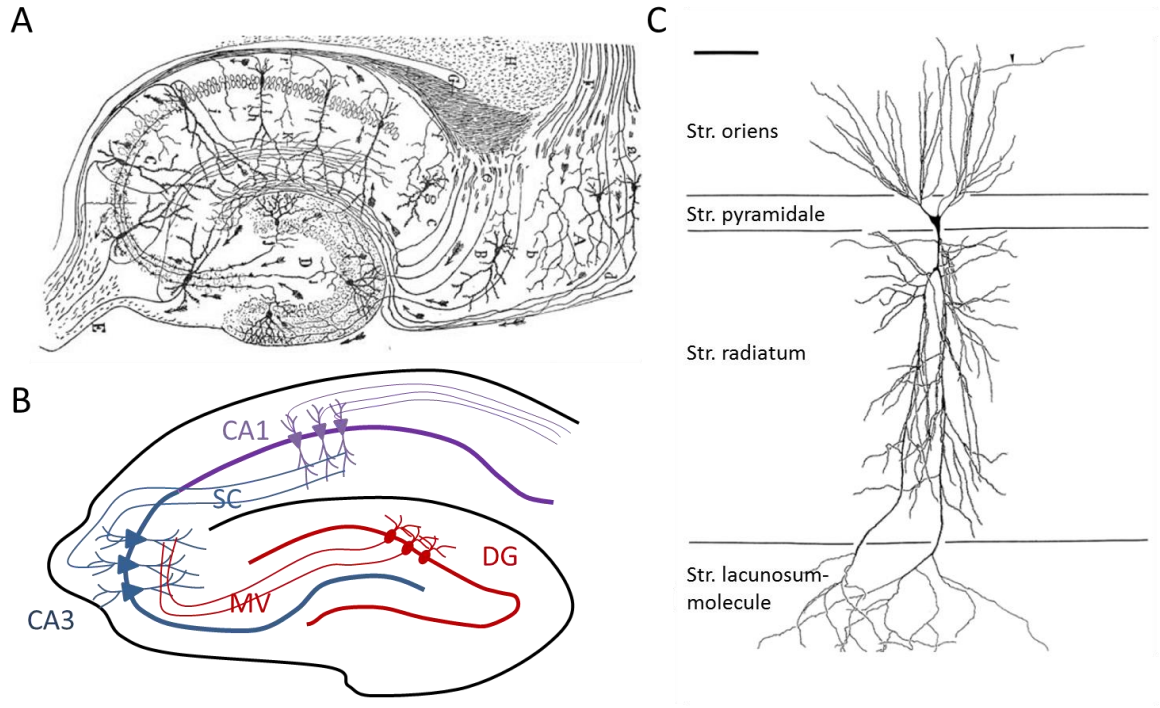

Figure 1 Morphology and cytoarchitecture of the hippocampus. A) An early drawing of the hippocampus from Santiago Ramón y Cajal from 1911 already showed the main components of the hippocampal morphology (Andersen et al., 2007). **B)** Neuronal circuitry in the hippocampus. Granule cells (red) in the dentate gyrus (DG) project their axons ('Mossy fibers', MV) to the dendrites of pyramidal neurons in the CA3 region (blue), which send their axons ('Schaffer collaterals', SC) via the str. radiatum to the dendrites of the CA1 pyramidal neurons (purple). CA1 pyramidal neurons then project their axons to the entorhinal cortex. Adapted from Deng et al., 2010. **C)** Drawing of a CA1 pyramidal neuron depicting the location of its cell body and dendrites in respect to the layered structure of the CA1 region. The neurons receive synaptic input mainly on its dendrites that extend from the soma located in the str. pyramidale into the str. oriens (basal dendrites) and the str. radiatum/lacunosum moleculare (apical dendrites). Scale bar, 100 µm. Adapted from Ishizuka et al, 1995.

1.2 Synaptic transmission and neuronal excitability

Neuronal activation largely depends on changes of the neuronal membrane potential that is set by the intra- and extracellular ion concentrations and their respective membrane conductance. During resting conditions, the neuronal membrane is predominantly permeable for K^+ ions via open K^+ channels. Consequently, the negative resting membrane potential is mainly determined by the equilibrium potential for K^+. Changes of the membrane conductance of particular ions by, for instance, activation of neurotransmitter receptors during synaptic transmission can evoke ion fluxes across the membrane, an altered membrane potential and potentially neuronal activation.

Synaptic transmission consists of the activation of a presynaptic terminal, the release of neurotransmitters and the subsequent activation of the postsynaptic terminal. Presynaptic terminals respond to a depolarization by opening of voltage-gated Ca^{2+} channels and subsequent release of neurotransmitters into the synaptic cleft. An example of an excitatory neurotransmitter is glutamate, which can bind to ionotropic glutamate receptors, such as α-amino-3-hydroxy-5-methyl-4-isoxazolepropionic acid receptors (AMPARs) and N-methyl-D-aspartate receptors (NMDARs) on the postsynaptic terminals. This can result in an opening of these receptors, the influx of cations (excitatory postsynaptic current, EPSC) and, subsequently, in a depolarization of the postsynaptic neurons (excitatory postsynaptic potential, EPSP) (Kandel et al., 2013). In contrast to glutamate, the release of the inhibitory neurotransmitter γ-aminobutyric acid (GABA) by interneurons activates ionotropic $GABA_A$ receptors ($GABA_ARs$), causes an influx of negatively charged Cl^- ions (inhibitory postsynaptic current, IPSC) and hyperpolarizes the postsynaptic membrane potential (Kandel et al., 2013; Pelkey et al., 2017). Taken together, the integration of excitatory and inhibitory synaptic inputs can change the neuronal membrane potential. When the membrane potential depolarizes and reaches the opening-threshold for voltage-gated Na^+ channels, Na^+ ions enter the neurons and lead to action potential firing. Subsequently, voltage-gated K^+ channels open that lead to an efflux of K^+ ions and a repolarization of the membrane potential. Consequently, the extracellular K^+ concentration increases. Since an elevated extracellular K^+ concentration renders the K^+ equilibrium potential less negative (see also chapter 1.4.1), extracellular K^+ has to be efficiently cleared. Otherwise, the repolarization of the neuronal membrane potential would be less efficient and promote prolonged membrane depolarization. In turn, an excitatory synaptic input that previously evoked a sub-threshold depolarization can reach the opening-threshold for voltage-gated Na^+ channels and, in turn, lead to neuronal activation (Kandel et al., 2013). In addition to extracellular K^+, also excessive extracellular glutamate accumulations can increase neuronal excitability by the increased activation of glutamate receptors. When glutamate is present at the synapses at higher concentrations and/or for

longer periods, the postsynaptic depolarization is larger and the neuronal activation is more likely. Both extracellular K^+ and glutamate levels are controlled by astrocytes via diverse mechanism in order to limit neuronal hyperexcitability.

1.3 Astrocytes and their network

Astrocytes can be categorized into protoplasmic and fibrous astrocytes. This was already described by the Spanish neuroscientist Santiago Ramón y Cajal in 1909 (Ramón y Cajal, 1909). Fibrous astrocytes are found in the white matter and exhibit several long fiber-like processes, whereas protoplasmic astrocytes in the grey matter show several major branches with numerous fine processes. Protoplasmic astrocytes exhibit relatively small somata, several main branches that extensively ramify into fine and fuzzy processes. (Ramón y Cajal, 1909; Sofroniew and Vinters, 2010). These processes are in close contact with synapses (Ventura and Harris, 1999; Witcher et al., 2007). Each astrocyte occupies an individual territory with only a limited overlap at their boundaries to the adjacent astrocytes. (Figure 2A) (Bushong et al., 2002; Halassa et al., 2007a; Ogata and Kosaka, 2002).

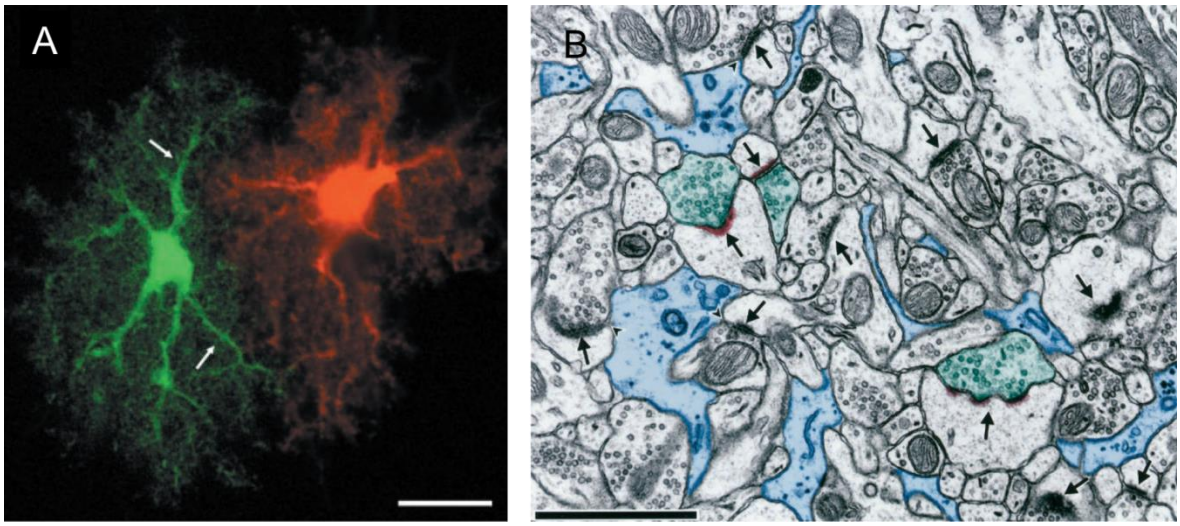

Figure 2 Morphology and organization of astrocytes in the hippocampus. A) Two adjacent astrocytes were visualized by dye-injections (green, Alexa Fluor 488; red, Alexa Fluor 594) and show the typical spongiform morphology in non-overlapping territories. The arrows indicate main astrocytic branches that further ramify into fine processes and protrusions. Scale bar, 15 µm. Taken from Bushong et al. (2002). **B)** Electron microscopy of the hippocampus reveals astrocyte protrusions (blue), presynaptic terminals (green) and postsynaptic densities (red) in close vicinity to each other, but only a subset of synapses (arrows) is directly contacted by an astrocyte, as indicated by the arrowheads. Scale bar, 1 µm. Taken from Ventura and Harris (1999).

The shape of these territories is not uniform throughout the CNS but can vary between different brain regions. For instance, astrocytes in the CA1 str. radiatum of the hippocampus exhibit elongated territories along pyramidal cell dendrites, whereas astrocytes in the CA1 str. lacunosum moleculare show no such polar orientation (Anders et al., 2014; Nixdorf-Bergweiler et al., 1994; Wallraff et al., 2006). The area occupied by astrocytes in the CA1 str. radiatum is gradually increasing during development but reaches levels between ~2000-3500 μm^2 in adult rodents. This corresponds to a maximal spatial extent of roughly 50-100 µm (Nixdorf-Bergweiler et al., 1994; Ogata and Kosaka, 2002).

Astrocytes form large networks via gap junction channels (Figure 3) that allow intercellular trafficking of ions, metabolites and water with a cut-off selectivity of 1-1.2 kDa. These channels are formed by two hemichannels (‘connexons’) on adjacent astrocytes that are composed of six transmembrane proteins (‘connexins’, Cxs) (Giaume et al., 2010; Nagy and Dermietzel, 2000). The expression profile of Cx isoforms changes during development, but Cx30 and 43 were found to represent the main astrocytic connexins in adulthood (Dahl et al., 1996; Dermietzel et al., 1989; Nagy and Dermietzel, 2000). The first indication for this extensive coupling was reported by Kuffler and colleagues for the optic nerve of amphibians by simultaneous electrophysiological recordings in two adjacent glial cells. In this study, a current injection into one cell produced a membrane depolarization in the adjacent cell indicating electrical coupling (Kuffler et al., 1966). Since then, the knowledge about the astrocyte network has been continuously increasing. Nowadays, a commonly used technique to investigate the astrocyte network is its visualization with fluorescent dyes. This technique employs a fluorescent dye (< 1-1.2 kDa) injected into a single astrocyte, the dye diffusion through the gap junction channels and the subsequent labeling of coupled cells (Anders et al., 2014). In addition to the gap junction channels that couple adjacent astrocytes, also reflexive (or autocellular) gap junctions are found, i.e. gap junctions channel between processes of the same astrocyte (Genoud et al., 2015; Giaume et al., 2010). The importance of the astrocyte gap junction coupling for several brain functions became increasingly clear during the last decades (Giaume et al., 2010; Pannasch and Rouach, 2013). For instance, astrocytes were shown to supply neurons with metabolites from the blood stream via their gap junction coupled network and thus sustain the neuron’s activity (Rouach et al., 2008). Moreover, there is abundant evidence to support the important role of the astrocyte network for shaping synaptic transmission. Genetic deletion of Cx30 and 43 specifically from astrocytes was shown to facilitate synaptic transmission and plasticity (Pannasch et al., 2011) and modulate neuronal network activity (Chever et al., 2016; Pannasch et al., 2012). However, the mechanism underlying these effects and the specific role of the different connexins

are difficult to identify. In contrast to the facilitated transmission in hippocampal slices with Cx30 and 43-deficient astrocytes (Pannasch et al., 2011), synaptic transmission was attenuated and neuronal glutamate release was decreased when only Cx43 was absent in astrocytes (Chever et al., 2014a). Moreover, the specific deletion of Cx30 from astrocytes resulted in an altered astrocytic morphology and an unusual invasion of their fine processes into the synaptic cleft which was accompanied by increased glutamate uptake and attenuated synaptic transmission (Ghézali et al., 2018; Pannasch et al., 2014). Taken together, the gap junction-mediated astrocyte network was shown to affect neuronal function by various mechanisms, but the differentiation between the pure function as a channel and the channel-independent functions, such as cellular adhesion, remains difficult.

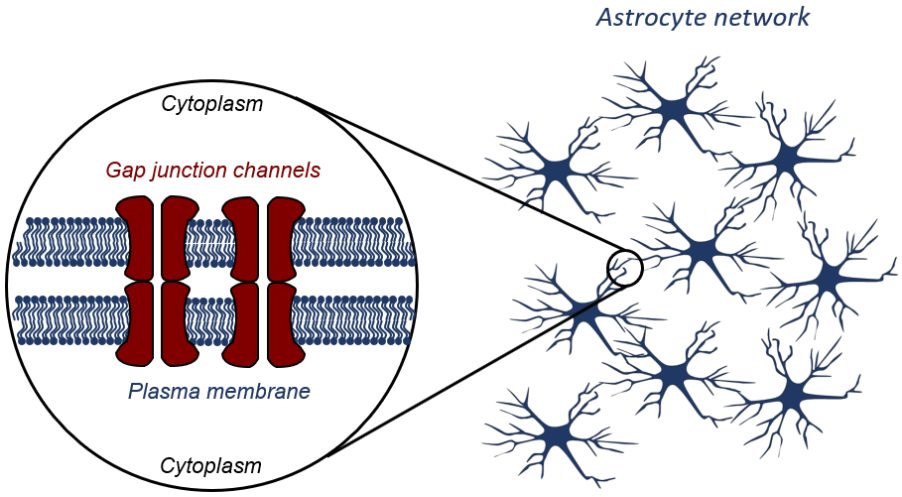

Figure 3 Formation of the astrocyte network via gap junction channels. Astrocytes express on their plasma membrane (blue) gap junction channels (red) that allow the intercellular trafficking of ions and small molecules between adjacent astrocytes. In addition, reflexive gap junction channels also couple to processes of the same astrocyte. These channels are formed by two opposing hemichannels, which are composed from six transmembrane proteins ('Connexins'). Adapted from Giaume et al. (2010).

1.4 Extracellular ions and neurotransmitter homeostasis

Astrocytes are known to contribute to the clearance of extracellular ions and neurotransmitters. In particular the homeostasis of extracellular K^+ and glutamate are known to be tightly controlled by astrocytes since both can drastically impact on neuronal functions.

1.4.1 Uptake of extracellular K^+

Astrocytes contribute to the homeostasis of extracellular K^+, whose concentration inevitably rises nearby electrically active neurons. This is of particular importance since the extracellular K^+ concentration ($[K^+]_o$) affects neuronal functions, such as the membrane potential, and, in turn, neuronal excitability. According to the Goldman Equation, which describes the membrane potential on the basis of the intra- and extracellular ion concentrations and their particular membrane conductances, increasing the extracellular K^+ concentration leads to a depolarization of the membrane potential shifting it more closely to the threshold for opening of voltage-gated ion channels (Kandel et al., 2013). This was already shown by early studies that revealed facilitated action potential firing and synaptic transmission by increasing the extracellular K^+ concentration by several millimolar (mM) (Balestrino et al., 1986; Hablitz and Heinemann, 1987; Hablitz and Lundervold, 1981; Rausche et al., 1990; Voskuyl and ter Keurs, 1981). During resting conditions, the basal extracellular K^+ concentration is approximately 3 mM (Bradbury and Kleeman, 1967; Rasmussen et al., 2019). Since neurons open K^+ channels after their activation in order to repolarize the membrane potential, the extracellular K^+ concentration can drastically increase (Kandel et al., 2013). The amount of released K^+ can, of course, vary and it depends on the extent of neuronal activity. For instance, visual stimulation evoked transient extracellular K^+ elevations ('K^+ transients') of 5-200 µM in the visual cortex of anesthetized cats (Connors et al., 1979) and innoxious stimulation by moving a brush over the skin of a cat resulted in extracellular K^+ elevations up to 0.4 mM in their spinal cord (Heinemann et al., 1990). A more recent study showed that running onset in freely moving mice was accompanied by extracellular K^+ elevations of around 0.6-1 mM in the visual and motor cortex (Rasmussen et al., 2019). Higher extracellular K^+ concentrations of around 10 mM were observed in the cortex of cats during prolonged electrical stimulations and seizure activity (Heinemann and Lux, 1977; Moody et al., 1974). The involvement of astrocytes in the clearance of those extracellular K^+ elevations was already postulated in the 1960s (Hertz, 1965) and confirmed in further studies that showed intracellular K^+ accumulation via passive and active uptake mechanisms (Ballanyi et al., 1987; Coles and Orkand, 1983). Astrocytes are well suited for this purpose by expressing various K^+ channels, cotransports and pumps (Kofuji and Newman, 2004; Seifert et al., 2016; Walz, 2000). The predominant K^+ channel of astrocytes is the inward-rectifier potassium channels 4.1 (Kir4.1) with an enriched expression at synapses and at their blood vessel-contacting endfeet (Higashi et al., 2001; Nagelhus et al., 2004). In addition, astrocytes also express Ca^{2+}- and voltage-dependent K^+ channels and passive two-pore K^+ channels (Seifert et al., 2009, 2016). Thus, astrocytes exhibit a large K^+ conductance, a passive current pattern and a low membrane potential, which is largely

determined by the transmembrane K^+ concentration gradient (Djukic et al., 2007; Savtchenko et al., 2018; Seifert et al., 2009). Since the astrocytic membrane potential (V_m) is mainly determined by the large membrane conductance for K^+ (g_K), it is close to the K^+ equilibrium potential (E_K). The equilibrium potential of an ion is the membrane potential at which no net flow of the particular ion occurs over the membrane and is described by the Nernst equation:

$$E_K = \frac{RT}{zF} \times \ ln \frac{[K^+]_o}{[K^+]_i}$$

This potential depends on the universal gas constant (R), the temperature in Kelvin (T), the number of valence electrons (z), the Faraday constant (F) and the intra- ($[K^+]_i$) and extracellular ion concentration ($[K^+]_o$). Since the basal extracellular K^+ concentration is relatively low compared to the astrocytic cytoplasm, the equilibrium potential for K^+ is negative. Deviations of the membrane potential from the equilibrium potential for K^+ will lead to a K^+ current (I_K) either into ($E_K > V_m$) or out of ($E_K < V_m$) the astrocyte (Kandel et al., 2013):

$$I_K = \ g_K \ (V_m - E_K)$$

During resting conditions, the astrocytic membrane potential is slightly less negative compared to the K^+ equilibrium potential since K^+ is constantly transported into the cytoplasm by pumps and transporters in the membrane (see below). Consequently, a constant efflux of K^+ is mediated via the open K^+ channels. Conversely, elevations of the extracellular K^+ concentration lead to an influx of K^+ (or reduced K^+ efflux) and a corresponding depolarization of the astrocytic membrane potential until the new equilibrium potential for K^+ is reached (Larsen and MacAulay, 2014). Additionally, active uptake of extracellular K^+ is mediated by the Na^+/K^+-ATPase (D'Ambrosio et al., 2002; Jauch et al., 2002; Ransom et al., 2000; Xiong and Stringer, 2000) that is also expressed by astrocytes (Karus et al., 2015; Larsen et al., 2014). It expels three Na^+ ions from the cytoplasm in exchange for two K^+ ions in an ATP-dependent manner (Kandel et al., 2013). Astrocytes also express the $Na^+/K^+/2Cl^-$-cotransporter 1 (NKCC1) (Blaesse et al., 2009) that was shown to mediate intracellular K^+ accumulation in astrocytes when exposed to high extracellular K^+ concentrations (Walz and Hertz, 1984). However, inhibition of NKCC1 had no effect on extracellular K^+ transients evoked by neuronal activity (Larsen et al., 2014; Xiong and Stringer, 2000).

In summary, astrocytes possess several mechanisms to clear K^+ from the extracellular space (ECS) which have been termed 'K^+ net uptake'. This comprises the uptake of extracellular K^+, the transient intracellular K^+ storage and the subsequent release after

normalization of the extracellular K^+ concentration (Kofuji and Newman, 2004; Walz, 2000). A second mechanism that was proposed to contribute to extracellular K^+ clearance is 'spatial K^+ buffering'.

1.4.2 Concept of spatial K^+ buffering

This concept was originally proposed by Richard Orkand in 1966 (Orkand et al., 1966) and proposes the distribution of K^+ through a coupled glial network. However, it took another 20 years and several more studies until this concept was finally elaborated. First indications for a glia-mediated distribution of K^+ came from work performed on amphibian Müller cells, specialized glial cells that span across the retina and contact the vitreous humor with their endfeet. They display a high membrane conductance for K^+ at their endfeet (Newman, 1984), which enables them to redistribute extracellular K^+ through a single cell by a mechanism termed 'K^+ siphoning'. Evidence for this mechanism was obtained from dissociated Müller cells that spatially redistributed extracellular K^+ more efficiently than simple extracellular diffusion (Newman et al., 1984) as well as from Müller cells in the intact retina that mediated K^+ elevations in the vitreous humor after light stimulation (Karwoski et al., 1989).

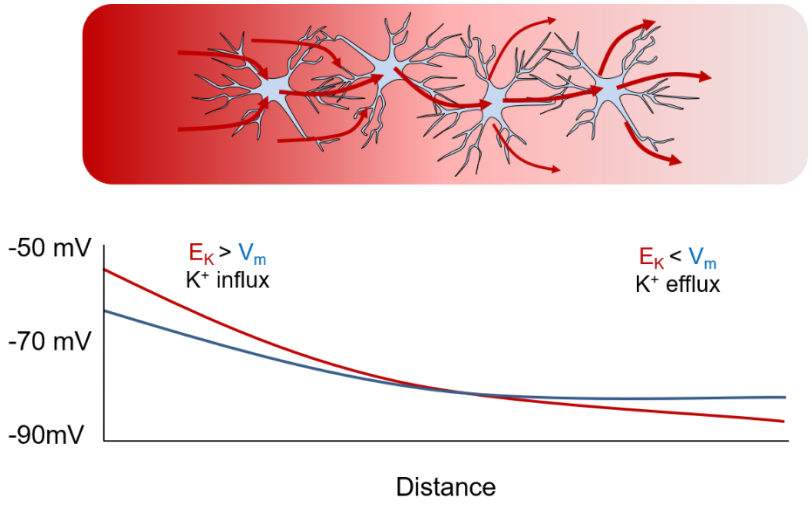

Figure 4 The concept of spatial K^+ buffering. The local increase of the extracellular K^+ concentration results in a K^+ concentration gradient in the ECS as indicated by the red intensity gradient (top panel). At those sites, the difference between the equilibrium potential for K^+ (E_K, red) and the astrocytic membrane potential (V_m, blue) drives K^+ to enter the astrocyte. The resulting depolarization then spreads passively through the gap junction coupled network via a K^+ current that renders V_m more negative than E_K and, in turn, leads to a constant K^+ influx. At sites with a lower extracellular K^+ concentration, V_m exceeds E_K and K^+ is released into the ECS. As a result, K^+ is redistributed from sites of elevated extracellular K^+ concentrations to sites that exhibit lower extracellular K^+ levels. Adapted from Orkand (1986).

Since coupled glial cells can be considered as one elongated cell, their network was then proposed by Richard Orkand to contribute to the clearance of extracellular K^+ via the spatial redistribution of K^+ (Figure 4): At sites with an increased extracellular K^+ concentration, K^+ enters the astrocyte driven by the difference between the local K^+ equilibrium potential and the membrane potential. The gap junction channels between adjacent astrocytes but also between processes of the same astrocyte (reflexive gap junction channels) connect astrocytic domains exposed to elevated extracellular K^+ concentrations ('active domains') to those exposed to lower extracellular K^+ concentrations ('resting domains'). Thus, gap junction coupling facilitates intracellular K^+ diffusion and electrically couples active astrocytic domains and those at rest. As a consequence, K^+ is redistributed between these domains via a K^+ current within the cytosol of a single astrocyte and the gap junction coupled network. This renders the local astrocytic membrane potential at the active domain more negative relative to the K^+ equilibrium potential and, thus, enables a steady local K^+ influx. At sites with a lower extracellular K^+ concentration, the membrane potential exceeds the K^+ equilibrium potential which then results in a K^+ efflux. Overall, this mechanism allows the gap junction coupled astrocytes to distribute K^+ through their network without a net K^+ accumulation and, in turn, facilitate K^+ clearance (Orkand, 1986). However, the functional significance of astrocyte gap junction coupling for K^+ clearance remains unclear.

In addition to the extracellular K^+ concentration gradient, a further requirement for the concept of spatial K^+ buffering is the high astrocytic membrane K^+ conductance in order to mediate the passive in- and efflux of K^+ (Larsen and MacAulay, 2014; Orkand, 1986). Indeed, pharmacological inhibition or genetic deletion of Kir4.1 from astrocytes resulted in augmented artificially evoked extracellular K^+ transients (Jauch et al., 2002; Larsen et al., 2014), slowed recovery rates of extracellular K^+ transients (Chever et al., 2010; Haj-Yasein et al., 2011) and increased basal K^+ concentrations (D'Ambrosio et al., 2002). However, this provides no clear insight into the involvement of astrocytic gap junction channels in K^+ clearance because inhibition of Kir4.1 channels would also impair spatial K^+ buffering if K^+ were to be redistributed independently of gap junction channels within one astrocyte territory, comparable to the Müller cell in the retina (Karwoski et al., 1989; Newman et al., 1984).

Other studies investigated the contribution of the gap junction coupled astrocyte network to K^+ clearance by a genetic deletion of Cx30 and 43 in astrocytes and found augmented stimulus-evoked K^+ transients and slowed astrocytic K^+ uptake currents (Pannasch et al., 2011; Wallraff et al., 2006). Although this points towards an impaired K^+ clearance when the astrocyte network is disrupted, developmental alteration, such as an altered astrocyte morphology, induced by the genetic deletion of Cx30 (Ghézali et al., 2018; Pannasch et

al., 2014) cannot be excluded to have mediated the observed effects. Interestingly, the astrocyte specific deletion of the Tsc1 gene (a model for tuberos sclerosis complex) resulted in reduced astrocyte gap junction coupling and was associated with augmented extracellular K^+ transients (Xu et al., 2009). In contrast, attenuated extracellular K^+ transients, facilitated recovery and increased astrocytic gap junction coupling was found in hippocampal slices with an astrocyte specific deletion of the water channel aquaporin 4 (Strohschein et al., 2011). Again, these experiments do not rule out that the observed effects on the K^+ transients were influenced by side effects of the gene deletion. For instance, an increased extracellular space was found in mice deficient for the aquaporin (Yao et al., 2008). This could account for the observed attenuated extracellular K^+ transients since the volume in which the K^+ was released was larger. Furthermore, the astrocyte specific deletion of the Tsc1 gene was reported to alter the number of astrocytes and the neuronal organization (Uhlmann et al., 2002) and thereby could have affected the observed attenuated extracellular K^+ transients observed by Xu et al. (2009).

Other studies used pharmacological agents in order to acutely inhibit gap junction coupling and observed an increased basal K^+ concentration in the cortex of anesthetized mice (Bazzigaluppi et al., 2017). However, these gap junction inhibitors are not specific for astrocytic gap junction channels, but also inhibit neuronal gap junction channels (Zsiros and Maccaferri, 2005). As a consequence, altered extracellular K^+ concentration could also be a result of an altered neuronal activity and activity-dependent K^+ release. Moreover, inhibition of astrocytic coupling might impair the supply of metabolites (Rouach et al., 2008) and thus could affect K^+ homeostasis indirectly by modulating the energy-dependent Na^+/K^+-ATPase activity. Furthermore, changes of neuronal activity, for instance via hemichannel inhibition (Chever et al., 2014b), could also underlie the altered extracellular K^+ homeostasis independently from an impaired astrocytic coupling. These studies provide important knowledge about the K^+ homeostasis in various conditions but do not allow drawing direct conclusions on the channel function of astrocyte gap junctions for K^+ clearance.

In summary, astrocytes contribute to the clearance of extracellular K^+ by various mechanisms. Active uptake of extracellular K^+ is mediated by the energy-dependent activity of the Na^+/K^+-ATPase or by the cotransport with Na^+ via the NKCC1. On the other hand, passive K^+ influx into the astrocyte is be mediated by K^+ channels (e.g. Kir 4.1 channels) when the equilibrium potential for K^+ is less negative compared to the membrane potential. Spatial redistribution of K^+ inside an astrocyte or their network has been proposed to facilitate this passive K^+ influx by limiting the K^+-induced membrane depolarization (Orkand, 1986). However, at least three different scenarios for intracellular K^+ redistribution are conceivable. First, active astrocytic domains that are exposed to an

increased extracellular K^+ concentration are efficiently connected to those at rest without gap junction channels. As a consequence, an intracellular K^+ redistribution would limit local depolarization and facilitate passive K^+ uptake independently of gap junction coupling. Second, reflexive gap junction channels connect active and resting astrocytic domains within the same astrocyte territory. The resulting increased complexity might facilitate intracellular K^+ redistribution, limit the local depolarization and promote the K^+ uptake. Third, gap junction channels between adjacent astrocytes would also connect active and resting astrocytic domains and thus limit local depolarization by the same mechanism. Conversely, acute uncoupling of the astrocytic gap junction channels would be expected to facilitate K^+-induced depolarizations and impair K^+ uptake. In turn, this would lead to augmented extracellular K^+ accumulation. Interestingly, acute inhibition of Kir4.1 channels, the mediator of the high astrocytic K^+ conductance (Djukic et al., 2007; Seifert et al., 2009) and spatial K^+ buffering (Larsen and MacAulay, 2014) has led to increased peak amplitudes of extracellular K^+ transients (Jauch et al., 2002; Larsen et al., 2014). Consequently, acute inhibition of gap junction channels is expected to have a similar effect if involved in spatial K^+ buffering.

1.4.3 Extracellular glutamate clearance

Glutamate is the predominant excitatory neurotransmitter in the brain (Danbolt, 2001; Rose et al., 2018) and mediates excitatory synaptic transmission via activating AMPARs and NMDARs in the synaptic cleft (Kandel et al., 2013). However, synaptically-released glutamate can also escape the synaptic cleft (‘spill-over’) and act on extrasynaptic glutamate receptors or even on neighboring synapses (Asztely et al., 1997; Kullmann et al., 1996; Rose et al., 2018). This can have critical consequences since the activation of extrasynaptic NMDARs can induce excitotoxicity, i.e. the induction of cell death (Zhou et al., 2015). Furthermore, it was shown that glutamate can spill-over to neighboring synapses and facilitate synaptic cross-talk by the activation of NMDARs (Asztely et al., 1997). Thus, there is need for an efficient control of the extracellular glutamate levels. For this purpose, astrocytes express high-affinity glutamate transporters that were shown to remove the majority of synaptically released glutamate from the ECS. The predominant glutamate transporters in rodent hippocampal astrocytes are the glutamate/aspartate transporter (GLAST) and the glutamate transporter-1 (GLT-1) that mediate glutamate uptake via a Na^+ cotransport and the export of K^+ (Levy et al., 1998; Nicholls and Attwell, 1990; Rose et al., 2018; Stallcup et al., 1979). For instance, it was revealed that glutamate spill-over and the concomitant activation of extrasynaptic NMDARs was facilitated when glutamate transporters were acutely inhibited (Asztely et al., 1997). Astrocyte processes

are typically not found in the synaptic cleft (Kikuchi et al., 2020; Medvedev et al., 2014; Ventura and Harris, 1999; Witcher et al., 2007) and thus do not interfere with the activation glutamate receptors in the cleft. Instead, they have been suggested to limit the spread of glutamate out of the cleft in order to prevent the activation of extrasynaptic receptors (Zheng et al., 2008). The importance of astrocytic synapse coverage was further revealed by a study that found a facilitated activation of presynaptic mGluRs and a concomitant increased neurotransmitter release when astrocytic synapse coverage was reduced (Oliet et al., 2001). In addition to the facilitated activation of extrasynaptic mGluRs (Oliet et al., 2001; Zheng et al., 2008) and NMDARs (Asztely et al., 1997) during impaired glutamate clearance, the activation of AMPARs on adjacent synapses can also not be excluded (Rose et al., 2018). Taken together, spatial arrangement of the astrocytic synapse coverage is an important factor for the regulation of synaptic glutamate signaling. Interestingly, the surface expression of GLT-1 on cultured astrocytes was shown to be regulated by intracellular Ca^{2+} signaling (Stenovec et al., 2008). Additionally, GLT-1 was shown to be highly motile in the membrane of hippocampal astrocytes and the inhibition of GLT-1 membrane diffusion prolonged EPSCs indicating an impaired glutamate clearance (Murphy-Royal et al., 2015). In turn, glutamate clearance could not only be affected by an altered synapse coverage but also by an distorted astrocytic Ca^{2+} signaling or altered membrane properties (Henneberger, 2017; Rose et al., 2018).

In summary, astrocytes possess efficient clearance mechanism to control the extracellular concentration of glutamate and K^+. However, the extracellular concentration of ions and neurotransmitter depends not only on the efficiency of such clearance mechanisms or their amount released by neurons. In fact, the structure and size of the extracellular space also determines the extracellular ion and neurotransmitter concentration.

1.4.4 The extracellular space and extracellular homeostasis

In addition to the cellular structures, the brain comprises an extracellular space (ECS), the space that separates cellular structures (Figure 5A). As reviewed by Eva Syková and Charles Nicholson, the ECS contains the extracellular fluid and macromolecules of the extracellular matrix. Its structure can be described by its volume fraction that is defined as the volume of the ECS relative to the volume of the brain tissue (Nicholson and Syková, 1998; Syková and Nicholson, 2008). The ECS structure is not uniform throughout brain regions and development (Syková and Nicholson, 2008). For instance, it was shown that the ECS volume fraction in the rat corpus callosum and cortex decreased from more than 30% at postnatal day 3-4 to around 20% at postnatal day 21 (Lehmenkühler et al., 1993; Voříšek and Syková, 1997). Further reductions of the ECS fraction were observed for the

hippocampus when rats at the age of around 3 months were compared with rats at an age of 2.5 years. (Syková et al., 1998, 2002). These and other studies led to the conclusion that the ECS fraction decreases throughout the entire postnatal life (Syková and Nicholson, 2008).

The extracellular ion and neurotransmitter homeostasis is controlled by various cellular, in particular astrocytic, mechanisms. However, also the structure of the ECS is involved in their homeostasis by determining the volume in which ions and neurotransmitter are released and by shaping their diffusion. As a consequence, structural changes of the ECS can have direct impact on the extracellular ionic concentrations and diffusion (Syková and Nicholson, 2008). In other words, the same number of ions or neurotransmitter released either by cellular structures or artificially by a pipette will generate a high extracellular concentration when the ECS is small and vice versa (Figure 6B).

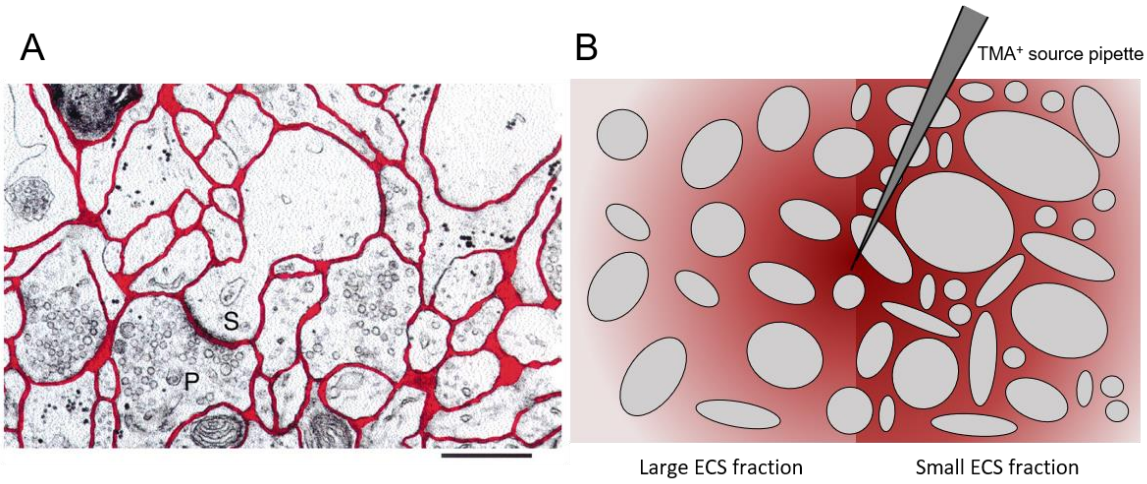

Figure 5 The structure of the extracellular space (ECS). A) The ECS (red) separates cellular components (grey), such as presynaptic terminals (S) and spines (P) as depicted in this electron microscopy picture of the rat cortex. Scale bar, 1 µm. Taken from Nicholson and Syková (1998). **B)** Extracellular diffusion of molecules and ions is shaped by the ECS structure. Application of an ion (e.g. TMA^+) via a pipette into the ECS will result in an extracellular concentration gradient of that particular ion (red intensity gradient). This concentration gradient depends among other on the volume fraction of the ECS. Increases of cellular components (grey) by, for instance cellular swelling, can reduce the ECS fraction (right part of the panel) and affect the extracellular ion concentration. Adapted from Nicholson and Syková (1998).

Interestingly, evoked reductions of the ECS fraction were shown to augment epileptiform activity in the rat hippocampus. The authors attribute these observations to enhanced extracellular K^+ or glutamate accumulation during neuronal activity due to the restricted ECS and impaired diffusion (Kilb et al., 2006; Traynelis and Dingledine, 1989). On the other hand, elevations of the extracellular K^+ concentration itself can also reduce the ECS

fraction by inducing swelling of cellular structures, in particular astrocytes (Syková et al., 1999). Accordingly, ECS shrinkage can be observed during neuronal stimulation in hippocampal slices (Larsen et al., 2014; Pannasch et al., 2011) and in the cortex of anesthetized rat during seizure activity (Slais et al., 2008). Although the K^+ induced cellular swelling is generally accepted to be mediated by a K^+ uptake accompanying water influx, the exact mechanism underlying the cellular swelling remains not fully understood (Larsen et al., 2014; MacAulay and Zeuthen, 2012).

In summary, there is evidence that the shrinkage of the ECS can impact neuronal function by constraining the extracellular diffusion of ions and neuroactive substances and, in turn, their homeostasis.

1.5 Gliotransmission

Apart from clearing ions and neurotransmitter from the ECS, astrocytes also release neuroactive substances (‘gliotransmitter’) in order to directly modulate neuronal functions. For that purpose, astrocytes processes are in close contact with synapses in order to sense neuronal activity and respond with the release of gliotransmitter.

1.5.1 The tripartite synapse

A single hippocampal astrocyte territory is estimated to comprise more than 100000 synapses. Approximately more than half of their clefts are apposed by an astrocyte protrusion (Figure 2B) (Bushong et al., 2002; Halassa et al., 2007a; Witcher et al., 2007). However, this coverage can vary between synapse morphologies and the procedure of preparation (Ventura and Harris, 1999; Witcher et al., 2007). The distance between synapses and astrocyte protrusions can range from less than a hundred to a few hundred nanometers as shown by an electron-microscopy study of the dentate gyrus (Medvedev et al., 2014). However, this structural neuron-astrocyte interplay has been demonstrated to be dynamic. In fact, astrocytes can approach and withdraw their fine processes from the synapses within minutes in an activity-dependent manner (Bernardinelli et al., 2014; Haber et al., 2006). This close contact and the observation that astrocytes respond to neuronal activity with intracellular Ca^{2+} elevations and the concomitant release of neuroactive substances (‘gliotransmitter’) has led to the concept of the ’tripartite synapse’. This concept describes the astrocytes in addition to the presynaptic and postsynaptic terminal as the third active component of the synapse (Araque et al., 1999). Intracellular Ca^{2+} elevations of cultured astrocytes in response to extracellular glutamate were first observed in the early nineties of the last century (Cornell-Bell and Finkbeiner, 1991;

Cornell-Bell et al., 1990). Since then, the knowledge about astrocyte Ca^{2+} signaling has been remarkably increasing. For instance, astrocytes were shown to express a variety of ion channels and neurotransmitter receptors that enable them to sense and integrate neural activity into intracellular Ca^{2+} elevations (Verkhratsky and Steinhäuser, 2000). As summarized by Bazargani and Attwell in 2016, extracellular Ca^{2+} may enter the astrocytic cytosol via activation of Ca^{2+}-permeable ion channels. Additionally, the activation of metabotropic neurotransmitter receptors (e.g. metabotropic receptors for glutamate (mGluR) or GABA ($GABA_BR$)) was shown to trigger Ca^{2+} release from internal stores via a G-protein dependent signal transduction. Also, the reversal of the Na^+/Ca^{2+} exchanger (NCX) by an intracellular accumulation of Na^+ can give rise to intracellular Ca^{2+} elevations (Bazargani and Attwell, 2016). Although the mechanism is still under debate, intracellular Ca^{2+} elevations in astrocytes were shown to be associated with the release of gliotransmitters (Sahlender et al., 2014).

1.5.2 Impact on synaptic transmission

Many studies have revealed that glutamatergic synaptic transmission is modulated by gliotransmitters (Halassa et al., 2007b; Perea and Araque, 2010). One of these gliotransmitters that are released by astrocytes is glutamate. It was suggested that glutamate released from astrocytes can activate NMDARs on several hippocampal pyramidal neurons simultaneously and thereby might contribute to neuronal excitability and synchronization (Angulo et al., 2004; Fellin et al., 2004). Furthermore, activation of neuronal mGluRs by astrocytic glutamate can promote neurotransmitter release (Perea and Araque, 2007). Moreover, astrocytes have been reported to release adenosine triphosphate (ATP) that can facilitate synaptic transmission (Gordon et al., 2005). Conversely, released ATP that is converted to adenosine (ATP/adenosine) was shown to depress synaptic transmission and impair synaptic plasticity (Pascual et al., 2005).

Astrocytes also react to GABAergic transmission with intracellular Ca^{2+} elevations (Boddum et al., 2016; Egawa et al., 2013; Mariotti et al., 2016; Matos et al., 2018; Meier et al., 2008; Perea et al., 2016; Ribak et al., 1996). Plenty of studies focused on the impact of gliotransmission on inhibitory synaptic transmission (Losi et al., 2014; Mederos and Perea, 2019; Roux and Buzsáki, 2015). For instance, an early study found that Ca^{2+}-dependent glutamate release potentiated inhibitory synaptic input onto CA1 pyramidal neurons (Kang et al., 1998). It was further shown that glutamate released from astrocytes can also modulate inhibitory input onto interneurons (Liu et al., 2004a, 2004b). In addition, ATP/adenosine release by astrocytes upregulated synaptic inhibition onto pyramidal neurons (Matos et al., 2018) and attenuated excitatory transmission (Boddum et al.,

2016). Furthermore, astrocytic ATP release potentiated interneuron activity and increased inhibitory transmission onto pyramidal neurons (Bowser and Khakh, 2004). Taken together, astrocytes can modulate inhibitory synaptic transmission by various mechanisms. The contribution of a particular gliotransmitter and its potential target during a specific (experimental) condition remains, however, elusive and hard to predict.

In summary, astrocytes are an essential regulator for both excitatory and inhibitory synaptic transmission via several mechanisms, but the net effects of their modulation on network activity are hard to predict.

1.5.3 Impact on synaptic plasticity

Synaptic transmission is not static but can undergo significant changes, i.e. the strengthening or weakening of synaptic transmission (Bliss and Lømo, 1973). Donald Hebb postulated already in 1949 that the underlying mechanism of learning and memory requires changes in synaptic strength (Hebb, 1949; Nicoll, 2017). Experimental evidence for this concept originated more than 20 years later with the discovery of long-term potentiation (LTP) in the hippocampus. It was observed that brief high-frequency stimulations (HFS) of the perforant path fibers led to rapid and sustained increase of the synaptic strength of granule cells in the dentate gyrus (Bliss and Lømo, 1973). Similar was then also observed for CA1 pyramidal neurons after SC stimulation (Andersen et al., 1977). I.e. the same presynaptic stimulus applied before the synaptic potentiation evoked larger postsynaptic responses after potentiation. Although there are different mechanism to induce LTP (Nicoll, 2017), potentiation of hippocampal CA1 synapses was shown to rely on the activation of the postsynaptic NMDARs (Collingridge et al., 1983). The NMDAR requires for its activation in addition to glutamate binding, the binding of the coagonist D-serine (Mothet et al., 2000; Priestley et al., 1995) or glycine (Johnson and Ascher, 1987) and a membrane depolarization in order to release the Mg^{2+} block, which prevents the channel from opening during resting conditions (Mayer et al., 1984). A HFS can lead to a membrane depolarization that is sufficient to relief the highly-voltage sensitive Mg^{2+} block of the NMDAR (Mayer et al., 1984). The activation of the NMDAR results in a Ca^{2+} influx (Ascher and Nowak, 1988; MacDermott et al., 1986; Schiller et al., 1998) that was shown to mediate the induction of LTP (Lynch et al., 1983). The following expression of LTP involves the activation of different Ca^{2+}-dependent protein kinases (Herring and Nicoll, 2016; Malenka and Bear, 2004) that results, for instance, in an increase of the AMPAR conductance (Soderling and Derkach, 2000), the insertion of additional AMPARs (Isaac et al., 1995; Liao et al., 1995; Shi et al., 1999) and finally in an increased synaptic strength.

Astrocytes were shown to provide and release the NMDAR coagonist D-serine (Mothet et

al., 2005; Schell et al., 1995) in a Ca^{2+}-dependent manner and thereby control synaptic plasticity (Henneberger et al., 2010; Panatier et al., 2006). In summary, astrocytes do not only modulate synaptic transmission but also synaptic plasticity by the release of gliotransmitter.

1.6 Astrocytes and epilepsy

In addition to their importance for physiological brain functions, malfunction of astrocytes was found in many neurodegenerative diseases, such as epilepsy (Steinhäuser et al., 2015). Epilepsy is a neurological disorder and characterized by unpredictable abnormal electrical brain activity that can cause body convulsions ('seizures') (Chang and Lowenstein, 2003; Jefferys, 1990; Steinhäuser et al., 2015). Approximately 0.5-1% of the world's population suffers from epilepsy (Sander and Shorvon, 1996). A common type of epilepsy is the mesial temporal lobe epilepsy (MTLE) that is characterized by seizures originating in the hippocampal formation (Andersen et al., 2007; King and Spencer, 1995). MTLE is often associated with a hippocampal sclerosis that is characterized among others by hippocampal neuronal loss and astrogliosis (Thom, 2014). In general, astrogliosis can be observed in response to various brain injuries or other pathological conditions and describes the malfunction of astrocytes. This is associated with several molecular and cellular alterations, such as increased astrocyte proliferation and morphology changes (Pekny and Pekna, 2014; Sofroniew and Vinters, 2010). Historically, research on epilepsy focused on the role of neurons and resulted in the development of several anti-epileptic drugs (Vossler et al., 2018). However, these drugs mainly focus on neuronal functions and treat rather the symptoms than the underlying disorder (Bedner et al., 2015; Löscher and Schmidt, 2011). On the other hand, more recent studies focused on the potential involvement of astrocytes in the context of epilepsy due to their significant involvement in many basic brain function (Seifert and Steinhäuser, 2013; Seifert et al., 2006, 2010; Steinhäuser et al., 2015). Interestingly, astrocytes in resected hippocampi from patients suffering from pharmacoresistant MTLE exhibited an abnormal morphology and a complete lack of gap junction coupling as reported by Bedner and colleagues in 2015. In the same study, a mouse model that reproduced the key features of human MTLE then revealed that astrocyte uncoupling preceded neuronal death and the generation of spontaneous seizures. This indicated that astrocyte dysfunction might cause the generation of MTLE (Bedner et al., 2015). Several other studies focused on the molecular and cellular mechanisms underlying a proepileptiform effect of astrocyte malfunction (Steinhäuser et al., 2015).

One of these mechanisms that is believed to underlie epileptic activity is an impaired

extracellular K^+ clearance (Chapter 1.4.1 and 1.4.2). Indeed, the expression of the predominant astrocytic K^+ channel Kir4.1 was found to be reduced in sclerotic hippocampi from MTLE patients (Das et al., 2012; Heuser et al., 2012). This finding was further corroborated by extracellular K^+ elevations that were augmented after acute inhibition of Kir4.1 channels in non-sclerotic hippocampal slices from humans and rats, whereas this was not the case in sclerotic tissue (Heinemann et al., 2000; Jauch et al., 2002; Kivi et al., 2000). Furthermore, astrocyte uncoupling via the genetic deletion of Cx30 and 43 resulted in slowed K^+ uptake and increased epileptiform activity which was explained by impaired spatial K^+ buffering (Wallraff et al., 2006).

In addition, impaired glutamate clearance (Chapter 1.4.3) has been proposed to be involved in the generation of epileptic activity (Demarque et al., 2004; During and Spencer, 1993; Tanaka et al., 1997). Indications for that originated from a study by During and Spencer in 1993 that investigated the concentration of glutamate in the hippocampus of epilepsy patients via microdialysis. It turned out that the glutamate concentration before seizure onset was higher in the epileptic hippocampus compared to the contralateral site which points towards an impaired glutamate clearance in the epileptic hippocampus (During and Spencer, 1993). Although the impact of an altered glutamate transporter expression and function was investigated by several experimental approaches that led to controversial results (Steinhäuser et al., 2015), it is not unlikely that impaired glutamate clearance contributes to epileptic activity. This is supported by the occurrence of spontaneous seizures in mice with impaired glutamate clearance by the genetic deletion of the glutamate transporter GLT-1 (Tanaka et al., 1997) or the direct infusion of a pharmacological inhibitor for glutamate transporters (Demarque et al., 2004).

Another astrocytic mechanism that could be involved in the generation of epileptic activity is the glutamate/GABA-glutamine cycle (Eid et al., 2004, 2008; Ortinski et al., 2010). This cycle comprises the uptake of extracellular glutamate or GABA by astrocytes, the conversion into glutamine by the enzyme glutamine synthetase (GS), the release of glutamine back into the ECS and its uptake by neurons, where it is metabolized back to glutamate or GABA (Bak et al., 2006). Since intracellular glutamate accumulations were shown to slow down glutamate transporter currents (Otis and Jahr, 1998), impaired GS activity could mediate such a glutamate accumulation and impair extracellular glutamate clearance. Indeed, decreased levels of GS were found in hippocampi from MTLE patients (Eid et al., 2004). Furthermore, the infusion of a pharmacological inhibitor of GS in the rat hippocampus evoked recurrent seizures (Eid et al., 2008). On the other hand, impaired inhibitory synaptic transmission could also underlie epileptic activity as suggested by Ortinski and colleagues. Interestingly, virally-induced astrogliosis in mice hippocampi reduced GS expression and inhibitory synaptic transmission onto CA1 pyramidal neurons

while excitatory transmission was unaffected. It was argued that these findings originated from an interrupted glutamine supply to neurons and consequently an impaired GABA production (Ortinski et al., 2010).

Moreover, astrocytic Ca^{2+} signaling and concomitant gliotransmission (Chapter 1.5) have often been associated with epileptic activity (Carmignoto and Haydon, 2012; Henneberger, 2017). Interestingly, the expression of astrocytic mGluRs that are known to mediate astrocytic Ca^{2+} signaling was increased in an epilepsy animal model (Aronica et al., 2000; Ulas et al., 2000). In fact, it was shown that astrocytes respond with Ca^{2+} elevations during epileptiform activity (Fellin et al., 2006; Gómez-Gonzalo et al., 2010; Tian et al., 2005). In addition, it was shown by Gómez-Gonzalo and colleagues that during conditions of enhanced neuronal excitability in the entorhinal cortex, evoked astrocytic Ca^{2+} signaling was associated with NMDAR-mediated inward currents in EC neurons and was able to promote ictal-like epileptiform discharges. Furthermore, the local subthreshold application of NMDA alone failed to evoked ictal discharges in this study, but in combination with the activation of astrocytes ictal-like discharges were evoked. Conversely, inhibition of Ca^{2+} signaling attenuated ictal-like epileptiform activity (Gómez-Gonzalo et al., 2010). In addition, impairing the machinery for vesicular release in astrocytes also reduced the frequency of seizures in vivo as well as epileptiform activity in hippocampal slices (Clasadonte et al., 2013). The authors argued that these findings were based on an impaired astrocytic glutamate release and the concomitant reduced activation of extrasynaptic NMDARs that were previously indicated to favor synchronize neuronal activity (Fellin et al., 2004). However, other gliotransmitters, such as D-serine (Henneberger et al., 2010), could also underlie these observations. Taken together, there are several indications that abnormal astrocytic Ca^{2+} signaling and gliotransmission can reduce the threshold for the generation of epileptiform activity via a positive feedback loop that might integrate neuronal activity and enhance excitability (Steinhäuser et al., 2015).

As already mentioned above, gliotransmission could also have an inhibitory effect by reducing the inhibition on inhibitory interneurons via mGluR activation (Liu et al., 2004b) or by increasing inhibitory input on excitatory neurons via ATP/adenosine signaling (Matos et al., 2018). Whether an impairment of these inhibitory effects could lead to neuronal hyperexcitability and, thus, be involved in epileptic activity remains speculative since the interactions of astrocytes and inhibitory interneurons during epilepsy are incompletely understood. Taken together, astrocytes possess various mechanisms in order to modulate neuronal functions. However, plenty of studies indicated that a malfunction of these mechanisms is involved in epileptic activity.

1.6.1 Proepileptiform astrocyte morphology changes

Astrocytes contact synapses with their fine peripheral processes (Ventura and Harris, 1999; Witcher et al., 2007), which enable them to modulate many neuronal functions (Araque et al., 1999; Perea and Araque, 2010). Consequently, alterations of this spatial relationship could impair the neuron-astrocyte signaling and act proepileptiform by, for instance, amplifying, prolonging or disinhibiting neuronal activity (Henneberger, 2017). Indeed, an abnormal astrocyte morphology was observed in the hippocampus of patients suffering from MTLE (Bedner et al., 2015). In addition, loss of the nonoverlapping astrocytic domain organization was observed in different mouse models of epilepsy (Oberheim et al., 2008). However, these morphology changes represent rather long-term alterations and provide no information about astrocyte morphology changes during the onset of epileptiform activity. Since fine astrocytic processes are highly motile and show structural plasticity in response to neuronal activity (Bernardinelli et al., 2014; Haber et al., 2006), astrocyte morphology changes could rapidly occur during the onset of epileptiform activity and facilitate neuronal excitability.

Previous unpublished work from our laboratory by Dr. S. Anders revealed that the induction of epileptiform activity in acute hippocampal slices led to rapid astrocyte morphology changes (Anders, 2016). The main results of this study originated from experiments based on the penicillin-induced epilepsy model. This model utilizes the ability of penicillin G to inhibit the $GABA_AR$ mediated Cl^- flux (Tsuda et al., 1994) and the corresponding disinhibition, which results in an increased neuronal excitability. The proconvulsive action of penicillin was first observed during the Second World War with patients that generated body convulsions upon intraventricular application of penicillin in order to treat their head injuries (Walker et al., 1945). Based on these observations, the penicillin-induced epilepsy model was established and allowed the induction epileptiform activity in vivo by intraperitoneal injection (Chen et al., 1986) or direct application of penicillin to the hippocampus (Dichter and Spencer, 1969) and in vitro by the perfusion of hippocampal slices with a penicillin containing solution (Schwartzkroin and Prince, 1977). In contrast to other epilepsy models, such as the kainate or pilocarpine epilepsy model (Curia et al., 2008; Lévesque and Avoli, 2013; Turski et al., 1984) that induce epileptic activity by the injection of the particular epileptogenic agent into a living animal, the acute application of penicillin to hippocampal slices simplifies investigations by allowing direct manipulation of the extracellular ion concentrations or the application of drugs (Schwartzkroin and Prince, 1977). In the aforementioned work, Dr. S. Anders observed that the acute application of penicillin to hippocampal slices obtained from rats and mice led to the induction of epileptiform discharges, which were accompanied by a significant shrinkage of the fine peripheral astrocytic processes in the CA1 str. radiatum (Figure 6).

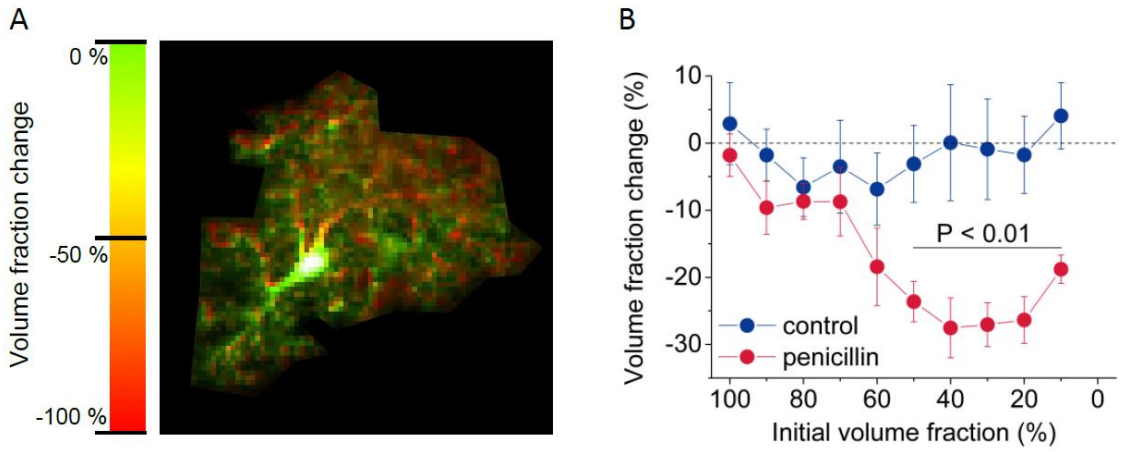

Figure 6 Epileptiform activity induced astrocyte morphology changes of the fine and medium-large processes. A) This image depicts a color- and brightness-coded example of an astrocyte. The initial astrocytic volume fraction (a measure for the relative volume occupied by the astrocyte) is encoded by the brightness. At its soma, the astrocyte occupies the entire volume and thus shows the brightest pixels. In contrast, the fine astrocytic processes in the periphery do not occupy the entire volume of the territory and thus show a lower brightness. The color encodes the relative change of the volume fraction in percent, i.e., greenish structures did not change their volume fraction, whereas structures depicted in red showed a substantial reduction of their initial volume fraction. **B)** Quantification of the astrocyte morphology changes that were induced by the application of penicillin and the concomitant epileptiform activity. It was shown that the reduction of the volume fraction, i.e. the shrinkage of the astrocytic structures, was most prominent for the structures with a low initial volume fraction such as fine and medium-large astrocyte processes. Reproduced from Anders (2016).

These morphology changes occurred within minutes after the onset of the epileptiform discharges and persisted after the penicillin was removed and inhibitory synaptic transmission was restored. Importantly, the epileptiform discharges persisted as well after the inhibitory synaptic transmission was restored. It was further shown that the astrocytic morphology changes were presumably mediated by the reorganization of the actin cytoskeleton since inhibition of the Rho associated protein kinase (ROCK) prevented the morphology changes (Anders, 2016). Rho is among Rac and Cdc42 a small GTPase that is involved in cytoskeletal reorganizations. Their down-stream effector is ROCK which phosphorylates several substrates involved in cellular morphology (Amano et al., 2010). For example, ROCK was shown to phosphorylate the LIM-kinase that in turn prevents actin depolymerization by phosphorylating cofilin (Maekawa et al., 1999). Furthermore, it was demonstrated that the inhibition of ROCK induced stellation of cultured astrocytes (Höltje et al., 2005; Racchetti et al., 2012). Thus, Dr. Anders suggested that the Rho-ROCK pathway was a key regulator for the astrocyte morphology changes. Interestingly,

inhibition of the ROCK-pathway not only prevented the changes in the astrocyte morphology, but it also reduced the frequency of epileptiform discharges. This indicates that the alterations in the astrocytic morphology facilitated the persistence of the epileptiform discharges by a proepileptiform mechanism. Although it was demonstrated that the altered morphology was accompanied by a reduced intra- and intercellular diffusion, the exact underlying mechanism that maintains the persistent epileptiform discharges and the mechanistic link between morphology changes and epileptiform activity remained unclear (Anders, 2016).

2 Aim of the study

The view on astrocytes has changed dramatically in the last decades. Form being considered as merely “nerve glue” in the early stages of neuroscience, astrocytes turned out to be active elements of the brain that shape neuronal activity. Although the involvement of astrocytes in many brain functions is continuously being unraveled, many mechanisms are still under debate and need further investigation. Especially the role of astrocytes in pathophysiological conditions, such as epilepsy, is of high interest since astrocytes could be a new target for therapeutic approaches. Therefore, this study answered the two following questions.

Does acute inhibition of gap junction channels and the disruption of the astrocyte network impair extracellular K^+ clearance?

Gap junction coupling and the formation of an extensive network is a key feature of astrocytes (Giaume et al., 2010; Nagy and Dermietzel, 2000). This network has been proposed to facilitate extracellular K^+ clearance by a concept known as ‘spatial K^+ buffering’. This concept comprises the spatial distribution of K^+ from sites with an elevated extracellular K^+ concentration to sites with a lower extracellular K^+ concentration via the gap junction channels (Orkand, 1986). Indeed, a disruption of this network by an astrocyte specific gene deletion of the gap junction channel-forming connexins was found to impair extracellular K^+ clearance and affect neuronal excitability (Pannasch et al., 2011; Wallraff et al., 2006; Xu et al., 2009). However, this genetic deletion was later shown to affect the astrocyte morphology (Ghézali et al., 2018; Pannasch et al., 2014) which could have altered K^+ clearance independently from gap junction channels. Another study revealed impaired K^+ clearance after the pharmacological inhibition of gap junctions channels in vivo (Bazzigaluppi et al., 2017). However, these pharmacological inhibitors are known to be unspecific, e.g. they also block neuronal gap junctions, and have other side effects on neurons (Rouach et al., 2003; Tovar et al., 2009). Therefore, the altered extracellular K^+ concentration could have been caused by effects on neuronal activity-dependent K^+ release and thus prevent a clear interpretation. The aim of this present study was to elucidate if and under which conditions astrocytic gap junction coupling contributes to K^+ clearance. In order to circumvent the experimental limitations of previous studies, a pharmacological approach was employed in order to acutely disrupt the astrocyte network and to avoid long-term developmental adaptions of astrocytes. Furthermore, the potential side effects of the gap junction inhibitors on neuronal activity-dependent K^+ release were

minimized in the majority of experiments by an iontophoretic K^+ application in the absence of neuronal activity. Thus, this study provides new insights into the conditions in which gap junction channels contribute to extracellular K^+ clearance.

Which mechanism underlies the proepileptiform effect of rapid astrocyte morphology changes and uncoupling?

Previous work from our laboratory has demonstrated that the induction of epileptiform activity leads to rapid morphology changes of astrocytes. These morphology changes comprised the shrinkage of the fine peripheral astrocyte processes. Preventing the morphology changes by inhibition of the ROCK-pathway resulted in an attenuation of the epileptiform activity which indicates a proepileptiform effect of the morphology changes (Anders, 2016). Since astrocytes locate their fine processes in close proximity to synapses, they are able to regulate synaptic transmission via the clearance of glutamate, K^+ or the Ca^{2+}-dependent release of gliotransmitter (Perea and Araque, 2010; Rose et al., 2018; Walz, 2000). Impairments of this tight interplay could, in turn, lead to neuronal hyperexcitability and a reduced threshold for epileptiform activity (Henneberger, 2017). The observed morphology changes after induction of epileptiform activity were accompanied by an reduced intra- and intercellular diffusion (Anders, 2016). Consequently, intracellular Ca^{2+} signaling could be impaired which, in turn, might affect gliotransmission that modulates inhibitory synaptic transmission. In addition, Na^+-dependent glutamate clearance could be impaired by increased intracellular Na^+ accumulations (Karus et al., 2015) or by an impaired surface diffusion of glutamate transporters (Henneberger, 2017; Murphy-Royal et al., 2015). Furthermore, a facilitated activity-dependent ECS shrinkage was previously observed in hippocampal slices with coupling-deficient astrocytes (Pannasch et al., 2011). In turn, the observed impaired intra- and intercellular diffusivity in astrocytes after epileptiform activity could facilitate astrocytic swelling and the shrinkage of the ECS. Consequently, the extracellular ion and neurotransmitter homeostasis could be distorted and mediate the proepileptiform effect. These scenarios could hypothetically underlie the observed proepileptiform effect of the astrocytic morphology changes. Therefore, spontaneous inhibitory synaptic transmission onto CA1 pyramidal cells, the clearance of extracellular glutamate and K^+, and the structure of the ECS were investigated when epileptiform activity was induced and compared to control conditions.

3 Materials & Methods

3.1 Animals

All used animals in this study were handled according to the European Union and national government regulations. Male Wistar rats and FVB (Friend leukemia virus B) mice were purchased from Charles River (Sulzlfeld, Germany) and kept in the 'Haus für experimentelle Tiermedizin' of the University Hospital Bonn with a 12h/12h dark-light cycle until they were used for experiments. The other transgenic mice (APP/PS1 and CCL17KO) were obtained from the animal facilities of the 'Deutsches Zentrum für Neurodegenerative Erkrankungen' (DZNE) and the 'Life & Medical Sciences-Institut' (LIMES).

3.2 Drugs and chemicals

Table 1 Drugs and chemicals

Compound	Supplier
Alexa Fluor 488 Hydrazide	Thermo Fisher Scientific, Waltham, US
Alexa Fluor 594 Hydrazide	Thermo Fisher Scientific, Waltham, US
Ascorbic acid	AppliChem GmbH, Darmstadt, Germany
Atipamezol (Antisedan®)	Orion Pharma GmbH, Hamburg, Germany
ATP (disodium salt)	AppliChem GmbH, Darmstadt, Germany
Bepanthen®	Bayer AG, Leverkusen, Germany
$CaCl_2$ 1M solution	Sigma Aldrich, St. Louis, US
Carbenoxolone	Sigma Aldrich, St. Louis, US
Carprofen (Rimadyl®)	Zoetis, New Jersey, US
D-APV	Abcam, Cambridge, UK
di(Tris)-Phosphocreatine	Sigma Aldrich, St. Louis, US
Dichloromethane	Sigma Aldrich, St. Louis, US
Dimethylsulfoxid	Sigma Aldrich, St. Louis, US
Ethanol 99%	AppliChem GmbH, Darmstadt, Germany
Fentanyl	Rotexmedica, Trittau, Germany
Flumazenil	Braun, Melsungen, Germany
Gentamicin (Refobacin®)	Almirall, Barcelona, Spain
Glucose	AppliChem GmbH, Darmstadt, Germany

GTP (sodium salt)	Sigma Aldrich, St. Louis, US
HEPES	AppliChem GmbH, Darmstadt, Germany
IE190	WPI, Sarasota, USA
Isofluran (Forene®)	AbbVie, Mainz, Germany
KCl	AppliChem GmbH, Darmstadt, Germany
KOH	Sigma Aldrich, St. Louis, US
L-glutamic acid	AppliChem GmbH, Darmstadt, Germany
LY341495	Tocris, Bristol, UK
Meclofenamic acid	Sigma Aldrich, St. Louis, US
Medazolam	Rotexmedica, Trittau, Germany
Medetomidin (Domitor®)	Orion Pharma GmbH, Hamburg, Germany
Methanosulfonic acid	Sigma Aldrich, St. Louis, US
$MgCl_2$ ($6xH_20$)	AppliChem GmbH, Darmstadt, Germany
$MgSO_4$ ($7x\ H_2O$)	AppliChem GmbH, Darmstadt, Germany
MRS2179	Tocris, Bristol, UK
NaCl	AppliChem GmbH, Darmstadt, Germany
NaH_2PO_4	AppliChem GmbH, Darmstadt, Germany
$NaHCO_3$	AppliChem GmbH, Darmstadt, Germany
Naloxon	Braun, Melsungen, Germany
NaOH	AppliChem GmbH, Darmstadt, Germany
NBQX (disodium salt)	Abcam, Cambridge, UK
Penicillin G (sodium salt)	Sigma Aldrich, St. Louis, US
Potassium ionophore I - cocktail A	Sigma Aldrich, St. Louis, US
Potassium ionophore I - cocktail B	Sigma Aldrich, St. Louis, US
QX314 chloride	Tocris, Bristol, UK
Sodium pyruvate	AppliChem GmbH, Darmstadt, Germany
Sucrose	AppliChem GmbH, Darmstadt, Germany
Tetramethylammonium chloride	Sigma Aldrich, St. Louis, US
Texas Red Dextran	Thermo Fisher Scientific, Waltham, US
Trimethylchlorosilane	Sigma Aldrich, St. Louis, US
TTX citrate	Abcam, Cambridge, UK
Xylocain	Astra Zeneca, Wedel, Germany
Y27632 dihydrochloride	Abcam, Cambridge, UK

3.3 Preparation of acute brain slices

In order to anesthetize the animals, ~1 ml isoflurane was dropped onto a tissue in a glass cylinder with a volume of 10 l. After the isoflurane vaporized, the animal was placed in the glass cylinder until it fell asleep. The state of anesthesia was tested by gently pinching the hind paws of the animal. When the animal showed no motor reaction upon the pinch, the animal was considered as deeply anesthetized. Then, the rat or mouse was quickly decapitated with a guillotine or a pair of scissors, respectively. The fur of the head was then cut with a scalpel to expose the skull and the head was put in ice-cold slicing solution (Table 2), which was bubbled with carbogen (95% O_2 / 5% CO_2) for 15 minutes before use.

Table 2 Slicing solution

	Concentration (mM)	**Osmolartiy (mOsm/kg)**	**MW (g/ml)**
Sucrose	105.00	105.00	342.30
NaCl	60.00	120.00	58.44
KCl	2.50	50.00	74.56
$MgCl_2$ $6H_20$	7.00	21.00	203.30
NaH_2PO_4	1.25	2.50	119.98
Ascorbic acid	1.30	1.30	176.12
Sodium pyruvate	3.00	6.00	110.00
$NaHCO_3$	26.00	52.00	84.01
Glucose	10.00	10.00	180.16

+ 0.5 mM $CaCl_2$ (1 M stock solution), osmolarity 300-310 mOsm/kg, pH 7.4

Next, the skull was cut with small scissors along the midline from posterior to anterior, opened to the sides and the brain was removed. The brain was then cut with a steel blade (Ted Pella Inc.,Redding, USA) in a petri-dish filled with ice-cold slicing solution. The forebrain and cerebellum were removed, the two hemispheres were separated along the midline and were cut on the dorsal and ventral site in order to create an even plane. The two hemispheres were subsequently glued with their dorsal sides to a metal holder. The metal holder was then inserted into the slicing chamber that was filled with constantly carbogen-bubbled ice-cold slicing solution. A vibratome equipped with a ceramic blade (Campden Instruments, Loughborough, UK) was used to cut the brain horizontally into 300 or 350 µm thick slices, which were stored in the slicing chamber until the slicing

procedure was finished. Afterwards, the brain slices were stored in a beaker filled with slicing solution in a water bath (Grant Instruments, Shepreth, UK) at 34°C for 15 minutes on a net in a custom-made holder. Finally, the brain slices were transferred into a beaker filled with carbogen-bubbled artificial cerebrospinal fluid (aCSF; Table 3) and stored at room temperature for at least one hour before being used for experiments.

Table 3 Artificial cerebrospinal fluid (aCSF)

	Concentration (mM)	**Osmolartiy (mOsm/kg)**	**MW (g/mol)**
NaCl	131.00	262.00	58.44
KCl*	3.00 (4.00)	6.00 (8.00)	74.56
$MgSO_4$ $7H_2O$	1.30	2.60	246.48
NaH_2PO_4	1.25	2.50	119.98
$NaHCO_3$	21.00	42.00	84.01
Glucose	10.00	10.00	180.16

+ 2 mM $CaCl_2$ (1 M stock solution), osmolarity 297-303 mOsm/kg, pH 7.4

* [KCl] was increased to 4 mM in a subset of experiments

3.4 Electrophysiology

3.4.1 Electrophysiological setups

The electrophysiological setups were placed on a vibration isolated table in a Faraday cage in order to minimize movements and electrical interference from the surroundings. Electrophysiological recordings were performed either in a submersion-type recording chamber (Figure 7) or in an interface-type recording chamber (Figure 8).

The submersion-type chamber was constantly supplied with carbogen-bubbled aCSF solution at a rate of 3-5 ml/min via a perfusion system made of two separate 50 ml aCSF reservoirs connected to the submersion-type chamber via a three-way valve and a silicon tube. While entering the chamber, the temperature of aCSF was increased by a heater to 34°C and monitored using a sensor in the chamber (Warner Instruments, Hamden, USA). At the opposing site of the chamber the aCSF was removed by a peristaltic pump and returned to one of the reservoirs. In order to avoid movements of the brain slice during the experiment, a “harp” (nylon-twines between a U-shaped platinum wire) was placed on top of the brain slice. The submersion-type chamber was mounted below a microscope

(Scientifica, Uckfield, UK or Olympus, Tokyo, Japan; Chapter 3.8.1) equipped with a camera in order to display the light microscopy view on a monitor. Under visual control, one manually and two electrically driven micromanipulators were used to position the electrodes in the chamber under the objective. A concentric bipolar stimulation electrode (CBARC75; FHC, Bowdoin; USA) was attached to the manually driven micromanipulator and connected to a stimulus isolator, which was used to set the stimulation intensity. Depending on the conducted experiments, headstages with pipette holders for patch-clamp recordings (Chapter 3.4.3 & 3.4.4), extracellular field recordings (Chapter 3.4.2), extracellular ion-selective recordings (Chapter 3.6.3 & 3.6.4) and iontophoretic applications (Chapter 3.5) were mounted onto the two electrically driven micromanipulators. The signals from the patch-clamp, extracellular field and ion-selective recordings were then cleared from 50 Hz electrical interferences (HumBug, Quest Scientific Instruments, North Vancouver, CA) and digitalized with an analogue digital converter (Digidata 1440A, Molecular Devices, San Jose, USA). The analogue digital converter was also used to trigger the stimulus isolator (DS3, Digitimer Ltd., Welwyn Garden City, UK) and to control the iontophoresis amplifier. Recordings and stimulations were controlled by the software Clampex (Molecular Devices, San Jose, USA) and stored on a computer for further analysis.

The interface-type recording chamber (custom-made by the lab of Prof. Dr Heinemann, Charité-Universitätsmedizin Berlin, Germany) was equipped with a water reservoir, which was heated to 34°C and constantly bubbled with carbogen. Two openings allowed constant supply of the carbogen to the recording chamber and created a warm and humid atmosphere. The aCSF was stored in a reservoir, constantly bubbled with carbogen and supplied to the recording chamber via a silicon tube at a rate of 3-5 ml/min. The silicon tube was partly guided through the water reservoir in order to warm up the aCSF before entering the chamber. At the opposite side of the chamber, the aCSF was removed and returned to the reservoir via a peristaltic pump. Under visual control by a binocular loupe, a bipolar stimulation electrode and headstages with pipette holders for extracellular field (Chapter 3.4.2) and K^+ recordings (Chapter 3.6.3) were positioned in the brain slice by manually-driven micromanipulators. The recorded signals were then cleared from 50 Hz electrical interferences (HumBug, Quest Scientific Instruments, North Vancouver, CA) and digitalized with an analogue digital converter (USB-6221, National Instruments, Austin, USA), which was connected to a computer. For electrical stimulation, the analogue digital converter triggered a stimulus isolator (DS3, Digitimer Ltd., Welwyn Garden City, UK) that set the stimulus intensity of the stimulation electrode (CBARC75; FHC, Bowdoin, USA). The software WinWCP (V.4.8.9, Strathclyde Electrophysiology Software, Glasgow, UK) was used to control the stimulations and to store the recordings for further analysis on the

computer. At both experimental setups, pharmacological agents were added from a stock solution directly to the perfusion system. Unless stated differently, all stock solutions were prepared with distilled H_2O.

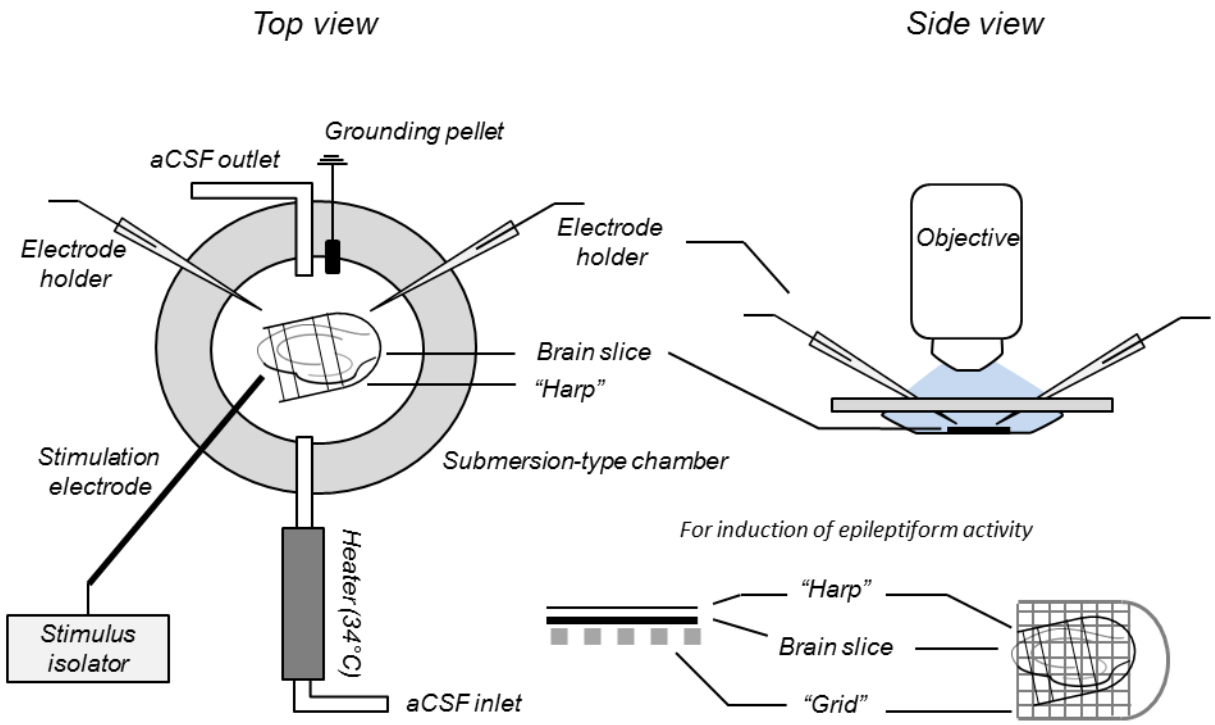

Figure 7 The submersion-type recording chamber was incorporated into a two-photon excitation fluorescence microscope system. The brain slice was placed on the bottom of the chamber and observed with an objective from above. For light microscopy, the brain slice was illuminated from below with an infrared light source, while the laser beam for two-photon excitation microscopy came through the objective from above. The supplied aCSF was heated to 34°C and removed by a peristaltic pump on the other site of the chamber. In order to prevent the brain slice from moving, a "harp" was placed on top. Electrodes for recording and stimulation were positioned under visual control in the brain slice. A silver-chloride grounding pellet in the chamber was connected to the used headstages**,** the vibration isolated table and a grounding point. For the induction of epileptiform activity, the brain slices were placed on top of a "grid" in order to improve the aCSF perfusion.

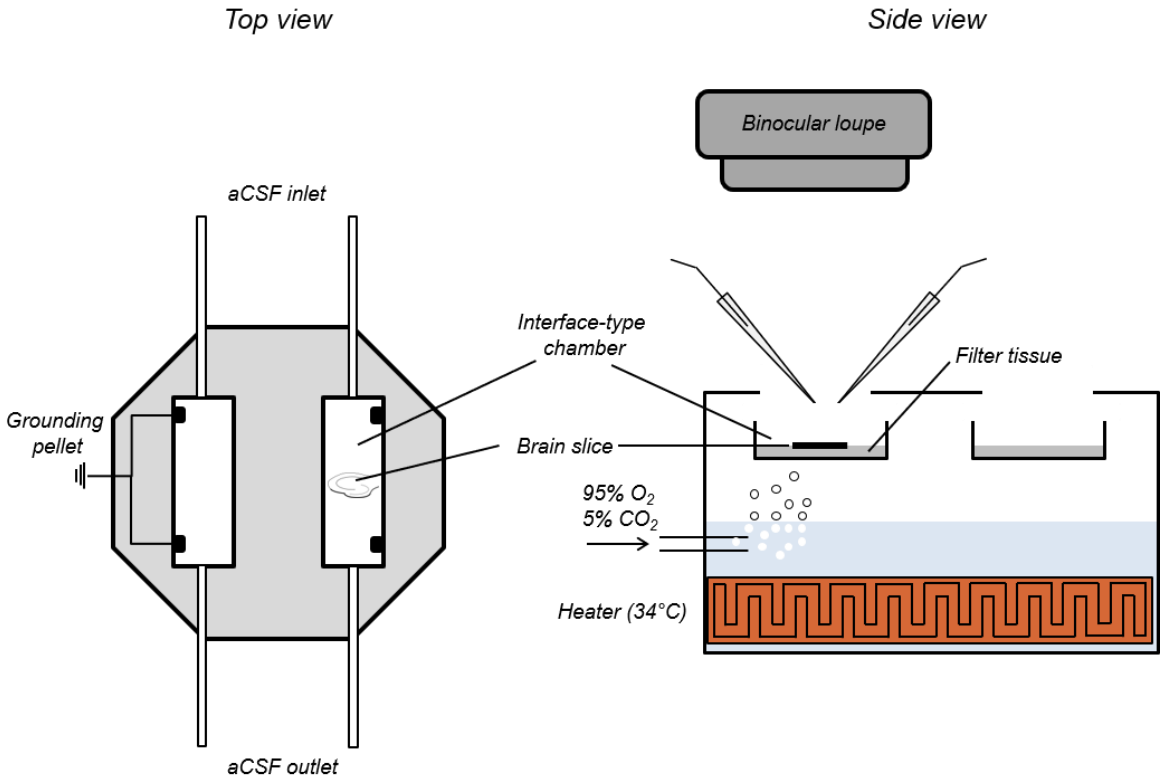

Figure 8 The interface-type recording chamber was heated to 34°C by the underlying water-bath and constantly supplied with carbogen. Two layers of filter tissue covered the bottom of the chamber in order to distribute the supplied aCSF evenly. The brain slice was then transferred on top of a small piece of filter tissue into the recording chamber. Stimulation and recordings electrodes were positioned under visual control of a binocular loupe in the brain slice. Two silver-chloride grounding pellets in the chamber were connected to the used headstages**,** the vibration isolated table and a grounding point.

3.4.2 Extracellular field recordings

In order to record in the submersion-type chamber (Chapter 3.4.1), a hippocampal slice was transferred within the large end of a Pasteur glass pipette from the storage beaker into the chamber and the “harp” was placed on top. Next, a glass capillary with filament (GB150F-10, Science Products, Hofheim, Germany) was pulled with a horizontal pipette puller (Model P-1000, Sutter Instruments, Novato, USA), filled with ~5 µl aCSF (Table 3) and mounted onto the pipette holder (G23 Instruments, London, UK) of the headstage (Multiclamp 700b, Molecular Devices, San Jose, USA). The pipette holder contained a Teflon-coated silver wire with a silver-chloride coated tip that connected the aCSF with the headstage. The pipettes for field recordings had resistances of ~3-5 MΩ and a tip size of around 1-3 µm. Field potentials were recorded as a direct-current (DC) signal in the current-clamp (CC) mode. For this purpose, the tip of the recording pipette was placed in the CA1 str. radiatum and/or str. oriens close to the pyramidal cell layer at a depth of 40 to

100 µm in the brain tissue. In order to activate SCs and, in turn, evoke axonal and field excitatory postsynaptic potentials (fEPSPs), the bipolar stimulation electrode was placed in the str. radiatum at the border of the CA3/CA1 region. Field potentials were recorded at a sampling frequency of 20-33 kHz and low-pass filtered (Bessel characteristics) at a cut-off frequency of 6-10 kHz.

For recordings in the interface-type recording chamber (Chapter 3.4.1), the bottom of the recording chamber was covered with a layer of filter tissues in order to distribute the aCSF. Small pieces cut from tights placed on top of the filter tissues at the edges of the chamber limited the level of aCSF. Next, a hippocampal slice was transferred on top of a ~1x1 cm piece of filter tissue from the storage beaker into the recording chamber. That way, the hippocampal slice was placed at the interface of aCSF and the carbogen. In order to record field potentials, glass pipettes were pulled, filled with aCSF and inserted into the pipette holder of the headstage (EXT-02B, npi electronic, Tamm, Germany) as described above. The field potentials were evoked with a bipolar stimulation electrode placed at the border of the CA3/CA1 region and recorded in the CA1 str. radiatum and/or str. oriens close to the pyramidal cell layer as an alternating current (AC) signal. The signals were recorded at a sampling frequency of 10-20 kHz and then band-passed filtered (0.1 Hz-20 kHz; EXT-02B, npi electronic, Tamm, Germany). The used stimulation protocols and intensities for the specific experiments are indicated in the corresponding method-chapters.

For quantification of the evoked neuronal activity, the axonal fiber volley (FV) amplitude, the fEPSP slope and the paired-pulse ratio (PPR) were analyzed (Figure 9). The FV was recorded in the str. radiatum and reflects the number of axons activated by the electrical stimulation (Andersen et al., 2007). Its amplitude was defined as the most negative potential deflection relative to baseline (potential before stimulation onset) shortly after the end of the stimulation and before the onset of the fEPSP. The synaptic transmission following the axonal activation was quantified by the slope of the corresponding fEPSP since it proportional to the postsynaptic currents. The slope (Equation 1) was measured during the linear rising (str. oriens close to str. pyramidale) or falling phase (str. radiatum) of the evoked fEPSP.

(1)
$$fEPSP\ slope = \frac{y_2 - y_1\ (mV)}{x_2 - x_1\ (ms)}$$

The PPR, an indirect determinant for the presynaptic release probability, was calculated from the slopes of two consecutively evoked fEPSPs (Equation 2). A PPR > 1 represents a paired-pulse facilitation and is mediated by a higher presynaptic neurotransmitter

release during the second stimulation. This occurs when the release probability is low and, thus, more neurotransmitter containing vesicles remain in the presynaptic terminal after the first stimulation. These then increase the pool of releasable vesicles during the second stimulation and lead to a larger postsynaptic response (Debanne et al., 1996).

(2) $$PPR = \frac{fEPSP\ slope\ 2}{fEPSP\ slope\ 1}$$

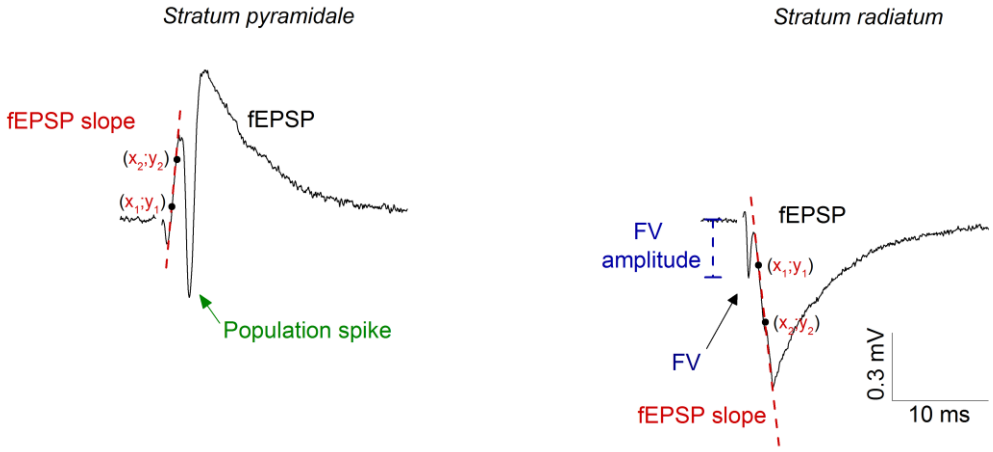

Figure 9 Properties of evoked field potentials. Examples of evoked field potentials by Schaffer collateral (SC) stimulation recorded in the CA1 str. pyramidale (Left) and str. radiatum (Right) (Stimulation artifacts were removed). In the str. pyramidale, axonal stimulation evoked field excitatory postsynaptic potentials (fEPSP) consisting of a positive voltage deflection and a population spike (green) of negative polarity. In the str. radiatum, a fiber volley (FV), representing the axonal activation, and a fEPSP of negative polarity were recorded upon SC stimulation. The slopes (red dashed lines) were determined in the linear rising or falling phase (between the two black dots) of the fEPSPs. The amplitude of the FV (blue dashed line, right panel) was determined from baseline level to the most negative voltage deflection before the onset of the fEPSP.

3.4.3 Whole-cell patch clamp recordings of astrocytes

Whole-cell patch clamp recordings from astrocytes were performed in the submersion-type chamber incorporated in the microscope from Scientifica (Chapter 3.8.1). Astrocytes in the CA1 str. radiatum were identified at a depth of at least 50 µm in a 300 µm thick rat brain slice using the infrared camera view that was augmented by a Dodt contrast. Next, a glass capillary with filament (GB150F-10, Science Products, Hofheim, Germany) was pulled with a horizontal pipette puller (Model P-1000, Sutter Instruments, Novato, USA) and filled with ~5 µl potassium methanesulfonate (KMS) based intracellular solution (Table 4) containing 80 µM Alexa Fluor 594 Hydrazide and 300 µM Texas Red Dextran 3

kDa. The patch pipette was inserted into the pipette holder (G23 Instruments, London, UK) of the headstage (Multiclamp 700b, Molecular Devices, San Jose, USA) as described for extracellular field recordings (Chapter 3.4.2), but was kept in the voltage-clamp (VC) mode. In the VC mode, the patch-pipette is set to a specific potential (holding potential) and the current injected by the amplifier needed to achieve this potential is measured.

Table 4 KMS based intracellular solution

	Concentration (mM)	**Osmolarity (mOsm/kg)**	**MW (g/mol)**
Methanesulfonic acid	135.00	135.00	96.11
KOH	135.00	135.00	56.11
HEPES	10.00	10.00	238.30
di(Tris)-Phosphocreatine	10.00	10.00	453.40
$MgCl_2$ $6H_2O$	4.00	12.00	203.30
Na_2-ATP	4.00	12.00	554.10
Na_X-GTP	0.40	1.60	523.20

438 µl Methanosulfonic acid was mixed with 30 ml dd H_2O. pH was adjusted with 1 M KOH, pH 7.2, osmolarity 290 mOsm/kg

In the bath solution, no holding potential was set and the corresponding current was offset-corrected to zero. Next, a voltage step of -10 mV was repeatedly applied for 100 ms and the amplitude of the corresponding current was used to calculate the resistance of the patch-pipette applying Ohm's law. Patch-pipettes with a resistance of 3.5-5 MΩ were then used for patch clamp recordings of astrocytes. In order to prevent the pipette from clogging while approaching the identified astrocyte in the brain slice, slight positive pressure was applied to the patch-pipette by a 1 ml syringe connected to the pipette holder with a silicon tube. When the pipette tip was positioned in close proximity to the astrocyte soma, a small pit on the cell membrane induced by the positive pressure was visible and the resistance of the pipette increased. At this point, the positive pressure was released from the patch pipette and, in turn, the cell membrane sealed the pipette tip resulting in a resistance of several hundred MΩ. In order to increase the seal resistance, slight negative pressure was applied to the pipette until a resistance of >1 GΩ was established. Then, a holding potential of -70 mV was applied and capacitive artifacts were compensated. Finally, the cell membrane was opened by short suction pulses on the mouthpiece of the syringe holder resulting in electrical contact to the cytoplasm (whole-

cell configuration). In this configuration, originally established by Neher and Sakmann (Neher and Sakmann, 1976), electrical properties of astrocytes were accessed and astrocytes were filled via the pipette with fluorescent dyes (Alexa Fluor 488 & Texas Red Dextran 3 kDa) in order to visualize their morphology and network, respectively (Chapter 3.8.2).

In the whole-cell configuration, the access to the cell cytoplasm is limited by the size of the pipette tip and the quality of the membrane opening. This was quantified by the access resistance (R_a), which was determined in the VC mode by applying a 10 mV voltage step (ΔV) and the corresponding current (Figure 12C). During the initial phase of the voltage step, the current charges the capacitance of the cell membrane (Impedance virtually 0) and is, thus, predominantly defined by R_a. Therefore, R_a was calculated by the peak amplitude of the current (I_{peak}) shortly after the onset of the voltage step and ΔV using Ohm's law (Equation 3) (Numberger and Draguhn, 1996).

(3) $$R_a = \frac{\Delta V}{I_{peak}}$$

Next, the membrane (or input) resistance (R_m) and resting membrane potential (MP) were quantified in the CC mode. In the CC mode, the current injected by the amplifier is defined and the corresponding potential is measured. When no current was applied to the cell, the resting MP defined the measured potential. In order to determine the R_m, a current (ΔI) was applied to the cell in 100 pA steps and the corresponding potential change was recorded (Figure 12B). Since a current injection led to an artificial voltage drop at R_a, the potential was compensated using the bridge balance function. Thus, the R_m was calculated using Ohm's law from ΔI and the membrane potential after a steady state ($V_{steady\ state}$) was reached (when the membrane capacitance was completely charged) (Equation 4).

(4) $$R_m = \frac{V_{steady\ state}}{\Delta I}$$

3.4.4 Whole-cell patch clamp recordings of CA1 pyramidal neurons and inhibitory input

The inhibitory input of CA1 pyramidal neurons was investigated by recording spontaneous inhibitory postsynaptic currents (sIPSC). For this purpose, whole-cell patch clamp recordings from CA1 pyramidal neurons were performed with 300 µm thick rat

hippocampal slices in the submersion-type chamber incorporated in the Scientifica two-photon excitation fluorescence microscope (Chapter 3.8.1). In order to silence excitatory synaptic input and, in turn, isolate $GABA_AR$-mediated currents, 10 µM NBQX and 50 µM D-APV were added to the extracellular solution. The general procedure of patch-clamp recordings of a CA1 pyramidal neuron was similar to the recordings of astrocytes as described in chapter 3.4.3. In contrast, patch-pipettes were filled with a KCl-based intracellular solution in order to obtain isomolar Cl^- concentrations inside and outside the patched cell (Table 5). In addition, 40 µM Alexa Fluor 594 and 2 mM QX314 were added to the intracellular solution to visualize the morphology of the patched neuron and to inhibit voltage-gated sodium channels specifically in the patched neuron, respectively. After establishing of the whole-cell configuration, the neuron was clamped to -70 mV in the VC mode and filled with the intracellular solution for five minutes. Next, sIPSCs were recorded at a sampling frequency of 33 kHz (online low-pass filtered (Bessel characteristics) at a cut-off frequency of 20 kHz) during five periods of five seconds every 30 s. Analysis was performed with pClamp (Molecular Devices, San Jose, USA) using the template-search event detection function to isolate the individual sIPSCs (offline low-pass filtered (RC characteristic) at a cut-off frequency of 1 kHz). In order to determine the decay time constant (τ) and full-width at half maximal amplitude (FWHM), only sIPSCs that were clearly separated from other sIPSCs were analyzed. The FWHM was obtained from single sIPSCs. For the decay time constant, all sIPCSs were first averaged and then analyzed by a monoexponential decaying function ($y = A \times \exp(-x/\tau)$) from 90% of the sIPSC amplitude back to baseline.

Table 5 KCl based intracellular solution

	Concentration (mM)	**Osmolartiy (mOsm/kg)**	**MW (g/mol)**
KCl	135.00	270.00	74.56
HEPES	10.00	10.00	238.30
di(Tris)-Phosphocreatine	10.00	10.00	453.40
$MgCl_2$ $6H_2O$	2.00	6.00	203.30
Na_2-ATP	4.00	12.00	554.10
Na_X-GTP	0.40	1.60	523.20

pH was adjusted with 1 M KOH, pH 7.2, osmolarity 290 mOsm/kg

3.4.5 Induction of spontaneous epileptiform activity

The experiments addressing the functional consequences of astrocyte morphology changes and uncoupling induced by epileptiform activity consisted generally of a 10-minute-long baseline period which was followed by pharmacologically induced epileptiform activity. For the induction of epileptiform activity, the hippocampal slices were treated with an aCSF containing 4 mM penicillin G sodium salt for 30 minutes. In a subset of experiments, the penicillin was applied together with a modified aCSF without $MgSO_4$ (0 Mg^{2+} aCSF). Afterwards, regular aCSF containing 10 µM NBQX and 50 µM D-APV was applied to the hippocampal slices in order to wash out the penicillin and inhibit synaptic transmission. When these experiments were performed in a submerged-type recording chamber, the hippocampal slices were placed on a custom-made grid in order to provide an improved slice perfusion. This grid consisted of a U-bended injection needle with a small grid-like net (common fly-net) glued on top. In order to further facilitate epileptiform activity, the basal KCl concentration of the aCSF was, if not stated otherwise, increased to 4 mM throughout these experiments

3.5 Micro-iontophoresis of glutamate, K^+ and TMA^+

For local and precise application of glutamate$^-$, K^+ or TMA^+, a micro-iontophoresis system (MVCS-02, npi, Tamm, Germany) was used. The iontophoresis technique operated by the application of a current to a pipette filled with the ion of interest and, in turn, to the ejection of that particular ion. Positively charged ions (K^+ and TMA^+) were ejected via a positive current, whereas a negative current was used for the negatively charged glutamate. To this end, iontophoresis pipettes were pulled from glass capillaries with filament (GB150F-10, Science Products, Hofheim, Germany) with a horizontal puller (Model P-1000, Sutter Instruments, Novato, USA) to yield tip openings of only approximately 100 nm. Next, the iontophoresis pipettes were filled with a solution containing 150 mM L-glutamic acid (adjusted to pH 7.0 with NaOH), 150 mM KCl, 3 M KCl or 100 mM TMA^+Cl^-. Additionally, 60 µM of the fluorescent dye Alexa Fluor 594 were added to the solution in order to visualize the pipette in the brain slice. In the bath solution, the pipette capacitance was compensated until the application of a rectangular test-pulse (10 nA for 10 ms) led to a rectangular voltage response. Afterwards, the pipette resistances were determined with a built-in routine of the amplifier and ranged from 70-120 MΩ for pipettes filled with 150 mM L-glutamic acid, 150 mM KCl and 100 mM TMACl. Pipettes filled with 3 M KCl exhibited resistances between 8-12 MΩ. In order to prevent a leakage out of the pipette, a small retain current of ±5-15 nA (positive for glutamate$^-$; negative for K^+ and TMA^+) was

constantly applied. The amplitude and duration of the injection current are indicated in the corresponding method-chapters.

3.6 Ion-sensitive microelectrodes

Ion-sensitive microelectrodes were used in order to investigate the extracellular concentration of K^+ or TMA^+. In general, such electrodes consisted of two compartments, the ion-sensitive and the reference compartment.

The ion-sensitive compartment consists of a liquid ion exchanger solution (ionophore) that is highly selective for a particular ion and a back-fill solution that contains this ion. Accordingly, a Nernst potential across the ion exchanger is generated that depends on the specific ion concentrations inside and outside of the compartment, i.e. changes of the exterior ion concentration will also change the Nernst potential across the ion exchanger (A 10-fold exterior concentration increase of a monovalent ion at 21°C will change the Nernst potential by ~58 mV). In addition, the ion-sensitive compartment also samples any ambient potential. In order to only obtain the potential that depends on the exterior concentration of the particular ion, the ambient potential was measured with the reference compartment (E_{ref}) and subtracted from the potential of the ion-sensitive compartment (E_{ion}). This differential potential ($E_{electrode}$) was then used to deduce the actual extracellular ion concentration (Chapter 3.6.2) in the brain slice (Equation 5) (Nicholson, 1993).

(5) $$E_{electrode} = E_{ion} - E_{ref}$$

3.6.1 Fabrication of K^+ and TMA^+-sensitive microelectrodes

The procedure of fabrication was adapted from Heinemann and Dieter Lux, 1977; Lux and Neher, 1973 and Wallraff et al., 2006. Theta borosilicate glass capillaries (Inner diameter: 2 mm; wall: 0.3 mm; septum: 0.22 mm; Hilgenberg, Malsfeld, Germany) were pulled with a horizontal pipette puller (P- 87, Sutter Instruments, Novato, USA) to a tip opening of approximately 1-2 µm. The pulled capillaries were then fixed in a custom-made holder in front of a stereo microscope. Next, the reference compartment was filled with 154 mM NaCl and a silver-chloride coated silver wire was inserted. In order to visualize the position of the electrode in the brain slice, the reference compartment also contained 60 µM of the fluorescent dye Alexa Fluor 594. For fabrication of K^+-sensitive microelectrodes (KSMs), the K^+-sensitive compartment was filled with 150 mM KCl and connected with a shortened microloader pipette tip (Microloader™, Eppendorf, Hamburg, Germany) via a silicon tube to a 1 ml syringe. Both compartments were then sealed with hard wax

(Deiberit 502, Siladent, Goslar, Germany). In order to render the inner tip of the K^+-sensitive compartment hydrophobic ('silanization'), the glass was treated with a mixture (21:1) containing Dichloromethane and Trimethylchlorosilane. For this purpose, the tip of the pipette was lowered into the silanization mixture and slight negative pressure was applied to the K^+-sensitive compartment by pulling the plunger of the connected syringe. As a result, the tip of the K^+-sensitive compartment was filled with the silanization mixture. By pushing the plunger of the pipette, slight positive pressure was applied and, in turn, the silanization mixture was released from the pipette. This procedure was then repeated five to ten times. Afterwards, the pipette tip was transferred into a mixture containing a K^+ ionophore (Potassium ionophore I - cocktail A or B) and filled by applying negative pressure. When a column of approximately 300-500 µm was reached, the negative pressure was removed and the K^+ ionophore mixture was allowed to equilibrate for roughly five minutes while the pipette tip remained in the mixture. Finally, the microloader pipette tip in the K^+-sensitive compartment was replaced by a silver-chloride coated silver wire and again sealed with hard wax.

For the fabrication of Tetramethylammonium-sensitive microelectrodes (TSM), the same procedure was applied, but 150 mM Tetramethylammonium chloride (TMACl) and a TMA^+-sensitive ionophore solution (IE190) were used for the TMA^+-sensitive compartment.

3.6.2 Calibration and characterization of ion-sensitive microelectrodes

Before being used in a brain slice, the ion-sensitive microelectrode sensitivity to the particular ion of interest was tested. To this end, the electrodes were calibrated in two solutions (Cal_1 & Cal_2) containing different concentrations of the particular ion of interest ($[Ion]_{cal1}$ & $[Ion]_{cal2}$). The corresponding differential potentials measured by the ion-sensitive microelectrode (E_{cal1} & E_{cal2}) were determined and the potential difference was calculated (ΔE_{cal}). For subsequent application in an experiment, only ion-sensitive microelectrodes were used that exhibited a potential change of at least 50 mV to a tenfold change of the concentration of the ion of interest. Additionally, the resistances of the two compartments were measured by a built-in circuit of the differential amplifier for ion-selective measurements.

In order to test the sensitivity of the KSMs to K^+, the potential measured by the KSM was determined in calibration solutions containing 3 or 30 mM KCl and 154 mM NaCl (Table 6). In a subset of experiments, calibration solutions containing 1 or 10 mM KCl were additionally used. In general, the KSMs responded to a 10-fold increase of the $[K^+]$ with a Nernst-like potential increase (ΔE_{cal}) of around 50 to 60 mV (Figure 10A). There was no

difference of the potential changes in response to 10-fold increase (3 to 30 mM) between the two different K^+ ionophore cocktails (Ionophore A or B) used to prepare KSMs (A, 55.40 ± 0.25 mV, n = 80; B, 55.73 ± 0.18 mV, n = 40; p = 0.417, Mann-Whitney U test). This potential change was later on used to convert the measured potential of the KSM into the actual $[K^+]_o$ in the hippocampal slice (see below). A subset of KSMs was also tested for their potential response to $[K^+]$-changes in the sub-millimolar range. This revealed that the KSMs showed Nernst-like responses to $[K^+]$ changes and only depart from this in the low sub-millimolar range (Figure 10B). However, this is a magnitude below the basal K^+ concentration in our experiments and should not interfere with the measurements.

Table 6 Calibration solutions for K^+-sensitive microelectrodes

	Calibration solution 1	**Calibration solution 2**
KCl	3.00 mM	30.00 mM
NaCl	154.00 mM	154.00 mM

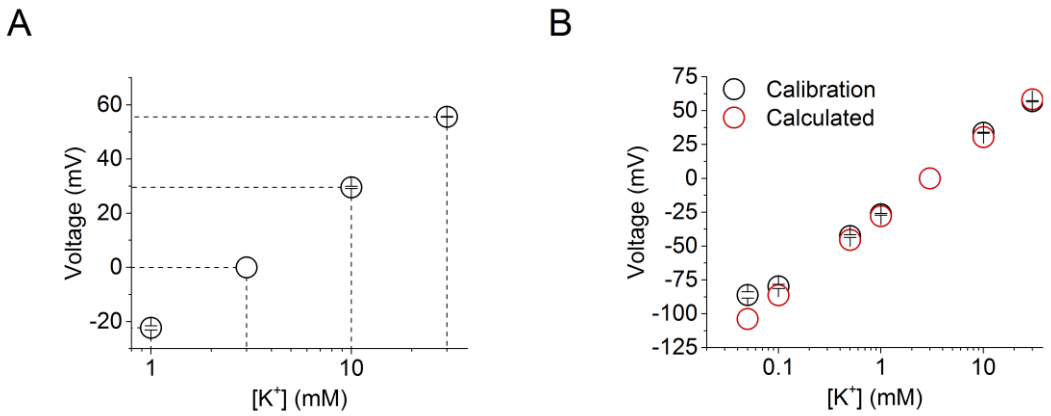

Figure 10 Calibration of K^+-sensitive microelectrodes (KSMs). A) The KSM (Ionophore cocktail A & B) were calibrated before each experiment in a solution containing 3 or 30 mM KCl and 154 mM NaCl each. Additionally, solutions containing 1 or 10 mM KCl were used in a subset of experiments. The potentials for 1, 10 and 30 mM were recorded relative to the potential for 3 mM (offset-corrected to 0 mV) (1 mM KCl, -23.40 ± 0.56 mV, n = 10; 10 mM KCl, 30.45 ± 0.60 mV, n = 10; 30 mM KCl, 55.51 ± 0.18 mV, n = 124). **B)** KSMs (Ionophore cocktail A & B, n = 5) exhibited voltage-responses (black) to changes of the $[K^+]$ in the sub-millimolar range (0.1 mM, 6.40 ± 1.46 mM; 0.5 mM, 43.5 ± 1.92 mM, 1 mM, 59.6 ± 1.83 mV; 3 mM, 86.10 ± 2.37 mV; 10 mM, 119.80 ± 2.35 mV; 30 mM, 143.10 ± 2.17 mV). The expected voltage responses (red) were calculated with the Nernst-equation for 21 °C.

Tetramethylammonium-sensitive microelectrodes (TSMs) were also tested for their sensitivity to TMA^+ before each experiment by two calibration solutions containing 1 or 10 mM TMA^+ (Table 7). Only TSMs that responded to this 10-fold increase of the [TMA^+] with a potential increase (ΔE_{cal}) of around 50 to 60 mV were used for the experiments (57.63 ± 0.44 mV; n = 23). A subset of electrodes was also tested for their sensitivity in the sub-millimolar range. This revealed that the TSMs showed Nernst-like behavior to changes of the [TMA^+] and only depart from this in the low sub-millimolar range. To correct for that, the calibration curve was fitted with the Nicolsky-Eisenman equation and the analysis was adapted accordingly (analyzed by Prof. Dr. C. Henneberger) (Nicholson, 1993).

Table 7 Calibration solutions for TMA^+-sensitive microelectrodes

	Calibration solution 1	**Calibration solution 2**
TMACl	1.00 mM	10.00 mM
KCl	3.00 mM	3.00 mM
NaCl	150.00 mM	141.00 mM

The potential change obtained during the calibration (ΔE_{cal}) was then used in order to generate a calibration curve and, in turn, deduce the ion concentration in the brain slice ($[Ion]_{exp}$) from the measured potential change during the experiment (ΔE_{exp}). The calibration curve derived from the Nernst equation that describes the measured potentials (E_{cal1} & E_{cal2}) by constant factors (summarized in s with R, universal gas constant; T, temperature; z, valence; F, Faraday constant), the particular ion concentration in the ion-sensitive compartment and the ion concentration of the calibration solution (Equation 6 & 7). Accordingly, ΔE_{cal} can be described with the constant factors and the ion concentration of the calibration solutions by the Nernst equation (Equation 8 & 9). Using calibration solutions differing in their ion concentration by the factor 10, ΔE_{cal} equates s and thus served as the slope of the calibration curve (Equation 11 & 11). In order to generate the calibration curve, ΔE_{cal} was then used as the summarized constant factors for the Nernst equation that describes the potential change measured in the brain slice (ΔE_{exp}) by the basal ion concentration ($[Ion]_{basal}$) and the ion concentration corresponding to the potential change ($[Ion]_{exp}$) (Equation 12). By solving equation 13 for $[Ion]_{exp}$, the ion concentration in the brain slice was then calculated from the measured potential change, the factor s (i.e. ΔE_{cal}) and the basal ion concentration (Equation 13-15).

(6) $$E_{cal1} = \frac{RT}{zF} \times \ ln \frac{[Ion]_{cal1}}{[Ion]_{intra}} = s \ \times \log \frac{[Ion]_{cal1}}{[Ion]_{intra}}$$

(7) $$E_{cal2} = \frac{RT}{zF} \times \ ln \frac{[Ion]_{cal2}}{[Ion]_{intra}} = s \ \times \log \frac{[Ion]_{cal2}}{[Ion]_{intra}}$$

(8) $$\Delta E_{cal} = E_{cal2} - E_{cal1} = s \ \times \left(\log \frac{[Ion]_{cal2}}{[Ion]_{intra}} - \ \log \frac{[Ion]_{cal1}}{[Ion]_{intra}} \right)$$

(9) $$\Delta E_{cal} = s \ \times \log \frac{[Ion]_{cal2}}{[Ion]_{cal1}}$$

(10) $$\Delta E_{cal} = s \ \times \log \frac{30 \ mM \ K^+}{3 \ mM \ K^+} \text{ or } \Delta E_{cal} = s \ \times \log \frac{10 \ mM \ TMA^+}{1 \ mM \ TMA^+}$$

(11) $$\Delta E_{cal} = s$$

(12) $$\Delta E_{exp} = s \times \ \log \frac{[Ion]_{exp}}{[Ion]_{basal}}$$

(13) $$\log [Ion]_{exp} = \frac{\Delta E_{exp}}{s} + \log \, [Ion]_{basal}$$

(14) $$[Ion]_{exp} = \ 10^{\frac{\Delta E_{exp}}{s} + \log [Ion]_{basal}}$$

(15) $$\Delta [Ion]_{exp} = \left(10^{\frac{\Delta E_{exp}}{s} + \log [Ion]_{basal}} \right) - [Ion]_{basal}$$

3.6.3 Extracellular K^+ recordings

The extracellular K^+ concentration was measured with a K^+-sensitive microelectrode (KSM) in 350 µm thick rat hippocampal slices. These experiments were conducted in the interface-type and submerged-type chamber with an aCSF containing 3 mM KCl at 34°C. To this end, the KSM was connected to the headstage of the ion-sensitive amplifier (ION-01M, npi, Tamm, Germany) and then calibrated as described in Chapter 3.6.2. The differential signal of the KSM was amplified by the factor 100, low-pass filtered with 1 kHz (Bessel; LPBF-01GX, npi, Tamm, Germany) and sampled as a DC signal at a frequency of 10 kHz. The ionophore cocktail that was used for the particular experiments can be retrieved from Table 8.

Table 8 Overview of the experiments and the used ionophore cocktail

Experiment	Chapter	Ionophore cocktail
K^+ transients evoked by axonal & synaptic activity	4.1.2	A
K^+ transients evoked by axonal activity	4.1.3	A
K^+ spread in the ECS	4.1.4	A
Small iontophoretically evoked K^+ transients	4.1.5	A & B
Large iontophoretically evoked K^+ transients	4.1.5	A & B
Iontophoretic K^+ application with varying current amplitude and duration	4.1.6	B
K^+ transients during a reduced ECS fraction	4.1.8	B

In the interface-type chamber, the KSM was placed in the str. radiatum of the CA1 region and K^+ transients were evoked by SC stimulation with a bipolar stimulation electrode at the CA3/1 border simultaneously to field potential recordings as described in Chapter 3.4.2. During the experiments with intact synaptic transmission, neuronal activity and corresponding K^+ transients were evoked at an interval of 30s with a paired-pulse stimulation with an interstimulus interval of 50 ms. The stimulus intensity was adjusted to obtain ~75% of the maximum fEPSP amplitude. In the presence of the glutamate receptor blockers NBQX (10 µM) and D-APV (50 µM), K^+ transients were evoked by a high-frequency stimulation (HFS, 50 pulses at 100 Hz, 100 µs pulse-duration) at an interval of 1 minute. The stimulus intensity was adjusted to obtain maximal FV amplitudes.

In the submerged-type chamber, recordings of the extracellular K^+ concentration were performed in the presence of 1 µM TTX, 10 µM NBQX and 50 µM D-APV in order to silence neuronal activity and, in turn, prevent activity-dependent K^+ release. Accordingly, K^+ transients were evoked by the iontophoretic K^+ application (Chapter 3.5) and measured in the CA1 str. radiatum at a depth of 50-120 µm. All experiments consisted of a baseline period followed by either a period of drug treatment (Meclofenamic acid, MFA or Carbenoxolone, CBX) or a prolonged baseline period (Control). The baseline period (Baseline) was recorded and used for further analysis when the evoked small and large K^+ transients showed stable peak amplitudes over a period of 30 and 10 consecutive K^+ injections, respectively. These 'Small' and 'Large' K^+ transients were evoked with iontophoresis pipettes filled with 150 mM KCl (800 nA for 200 ms, 15 s interval) and 3 M KCl (900 nA for 500 ms, 45 s interval), respectively. For experiments with K^+ transients of variable peak amplitudes ('ramps'), iontophoresis pipettes were filled with 3 M KCl and K^+ was applied at an interval of 20 s with different injection current amplitudes (190, 380,

570, 760 and 950 nA for 500 ms) or durations (900 nA for 100, 200, 300, 400, 500 and 600 ms). The complete time course of the 'ramp'-experiments consisted of 30 test-injections (200 nA for 500 ms or 900 nA for 200 ms) followed by the first two consecutive 'ramp'-injections, followed by 45 additional test-injection and, finally, the last two consecutive 'ramp'-injections. Here, the first 30 test-injection were used as a baseline period before CBX was applied following the first two consecutive 'ramp'-injections. In a subset of experiments, the two consecutive 'ramp'-injections with modulated current amplitude were directly followed by two duration-modulated 'ramp'-injections.

After the experiments, the sites of K^+ injection and measurement were recorded by obtaining an image-stack (x-y-z) of the KSM and the iontophoresis pipette. The distance between the tips was then calculated using the Pythagorean theorem.

For obtaining the actual extracellular ion concentration from the potential measured with the KSM, all recordings were offset corrected to the potential before the onset of the K^+ transients and then converted using the modified Nernst equation as shown in chapter 3.6.2 ($[Ion]_{basal}$ = 3 mM). Only the potentials that were recorded during the experiments employing the hypoosmolar solution (Chapter 4.1.8) were not offset corrected. Instead, offset shifts were also converted into concentration and subsequently used as $[Ion]_{basal}$ in the modified Nernst equation.

In order to analyze the decay of the evoked extracellular K^+ transients, the time course of the K^+ transients (when it had declined to 90% of its peak amplitude) was fitted with either a monoexponentially (16) or a biexponentially (17) decaying function.

(16)
$$y = A \times e^{(-\frac{x}{\tau})}$$

(17)
$$y = A_{fast} \times e^{\left(-\frac{x}{\tau_{fast}}\right)} + A_{slow} \times e^{\left(-\frac{x}{\tau_{slow}}\right)}$$

3.6.4 Analysis & modulation of the ECS structure

For the analysis of the ECS structure, the real-time TMA^+-iontophoresis approach in combination with TSMs (Chapter 3.6) was employed. This method was already established in the late 1970s by Charles Nicholson and his colleagues. It employs the application of specific ions into the ECS, its subsequent extracellular diffusion and its detection at a distance from its source (Figure 5B). Commonly used ion is Tetramethylammonium (TMA^+) since it is mostly not taken up by cellular structures. Thus, their extracellular diffusion and concentration is largely shaped by the structure of the ECS. The extracellular concentration of the TMA^+ is then measured with a TMA^+-sensitive

microelectrode (TSM) at a distance of a few hundred micrometer from its source. The corresponding time-dependent TMA^+ concentration profile thus depends on the ECS structure, which can be retrieved by curve-fitting of this profile with a function that incorporates the ECS volume fraction, the tortuosity, the amount of applied TMA^+, the distance between TMA^+ release and recording site and unspecific uptake (Nicholson, 1993; Nicholson and Phillips, 1981; Syková and Nicholson, 2008).

350 µm thick rat hippocampal slices were placed in the submersion-type recording chamber and superfused with 34°C warm aCSF. This aCSF contained 0.5 or 1 mM TMACl in order to provide a known basal extracellular TMA^+ concentration for the conversation of the recorded potential into the extracellular TMA^+ concentration. Inhibitors for voltage-gated Na^+ channels (1 µM TTX), AMPARs and NMDARs (10 µM NBQX and 50 µM D-APV) were either present throughout the experiment (Chapter 4.1.7) or added at a later time-point (Chapter 4.2.2). Next, an iontophoresis pipette filled with 100 mM TMACl and a TSM was placed in the CA1 str. radiatum at distance of 100-200 µm (Figure 11A). Then TMA^+ was injected into the ECS with a steady +20 nA current via the iontophoresis pipette in order to maintain a constant transport number throughout the experiment. The corresponding slow increase of the basal TMA^+ concentration was simultaneously recorded with the TSM. When the basal TMA^+ concentration reached a stable level, additional TMA^+ was applied with +120 nA for 30s at an interval of 1.5 or 2 minutes. The corresponding potential change recorded with the TSM was then converted into the actual extracellular TMA^+ concentration using the modified Nernst equation (Chapter 3.6.2). To this end, the recorded potentials were not offset corrected and the particular elevated basal TMA^+ concentration ($[TMA^+]_{basal}$) was used for conversion. This resulted in an extracellular TMA^+ transient as the example in Figure 11B depicts. In order to extract the ECS structure from such a diffusion profile, the profiles were fitted with the following equation (Syková and Nicholson, 2008) via a custom-written Matlab (MathWork, Natick, USA) routine (by Prof. Dr. C. Henneberger).

The equation describes the extracellular TMA^+ concentration over time by several factors. The source strength of the iontophoretic TMA^+ application (Q), which is defined by application current (I), the Faraday constant (F), the valency of TMA^+ (z) and the transport number (n) (Equation 18). The transport number represents the fraction of applied current that actually expels an ion. It scales the application current and thus allows an estimation of the actual applied amount of TMA^+. Typically, each iontophoresis pipette is tested in agarose gel for its transport number before each experiment.

(18)
$$Q = \frac{I \times n}{Fz}$$

The TMA^+ concentration (C) at time t was measured at a particular distance (r) from the TMA^+ source and is defined by Q, the ECS fraction (α), the TMA^+ diffusion coefficient in the ECS (D*) and the unspecific TMA^+ uptake by cellular structures (k). The function 'erfc' is the complementary error function. The rising phase of the TMA^+ transient during the TMA^+ application period (t_a = 30 s) and the falling phase after the application period ($t>t_a$) is described by equation 19 and equation 20, respectively (Hrabětová and Nicholson, 2007).

(19)
$$C(t) = \frac{Q}{8\pi D^* \alpha r}\left[erfc\left(\frac{r}{2\sqrt{tD^*}} + \sqrt{\frac{k}{D^*}} \times \exp\left(\sqrt{tD^*}\right)\right) + erfc\left(\frac{r}{2\sqrt{tD^*}} - \sqrt{\frac{k}{D^*}} \times \exp\left(-\sqrt{tD^*}\right)\right)\right]$$

(20)
$$C(t > t_a) = C(t) - C(t - t_a)$$

For the fitting procedure, the distance between TMA^+ source and site of measurement (r), the Faraday constant (F), valency of TMA^+ (z = 1) and the application current (I = 100 nA) were fixed and the other parameters were determined by the curve fitting. Since the transport number (n) was not determined for the used iontophoresis pipettes in an agarose gel before use, n was also determined by the curve fitting. Consequently, no statement about the actually expelled amount of TMA^+ was possible. In turn, this diffusion analysis provided no estimate about the absolute values of the ECS characteristics, such as its volume fraction (α). However, the relative changes of the extracellular volume fraction (α) during an experiment over time can be retrieved from this analysis (Figure 11B).

In order to modulate the ECS fraction, different hypoosmolar aCSF solutions were applied to the hippocampal slices. The aCSF's osmolarity was decreased to 220 mOsm/kg or 180 mOsm/kg by reducing the concentration of NaCl to ~85.5 mM or 68 mM, respectively. In a subset of experiments the osmolarity of the aCSF with the reduced NaCl concentration was adjusted to 300 mOsm/kg by adding Sucrose.

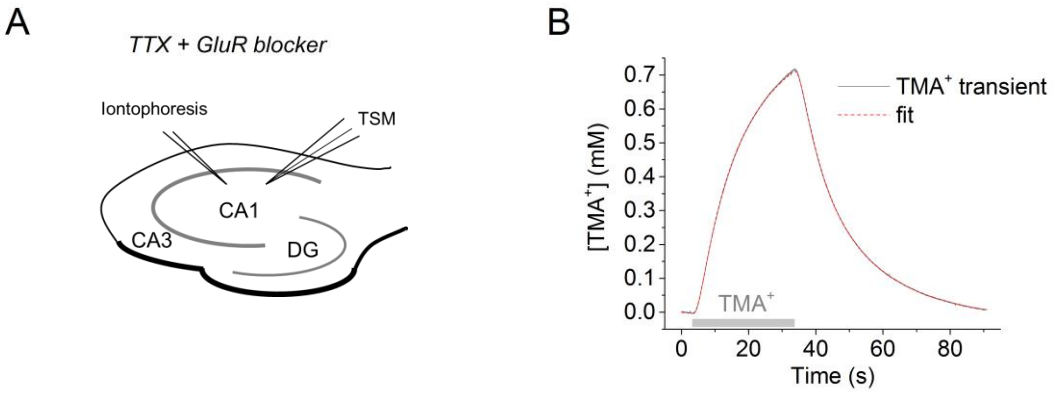

Figure 11 Analysis of the ECS structure by TMA^+ diffusion analysis. A) TMA^+ was injected into the ECS via an iontophoresis pipette in the CA1 str. radiatum. The extracellular TMA^+ concentration was then recorded with a TSM 100-200 µm distant from the iontophoresis pipette. **B)** TMA^+ was injected with a +120 nA current for 30 s, diffused in the ECS and finally resulted in the recorded TMA^+ transient. This transient was then fitted (see text) in order to retrieve the ECS structure. Figure by Prof. Dr. C. Henneberger.

3.7 Stereotactic virus injections

Extracellular glutamate transients in the hippocampus were investigated with the intensity-based glutamate-sensing fluorescent reporter (iGluSnFR) (Marvin et al., 2013). For this purpose, iGluSnFR was expressed under the control of the glial fibrillary acidic protein specifically by astrocytes after transfection with an adeno-associated virus (AAV) (AAV1.GFAP.iGluSnFR.WPRE.SV40, Vector Core, University of Pennsylvania, USA). The AAV was delivered to the hippocampi of 21 to 28 days old FVB mice by bilateral stereotactic injection. First, the mice were anesthetized by an intraperitoneal (i.p.) injection of a mixture of Fentanyl (0.05 mg/kg bodyweight (bw)), Medazolam (5 mg/kg bw) and Medetomidin (0.5 mg/kg bw) and placed on a heating plate at 36°C in order to maintain their body temperature. The mice were considered as deeply anesthetized when no motor reaction was observed to a gentle pinch of the paws. Next, the eyes were covered with eye ointment (Bepanthen®) to prevent them from drying-out and the hair on top of the head was removed with small scissors or an electric shaver. After the hair was removed, the skin was disinfected with 70% Ethanol and locally anesthetized by applying Xylocaine. The mice were then head-fixed in a stereotactic frame (Model 901, David Kopf Instruments, Tujunga, USA) and the scalp was cut along the midline with small scissors until bregma and lambda were visible. Small hooks (custom-made from injection needles) were used to drag the scalp apart and keep the skull exposed during the surgery. Afterwards, the stereotactic frame was used to move a micro-injection pump (UMP3, WPI, Sarasota, USA) with the AAV-filled syringe (NanoFil 10 µl, WPI, Sarasota, USA) above

the exposed skull. Using the tip of the injection needle (NanoFil 34G BVLD, WPI, Sarasota, USA), the position of the injection was determined (relative to bregma: anterior/posterior: -3.5 mm, lateral: ±3 mm, ventral: -2.5 mm) and marked on the skull with a surgical marker. At these positions, the skull was opened with a dental drill and, subsequently, the injection needle was lowered into the hole until the meninges were pierced. The needle was then again withdrawn and 50 nl of virus particles were ejected in order to ensure that the needle was not clogged. When this was the case, the small drop was removed from the tip and the needle was moved down to the final position in the brain. Next, 500-1000 nl of virus particles were injected at a rate of 50 or 100 nl/min. Afterwards, the needle was left in place for a few minutes until it was removed and the procedure was repeated for the other hemisphere. Finally, the scalp was sutured (Ethicon, Cincinnati, USA) and the wound was treated with an antibacterial crème (Gentamicin, 1 mg/g). The mice received an i.p. analgesic injection (Carprofen, 5mg/ kg bw) followed by mixture of Naloxone (1.2 mg/kg bw), Flumazenil (0.5 mg/kg bw) and Atipamezol (2.5 mg/kg bw) in order to stop the anesthesia. After recovery from anesthesia, the mice were transferred back to their home-cage and observed daily over a period of three days. Two to three weeks after the surgery, the mice were sacrificed and used for experiments.

3.8 Imaging

3.8.1 Two-photon excitation fluorescence microscopy setups

Imaging experiments were performed with a Scientifica two-photon excitation fluorescence microscope (Scientifica, Uckfield, UK) and a FV10MP system (Olympus, Tokyo, Japan) optically linked to a femtosecond Ti:sapphire pulse laser Vision S (Coherent, Santa Clara, US; nominal 73 fs pulse width). At both setups a neutral-density gradient filter (Thorlabs, Newton, USA) was integrated in the light path of the laser that allowed adjusting the laserpower under the objective and, likewise, at the focal plane. The Scientifica and the Olympus system were equipped with a 40x (NA 0.8) and a 25x (NA 1.0) objective (Olympus, Tokyo, Japan), respectively. For separating the spectra of the fluorescent signal at the Scientifica system, a dichroic mirror separated the fluorescent signal at 565 nm and reflected wavelengths smaller than 565 nm to a green filter (band-pass 500 to 550 nm, ‘green channel’) or transmitted wavelengths larger than 565 nm to a red filter (band-pass 600 to 660 nm, ‘red channel’). At the Olympus system, the fluorescent signal was separated at 570 nm and reflected to a green filter (band-pass 515 to 560 nm, ‘green channel’) or transmitted to a red filter (band-pass 575 to 630 nm, ‘red channel’), respectively. Subsequently, the fluorescence signals were detected and

amplified by photomultiplier tubes. The Scientifica and the Olympus system were controlled by the Matlab-based (MathWork, Natick, USA) software Scanimage (Scientifica, UK) and FV10-ASW (Olympus, Japan), respectively. For light microscopy of the brain slice, the microscopes from Scientifica and Olympus were equipped with an infrared light source and Dodt or differential interference contrast (DIC) optics, respectively, that were displayed on a monitor (Dell, US and Benq, China) via a camera (Watec Incorporated, Pine Bush, USA).

3.8.2 Visualization & quantification of the astrocyte network

For visualization of the astrocyte network and morphology, an astrocyte was patched at the Scientifica two-photon system, kept in the whole-cell configuration for 10 minutes as described in Chapter 3.4.3 and filled with the fluorescent dyes Alexa Fluor 488 and Texas Red Dextran 3 kDa. Since Alexa Fluor 488 is gap junction channel permeable and therefore can diffuse into adjacent coupled astrocytes, it was used to visualize the coupled network. In contrast, the gap junction channel impermeable Texas Red Dextran 3 kDa stayed in the patched astrocyte and was used to visualize the cell morphology. Subsequently, both dyes were excited with an excitation wavelength of 800 nm. Light is scattered in the brain tissue and consequently the laser power decreases with increasing depth in the tissue. In order to keep the laser power similar between experiments, the laser power under the objective was adjusted according to the depth of the imaged astrocyte in the tissue. In order to avoid photodamage induced by a high laser power, the laser power was adjusted to obtain approximately 2 mW at the patched astrocyte. Due to their different fluorescent spectra, the fluorescence signal from Alexa Fluor 488 was visualized in the green channel, whereas the Texas Red Dextran (3 kDa) signal was visualized in the red channel.

In order to image the astrocyte network, an x-y-z image stack (512 x 512 pixels, 0.65 µm/pixel) was obtained in 2 µm z-steps from the brain slice surface towards the last detectable fluorescent cell. The analysis of the gap junction coupled network was then performed in ImageJ (NIH, USA) and Excel 2010 (Microsoft, Redmond, USA). Fluorescent cells were manually identified in the green channel and their soma position in the image stack (x-y-z) as well as the background-corrected maximal mean soma fluorescence intensity (3.25 x 3.25 µm region of interest in x-y plane) were determined. Since the measured fluorescence intensity (F(z)) of a probe decayed monoexponentially (τ; 38.5 µm) with the depth (z) in the tissue, the actual soma fluorescence intensity (F_0) was calculated for each cell and used for further analysis (Equation 21 -22).

(21) $$F(z) = F_0 \times e^{-z/\tau}$$

(22) $$F_0 = \frac{F(z)}{e^{-z/\tau}}$$

Next, the depth-corrected soma fluorescence intensity (F_0) of each cell was normalized to the initially patched astrocyte. For quantifying the strength of gap junction coupling, the number of coupled cells (excluding the patched astrocyte) and their cumulative normalized fluorescence intensity were used. Cells that exhibited normalized fluorescence intensities below 1% were discarded from the analysis in order to prevent the inclusion of ambiguous and other faintly fluorescent structures (e.g. autofluorescence).

3.8.3 Imaging of extracellular glutamate transients using iGluSnFR

Imaging of extracellular glutamate was performed either at the Scientifica two-photon excitation fluorescence microscope (Scientifica, Uckfield, UK) and/or at the FV10MP system (Olympus, Tokyo, Japan) with an excitation wavelength of 910 nm. As described in the previous chapter, the laser power under objective was adjusted according to the depth of the imaged astrocyte in the tissue. Thus, the laser power at the imaged astrocyte was kept constant at 2 mM and photodamage was avoided. For this purpose, horizontal hippocampal slices were obtained from AAV-injected FVB mice that expressed the fluorescent glutamate sensor iGluSnFR specifically on the surface of astrocytes (Chapter 3.7). This green fluorescent protein-based sensor reacts to the binding of glutamate with a conformational change and, in turn, with an increase of the fluorescence intensity (Marvin et al., 2013). In order to evoke glutamate transients, glutamate was either directly applied by an iontophoresis pipette (Chapter 3.5) or glutamate release from synapses was triggered by axonal stimulation.

The experiments that used synaptic activity for evoking glutamate transients were performed on the FV10MP system and consisted of a line scan (8x Zoom, 14.65 µm, 74x715 pixel, 1.4 ms/line) over one second in a CA1 str. radiatum astrocyte territory simultaneously to axonal stimulation. A line scan is obtained by the repetitive imaging of a single line over time. This provides information about the spatial profile of the extracellular glutamate transients along the imaged line. In addition the repetitive imaging of this line provides information about the temporal profile of the extracellular glutamate transients. In each hippocampal slice, several randomly chosen astrocytes were imaged during

baseline conditions and after epileptiform activity. For evoking glutamate transients, SCs were stimulated (stimulation intensity was set to obtain a fEPSP with a slope of 60-70% of its maximal value) with five pulses at 20 Hz. This pulse-train was repeated 10 times at an interval of 15 seconds for each imaged astrocyte and the corresponding line scans were subsequently averaged for analysis. These line scans were then background-corrected and analyzed for the peak amplitude of the five evoked fluorescence peaks and the fluorescence decay (monoexponentially decaying function) after the last peak using a custom-written Matlab script (by Prof. Dr. C. Henneberger).

The experiments that used the iontophoretic application of glutamate were performed at the Scientifica two-photon excitation fluorescence microscope (Scientifica, Uckfield, UK) and the FV10MP system (Olympus, Tokyo, Japan) in collaboration with Dr. D. Minge. Astrocytes expressing iGluSnFR in the CA1 str. radiatum were imaged by a line scan close to the tip of the iontophoresis pipette (Scientifica, 8x Zoom, 41.57 µm, 512x1024 pixels, 2.64 ms/line; FV10MP, 13.8x Zoom, 27.79 µm, 386x1024 pixels, 2.64ms/line) simultaneously to the iontophoretic glutamate application. First, glutamate was applied three times for 250 ms with a 5 nA current injection via the iontophoresis pipette at an interval of 30 s. Afterwards, glutamate was applied three times with a 100 nA current in order to saturate the sensor. The respective line scans were then averaged and corrected for background. Next, the line scans corresponding to the 5 nA application were binned into sections of 1 µm and normalized to their basal fluorescence intensities (before the onset of glutamate application). For converting the normalized fluorescence intensities (F) of the 5 nA line scans into the actual glutamate concentration ([Glu]), the dissociation constant of iGluSnFR (K_d, 4.3 µM, determined previously by M. Herde, PhD), the normalized saturated (F_{max}) and the normalized basal fluorescence intensities (F_0) were used (Equation 23). Since the ambient extracellular glutamate concentration is relatively low (<100 nM) compared to the K_d of iGluSnFR (Cavelier and Attwell, 2005; Herman and Jahr, 2007; Meur et al., 2007), it was assumed that F_0 represents the fluorescence without glutamate bound.

(23)
$$[Glu] = K_D \times \frac{F - F_0}{F_{max} - F}$$

Subsequently, the accumulation of the applied glutamate was quantified for each line by the accumulation constant (τ) that was determined by fitting the glutamate concentration over the 250 ms of iontophoretic application with the following exponential function (Equation 24)

(24)
$$[Glu] = A \times (1 - e^{-\frac{t}{\tau}})$$

In order to standardize and allow a comparison of the accumulation constants between different experiments, the line with the fastest glutamate accumulation (smallest τ) was defined as closest to the point of glutamate application (tip of the iontophoresis pipette). Thus, the glutamate accumulation was compared between the respective lines relative to the glutamate application point.

Additionally, the spatial glutamate spread was quantified by fitting the fluorescence profile at the end of the glutamate application period (when the peak concentration was reached) by a gaussian function. The full-width at half maximum of this function was then used as a readout (Equation 25).

(25)
$$[Glu] = A \times e^{-0.5 \times \left(\frac{x - xc}{w}\right)^2}$$

3.9 Statistics

The data is presented as mean ± standard error of the mean (s.e.m.) with n as the number of samples. All statistical analyses were performed with Excel 2010 (Microsoft, Redmond, USA) and OriginPro 2016 (OriginLab, Northampton, USA). For testing the distribution of the data sets, the Shapiro-Wilk test was used. The statistical difference between normally distributed unpaired and paired data sets were tested with the two-sample Student's t-test and the paired two-sample Student's t-test, respectively. When the variances of the data sets, tested by the two-sample test for variance, were significantly different, the Welch-correction for the two-sample Student's t-test was used. Non-normally distributed unpaired and paired data sets were tested with the Mann-Whitney U test and the Wilcoxon's signed-rank test, respectively. For comparing more than two data sets, a one-way or two-way analysis of variance (ANOVA) with post-hoc test (indicated in the figure legends) was used. Statistical significance is indicated in the figures with asterisks (* $p < 0.05$; ** $p < 0.01$; *** $p < 0.001$) and the exact values are given in the figure legend and text.

4 Results

4.1 Impact of acute astrocyte uncoupling on K^+ homeostasis

The first part of this study examined the functional consequences of acute uncoupling of the astrocyte network on the homeostasis of extracellular K^+ in acute brain slices. First, a protocol for acute pharmacological gap junction uncoupling was established and tested using whole-cell patch-clamp recordings of astrocytes. Next, K^+-sensitive microelectrodes (KSMs) were employed to measure extracellular K^+ transients in parallel to gap junction uncoupling. In order to investigate under which conditions gap junction uncoupling affects the clearance of extracellular K^+, such extracellular K^+ transients were evoked by several experimental approaches. This included the electrical stimulation of axons and the concomitant activity-dependent K^+ release that resulted in rather small extracellular K^+ transients and the direct injection of K^+ into the ECS via an iontophoresis pipette. The latter was then used to evoke extracellular K^+ transients of different amplitudes. Finally, the iontophoresis approach was used in order to test the impact of acute gap junction uncoupling when the structure of the ECS was modulated.

4.1.1 Pharmacological uncoupling of the astrocyte network

A key feature of astrocytes is the formation of a large network via gap junction channels (Giaume et al., 2010; Nagy and Dermietzel, 2000). This network has been proposed to facilitate the clearance of extracellular K^+ via a mechanism termed 'spatial K^+ buffering' (Orkand et al., 1966).

In order to investigate the role of astrocytic gap junction coupling for K^+ homeostasis, pharmacological gap junction inhibitors were used, i.e. Meclofenamic acid (MFA) or Carbenoxolone (CBX). This approach was advantageous since it avoids long-term alterations of the astrocyte morphology that were induced by the genetic deletion of the gap junction channel forming connexins (Ghézali et al., 2018; Pannasch et al., 2014). The efficacy of these inhibitors to acutely uncouple the astrocyte network was tested in two subsets of experiments by visualizing the astrocyte network (Chapter 3.4.3 & 3.8.2) in the presence of MFA or CBX and compared to control conditions (no inhibitors present). For this purpose, the hippocampal slices were either treated with 50 µM CBX or 100 µM MFA for 10 minutes before an astrocyte in the str. radiatum of the CA1 region was patched and filled with the gap junction permeable fluorescent dye Alexa Fluor 488 (Figure 13B) and the gap junction-impermeable fluorescent dye Texas Red Dextran 3 kDa (TRD) (Figure 12A). After establishing the whole-cell configuration, electrical properties of the patched

astrocytes, i.e. the resting membrane potential and the input resistance, were determined. Patched astrocytes exhibited low membrane potentials and input resistances. There was no significant difference of these properties between astrocytes patched during control conditions and astrocytes in the presence of 100 µM MFA (Figure 12D&E) or 50 µM CBX (Figure 12F&G). This indicates that the MFA or CBX treatment induced no alterations of the basic astrocytic membrane properties, which itself could have impacted on K^+ clearance.

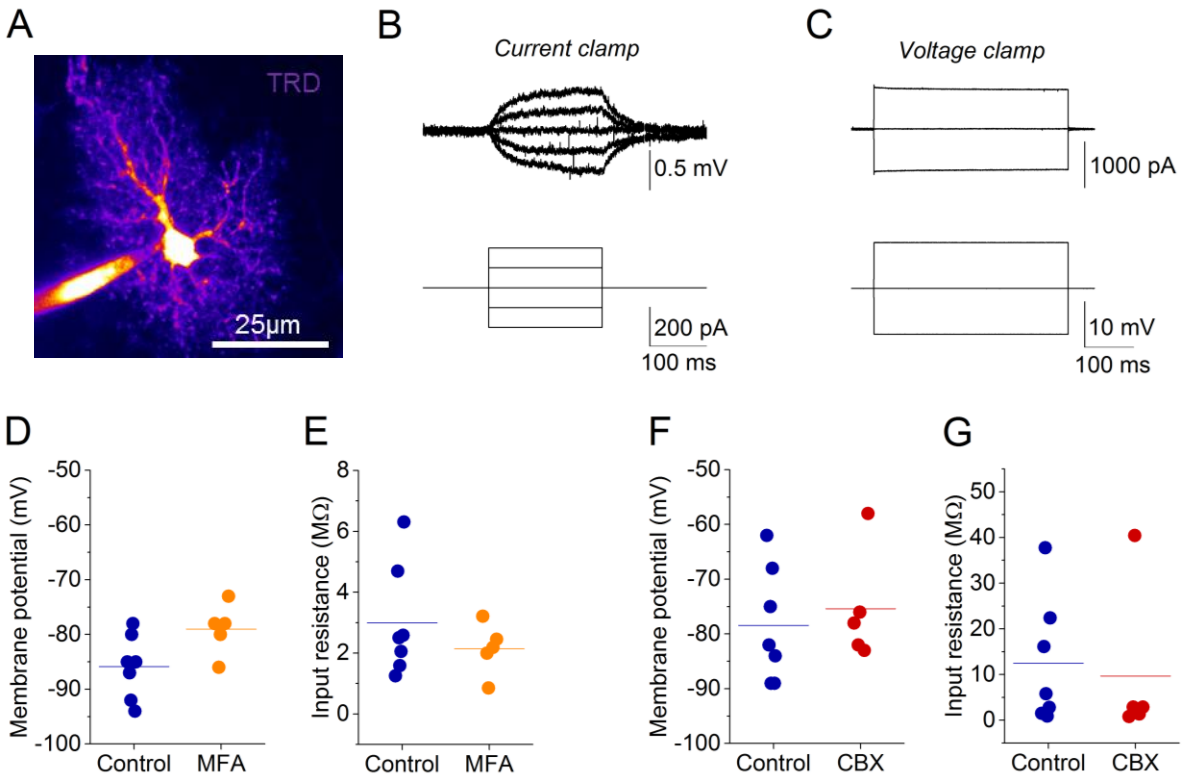

Figure 12 Electrophysiological membrane properties of patched astrocytes. A) This example image depicts an astrocyte in whole-cell configuration filled via the patch pipette with the fluorescent dye Texas Red Dextran 3 kDa (300 µM, TRD). **B)** Current clamp recording of an astrocyte. Somatic current injections (bottom) and resulting voltage responses (top) were used to determine the input resistance of the patched astrocyte. **C)** Voltage clamp recording of an astrocyte. Voltage steps of 10 mV were applied from a holding potential of -70 mV (bottom) and the corresponding peak current response (top) was used to calculate the access resistance (Figure 13). **D&F)** The membrane potential of astrocytes from the MFA-treated (Control, n = 5, -85.86 ± 2.20 mV; MFA, n = 7, -79.00 ± 2.10 mV; p = 0.055; two-sample Student's t-test) as well as CBX-treated slices were not different from their respective controls shortly after establishing the whole-cell configuration (Control, n = 5, -78.43 ± 3.96 mV; CBX, n = 7, -75.4 ± 4.53 mV; p = 0.627; two-sample Student's t-test). **E&G)** The input resistance of astrocytes from MFA-treated (Control, n = 5, 3.00 ± 0.69 MΩ; MFA, n = 7, 2.14 ± 0.38 MΩ; p = 0.358; two-sample Student's t-test) as well as the CBX-treated slices were not different from their respective controls shortly after establishing the whole-cell configuration (Control, n = 5, 12.48 ± 5.21 MΩ; CBX, n = 7, 9.69 ± 7.70 MΩ; p = 0.625; Mann Whitney U test). Values of the single recordings and their average are represented by dots and lines, respectively.

In addition, the access resistance, a determinant for the access of the patch-pipette to the cytoplasm, was determined. The access resistance of astrocytes patched during control conditions was not different from astrocytes patched in the presence MFA (Figure 13C, left panel) or CBX (Figure 13D, left panel). After 10 minutes of dye-filling, the patched astrocytes were further identified by their characteristic small soma (~10 µm) and fine processes, as an example in Figure 12A depicts. The access resistance increased significantly during the period of dye-filling in the MFA-treated slices and the respective control slices (Control, 69.54 ± 12.18%, n =7, p = 0.0016, paired Student's t-test; MFA, 87.14 ± 31.51%; n =5, p = 0.0147, paired Student's t-test). There was also a tendency towards increased access resistances over time in the CBX-treated slices and the respective control slices (Control, 35.83 ± 13.75%, n = 7, p = 0.0532, paired Student's t-test; CBX, 22.20 ± 6.96%; n = 5, p = 0.0261, paired Student's t-test), but there was no difference between the access resistance in control conditions and in the presence of MFA (Figure 13C, right panel) or CBX (Figure 13D, right panel), respectively. This indicated that the dye-filling into the patched astrocyte was not affected by the treatment with MFA or CBX. Conversely, an impaired dye-diffusion into the network was caused by a modulated gap-junction coupling and not by an inefficient supply of the dye via the patch-pipette. In control conditions, the gap junction permeable dye Alexa Fluor 488 diffused into neighboring cells and thereby the gap junction coupled network could be visualized (Figure 13B. left panel). In contrast, Alexa Fluor 488 was predominantly restricted to the patched astrocyte when the hippocampal slice was pre-treated for 10 minutes with MFA or CBX (Figure 13B, right panel). This was revealed by a significantly reduced number of coupled cells in MFA- (Figure 13E) or CBX-treated (Figure 13G) slices compared to their respective controls. In order to test if the few remaining coupled cells were also less efficiently coupled, their somatic fluorescence intensities were investigated. Indeed, the somatic fluorescence intensities of the remaining coupled cell after MFA (Figure 13F) or CBX (Figure 13H) treatment were significantly lower compared to the cells in an intact network during control conditions. This indicated that the treatment with MFA and CBX not only reduced the number of coupled cells, but also that these remaining cells were less efficiently coupled.

Taken together, these results show that the pre-treatment with either MFA or CBX for 10 minutes significantly impaired the dye-diffusion in the network without affecting the basic electrical properties of the patched astrocytes. These approaches were then used in the following experiments to investigate the impact of this acute gap junction uncoupling on the clearance of extracellular K^+.

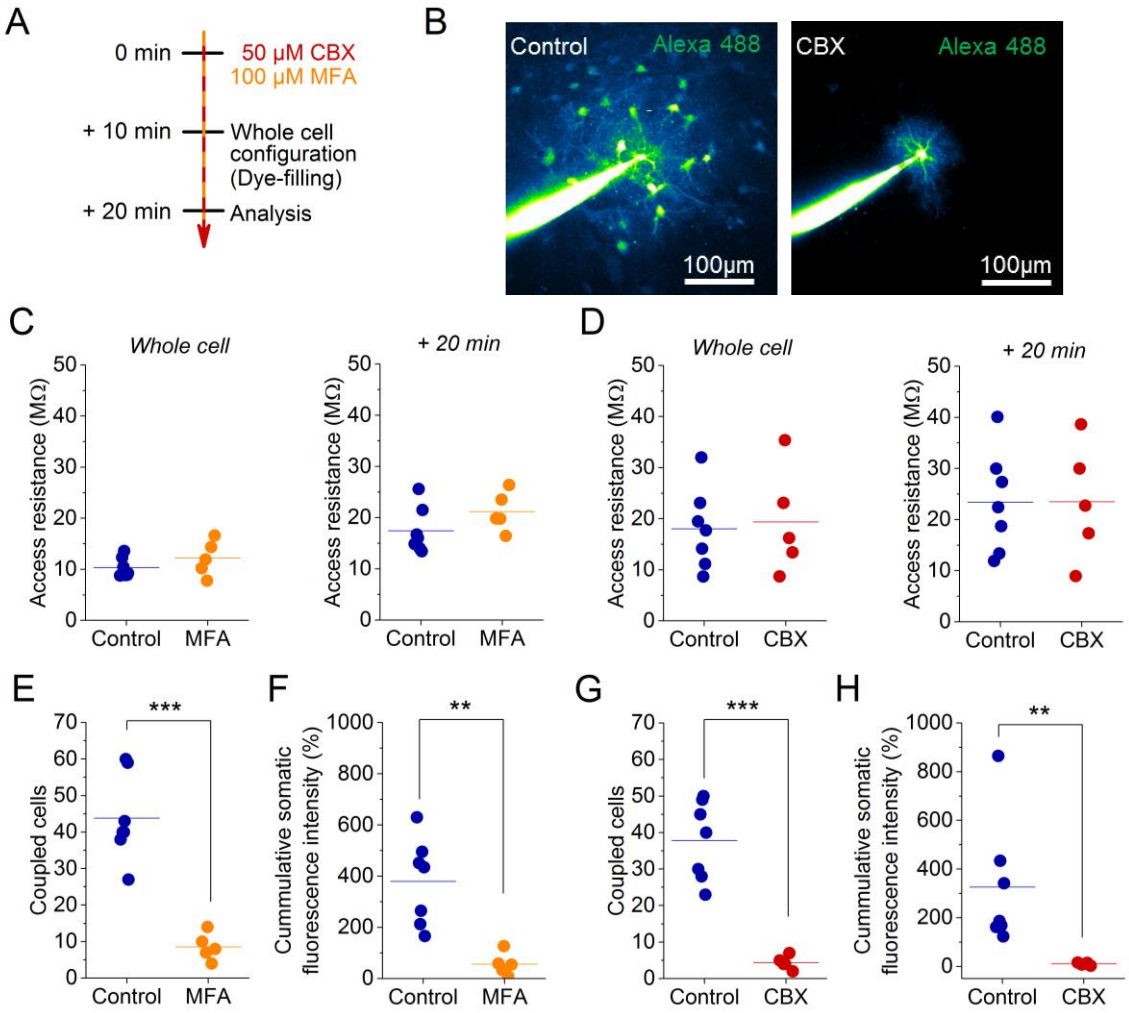

Figure 13 Pharmacological uncoupling of the astrocyte network. A) Experimental timeline. Hippocampal slices were treated with 50 µM CBX or 100 µM MFA for 10 minutes. Next, an astrocyte was patched and filled with the fluorescent dyes Texas red Dextran 3 kDa (300 µM) and Alexa Fluor 488 (80 µM). After 10 minutes, an image stack was obtained and the astrocyte dye-coupling was analyzed. **B)** In slices without drug-treatment (Control, left), Alexa Fluor 488 diffused from the patched astrocyte into adjacent cells and visualized the network. In contrast, Alexa Fluor 488 stayed predominantly in the patched astrocyte when the slice was pre-treated with MFA or CBX (right). **C-D)** The access resistance of astrocytes in drug-treated slices was not different from the respective controls shortly after opening the cell (Control, n = 7, 10.32 ± 0.73 MΩ; MFA, 12.18 ± 1.55 MΩ, n = 5; p = 0.257, two-sample Student's t-test & Control, n = 7, 18.04 ± 2.97 MΩ; CBX, n = 5, 19.37 ± 4.63 MΩ; p = 0.806, two-sample Student's t-test) or after 10 minutes of dye-filling (Control, n = 7, 17.45 ± 1.69 MΩ; MFA, n = 5, 21.20 ± 1.71 MΩ; p = 0.161, two-sample Student's t-test & Control, n = 7, 23.41 ± 3.76 MΩ; CBX, n = 5, 23.53 ± 5.11 MΩ; p = 0.923, two-sample Student's t-test). **E&G)** The number of coupled cells was reduced MFA-treated (Control, n = 7, 43.85 ± 4.47 cells; MFA, n = 5, 8.60 ± 1.66 cells; p < 0.001, two-sample Student's t-test) and CBX-treated slices (Control, n = 7, 37.85 ± 4.10 cells; CBX, n = 5, 4.40 ± 0.81 cells; p < 0.001, two-sample Student's t-test) compared to control. **F&H)** The cumulative soma fluorescence intensities of the coupled cells were reduced in MFA-treated (Control, n = 7, 379.42 ± 63.81%; MFA, n = 5, 56.27 ± 19.96%; p = 0.0018, two-sample Student's t-test) and CBX-treated slices (Control, n = 7, 326.05 ± 99.37%; CBX, n = 5, 10.18 ± 2.38; p = 0.0058; Mann Whitney U test) compared to control. Values of the single recordings and their average are represented by dots and lines, respectively.

4.1.2 Impact of acute astrocyte uncoupling on K^+ transients evoked by axonal and synaptic activity

Neurons open K^+ channels and release K^+ into the ECS in order to repolarize. Astrocytes are known to contribute to the removal of this extracellular K^+ by various mechanisms (Chapter 1.4.1). One mechanism that has been proposed to facilitate the extracellular K^+ clearance is the redistribution of K^+ through the gap junction-coupled astrocyte network (Chapter 1.4.2) (Orkand, 1986). However, the extent to which this mechanism contributes to K^+ clearance remained a matter of debate.

The first experiment investigating the role of gap junction coupling for K^+ homeostasis employed a common experimental arrangement for probing synaptic transmission (Chapter 3.4.2). These experiments were performed in the interface-type recording chamber and consisted of axonal stimulation at the CA3/1 border combined with the recording of field potentials and extracellular K^+ in the str. radiatum of the CA1 region (Figure 14A). A paired-pulse stimulation (50 ms interstimulus interval) of Schaffer collaterals (SCs) evoked two consecutive field potentials representing neuronal activity, i.e. axonal and synaptic activity (Figure 14B, bottom panel). Simultaneously, an increase of the extracellular K^+ concentration ('K^+ transient') was observed that lasted for several seconds (Figure 14B, top panel). This evoked extracellular K^+ elevations in the low millimolar range that are generally associated with physiological activity, such as light-evoked activity in the visual cortex (Connors et al., 1979) or activity in the spinal cord after skin-stimulation (Heinemann et al., 1990). After recording a 10-minutes baseline period, gap junction coupling was inhibited by adding 200 µM MFA to the extracellular solution for 10 minutes. The high K^+ conductance of the astrocytic membrane is a requirement for spatial K^+ buffering (Larsen and MacAulay, 2014; Orkand, 1986). The acute inhibition of the major mediator of this high conductance, the Kir4.1 channel, increased the peak amplitudes of evoked extracellular K^+ transients without affecting the decay of the extracellular K^+ concentration back to basal levels (Jauch et al., 2002; Larsen et al., 2014). Consequently, similar would be expected from an acute gap junction uncoupling when gap junction channels facilitate K^+ clearance via spatial K^+ buffering. In addition, a facilitated neuronal activity would also be expected since augmented extracellular K^+ accumulations would directly impact on neuronal excitability (Balestrino et al., 1986; Hablitz and Heinemann, 1987; Rausche et al., 1990; Voskuyl and ter Keurs, 1981).

In hippocampal slices obtained from juvenile (age of 3-5 weeks) Wistar rats, the synaptic transmission, quantified by the slope of the first paired-pulse stimulation evoked fEPSP, was unaffected by gap junction uncoupling (Figure 14D_1). In contrast, the paired-pulse ratio (PPR) was slightly, but statistically significantly increased by 4.45% (Baseline, 1.32 ± 0.04; MFA, 1.38 ± 0.04; n = 7, p = 0.00712, paired Student's t-test). This indicates that the

slope of the second paired-pulse evoked fEPSP was increased after the treatment with MFA and points towards a slightly decreased neurotransmitter release probability. However, gap junction uncoupling had no effect on the peak amplitude of the evoked K^+ transients (Figure 14F_1).

A previous study observed slowed decay rates of extracellular K^+ transients in hippocampal slices when the astrocyte network was disrupted by the astrocyte-specific genetic deletion of the gap junction forming connexins (Wallraff et al., 2006). However, the decay rates of evoked K^+ transients were unaffected by gap junction uncoupling in the present experiments (Figure 14E_1). This indicates that gap junction coupling was not involved in the clearance of extracellular K^+ transients under these experimental conditions. Although it cannot be excluded that the slightly increased slopes of the second paired-pulse evoked fEPSP were caused by a small augmentation of the evoked K^+ transients after gap junction uncoupling that was below the detection limit of the K^+-sensitive microelectrodes. However, the largely unaffected synaptic transmission as well as the unaffected extracellular K^+ transient amplitudes and decay rates indicate that K^+ clearance was to a great extent independent of astrocytic gap junction coupling. Conversely, this suggests that gap-junction independent mechanisms (e.g. Na^+/K^+-ATPase) mediated the clearance of extracellular K^+ under these conditions.

Since it has been reported in the literature that the extracellular space (ECS) fraction decreases with aging and, in turn, could influence the K^+ homeostasis and the role of gap junction channels (Syková and Nicholson, 2008), the experiments were repeated with hippocampal slices of adult (age of 8-10 weeks) Wistar rats. Again, gap junction uncoupling had no significant effect on the K^+ transient amplitude (Figure 14F_2, right panel) or decay (Figure 14E_2, right panel). In addition, no significant effect was observed on synaptic transmission (Figure 14D_2, right panel) or on the PPR (Baseline, 1.39 ± 0.08, MFA, 1.39 ± 0.06, n = 5, p = 0.996, paired Student's t-test). In order to exclude time-dependent effects, recordings without the application of MFA (Control) were performed, but fEPSP slopes, decay and peak amplitude of K^+ transients (Figure 14D_2-F_2, left panel) and the paired-pulse ratio were unaffected (PPR, Baseline, 1.36 ± 0.04; Control, 1.34 ± 0.02; n = 4; p = 0.565, paired Student's t-test). This indicates that also gap junction uncoupling has no impact on extracellular K^+ clearance in adult animals with a reduced ECS fraction.

Inhibitory neurons are also known to couple via gap junctions (Connors and Long, 2004; Fukuda and Kosaka, 2000; Kosaka and Hama, 1985) and, thus, were presumably also affected by the MFA. Consequently, interneuron activity could be altered that, in turn, impacts on neuronal activity and the corresponding K^+ release. Since evoked inhibitory feed-forward input from those interneurons impacts with a temporal delay and, thus, might

rather influences the later phase of the signal, the fEPSP amplitude was analyzed. However, fEPSP amplitudes were unaffected by MFA in hippocampal slices obtained from juvenile (Baseline, -2.20 ± 0.35 mV, MFA, -2.30 ± 0.41 mV, n = 7; p = 0.377, paired Student's t-test) and adult animals (Baseline, -2.18 ± 0.34 mV, Control, -2.28 ± 0.42 mV, n = 4, p = 0.382, paired Student's t-test; Baseline, -2.21 ± 0.14 mV, MFA, -2.10 ± 0.20 mV, n = 5, p = 0.267, paired Student's t-test).

Since a reduction of the ECS would lead to higher extracellular K^+ concentration when the same amount of K^+ is released into the ECS, the stimulation-evoked extracellular K^+ accumulation was quantified by the K^+ transient peak amplitude normalized to the corresponding neuronal activity (quantified by the fEPSP slope). However, the stimulation-evoked extracellular K^+ accumulations were similar in hippocampal slices from juvenile and adult animals despite their reported different ECS fractions (Juvenile, 0.096 ± 0.016 mM/mV*ms^{-1}, n = 7; Adult, 0.131 ± 0.033 mM/mV*ms^{-1}, n = 9; p = 0.372, two-sample Student's t-test). This suggests that the clearance mechanisms for extracellular K^+ also adapt in an age-dependent manner or that the potential increased extracellular K^+ concentration were below the detection level.

Taken together, these findings indicate that acute gap junction uncoupling has nearly no effect on synaptic transmission and K^+ transients evoked under the described experimental conditions. However, the evoked transients had relatively small peak amplitudes (0.12 ± 0.012 mM, n = 16, both age-groups) and, thus, might be controlled by other mechanisms than buffering assisted by astrocytic gap junction channels (e.g. Na^+/K^+-ATPase). The employed stimulation might also induce only short and spatially distributed axonal and synaptic activity and, in turn, only small and local K^+-depolarization of the astrocytic membrane. For instance, the average distance between gap junction channels of astrocytes in the barrel cortex of mice were reported to be around 1-1.2 µm (Genoud et al., 2015). If the local active astrocytic domains would be small enough, K^+ might be redistributed to neighboring astrocyte domains at rest without passing (or only a few) gap junction channels. Consequently, acute gap junction uncoupling would not interfere with local, small-scale K^+ buffering and could explain the observations. Since larger extracellular K^+ accumulations would also induce astrocyte membrane depolarizations over a larger area, gap junction channel might play a more pronounced role in limiting this K^+-induced depolarization. Therefore, the following experiments investigated the impact of gap junction uncoupling on K^+ transients with larger peak amplitudes.

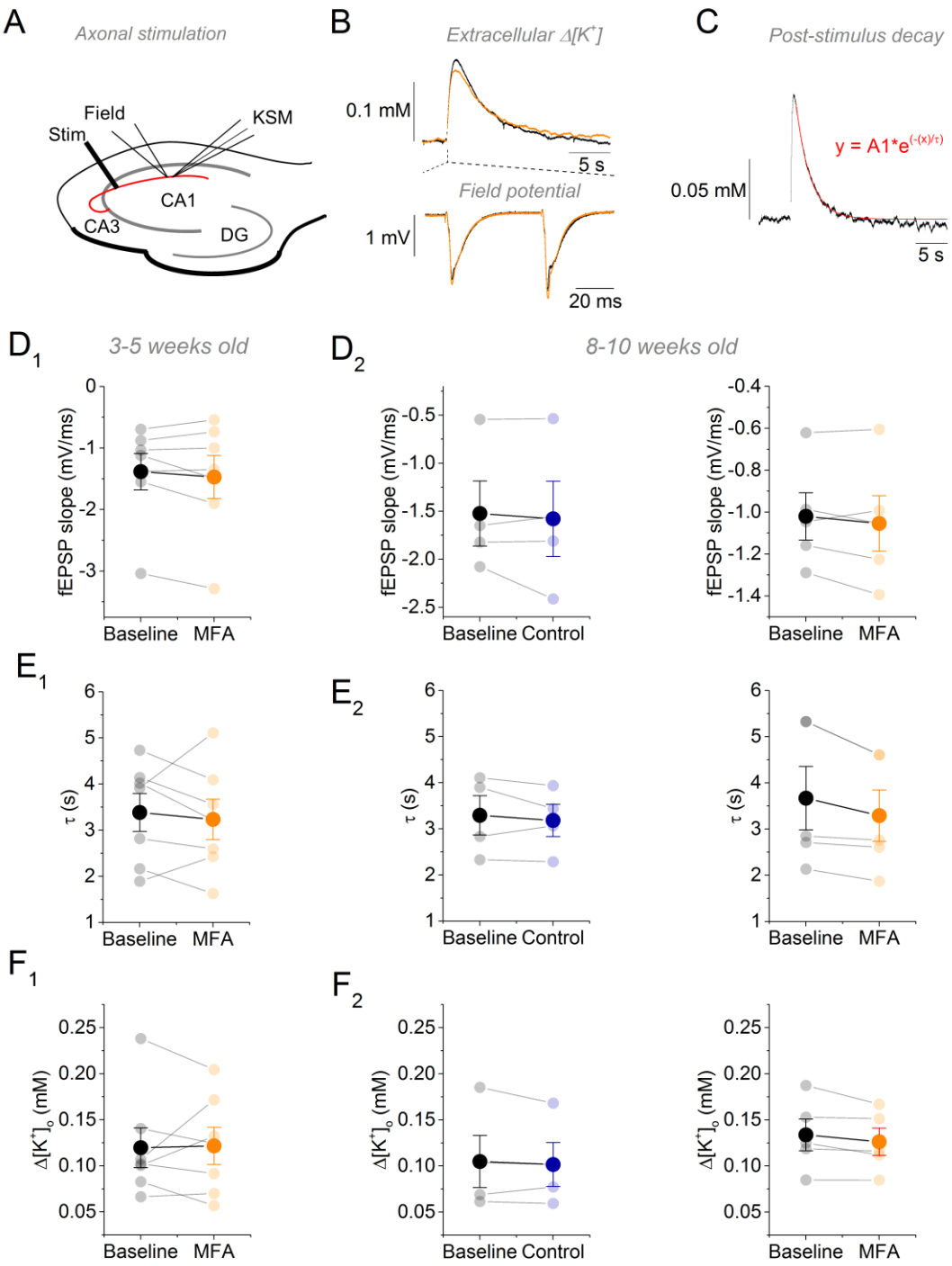

Figure 14 Astrocyte uncoupling has no effect on synaptic transmission and corresponding K^+ transients. A) Experimental arrangement. The stimulation electrode (Stim) was placed in the str. radiatum at the border of CA3 and CA1 region and corresponding field potentials (Field) and K^+ transients (KSM) were recorded in the CA1 str. radiatum. **B)** Paired pulse stimulation (20 Hz) evoked excitatory field potentials (fEPSPs, bottom) and corresponding extracellular K^+ transients (top) before (baseline, black) and after (orange) 10-15 minutes of MFA treatment. **C)** The decay of the K^+ transients was fitted with a monoexponentially decaying function (fit superimposed in red). **D-F)** In slices obtained from 3-5-week old animals, MFA application had no impact on the fEPSP slope (D_1, n = 7, p = 0.554, Wilcoxon's Signed Ranks test), K^+ transient decay constant (E_1, n = 7, p = 0.609, paired two-sample Student's t-test) and the K^+

transient amplitudes (F_1 n = 7, p = 0.932, Wilcoxon's Signed Ranks test). There was also no effect in slices obtained from 8-10-week old animals on the slope of the fEPSPs (D_2; Control, n = 4, p = 0.598, paired two-sample Student's t-test; MFA, n = 5, p = 0.318, paired two-sample Student's t-test), K^+ transient decay constant (E_2; Control, n = 4, p = 0.497, paired two-sample Student's t-test; MFA, n = 5, 0.056, paired two-sample Student's t-test) and the K^+ transient amplitudes (F_2; Control, n = 4, p = 0.572, paired two-sample Student's t-test; MFA, n = 5, p = 0.127, paired two-sample Student's t-test).

4.1.3 Impact of astrocyte uncoupling on K^+ transients evoked by axonal activity

The aim of this set of experiments was to evoke K^+ transients of larger amplitude compared to the previous chapter and probe the impact of acute gap junction uncoupling. We hypothesized that larger extracellular K^+ accumulations would depolarize a larger membrane area including also more gap junction channels. As a consequence, acute gap junction uncoupling would impair the K^+ redistribution through these channels and augment the local depolarization. This would result in a less efficient passive K^+ uptake and presumably in increased K^+ transient peak amplitudes.

In order to evoke larger extracellular K^+ accumulations, the same experimental arrangement as before was used (Figure 14A), but CA3-CA1 SCs were stimulated with 50 stimulation pulses at a frequency of 100 Hz (high frequency stimulation, HFS). Since this kind of stimulation can induce synaptic plasticity and, in turn, uncontrolled changes in K^+ release, postsynaptic activity was inhibited by blocking AMPAR and NMDAR (10 µM NBQX and 50 µM D-APV). Accordingly, the HFS evoked axonal activity that was represented by a train of 50 FVs (Figure 15A, bottom panels) and corresponding K^+ transients with peak amplitudes of ~0.5 mM. After recording of a baseline period for 5 minutes, the gap junction coupled network was inhibited by bath-applying 50 µM CBX for 10 minutes. Next, the axonal activity and the K^+ transients were compared to baseline conditions. The axonal activity, quantified by the mean of the 1^{st}, 10^{th}, 20^{th}, 30^{th}, 40^{th} and 50^{th} FV during the HFS, was not significantly altered by CBX in slices from juvenile Wistar rats (Figure 15C, left panel). Additionally, gap junction uncoupling had no significant effect on the peak amplitude or the decay of the evoked K^+ transients (Figure 15B, middle and right panel, respectively).

As already mentioned, age-dependent ECS shrinkage could influence the K^+ homeostasis and the role of gap junction channels (Syková and Nicholson, 2008). Thus, the same experiments were performed in slices from adult Wistar rats. In contrast to slices of juvenile Wistar rats, the FV and K^+ transient amplitudes were slightly, but statistically significant increased after gap junction uncoupling (Figure 15C, left and middle panel, respectively). Again, the decay of the K^+ transients was unaltered by gap junction uncoupling (Figure 15C, right panel). These observations are in line with experiments that

prevented the spatial K^+ redistribution by acute Kir4.1 channel inhibition and observed increased K^+ transient peak amplitudes (Jauch et al., 2002; Larsen et al., 2014). The unaltered decay rate of the evoked K^+ transients after gap junction uncoupling supports the general idea that the post-stimulus decay is mainly mediated by the Na^+/K^+-ATPase (D'Ambrosio et al., 2002; Larsen et al., 2014; Ransom et al., 2000). This further supports that astrocytic gap junction channels facilitate spatial K^+ buffering during the accumulation phase of extracellular K^+ and not during its decay back to baseline, as already suggested by Larsen et al. (2014).

In order to test an age-dependent difference of gap junction uncoupling, the K^+ transient and the mean FV amplitudes were normalized to their baseline values and compared between the two age groups. Both, the change of the FV amplitudes (Figure 16A) and the K^+ transient peak amplitudes (Figure 16B) after gap junction uncoupling were significantly larger in hippocampal slices from adult compared to juvenile animals. This observation was not due to larger K^+ accumulations in slices obtained from adult compared to juvenile animals. In fact, the K^+ accumulation during basal conditions, quantified by the K^+ transient peak amplitudes normalized to the corresponding mean FV amplitude, was smaller in hippocampal slices obtained from adult animals (Juvenile, 1.63 ± 0.21 mM/mV, n = 7; Adult, 1.02 ± 0.11 mM/mV, n = 10; p = 0.0134, two-sample Student's t-test). However, the mean basal FV amplitudes in hippocampal slices of juvenile animals were similar to those recorded in hippocampal slices of adult animals (Juvenile, 0.46 ± 0.047 mV, n = 7; Adult, 0.47 ± 0.06 mV, n = 10; p = 0.903, two-sample Student's t-test). This suggests that other factors independently of the age-dependent ECS shrinkage (Syková and Nicholson, 2008) modulates the extracellular K^+ homeostasis, such as the astrocytic maturation state (Nixdorf-Bergweiler et al., 1994).

Together, these results indicate that gap junction uncoupling does not affect axonal activity and K^+ clearance in juvenile animals under the described experimental conditions. In contrast, the increase of the FV amplitude and the peak amplitude of the corresponding K^+ transients in slices from adult animals could indicate an age-dependent role for gap junction coupling in K^+ clearance. However, there are two potential explanations for these observations. First, the CBX-induced gap junction uncoupling impairs the clearance of extracellular K^+, leading to increased K^+ transients and, in turn, to larger FV amplitudes by a K^+-mediated increased axonal excitability. Second, the axonal excitability is increased by a gap junction independent action of CBX and thereby causing increased K^+ release. Indeed, effects of CBX on neurons have been reported in the literature, such as broadening of action potentials (Tovar et al., 2009). In order to reduce potential side-effects of CBX on neurons and, in turn, on K^+ homeostasis, neuronal activity was completely inhibited in the following experiments. Instead, K^+ transients were directly

evoked via an iontophoretic application of K^+ into the ECS of hippocampal slices from adult Wistar rats.

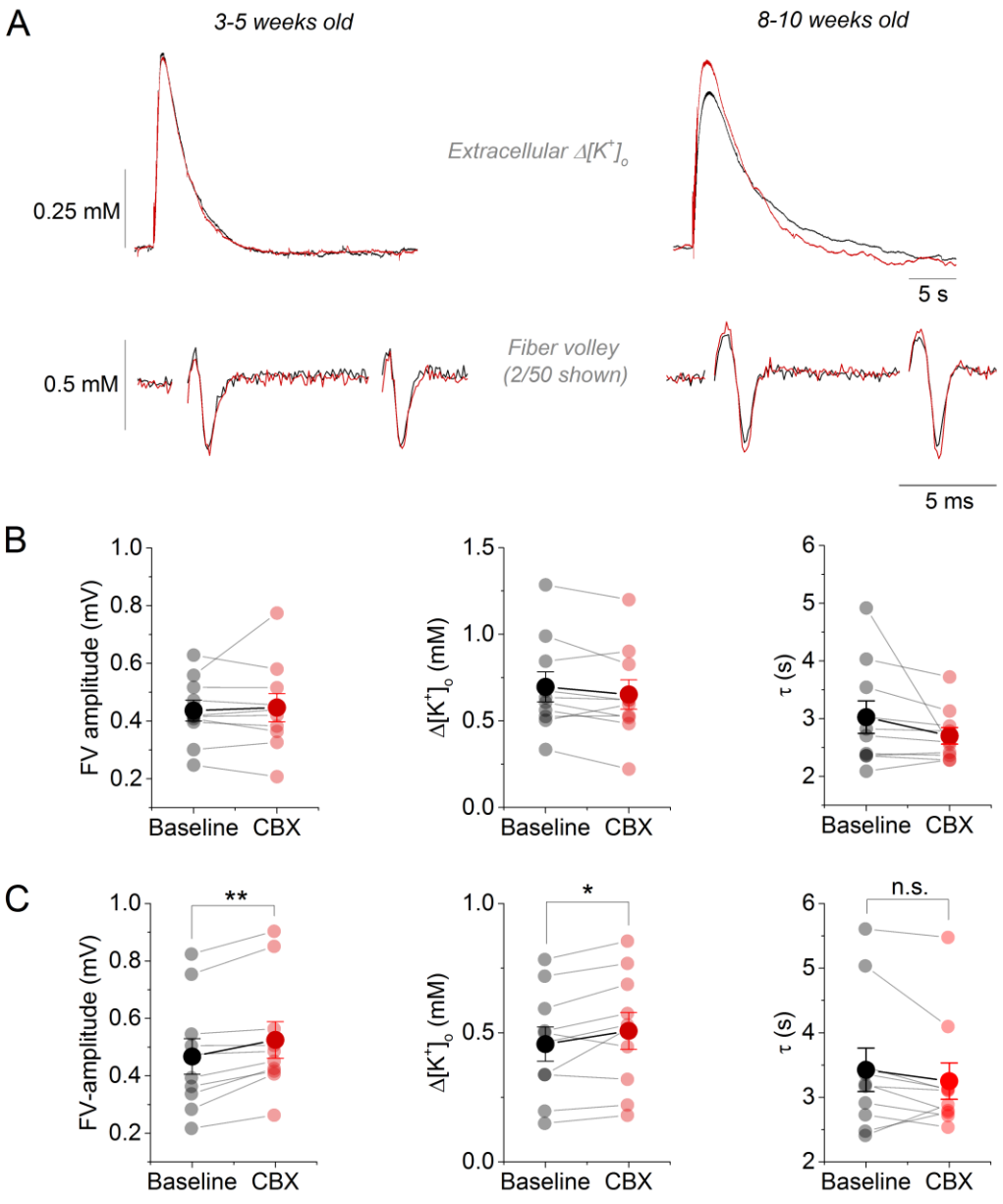

Figure 15 Impact of gap junction uncoupling on K^+ transients evoked by high-frequency axonal activity. A) Example traces of axonal activity (bottom) and the corresponding K^+ transients (top) before (black) and after (red) gap junction uncoupling with CBX recorded in the CA1 str. radiatum evoked by a high-frequency stimulation (50 pulses at 100 Hz) of CA3-CA1 SCs. For illustration, only two of the 50 evoked fiber volleys (FV) are shown. **B)** In hippocampal slices from juvenile Wistar rats (3-5 weeks) gap junction uncoupling had no effect on the FV amplitude (Baseline, 0.437 ± 0.036 mV; CBX, 0.44 ± 0.049 mV; n = 10, p = 0.686, paired Student's t-test), the K^+ transient peak amplitudes (Baseline, 0.696 ± 0.087 mM; CBX, 0.652 ± 0.085 mM; n = 10, p = 0.109, paired Student's t-test) and the decay constant (τ) of the K^+ transients (Baseline, 3.03 ± 0.282 s; CBX, 2.703 ± 0.142 s; n = 10,p = 0.198, paired Student's t-test). **C)** In hippocampal slices from adult Wistar rats (8-10 weeks), the FV amplitude (Baseline, 0.467 ± 0.062 mV; CBX, 0.525 ± 0.063 mV; n =

10, p = 0.00138, paired Student's t-test) and the K^+ transient peak amplitudes (Baseline, 0.456 ± 0.066 mM; CBX, 0.507 ± 0.071 mM, n = 10, p = 0.0299, paired Student's t-test) were increased after gap junction uncoupling. The decay (τ) of the K^+ transients was unaffected (Baseline, 3.425 ± 0.337 s; CBX, 3.251 ± 0.281 s; n = 10, p = 0.232, Wilcoxon's Signed Ranks test).

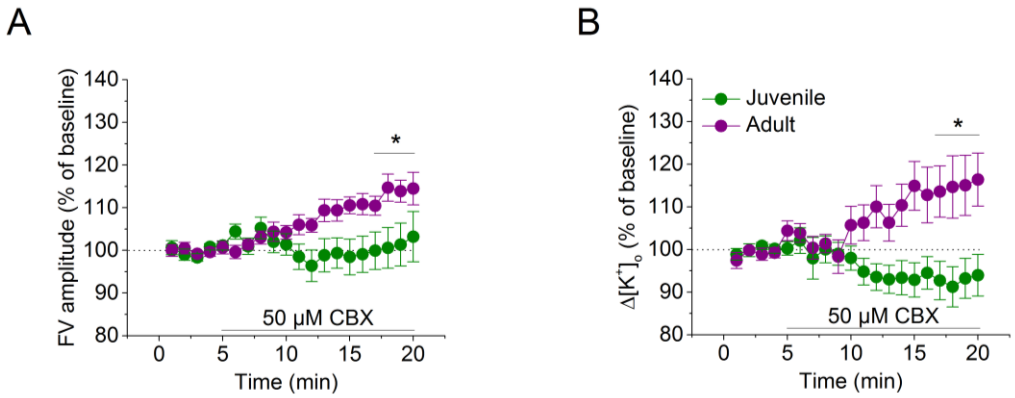

Figure 16 Age-dependent differences of CBX-induced gap junction uncoupling. A) The mean FV amplitudes (normalized to baseline) were significantly larger after CBX-treatment in hippocampal slices from adult compared to juvenile Wistar rats (Juvenile, 100.9 ± 4.836%, n = 10; Adult, 112.8 ± 2.58%, n = 10; p = 0.0427, two-sample Student's t-test). B) The K^+ peak amplitudes (normalized to baseline) were also significantly larger in hippocampal slices from adult compared to juvenile Wistar rats (Juvenile, 93.14 ± 4.41%, n = 10; Adult, 114.50 ± 6.35%, n = 10; p = 0.0129, two-sample Student's t-test).

4.1.4 Extracellular spread of iontophoretically induced K^+ transients

The previous experiments have indicated a role for astrocytic gap junction coupling in K^+ clearance in adult animals. Acute gap junction uncoupling slightly augmented the peak amplitude of extracellular K^+ transients evoked by axonal activity (Figure 15). However, it cannot be excluded that the observed effect on the K^+ transients was mediated by an increased activity-dependent neuronal K^+ release. In fact, CBX was found to modulate neuronal activity (Tovar et al., 2009) and thus could have caused the augmented K^+ transient peak amplitudes via an increased activity-dependent neuronal K^+ release independently of an impaired K^+ clearance. In addition, the employed axonal stimulation might have evoked a homogeneous extracellular K^+ elevation in the tissue and thereby attenuated an extracellular K^+ concentration gradient. Since such a gradient has been proposed to be required for the spatial K^+ redistribution (Orkand, 1986), the importance of gap junction uncoupling for K^+ redistribution was possibly underestimated during these experimental conditions.

In order to further investigate the impact of acute gap junction uncoupling K^+ clearance, the following experiments were performed in the absence of neuronal activity and, in turn, activity-dependent neuronal K^+ release. This was achieved by bath-applying 10 µM NBQX, 50 µM D-APV and 1 µM TTX throughout the experiment in order to inhibit AMPAR, NMDAR and voltage-gated Na^+ channels. Instead of neuronal activity, K^+ transients were evoked via an iontophoretic application of K^+ into the ECS (Chapter 3.5). This approach allowed injecting a constant amount of K^+ sequentially into the ECS by controlling the iontophoretic current amplitude and duration. As a consequence, extracellular K^+ transients were evoked as a point-source at a known location. This approach had two major advantages: First, the amount of K^+ injected into the ECS via the iontophoresis pipette was independent of neuronal activity and thus reduced the impact of potential CBX side-effects on extracellular K^+ transients. Second, the application of K^+ at a single point created an extracellular K^+ concentration gradient. Since an extracellular K^+ concentration gradient is one the requirements for spatial K^+ buffering (Orkand, 1986), this approach might promote the spatial redistribution of K^+ and, in turn, the role for gap junctions channels.

Before the impact of gap junction uncoupling under these experimental conditions was tested, the spatial spread of the iontophoretically applied K^+ was investigated. Thus, an estimate about the number of astrocytes in contact with the applied K^+ was achieved. Since the effect of gap junction uncoupling on the FV and K^+ transient amplitudes was observed in hippocampal slices obtained from adult animals (8-10 weeks old Wistar rats), the same preparation was used in the following experiments. The KSM was placed in the CA1 str. radiatum and large K^+ transients were evoked by iontophoretic K^+ application

(900 nA for 500 ms, 3 M KCl in iontophoresis pipette) at defined distances to the tip of the KSM. In order to avoid an interference of the extracellular K^+ spread by a damage of the ECS, the relatively large KSM was positioned once and only the fine iontophoresis pipette was moved stepwise in parallel or perpendicular to the pyramidal cell layer from distant to close positions (Figure 17A). The peak amplitude of the measured K^+ transients decreased with increasing distance between recording and K^+ application site (Figure 17B, left panel). This distance-dependent decline was then approximated with a monoexponentially decaying function (Figure 17B, right panel). In a subset of experiments, smaller K^+ transients (800 nA for 200 ms, 150 mM KCl in iontophoresis pipette) were evoked. Their spatial decay was not different compared to large K^+ transients (Small transients, 12.79 ± 1.02 µm, n = 4; large transients, 13.14 ± 0.95 µm, n = 18; p = 0.868, two-sample Student's t-test) and the data therefore pooled. Overall, the peak amplitudes declined with a decay constant of 13.08 ± 0.79 µm (n = 22) in the CA1 str. radiatum. Similar was observed in the CA1 stratum lacunosum moleculare (Breithausen et al., 2020). Consequently, it can be estimated that the applied K^+ spreads across the territory boundary into at least one neighboring astrocyte (see chapter 5.1.2). Furthermore, it was reported that the average distance between gap junction channels of astrocytes in the barrel cortex of mice is around 1-1.2 µm (Genoud et al., 2015). Considering the same for hippocampal astrocytes, the extracellular K^+ likely depolarized astrocytic membrane with reflexive gap junctions but also gap junctions coupling to neighboring astrocytes.

It has been shown that extracellular diffusion in the hippocampus is facilitated along the trajectory of the SCs (Mazel et al., 1998). Therefore, we asked if the extracellular K^+ diffusion is also direction-dependent. If this would be the case, the decline of the K^+ transient peak amplitudes over distance is expected to be less pronounced along the Schaffer collaterals (i.e. in parallel to the str. pyramidale). To test this, the distance-dependent decline of the K^+ transient peak amplitudes in parallel to the pyramidal cell layer was compared to perpendicular (Figure 17C, left panel). However, there were no differences between the two directions (Figure 17C, right panel). In summary, these experiments show that the iontophoretically injected K^+ spread into the ECS and resulted in a direction-independent concentration gradient. In addition, it can be assumed that the injected K^+ spread far enough to depolarize astrocytic membrane with gap junction channels that, in turn, could contribute to the K^+ clearance.

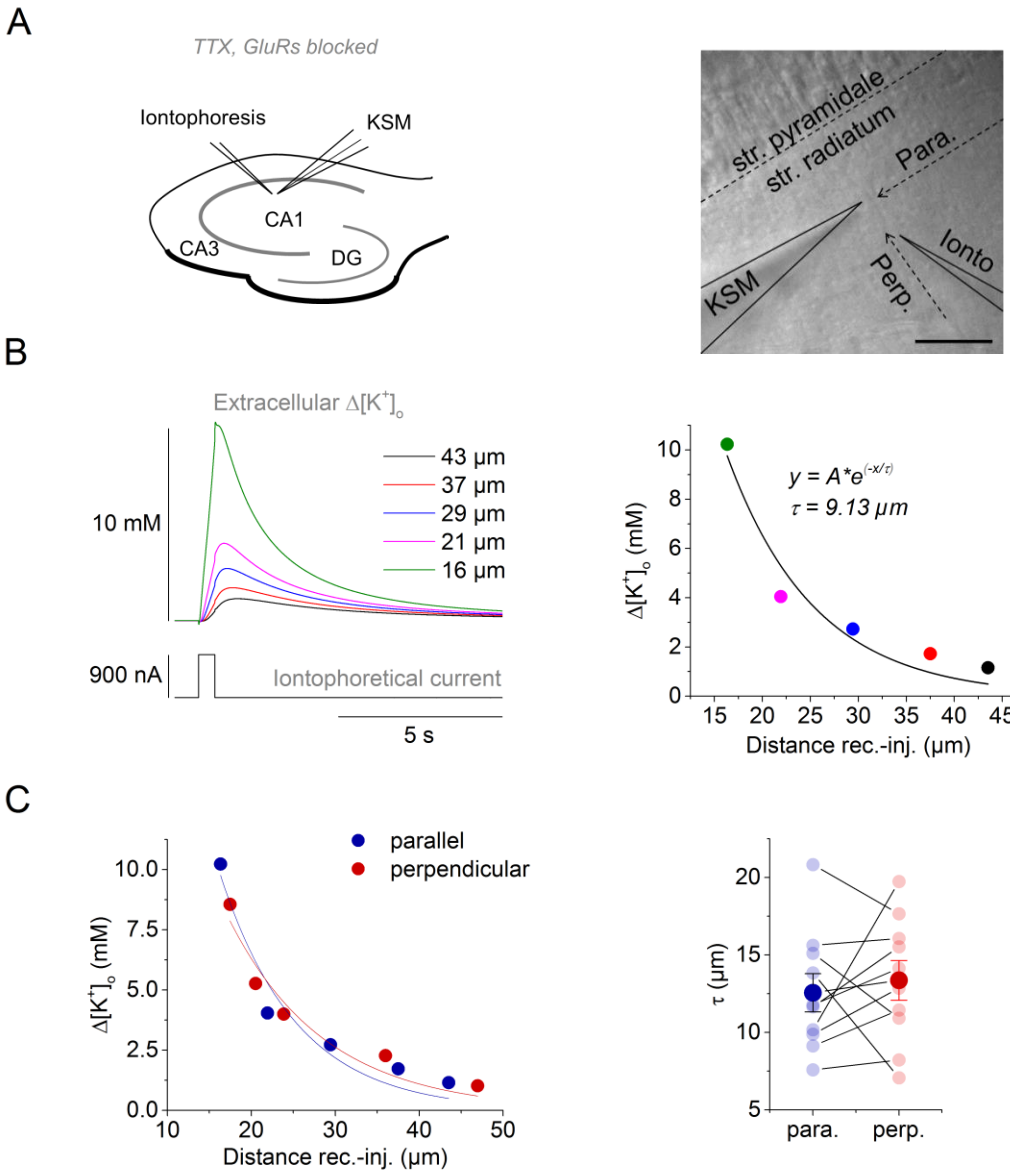

Figure 17 Extracellular K^+ diffusion in the CA1 str. radiatum. A) Experimental arrangement. The KSM was placed in the CA1 str. radiatum and K^+ was sequentially applied via the iontophoresis pipette at different spots in parallel and perpendicular to the str. pyramidale. Right: DIC image of the experimental arrangement. Scale bar: 50 µm. **B)** Left: Example K^+ transients measured by the KSM and evoked by iontophoretic application at different distances from the tip of the KSM. Right: The distance-dependent decline of the K^+ transient peak amplitudes (shown left) was fitted with a monoexponentially decaying function (black line). The decay constant (τ) was then used to quantify the size of the extracellular K^+ spread. **C)** Left: Example of K^+ transient peak amplitudes recorded in the same brain slice, but evoked at different distances in parallel (blue) and perpendicular (red) to the str. pyramidale. The lines represent the particular fit of the distance-dependent decline. Right: The distance-dependent decline of the K^+ transient peak amplitudes was not significantly different in parallel and perpendicular to the str. pyramidale (parallel, 12.56 ± 1.23 µm; perpendicular; 13.36 ± 1.28 µm, n = 10; p = 0.597, paired Student's t-test). These experiments were performed in collaboration with S. Kautzmann.

4.1.5 Impact of astrocyte uncoupling on iontophoretically induced K^+ transients

The previous experiments indicated that astrocytic gap junction coupling attenuates the peak amplitude of extracellular K^+ transients in hippocampal slices obtained from adult Wistar rats (Chapter 4.1.3). It was further shown that the iontophoretic application of K^+ evoked an extracellular K^+ gradient that spreads far enough to presumably depolarize the astrocytic membrane with several gap junction channels. Thus, we hypothesized that astrocytic gap junction coupling has an important role for K^+ redistribution during these experimental conditions. As a consequence, acute gap junction uncoupling might have a more pronounced effect on the extracellular K^+ transients.

First, it was tested if gap junction uncoupling impacts on clearance of K^+ transients with peak amplitudes in the lower millimolar range that are observed during physiological conditions (Rasmussen et al., 2019). For this purpose, K^+ transients were evoked via an iontophoretic K^+ application (800 nA for 200 ms) in the CA1 str. radiatum in the absence of neuronal activity as described above. In contrast, the K^+-sensitive microelectrode (KSM) and the iontophoresis pipette were placed once and then kept in position for the time course of the experiment. The distance between the K^+ source and the site of recording ranged from 5 to 88 µm and was negatively correlated with the peak amplitude of the measured K^+ transient, in line with the results described in the previous chapter (ρ = -0.765, $p < 0.001$, n = 29, Spearman's rank correlation). For probing the impact of gap junction uncoupling, K^+ transients were evoked for a baseline period with intact gap junction coupling followed by the treatment with 50 µM CBX or control conditions (no CBX applied) (Figure 18A). During the baseline period, the initial peak amplitudes of the evoked K^+ transients were on average 2.24 ± 0.457 mM (n = 30, Control and CBX). However, the initial peak amplitudes recorded in control slices were not significantly different from those that were subsequently treated with CBX (Figure 18B). Importantly, the distances between K^+ application and recording site in control conditions were not different from CBX-treated slices site (Control, 29.21 ± 5.46 µm, n = 14; CBX, 30.53 ± 5.77 µm, n = 15; p = 0.933, Mann Whitney U test). After the baseline period, gap junction coupling was inhibited by bath-application of 50 µM CBX for 10 minutes. In order to quantify the effect of CBX on the evoked K^+ transients, the peak amplitudes of the K^+ transients in CBX-treated and control slices were normalized to their respective values during the baseline period (Figure 18C, left panel). The relative change of the K^+ transient peak amplitudes was overall not significantly different after CBX treatment compared to control conditions (Figure 18C, right panel).

Next, it was investigated if gap junction uncoupling had a selective effect on only a subset of evoked K^+ transients, i.e. K^+ transients with a certain peak amplitude or K^+ transients that were evoked at a distinct distance to the recording site. For instance, it could be

possible that an effect of gap junction uncoupling becomes more pronounced the more gap junction channels were located between K^+ source and the recording site, because the contribution to the recorded K^+ transient would be larger. As a consequence, the impact of gap junction uncoupling on K^+ transients would be expected to increase with increasing distance to the K^+ source. In contrast, it could be argued that gap junction coupling only contributes to K^+ clearance by limiting substantial astrocytic membrane depolarization induced by large extracellular K^+ loads. Accordingly, gap junction uncoupling would have a larger impact on K^+ transients with larger peak amplitudes. In order to test these possibilities, the correlation of the relative change of the K^+ transient peak amplitudes and their initial peak amplitude during the baseline period was analyzed (Figure 18D). In addition, the correlation between the relative change of the peak amplitudes and the distance between the K^+ application and recording site was tested (Figure 18E). However, none of these parameters was significantly correlated with the relative change of the K^+ transient peak amplitude after gap junction uncoupling or control condition in these experiments.

The genetic deletion of the gap junction forming connexins from hippocampal astrocytes led to a complete disruption of the astrocyte network and to slowed decay rates of extracellular K^+ transients (Wallraff et al., 2006). In order to test if the acute pharmacological uncoupling of gap junction channels has a similar effect, the decay of the K^+ transients was analyzed with a monoexponentially decaying function (Figure 19A). During the baseline period, the decay constants of the K^+ transients in control conditions were not significantly different from CBX conditions (Figure 19B, left panel) and, in accordance with the literature (Strohschein et al., 2011; Wallraff et al., 2006), K^+ transients with higher peak amplitudes exhibited smaller decay constants ($\rho = -0.77$, $p < 0.001$, $n = 28$, Spearman's rank correlation). However, the decay constants of the K^+ transients were overall not different after CBX treatment compared to control conditions (Figure 19B, right panel). Again, the initial peak amplitude of the K^+ transients (Control, $\rho = -0.12$, $p = 0.69$, $n = 13$; CBX, $\rho = -0.22$, $p = 0.41$, $n = 15$; Spearman's rank correlation) and the distance between K^+ recording and application site (Control, $\rho = 0.022$, $p = 0.943$, $n = 13$; CBX, $\rho = -0.017$, $p = 0.950$, $n = 15$; Spearman's rank correlation) were not significantly correlated with the relative change of the decay constants. This suggests that gap junction coupling is not involved in mediating the decay back to basal levels of extracellular K^+ transients during these experimental conditions. In contrast to the study by Wallraff and colleagues (2016), extracellular K^+ transients were not evoked by neuronal activity and thereby could be cleared by different mechanisms. In addition, it cannot be excluded that the reported morphology changes of connexin-deficient astrocytes (Ghézali et al., 2018; Pannasch et

al., 2014) had mediated the slowed decay rates (Wallraff et al., 2006) and thus were not present in our experiments.

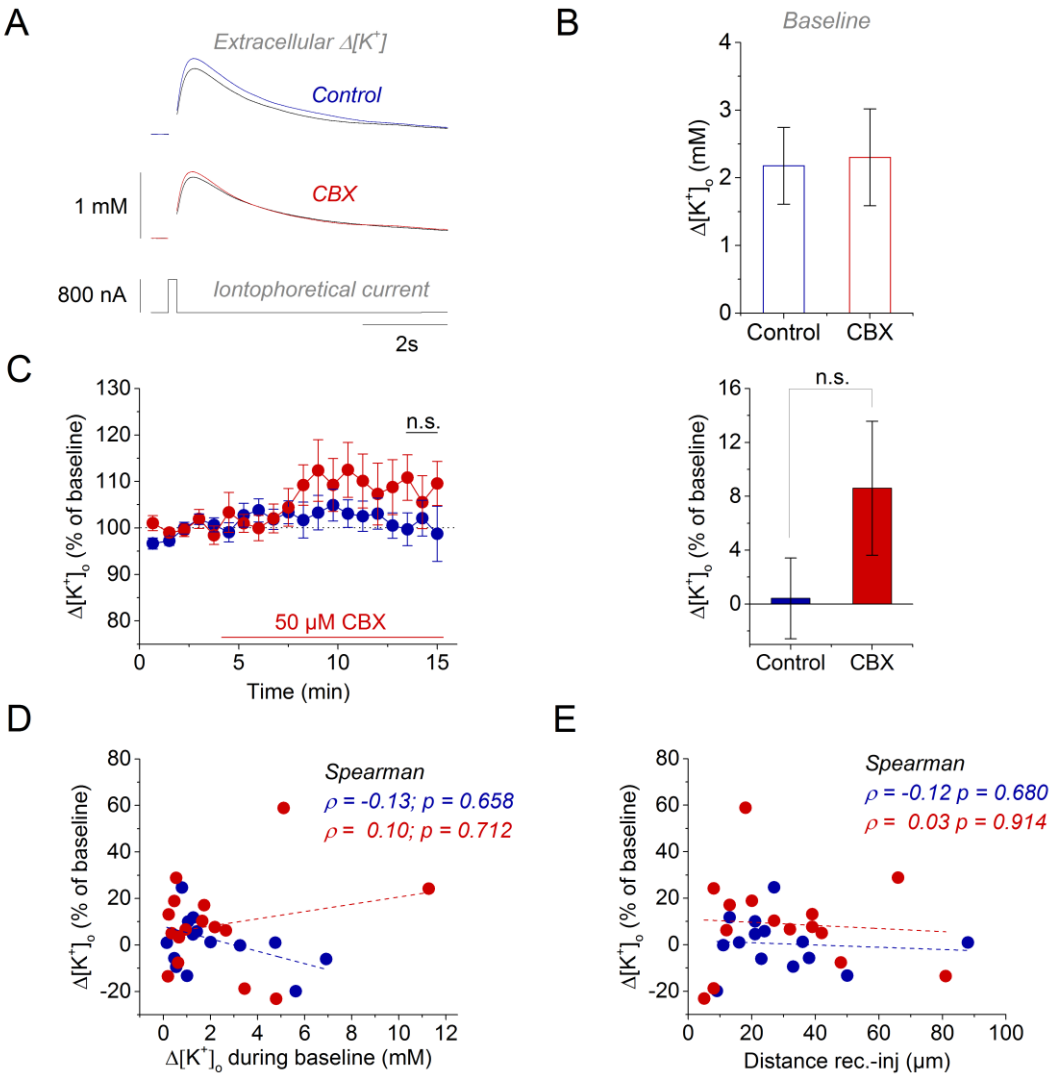

Figure 18 Peak amplitudes of small K^+ transients were unaffected by acute gap junction uncoupling. **A)** Small K^+ transients were evoked by iontophoretic K^+ application (800 nA for 200 ms) in the CA1 str. radiatum. K^+ transients were recorded during a baseline period (black) and then compared after the application of 50 µM CBX (red) for 10 minutes or during control conditions (blue). **B)** The basal peak amplitudes of the evoked K^+ transients in control recordings were not different from the basal peak amplitudes in CBX recordings (Control, 2.178 ± 0.568 mM, n = 14; CBX, 2.30 ± 0.716 mM, n = 16; p = 0.72, Mann Whitney U test). **C)** Left: Time course of the baseline-normalized K^+ transient peak amplitudes. After 10 minutes of CBX treatment, the normalized peak amplitudes were compared between CBX and control condition. Right: The change of the normalized peak amplitudes after CBX treatment was not significantly different compared to control condition (Control, 0.42 ± 2.99%, n = 14; CBX, 8.60 ± 4.97%, n = 16, p = 0.606, two- sample Student's t-test). **D)** No significant correlation was observed between the initial K^+ transient peak amplitudes and the change of the normalized K^+ transient peak amplitudes during CBX (n = 16) or control condition (n = 14) (Spearman's rank correlation). **E)** The change of the normalized K^+ transient peak amplitudes in CBX (n = 15) and control condition (n = 14) were also not correlated with distance between the K^+ application and recording site.

Taken together, these results indicate that acute gap junction uncoupling has no impact on the peak amplitude and the decay of iontophoretically evoked K^+ transients in the CA1 str. radiatum with peak amplitudes in the low millimolar range. These concentration values are generally associated with neuronal activity observed during typical electrophysiological experiments (Chever et al., 2010; D'Ambrosio et al., 2002; Strohschein et al., 2011; Wallraff et al., 2006; Xu et al., 2009) or during physiological conditions in vivo (Heinemann et al., 1990; Rasmussen et al., 2019). Larger extracellular K^+ accumulations in the range of ~10 mM were commonly associated with pathophysiological condition, such as epileptiform activity (de Curtis et al., 2018; Fisher et al., 1976; Moody et al., 1974). Interestingly, astrocytic gap junction coupling was found to be absent coupling in tissue from patients suffering from epilepsy (Bedner et al., 2015). This might indicate that astrocytic gap junction coupling is preferentially involved in the clearance of large extracellular K^+ accumulations and an uncoupling further augment those.

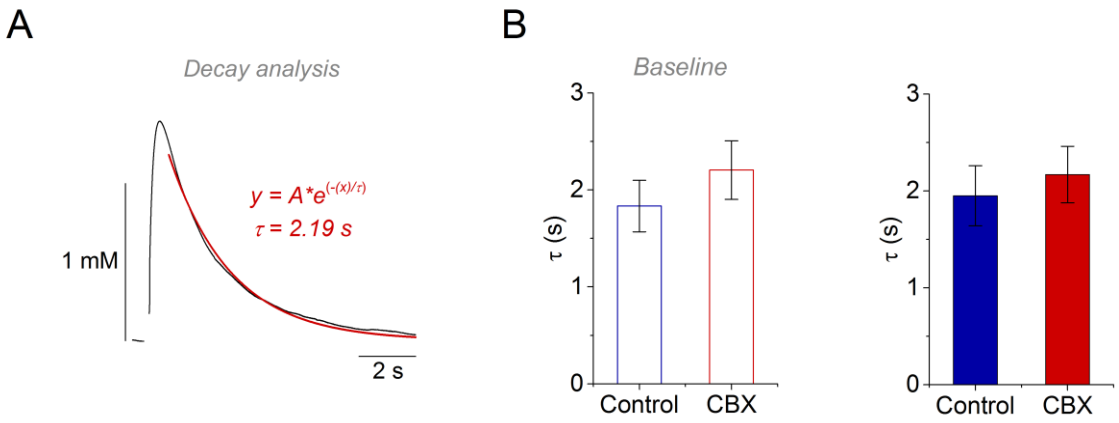

Figure 19 The post-stimulus decay of the small K^+ transients was unaffected by gap junction uncoupling. A) The post-stimulus decay of the K^+ transients was fitted with a monoexponentially decaying function (fit superimposed in red). For quantification, the decay constant (τ) of the function was used. **B)** Left: The initial decay constants during the baseline period in control conditions were not significantly different from CBX conditions (Control, 1.83 ± 0.265 s, n = 13; CBX, 2.20 ± 0.301 s, n = 15; p = 0.371, two-sample Student's t-test). Right: After gap junction uncoupling, the decay constants were not significantly different from control condition (Control, 1.94 ± 0.311 s, n = 13; CBX, 2.17 ± 0.291, n = 15; p = 0.610, two-sample Student's t-test).

In order to test if larger extracellular K^+ accumulations were preferentially affected by acute gap junction uncoupling, K^+ transients were evoked with a stronger iontophoretic K^+ injection (900 nA for 500 ms). This evoked K^+ transients with peak amplitudes of, on average, 8.70 ± 1.15 mM (n = 35) (Figure 20A). As expected, the peak amplitudes of the evoked K^+ transients during baseline conditions were again negatively correlated with the distance between recording and K^+ application site (ρ = -0.49, p = 0.00322, n = 34, Spearman's rank correlation). These distances were similar in control and CBX-treated slices (Control, 20.86 ± 2.04 µm, n = 15; CBX, 19.58 ± 2.47 µm, n = 19; p = 0.702, two-sample Student's t-test), as well as the initial peak amplitudes of the K^+ transients during the baseline period (Figure 20B). However, after the gap junction uncoupling by the application of CBX, the normalized peak amplitudes increased significantly compared to control condition (Figure 20C). Surprisingly, there was a trend towards a decrease of the K^+ transient peak amplitudes during control conditions relative to baseline (-6.48 ± 3.14%, n = 15, p = 0.0580, one-sample Student's t-test). This decrease could represent unspecific factors, such as slight drifts of the pipettes (increasing distance between K^+ source and recording site), clogging of the iontophoresis pipette (reduced amount of injected K^+) by particles from the back-fill solutions or a slight decrease of K^+-sensitive microelectrodes sensitivity for K^+. However, it can be assumed that these factors were also present in CBX conditions and, in turn, may lead to an underestimation of the effect of relative peak amplitudes.

Interestingly, the relative change of the K^+ transient peak amplitudes after gap junction uncoupling was significantly correlated with the initial peak amplitude during baseline conditions, i.e. the peak amplitudes of larger K^+ transients were stronger affected by CBX than K^+ transients with smaller peak amplitudes. Such a correlation was also found for the relative K^+ transient peak amplitudes in control conditions (Figure 20D). In addition, a significant negative correlation also revealed that the change of the relative peak amplitudes after gap junction uncoupling was most prominent for K^+ transients that were recorded close to the K^+ application site. However, no such correlation was found for control conditions (Figure 20E). This indicates that gap junction uncoupling particularly affected the peak amplitude of K^+ transients recorded close to the K^+ source (< 15 µm). Importantly, the CBX-induced change of these K^+ transients (< 15 µm) was independent of the used ionophore (A, 37.17 ± 15.78%, n = 4; B, 31.46 ± 18.19%, n = 3; p = 0.882, two-sample Student's t-test).

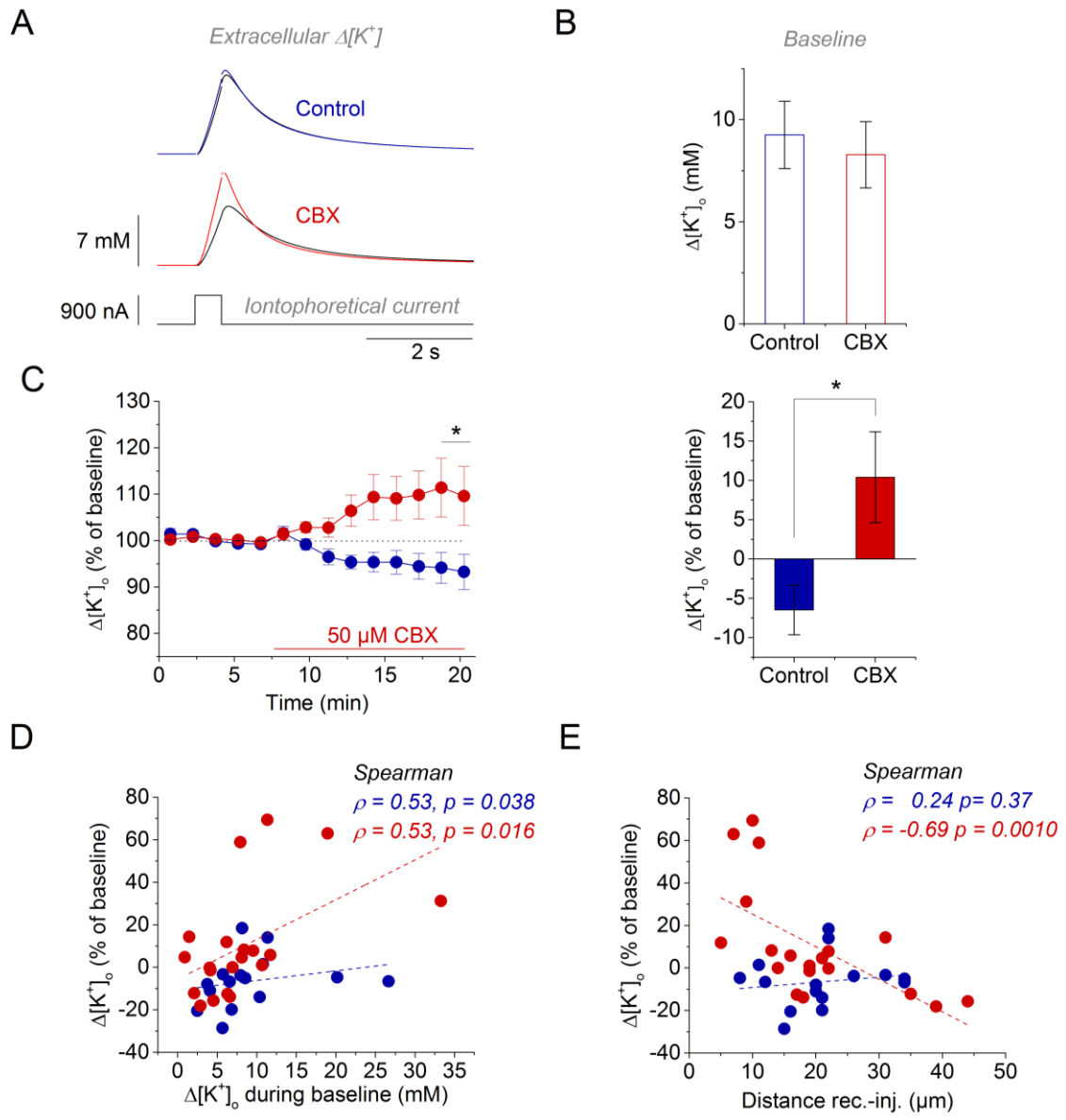

Figure 20 Peak amplitudes of large K^+ transients were increased after gap junction uncoupling. A) Large K^+ transients were evoked by iontophoretic K^+ application (900 nA for 500 ms) in the CA1 str. radiatum. K^+ transients were recorded during a baseline period (black) and then compared after the application of 50 µM CBX (red) or during control conditions (blue). **B)** During the baseline period, the peak K^+ transient peak amplitudes in control recordings were not different from CBX recordings (9.25 ± 1.65 mM, n = 15; CBX, 8.28 ± 1.62 mM, n = 20; p = 0.516, two-sample Student's t-test). **C)** Left: Time course of the baseline-normalized K^+ transient peak amplitudes. After 10 minutes of CBX treatment, the normalized peak amplitudes in CBX conditions were compared to control conditions. Right: The normalized K^+ transient peak amplitudes increased significantly after CBX treatment compared to control condition (Control, -6.48 ± 3.14%, n = 15; CBX, 10.42 ± 5.78%, n = 20, p = 0.0245, Mann Whitney U test). **D)** The change of the normalized K^+ peak amplitudes after gap junction uncoupling was significantly correlated (Spearman rank correlation) with the respective peak amplitude during the baseline period (Control, n = 15; CBX, n = 20) and **(E)** the distance between the site of recording and iontophoretic K^+ application (Control, n = 15; CBX, n = 19)**.** These correlations were not observed for control conditions.

In summary, these experiments revealed that large and local extracellular K^+ transients augmented after the acute uncoupling of astrocytic gap junction channels. In contrast, extracellular K^+ transients with amplitudes in the low millimolar range were unaffected. This suggests that astrocytic gap junction channels contribute to the clearance of extracellular K^+ loads that are generally associated with pathophysiological conditions (de Curtis et al., 2018; Fisher et al., 1976; Moody et al., 1974). Conversely, astrocytic gap junction channels seem not to be involved in the clearance of small extracellular K^+ loads that are generally associated with physiological conditions (Heinemann et al., 1990; Rasmussen et al., 2019). Taken together, these results indicate that astrocytic gap junction coupling facilitates the clearance of extracellular K^+ loads when a certain concentration is reached. Conversely, other K^+ clearance mechanisms seem to dominate the clearance of small extracellular K^+ loads. This suggests that K^+ clearance is assisted by astrocytic gap junction channels only when the other mechanisms are saturated and are not able to cope with the large amounts of extracellular K^+.

As already mentioned above, the genetic deletion of the gap junction forming connexins from hippocampal astrocytes augmented the peak amplitudes of extracellular K^+ transients. This was accompanied by a slowed decay rate of these extracellular K^+ transients (Wallraff et al., 2006). Thus, it was tested if the decay of the iontophoretically-evoked K^+ transients was affected by acute gap junction uncoupling.

In contrast to the K^+ transients with peak amplitudes in the low millimolar range, the decay of large K^+ transients was best approximated by a biexponentially decaying function (Figure 21A). During baseline conditions, the initial decay constants of the fast and the slow decay components in control recordings were not different from CBX recordings (Figure 21B, left & middle panel). In agreement with the literature (Ransom et al., 2000; Wallraff et al., 2006), the fast and slow decay constants decreased overall (Baseline and Control/CBX pooled) with increasing K^+ transient peak amplitudes (Figure 22; fast decay constant, $\rho = -0.86$, $p < 0.001$; slow decay constant, $\rho = -0.70$, $p < 0.001$, $n = 68$; Spearman's rank correlation). Also, the fraction of the fast decaying component became more prominent with increasing K^+ peak amplitudes (percentage of fast component, $\rho = 0.36$; $p = 0.0024$, $n = 68$, Spearman's rank correlation), but no difference between control and CBX conditions was observed (Figure 21B, right panel). Although there was a significant increase of the peak amplitudes after gap junction uncoupling (Figure 20), the decay of the large K^+ transients after CBX treatment was not different compared to control conditions (Figure 21C). This was observation was independent of the used ionophore cocktail. The change of the fast amplitude fraction (A, -4.19 ± 2.87%, n = 10; B, -0.34 ± 1.18%, n = 9; p = 0.713, Mann-Whitney U-Test), fast decay rate (A, 0.54 ± 7.45%, n = 10; B, 3.30 ± 4.98%, n = 9; p = 0.767, two-sample Student's t-test) and slow decay rate (A, -

21.94 ± 27.21%, n = 10; B, 2.09 ± 6.99%, n = 9; p = 0.713, two-sample Student's t-test) after CBX treatment recorded with ionophore cocktail A was not different from those recorded with ionophore cocktail B.

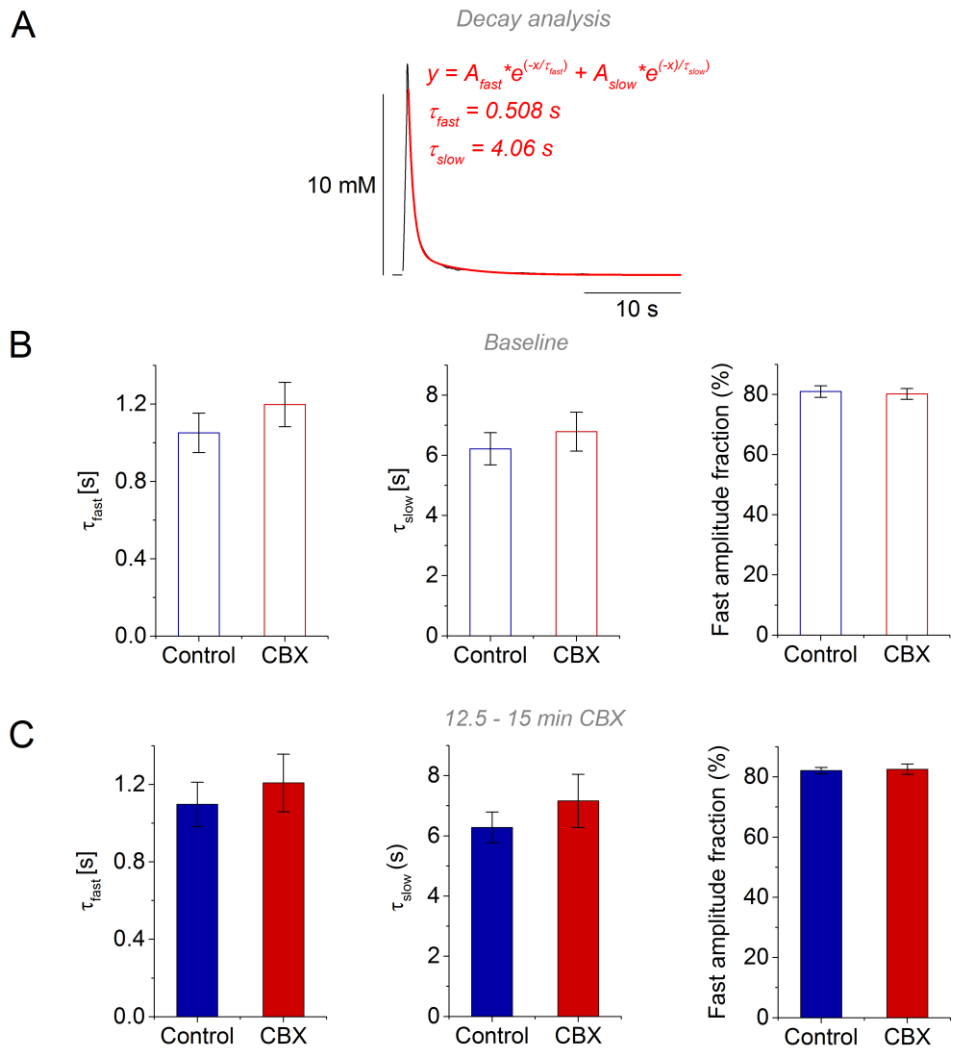

Figure 21 The post-stimulus decay of the large K^+ transients was unaffected by gap junction uncoupling. A) The decay of large K^+ transients was best approximated by a biexponentially decaying function (fit superimposed in red). **B)** During baseline conditions, the decay constant of the fast (Left panel; Control, 1.05 ± 0.102 s, n =15; CBX:,1.20 ± 0.115 s, n = 19, p = 0.362, two-sample Student's t-test) and the slow decay component (Middle panel; Control, 6.22 s ± 0.535 s, n = 15; CBX, 6.79 ± 0.648 s, n = 19; p = 0.518, two-sample Student's t-test), as well as the amplitude fraction of the fast component (Right panel; Control, 80.99 ± 1.95%, n = 15; CBX, 80.20 ± 1.84%; n = 19; p = 0.769, two-sample Student's t-test) in control recordings were not significantly different from CBX recordings. **C)** The decay constant of the fast (Left panel; Control, 1.10 ± 0.114 s, n = 15; CBX, 1.21 ± 0.149 s, n = 19; p = 0.576, two-sample Student t-test) and the slow decay component (Middle panel; Control, 6.28 ± 0.514 s, n = 15; CBX, 7.16 ± 0.885 s, n = 19; p = 0.835, Mann-Whitney U-Test), as well as the amplitude fraction of the fast component (Right panel; Control, 82.10 ± 1.08%, n = 15; CBX, 82.57 ± 1.70%, n = 19; p = 0.820, two-sample Student's t-test) in control conditions were not significantly different from CBX conditions.

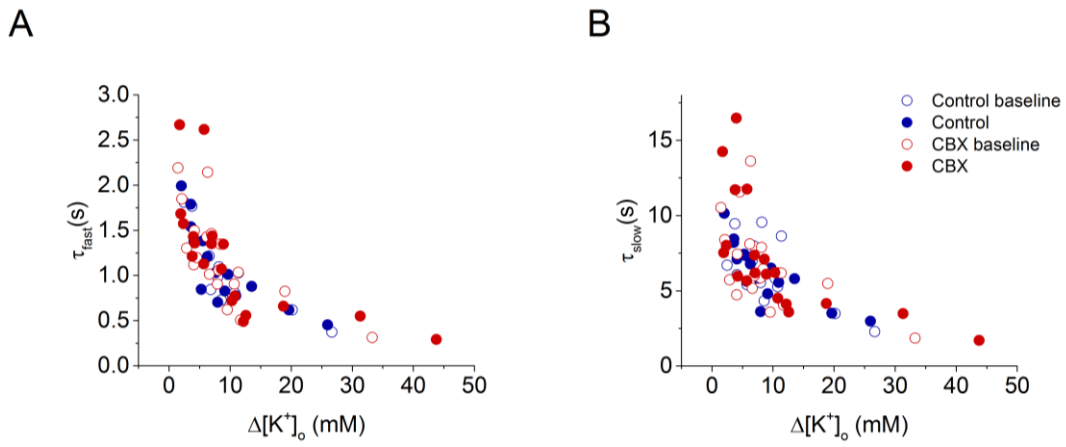

Figure 22 The decay constants were correlated with the K^+ peak amplitude. The fast (**A**) and the slow decay rate (**B**) correlated (Spearman rank correlation) significantly with the peak amplitude of the corresponding K^+ transient during baseline (Control; τ_{fast}, ρ = -0.90, $p < 0.001$; τ_{slow}, ρ = -0.47, p = 0.0786, n = 15; CBX, τ_{fast}, ρ = -0.79, $p < 0.001$, τ_{slow}, r = -0.54, p = 0.0178, n = 19) and after the treatment (Control; τ_{fast}, ρ = -0.87, $p < 0.001$, τ_{slow}, ρ = -0.91, $p < 0.001$, n = 15; CBX, τ_{fast}, ρ = -0.87, $p < 0.001$, τ_{slow}, ρ = -0.85, $p < 0.001$, n = 19).

Overall, these results show that the treatment with CBX impacted the peak amplitude of large K^+ transients. In contrast, the decay of the extracellular K^+ transients back to basal levels was unaffected by the gap junction uncoupling. In order to further investigate if the observed effect on the peal amplitude of the large K^+ transients was caused by CBX-induced acute gap junction uncoupling and not by other undefined CBX specific side-actions, the impact of MFA on large K^+ transients was tested. Since both, MFA and CBX, share the ability to acutely inhibit gap junction uncoupling (Chapter 4.1.1), a similar effect of MFA as observed with CBX would support the idea of gap junction uncoupling as the underlying mechanism for the increased K^+ peak amplitudes. Therefore, large iontophoretically evoked K^+ transients were recorded close (18.0 ± 1.73 µm, n = 4) to the K^+ application site, where previously the CBX-induced increase of the K^+ peak amplitudes was most prominent (Figure 20E). Indeed, after a baseline period, the peak amplitudes of the evoked K^+ transients increased significantly during the application of 200 µM MFA (Figure 23).

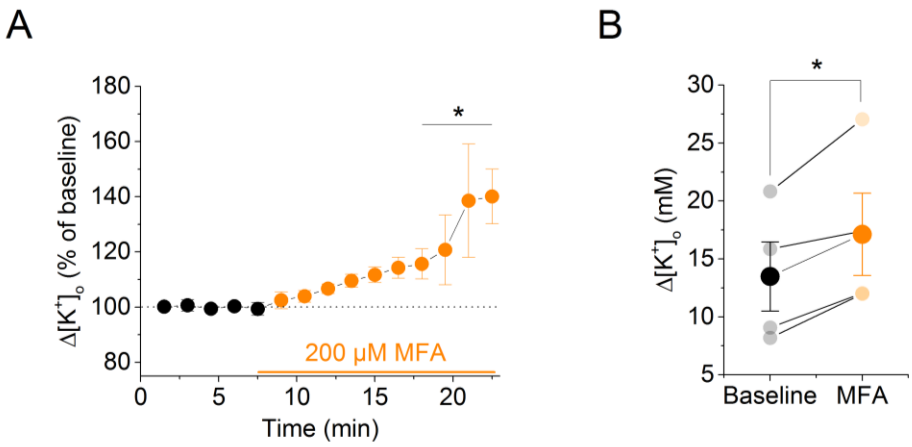

Figure 23 Large iontophoretically evoked K^+ transients showed increased peak amplitudes after gap junction uncoupling with MFA. A) Experimental time course. After the baseline recording, 200 µM MFA (in DMSO; final concentration in aCSF: 0.2%) was applied and K^+ transient peak amplitudes increased by 29.62 ± 7.52% (n = 4; p = 0.029; one-sample Student's t-test) **B)** The peak amplitudes during baseline were on average 13.49 ± 2.99 mM and increased to 17.12 ± 3.55 mM after MFA treatment (p = 0.034; n = 4; paired Student's t-test).

Taken together, these experiments show that acute pharmacological gap junction uncoupling increased the peak amplitude of large K^+ transients, but left the post-stimulus decay unaffected. This observation points towards an involvement of gap junction coupling in the clearance of extracellular K^+ during the K^+ application and build-up phase of the K^+ transients and not during the return to basal K^+ levels. This is line with the increased peak amplitudes and unaffected decay rates of extracellular K^+ transient after acutely inhibiting Kir4.1 channels that are proposed to mediate K^+ uptake during spatial K^+ buffering (Larsen et al., 2014). Also, the suggestion by Larsen and MacAuly based on the observations made by Karwoski and colleagues in the amphibian retina are in agreement with our observations. There, light-evoked extracellular K^+ elevations in the inner plexiform layer were redistributed into the vitreous humor through the Müller cell in a Ba^{2+}-sensitive manner ('K^+ siphoning') only during the light pulse, i.e. the phase of extracellular K^+ accumulation, but not during the decay phase (Karwoski et al., 1989; Larsen and MacAulay, 2014).

Interestingly, the increase of the K^+ peak amplitudes after CBX treatment was most prominent for K^+ transients recorded at distances closer than ~15 µm to the K^+ application site (Figure 20E). At these sites, the local extracellular K^+ transients showed also the largest peak amplitudes. Since the augmented K^+ peak amplitudes after gap junction uncoupling were only observed for extracellular K^+ transients with large peak amplitudes close to the K^+ source, it cannot be excluded that the distance to the K^+ source

determined the observed effect. Thus, it was tested if either the distance to the K^+ source or the initial K^+ transient peak amplitude determined an effect of CBX.

4.1.6 K^+ transients of different amplitude and duration

The distance between the K^+ recording and application site strongly determined the initial peak amplitude (Chapter 4.1.4). Consequently, it was not intuitively clear if the underlying factor for the observed prominent CBX-effect on K^+ transient recorded close, i.e. ~15 µm, to the K^+ application site (Figure 20), was the distance or the amount of applied K^+ (i.e. the initial K^+ peak amplitude). Thus, K^+ transients recorded closer than 15 µm from the K^+ application site evoked with either weak (800 nA for 200 ms, small peak amplitudes) or strong K^+ injections (900 nA for 500 ms, large peak amplitudes) were compared. On average, large K^+ transients were recorded at similar distances from the K^+ application compared to small K^+ transients (small K^+ transients, 9.20 ± 1.46 µm, n = 5; large K^+ transients, 9.86 ± 1.20 µm, n = 7; p = 0.737; two-sample Student's t-test) but exhibited significantly larger peak amplitudes (Figure 24A). However, there was virtually no effect of CBX on small K^+ transients recorded close to the K^+ application site, whereas CBX induced a significant increase of the peak amplitude of large K^+ transients (Figure 24B). This indicates that the initial peak amplitude of the K^+ transients determined if CBX had an effect and not the proximity to the K^+ source.

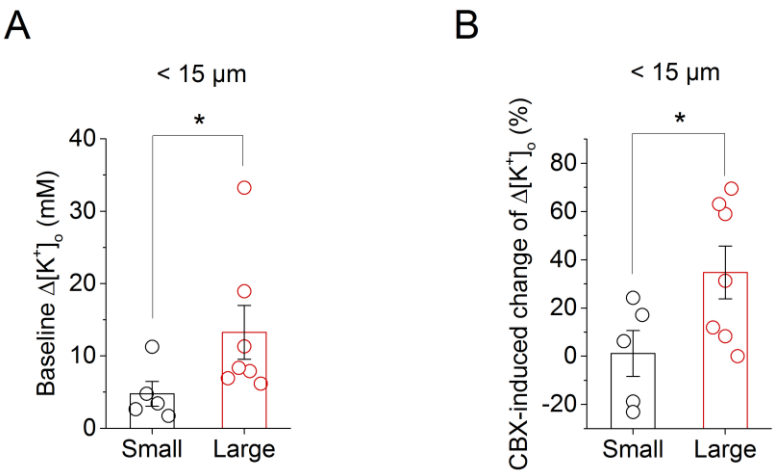

Figure 24 CBX differentially affected small and large K^+ transients close to the K^+ application site. A) Close to the K^+ application site (closer than 15 µm), small and large K^+ transients evoked by weak and strong K^+ injections, respectively, exhibited similar peak amplitudes (Small, 4.77 ± 1.699 mM, n = 5; Large, 13.27 ± 3.71 mM, n = 7; p = 0.0348, , Mann Whitney U test). **B)** The CBX induced change of the K^+ peak amplitudes was significantly larger for large K^+ transients compared to small K^+ transients (Small, 1.15 ± 9.49%, n = 5; Large, 34.72 ± 10.94%, n = 7; p = 0.0430, two-sample Student's t-test).

According to the hypothesis of the K^+ peak amplitude as the determining factor for a CBX effect, CBX should affect K^+ transients evoked at the same position, but with different peak amplitudes, differentially. In order to obtain further insights into the relationship of the initial K^+ peak amplitude and an effect of CBX, K^+ transients with increasing peak amplitudes were evoked in close proximity (< 15 µm) to the K^+ recording site during intact and inhibited gap junction coupling (Figure 25A). In detail, K^+ transients were evoked with test-pulses (200 nA for 500 ms) for a baseline period of 10 minutes. The test-pulses were used to control that the evoked K^+ transients exhibited stable peak amplitudes during this baseline period. Next, five consecutive K^+ transients were evoked with K^+ injections of increasing current amplitudes (180, 390, 570, 760 and 950 nA for 500 ms, 'ramp-injection', repeated twice) leading to increasing K^+ peak amplitudes. This was followed by the wash-in of CBX during a 10 minutes period of test-pulses and two 'ramp-injections'.

Indeed, K^+ transients showed increased peak amplitudes after gap junction uncoupling when their initial peak amplitude exceeded ~10-15 mM (Figure 25B). To exclude that ramps of K^+ injections themselves had an effect on the K^+ peak amplitudes, the K^+ transients evoked by the two 'ramp-injection' during intact gap junction coupling were compared. However, no significant difference was observed between the K^+ peak amplitudes evoked by the first and the second 'ramp-injection' (Figure 25C).

Next, the decay of the K^+ transients was investigated by a biexponentially decaying function (Figure 26A). Overall, the fast decay component was more pronounced for K^+ transients with larger peak amplitudes (ρ = 0.199, p = 0.0475, Spearman's rank correlation) but seemed to reach a steady state for K^+ transients evoked with 380 nA and more (roughly > 8-12 mM), whereas the fast and slow decay constants decreased with increasing K^+ transient peak amplitudes (fast decay constant, ρ = -0.71, p < 0.001; slow decay constant, ρ = -0.51, p < 0.001; Spearman rank correlations). This in line with previous studies on extracellular K^+ transients that also observed decreased decay rates and a more pronounced fast amplitude fraction with increasing K^+ peak amplitude (Strohschein et al., 2011; Wallraff et al., 2006). In turn, this suggests that the mechanisms, which mediate the decay of the extracellular K^+ concentration back to basal levels, increase their K^+ uptake rate with increasing extracellular K^+ concentrations. Although gap junction uncoupling with CBX had no impact on the fraction of the fast decay component (Figure 26B), the fast and slow decay time constants were overall significantly reduced (Figure 26C). In order to test if this reduction was caused by the gap junction uncoupling or a consequence of the increased peak amplitudes after uncoupling (Figure 25 and correlation above), all K^+ transients were pooled, grouped according to their peak amplitudes and then the decay time constants before and after uncoupling were compared in each group. However, these comparisons revealed no difference of the

decay time constants of K^+ transients with similar peak amplitudes during intact and inhibited gap junction coupling (Figure 26D).

These findings indicate that decreased decay time constants after gap junction uncoupling were a consequence of the increased peak amplitudes and not of gap junction uncoupling. Again, this is in agreement with the general idea that astrocytic gap junction coupling facilitates the clearance of extracellular K^+ during the K^+ application and build-up phase of the K^+ transients and not during the return to basal K^+ levels (Larsen and MacAulay, 2014; Larsen et al., 2014).

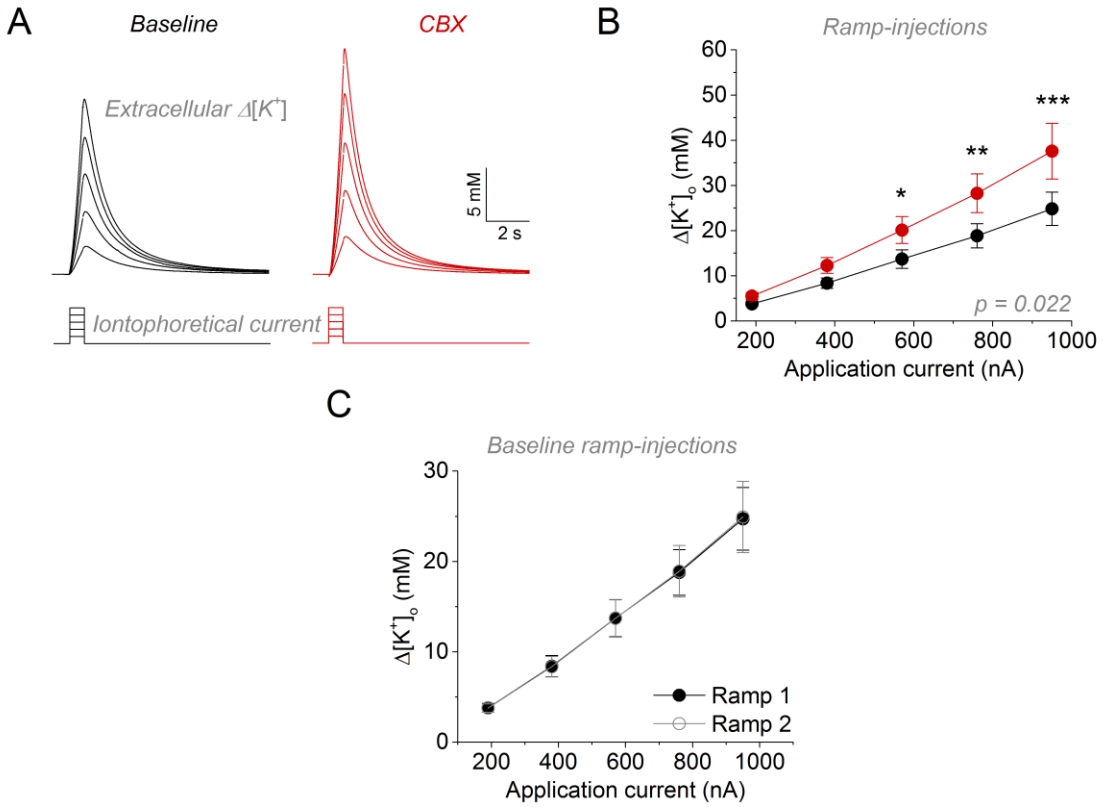

Figure 25 Gap junction uncoupling selectively affected K^+ transients evoked with larger iontophoretic current amplitudes. A) Example traces of K^+ transients evoked by 'ramp-injections' (180, 390, 570, 760 and 950 nA for 500 ms) during intact (baseline, black) and inhibited gap junction coupling (CBX, red). The shown K^+ transients represent an average of transients evoked by two consecutive ramp-injections. **B)** Peak amplitudes of K^+ transients were increased after gap junction uncoupling when evoked with 570 nA and above ($p = 0.0223$ for CBX, $n = 10$, two-way repeated measures ANOVA; p for interaction of current amplitude and CBX, $p < 0.001$, Holm-Bonferroni correction in post-hoc test; 190 nA, 3.78 ± 0.47 mM, 5.52 ± 0.78 mM, 0.565; 380 nA, 8.38 ± 1.15 mM, 12.29 ± 1.74 mM, 0.199; 570 nA, 13.72 ± 2.06 mM, 20.12 ± 2.98 mM, 0.0391; 760 nA, 18.85 ± 2.69 mM, 28.26 ± 4.28 mM, 0.00332; 950 nA, 24.83 ± 3.69 mM, 37.60 ± 6.17 mM, <0.001 (Bsl, CBX, p-value). **C)** The K^+ transients (shown as an average in A) evoked during baseline by the first 'ramp-injection' were not different compared to the second 'ramp-injection' ($p = 0.828$ for ramp, two-way repeated measures ANOVA, no significant interaction).

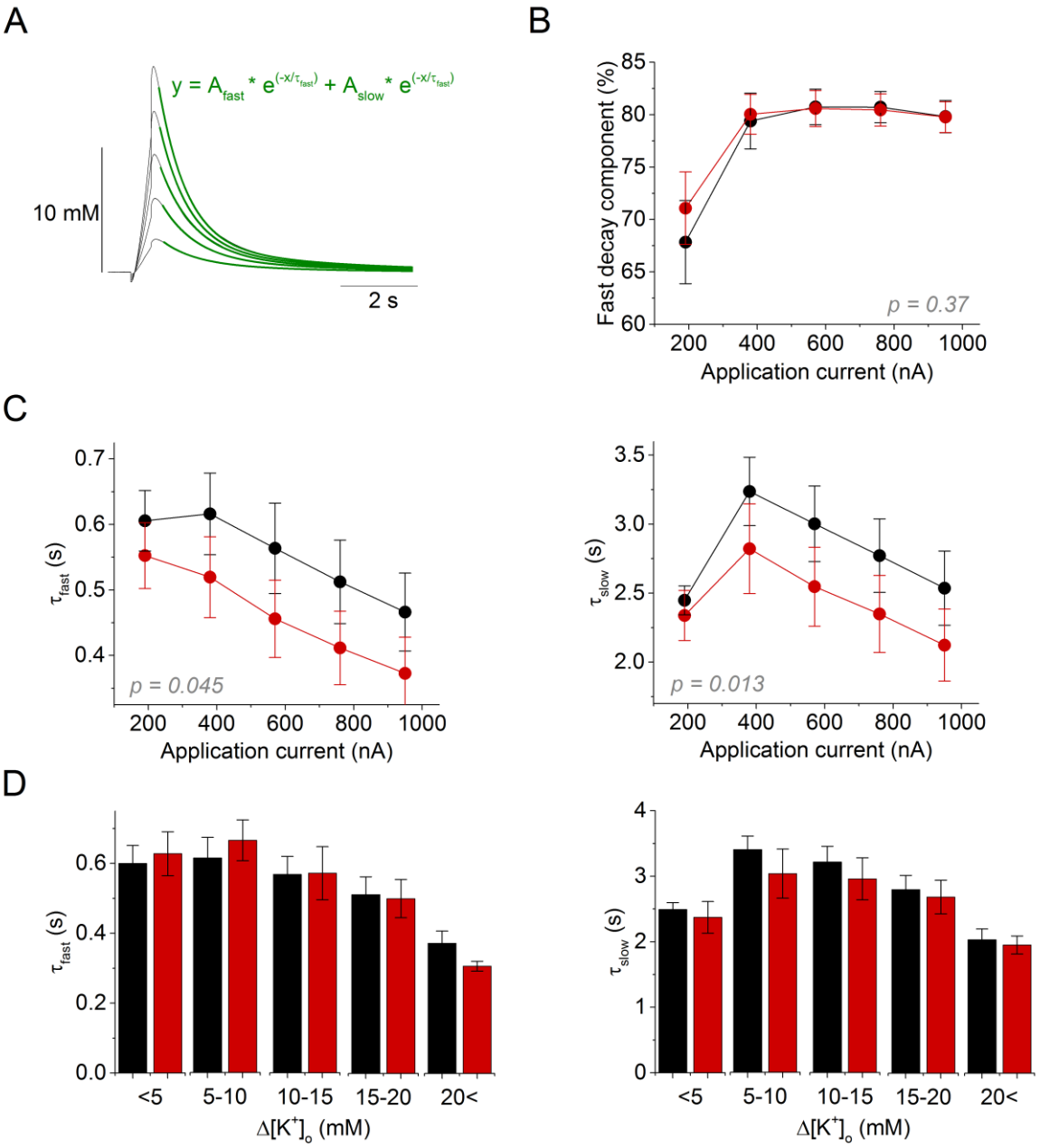

Figure 26 The decay of the K^+ transients was affected by their peak amplitude but not by gap junction uncoupling. A) The decay of the K^+ transients evoked with different iontophoretic current amplitudes was quantified by a biexponentially decaying function (superimposed green lines). **B)** The fraction of the fast decaying component was overall not affected by gap junction uncoupling by CBX (n = 10, p = 0.37 for CBX, two-way repeated measures ANOVA, no significant interactions of stimulation intensity and CBX effect). **C)** The fast (left panel) and slow decay time constants (right panel) significantly decreased after gap junction uncoupling (red) compared to baseline (black) (fast, p = 0.045 for CBX; slow, p = 0.013 for CBX, n = 10; two-way repeated measures ANOVA, no significant interactions of stimulation intensity and CBX effect). **D)** K^+ transients during intact gap junction coupling showed no significant difference in their fast (left panel) and slow decay time constants (right panel) compared to K^+ transients with similar amplitude during CBX conditions (fast, p = 0.98; slow, p = 0.20, n =10; two-way ANOVA).

In order to further support the hypothesis that the amount of applied K^+, i.e. the K^+ transient peak amplitude, was the determining factor for an effect of CBX and no other factors, an additional set of experiments with 'K^+ ramp injection' was performed. In contrast to the previous experiments, the iontophoretic current amplitude was kept constant whereas the duration of K^+ application was modulated. Again, these K^+ transients were evoked close to the recording site (< 15 µm) with different peak amplitudes during intact and inhibited gap junctions coupling (Figure 27A). The peak amplitudes of the K^+ transients were significantly increased after gap junction uncoupling when the transients were evoked with K^+ injections with a duration of 300 ms and more, i.e. K^+ transients were affected when they exhibited initial peak amplitudes larger than ~9-10 mM (Figure 27B). As observed during the previous experiments, the 'K^+ ramp injection' itself did not significantly affect the peak amplitude of the evoked K^+ transients during a second 'ramp injection' (Figure 27C).

Taken together, these experiments indicate that acute pharmacological gap junction uncoupling predominantly affect K^+ transients with peak concentrations that are commonly associated with pathophysiological conditions. In contrast, K^+ transients with smaller peak amplitudes seem to be unaffected by gap junction uncoupling under these conditions. In addition, these experiments indicate that the amount of applied K^+ is the determining factor for an effect of acute astrocyte gap junction uncoupling on extracellular K^+ transients. Since only the peak amplitude of the large extracellular K^+ transients were affected by acute gap junction uncoupling, astrocytic gap junction coupling might reduce the K^+-induced astrocyte membrane depolarization during the K^+ application period via fast K^+ redistribution within the astrocytic network or cytosol. As a consequence, extracellular K^+ is efficiently cleared from the ECS via a constant K^+ influx into the astrocyte, because the local membrane potential is kept below the equilibrium potential for K^+. The uncoupling of the astrocytic gap junction channels then impaired the fast K^+ redistribution and, in turn, induced a larger K^+-induced membrane depolarization. The resulting less efficient K^+ influx then led to facilitated extracellular K^+ accumulations (K^+ peak amplitudes). After the constant supply of K^+ to the ECS during the application phase, K^+ is probably no longer distributed through the gap junction channels and other mechanisms, such as the active K^+ uptake by the Na^+/K^+-ATPase, mediate the recovery of extracellular K^+ concentration back to basal levels. Consequently, the decay of extracellular K^+ transients would be unaffected by gap junction uncoupling, as observed in this study. The faster decay rates, which were observed after gap junction uncoupling, can be explained by the gap junction uncoupling induced augmented K^+ accumulations that, in turn, led to an increased Na^+/K^+-ATPase activity (Rose and Ransom, 1996; Walz and Hertz, 1982).

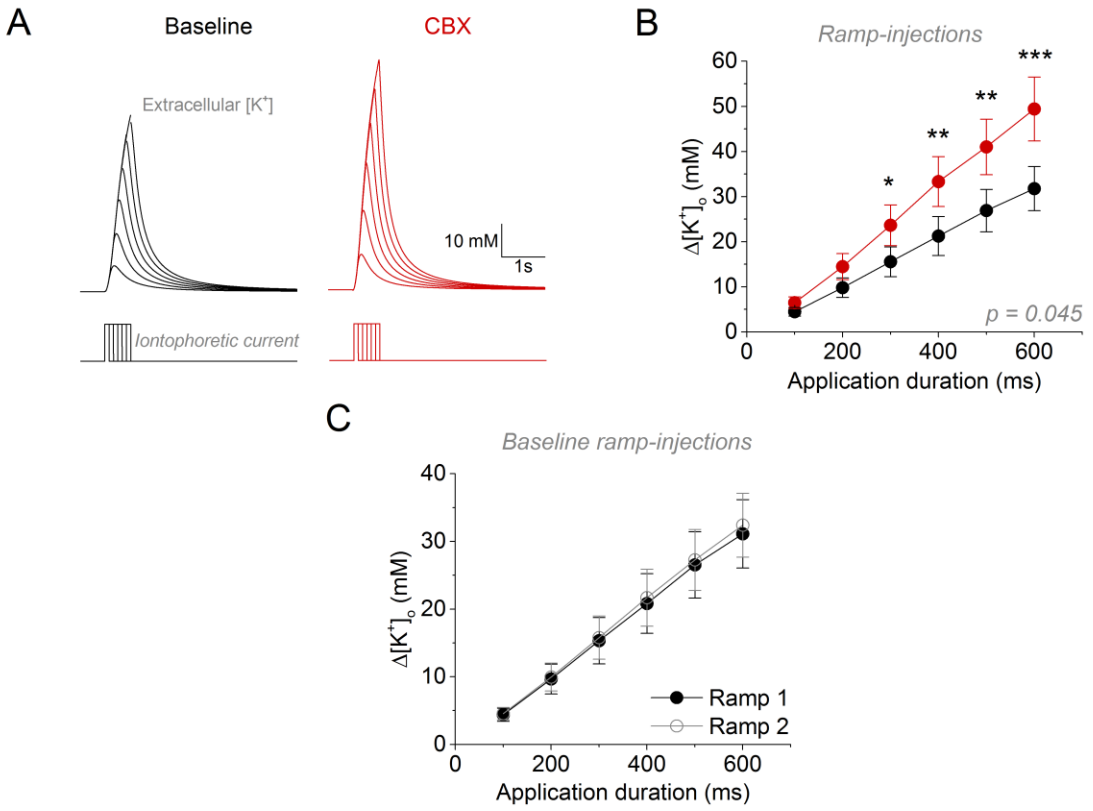

Figure 27 Gap junction uncoupling selectively affected K^+ transients evoked with longer iontophoretic K^+ applications. A) Example traces of K^+ transients evoked by an iontophoretic K^+ application over different durations (900 nA for 100, 200, 300, 400, 500 and 600 ms). **B)** Peak amplitudes of K^+ transients were increased after gap junction uncoupling when evoked with K^+ injections for 300 ms and more ($p = 0.045$ for CBX, n = 5, two-way repeated measures ANOVA; p for interaction of current amplitude and CBX, $p < 0.001$, Holm-Bonferroni correction in post-hoc test; 100 ms, 4.48 ± 0.94 mM, 6.48 ± 1.28 mM, 0.602; 200 ms, 9.82 ± 2.14 mM, 14.48 ± 2.88 mM, 0.231; 300 ms, 15.56 ± 3.31 mM, 23.66 ± 4.51 mM, 0.0450; 400 ms, 21.26 ± 4.31 mM, 33.32 ± 5.54 mM, 0.00464; 500 ms, 26.91 ± 4.70 mM, 41.02 ± 6.16 mM, p = 0.00166; 600 ms, 31.77 ± 4.88 mM, 49.42 ± 7.09 mM, < 0.001 (Bsl, CBX, p-value). **C)** The K^+ transients (shown as an average in A) evoked during baseline by the first 'ramp-injection' were not different compared to the second 'ramp-injection' ($p = 0.0640$ for ramp, two-way repeated measures ANOVA, no significant interaction).

4.1.7 Modulation of the extracellular space structure

Interestingly, it has been shown that pathophysiological conditions (Slais et al., 2008; Syková and Nicholson, 2008), such as epilepsy, were associated with a reduced extracellular space (ECS) . Shrinkage of the ECS can be induced by cellular swelling and was investigated in the following set of experiments.

A common approach to induce ECS shrinkage is the application of a hypoosmolar extracellular solution in order to induce cellular swelling (Kilb et al., 2006; Kume-Kick et al., 2002). This is mediated by an altered osmotic pressure and the corresponding water influx from the ECS into the cells that results in an increase of the cellular volume and, in

turn, a decreased ECS (Syková and Nicholson, 2008). In order to quantify the extent of ECS shrinkage in response to hypoosmolar conditions, the real-time TMA^+-iontophoresis approach was employed. In brief, this approach utilizes the diffusion of an ion, i.e. TMA^+, in the ECS as a determinant for the ECS structure. TMA^+ was iontophoretically applied as a point source and consequently diffused in the ECS. The TMA^+ concentration was then measured by a TMA^+-sensitive microelectrode (TSM) at a defined distance to the TMA^+ source (Figure 28A). Finally, the diffusion analysis described by Nichsolson and Phillips (1981) allowed to deduce the ECS structure, i.e. the fraction of the ECS (α) relative to the total tissue volume from the recorded TMA^+ transient.

The first step was to find a protocol to reduce the ECS fraction in response to hypoosmolar conditions and quantify the extent of the reduction. For this purpose, TMA^+ transients were evoked in the presence of the regular isomolar (297-300 mOsm/kg, baseline) aCSF, during the application of hypoosmolar aCSF (220 or 180 mOsm/kg, achieved by a reduced [NaCl]) and after the reapplication of isomolar aCSF (recovery). In response to the hypoosmolar conditions, the shape of the TMA^+ transients, for instance their peak amplitude, changed and returned back to baseline levels after the reapplication of isomolar aCSF (Figure 28B). The diffusion analysis of the TMA^+ transients revealed that in hippocampal slices from juvenile animals the ECS fraction was stable over the time course of the experiment when no hypoosmolar aCSF was applied (Control). In contrast, a trend towards a statistically significant reduction of the ECS fraction was observed when the hippocampal slices were treated with a hypoosmolar aCSF of 220 mOsm/kg for 30 minutes. When the osmolarity of the aCSF was further reduced to 180 mOsm/kg, the ECS fraction was significantly reduced during the hypoosmolar conditions. Likewise, in hippocampal slices obtained from adult animals, the treatment with hypoosmolar aCSF resulted in a significant reduction of the ECS fraction. It is noteworthy, that the ECS fraction reached virtually stable level during all hypoosmolar conditions after roughly 15 min and returned to basal levels upon the reapplication of isomolar aCSF in nearly all tested conditions (Figure 28C).

Taken together, these results show that the ECS fraction was robustly and reversibly reduced in an osmolarity-dependent manner by the application of hypoosmolar aCSF. However, the reduced osmolarity was achieved by lowering the NaCl content of the aCSF, which resulted in a change of the ionic composition during the period of hypoosmolar conditions. Since changes in the ionic composition themselves could affect the K^+ homeostasis, a different approach to reduce the ECS fraction was established next.

Instead of reducing the NaCl content only during the hypoosmolar conditions, the reduced NaCl content was kept constant over the course of the experiment. This was achieved by adding sucrose to the aCSF with the reduced NaCl content ('low Na^+ aCSF', 180 Osm/kg) until an isomolar osmolarity (300 mOsm/kg) was reached. This isomolar aCSF was then used during the baseline period. In order to induce ECS shrinkage, hypoosmolar aCSF without the additional sucrose (180 mOsm/kg) was applied to the hippocampal slice. This approach reduced the extracellular osmolarity, but kept the extracellular ionic composition constant over the experimental time-course. Similar as observed before, the ECS fraction decreased significantly during the hypoosmolar period by ~42% and recovered after the reapplication of isomolar aCSF (Figure 29). This approach was then used to investigate the impact of acute gap junction uncoupling during conditions of a reduced ECS fraction without altering the basal extracellular ion composition.

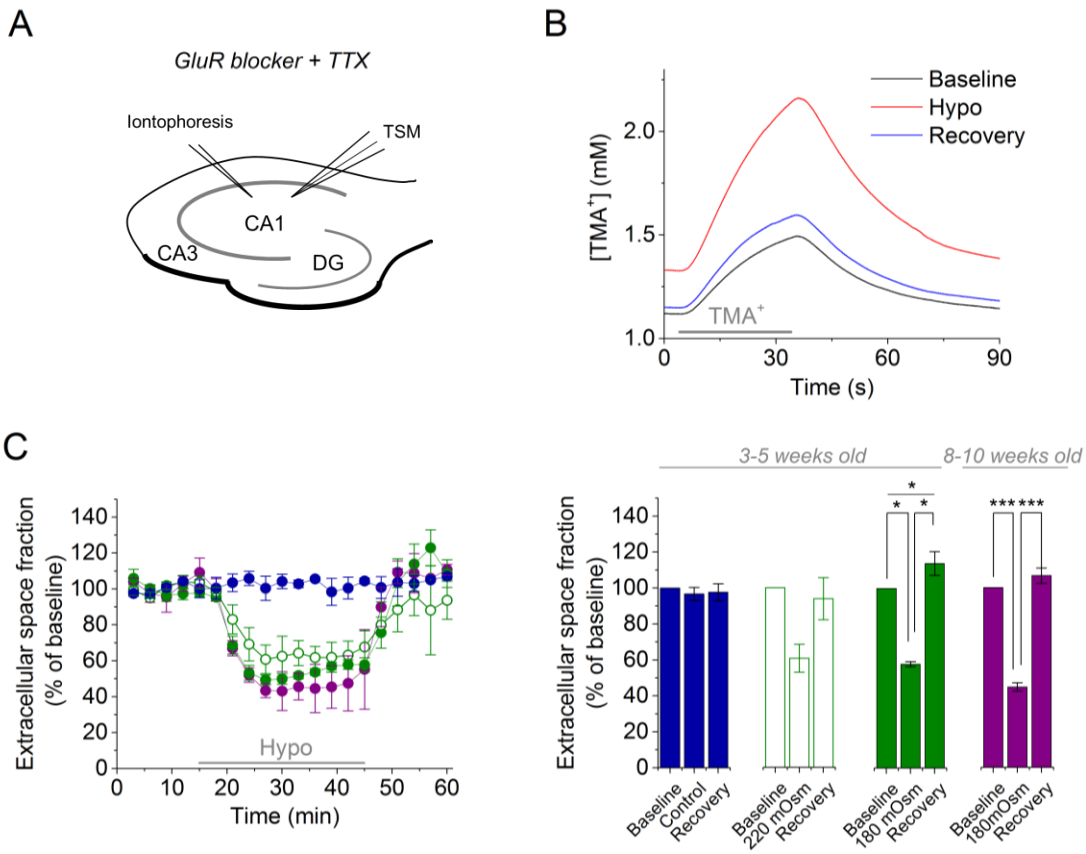

Figure 28 Modulation of the ECS fraction by hypoosmolar conditions. A) The ECS fraction was determined by the real-time tetramethylammonium (TMA^+) iontophoresis method with a TSM in the CA1 str. radiatum during inhibited neuronal activity. TMA^+ was applied by a constant 20 nA current and with a transient current injection of 120 nA for 30s, which resulted in an increase of the basal TMA^+ concentration and TMA^+ transients, respectively. The ECS fraction (α) was then deduced from the evoked TMA^+ transients by a diffusion analysis as described by Nicholson & Phillips (1981). **B)** Example TMA^+ transients during isomolar

conditions (black, baseline), hypoosmolar conditions (red, hypo) and after the return to isomolar conditions (blue, recovery). The reduction of the osmolarity was achieved by decreasing the content of NaCl. **C)** Left panel: Time course of the ECS fraction before, during and after the exposure to hypoosmolar aCSF in slices from juvenile and adult animals. Right panel: in juvenile animals, no statistically significant change of the ECS fraction was observed over time during control conditions ($p = 0.686$, $n = 4$, one-way repeated measures ANOVA) and when exposed to 220 mOsm/kg aCSF ($p = 0.0661$, $n = 4$, one-way repeated measures ANOVA). Exposure of 180 mOsm/kg aCSF to hippocampal slices from juvenile ($p < 0.001$, $n = 4$, one-way repeated measures ANOVA with Bonferroni post-hoc tests) and adult animals ($p < 0.001$, $n = 3$, one-way repeated measures ANOVA with Bonferroni post-hoc tests) resulted in a significant reduction of the ECS fraction.

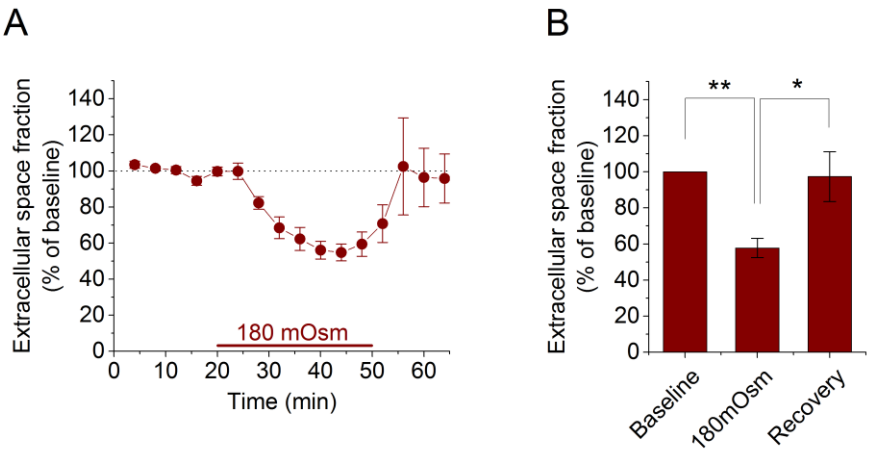

Figure 29 Reduction of the ECS fraction by hypoosmolar conditions during constant ionic composition. A) Time course of the ECS fraction before, during and after the exposure to hypoosmolar aCSF. The aCSF contained a reduced amount of NaCl (68.4 mM) and was adjusted to 300 mOsm/kg by the addition of sucrose. For the hypoosmolar challenge, aCSF without additional Sucrose (180 mOsm/kg) was applied for 30 minutes. **B)** The ECS fraction decreased significantly during the hypoosmolar conditions but recovered back to baseline values ($p = 0.01263$, $n = 5$, one-way repeated measures ANOVA with Bonferroni post-hoc tests).

4.1.8 Impact of astrocyte uncoupling on K^+ clearance during conditions of reduced ECS

Pathophysiological conditions such as epilepsy have been shown to be associated with shrinkage of the ECS and excessive extracellular K^+ accumulation (Slais et al., 2008; Syková and Nicholson, 2008). Thus, the following experiments addressed the question if gap junction coupling plays a role for the clearance of extracellular K^+ during conditions of a reduced ECS fraction. For instance, cellular swelling and the concomitant shrinkage of the ECS might impair the extracellular K^+ diffusion. Consequently, the same amount of applied K^+ would result in an augmented local extracellular K^+ increase compared to a

normal ECS. Since the extracellular K^+ diffusion would no longer/ less efficiently attenuate the local accumulation of K^+, the K^+ redistribution via astrocytic gap junction channels might be of special importance to limit the extracellular K^+ accumulations. Thus, the augmentation of iontophoretically-evoked extracellular K^+ transients during hypoosmolar conditions (induction of cellular swelling and ECS shrinkage) was expected to be more pronounced when gap junction coupling was acutely inhibited.

The protocol described in the previous chapter (Figure 29) to induce a reduction of the ECS was used in parallel to the iontophoretic application of K^+. K^+ was applied throughout the experimental time course with 900 nA for 500 ms in order to evoke large K^+ transients in the CA1 str. radiatum of hippocampal slices obtained from adult Wistar rats. First, the hippocampal slices were bathed in isomolar aCSF with a reduced NaCl content (adjusted to 300 mOsm/kg by adding sucrose) for at least 10 minutes (baseline period). K^+ transients were evoked at distances of 3 to 44 µm from the recording site (Control, 19.45 ± 4.33 µm, n =11; CBX, 18.56 ± 3.24 µm, n = 9; p = 0.870, two-sample Student's t-test) and exhibited during baseline conditions peak amplitudes on average of 6.06 ± 0.79 mM (n = 21). The basal peak amplitudes recorded in control slices were not different from slices that were subsequently treated with CBX (Control, 5.67 ± 1.06 mM, n = 11; CBX, 6.49 ± 1.24 mM, n = 10; p = 0.623, two-sample Student's t-test). Next, hypoosmolar aCSF (180 mOsm/kg, reduced NaCl content without sucrose) was applied to the hippocampal slices for 30 minutes. As expected, this resulted in an increase of the K^+ transient peak amplitudes (Figure 30A&B). However, the relative increase of the K^+ transient peak amplitudes was not affected when 50 µM CBX were applied together with the hypoosmolar aCSF compared to control conditions (hypoosmolar aCSF without CBX) (Figure 30B). This was also the case when only the peak amplitudes of K^+ transients recorded close to the K^+ application site (< 15 µm) were compared (Control, 315.77 ± 93.02% , n = 5; CBX, 157.16 ± 18.60%, n = 4; p = 0.165, two-sample Student's t-test). This was unexpected since these K^+ transients reached maximal values during the hypoosmolar conditions (Control, 40.46 ± 10.13 mM, n = 5; CBX, 24.43 ± 8.81 mM, n = 4, p = 0.285, two-sample Student's t-test) similar to those shown in the previous chapter that were affected by acute gap junction uncoupling (Figure 24 & Figure 25). Conversely, this suggests that during conditions of a reduced ECS, astrocytic gap junction coupling is not involved in the clearance of extracellular K^+ and other mechanisms dominate.

In addition to the peak amplitude of the extracellular K^+ transients, also the basal extracellular K^+ concentration increased during the hypoosmolar conditions (Figure 30C). K^+ release from astrocytes in order to normalize their cellular volume was already observed previously (Bender and Norenberg, 1994; Vitarella et al., 1994). Thus, the increased basal K^+ levels could represent such a volume-regulatory mechanism.

However, the basal K^+ concentration was also not affected by CBX during the hypoosmolar conditions (Figure 30C).

As expected from the previous findings, no significant differences between control and CBX were found for the fast amplitude fraction (Control, 76.93 ± 4.05%, n = 11; CBX, 83.59 ± 1.75%, n = 10; p = 0.170, Mann Whitney U test), fast decay constant (Control, 1.21 ± 0.36 s, n = 11; CBX, 1.32 ± 0.34 s, n = 10; p = 0.751, Mann Whitney U test) and the slow decay constant (Control, 9.53 ± 3.82 s, n = 11; CBX, 5.85 ± 1.16 s, n = 10; p = 0.971, Mann Whitney U test) of the K^+ transients decay after 25 minutes treatment with hypoosmolar aCSF (data not illustrated).

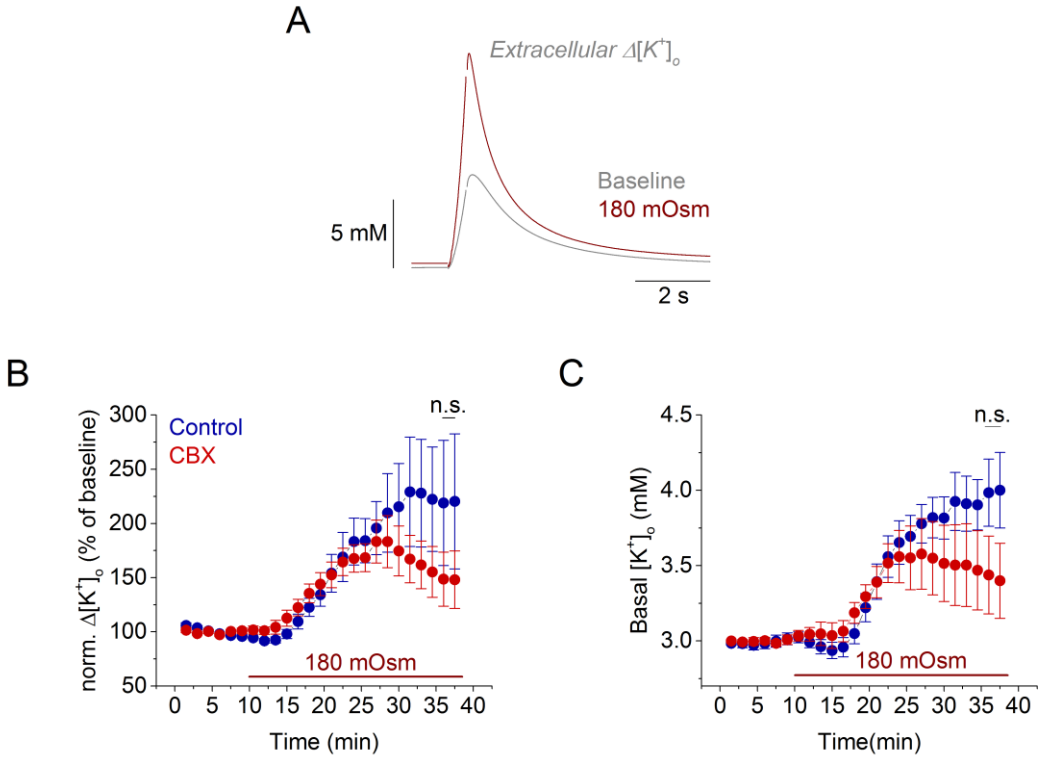

Figure 30 Increased basal K^+ levels and peak amplitudes during hypoosmolar conditions were not affected by gap junction uncoupling. A) Peak amplitudes of iontophoretically evoked K^+ transients and the basal K^+ concentration increased during hypoosmolar conditions in the CA1 str. radiatum of hippocampal slices from adult animals. Baseline aCSF: Isomolar, reduced [NaCl] and adjusted with sucrose to 300 mOsm/kg. 180 mOsm/kg aCSF: Hypoosmolar, reduced [NaCl] without sucrose. **B)** After the baseline period, hypoosmolar aCSF was applied either together with 50 µM CBX (red) or without (Control, blue). No statistically significant difference of control and CBX was found for the baseline-normalized K^+ transient peak amplitudes (Control, 218.66 ± 52.31%, n = 11; CBX, 148.67 ± 24.96%, n = 10; p = 0.597, Mann Whitney U test) and **(C)** the basal K^+ concentration (Control, 3.93 ± 0.21 mM, n = 11; CBX, 3.45 ± 0.26 mM, n = 10; p = 0.157, two-sample Student's t-test) after 25 minutes of treatment with hypoosmolar aCSF.

In summary, these experiments showed that extracellular K^+ accumulations were directly affected by the ECS shrinkage as observed by augmented peak amplitudes of the extracellular K^+ transients during hypoosmolar conditions. In addition, increased basal K^+ concentrations were observed that potentially represent a cellular volume-regulatory mechanism in order to counteract the induced cellular swelling. However, both the induced increase of the K^+ peak amplitude and the elevated basal K^+ levels were largely unaffected by gap junction uncoupling. This suggests that other gap junction independent mechanisms or involved in K^+ clearance during these conditions.

However, in a subset of recordings, the evoked K^+ transients decreased after they had peaked during the hypoosmolar conditions. In order to further investigate this observation, the single experiments were categorized by the time-course of their K^+ transient peak amplitudes. When the peak amplitudes showed such a decrease, the experiment was categorized as 'run-down', whereas experiments with peak amplitudes that plateaued or continuously increased over the experimental time-course were categorized as 'stable' (Figure 31A). This categorization was independent of the initial K^+ peak amplitude during baseline since no difference was detected between the two groups ('Run-down', 5.92 ± 1.27 mM, n = 12; 'Stable', 6.24 ± 0.86 mM, n = 9; p = 0.846, two-sample Student's t-test). In order to probe if gap junction uncoupling differentially affected K^+ transients with 'stable' or 'run-down' peak amplitudes, the K^+ amplitudes after 25 minutes of hypoosmolar treatment in the presence of 50 µM CBX were compared to control conditions. For K^+ transients that showed a 'run-down', no difference of the relative peak amplitudes in the presence of CBX was found compared to control conditions (Figure 31B, top panel). Furthermore, the time between the application of the hypoosmolar aCSF and the onset of the 'run-down' (time-point of the maximal increased K^+ peak amplitude) was similar in control and CBX conditions (Control, 17.21 ± 1.88 min, n = 7; CBX, 15.00 ± 1.00 min, n = 5; p = 0.378, two-sample Student's t-test), as well as the maximal K^+ peak concentration at this time-point (Control, 22.02 ± 10.51 mM, n = 7; CBX,17.60 ± 8.11 mM, n = 5; p = 1, Mann Whitney U test). Also, the corresponding basal K^+ concentrations in control conditions were not different from CBX-treated slices after 25 minutes of hypoosmolar (Figure 31B, bottom panel). The peak amplitudes of the K^+ transients that were categorized as 'stable' also revealed no statistically significant difference in the presence of CBX compared to control conditions (Figure 31C, top panel). Interestingly, statistically significant higher basal K^+ concentrations in control conditions compared to CBX were observed (Figure 31C, bottom panel).

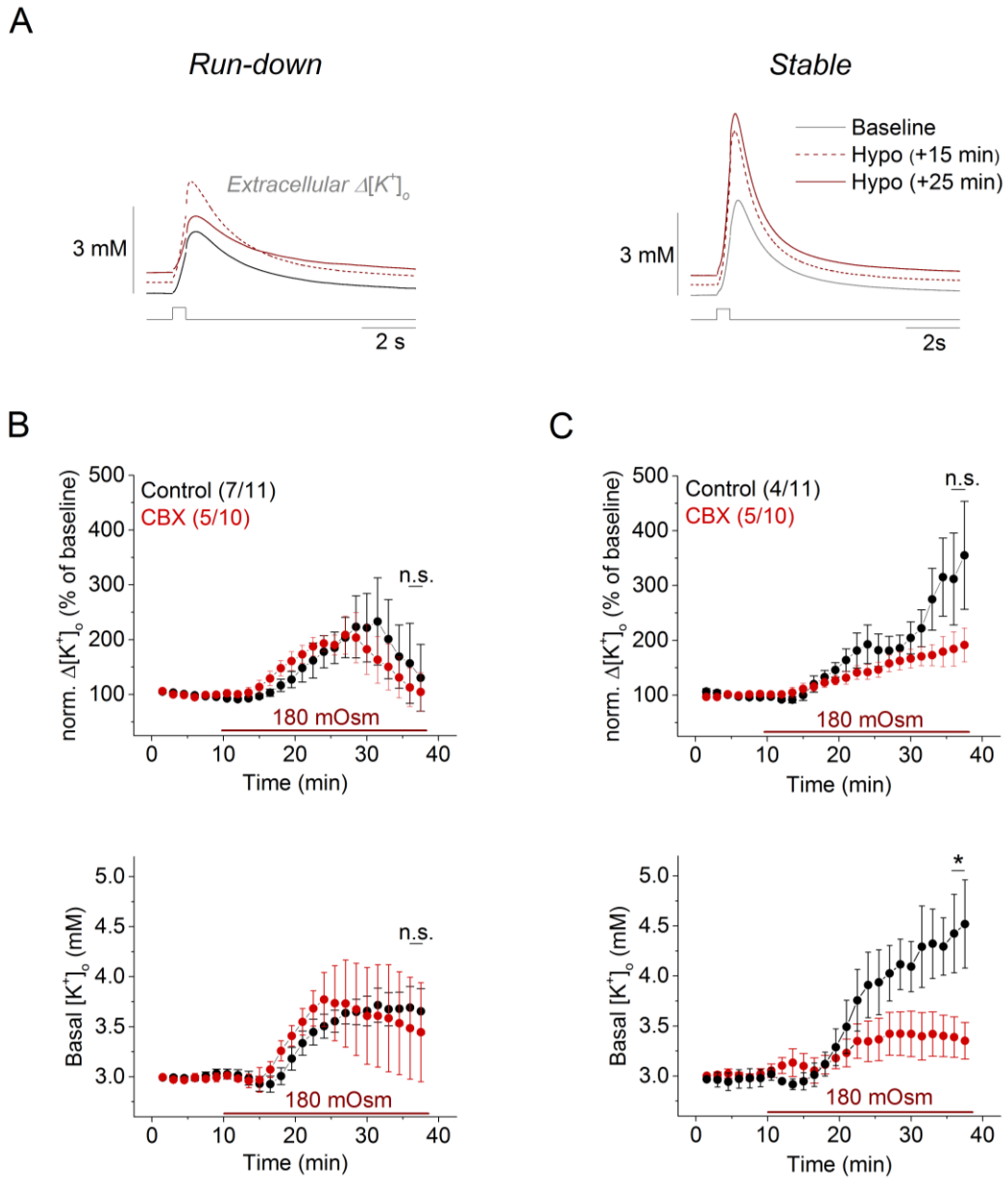

Figure 31 The peak amplitude of K^+ transients during hypoosmolar conditions decreased again in a subset of recordings. A) Example traces of K^+ transients that showed a decrease of their peak amplitudes after an initial increase (Left, 'Run-down') and K^+ transients that peak amplitudes plateaued or continuously increased during hypoosmolar conditions (Right, 'Stable'). **B)** The peak amplitudes of K^+ transients that showed a 'run-down' during the hypoosmolar condition were not different in the presence of CBX compared to control after 25 minutes of exposure to hypoosmolar aCSF (Top panel, Control, 165.29 ± 62.12%, n = 7; CBX, 112.93 ± 34.67%, n = 5; p = 0.745, Mann Whitney U test). The corresponding basal K^+ concentrations were also not affected by CBX compared to control conditions (Bottom panel, Control, 3.65 ± 0.18 mM, n = 7; CBX, 3.49 ± 0.51 mM, n = 5; p = 0.779, two-sample Student's t-test). **C)** CBX treatment had also no statistically significant effect on the peak amplitudes of K^+ transients that showed no 'run-down' during hypoosmolar conditions (Top panel, Control, 312.07 ± 83.70%, n = 4; CBX, 184.40 ± 31.02%, n = 5; p = 0.229, two-sample Student's t-test). The basal K^+ concentration was significantly more increased in control conditions compared to CBX treatment (Bottom panel, Control, 4.42 ± 0.39 mM, n = 4; CBX, 3.39 ± 0.20 mM, n = 5; p = 0.0405, two-sample Student's t-test).

Taken together, the differences in the time-course of the K^+ transient peak amplitudes ('stable' vs. 'run-down') indicate that extracellular K^+ accumulations were impacted differentially by ECS shrinkage. A simple explanation for that observation would be that the proposed volume-regulatory mechanism was differentially effective in normalizing the cellular volume and, in turn, the ECS at the different recording sites. Consequently, at sites with an effective volume-regulation, the induced extracellular K^+ transients would attenuate, whereas extracellular K^+ transients would further augment at site with an inefficient volume-regulation. However, the determining factor for the potential differences in the volume-regulation remains unclear, but the site of K^+ application and recording might have an influence on this. It could be argued that differences in the subcellular structures, such the size of astrocytic processes (fine processes in the periphery versus main branches), close to the recording site are differentially effective in regulating their volume und thus determine the different time-courses of the K^+ transients.

Interestingly, the increase of the basal extracellular K^+ concentration during the hypoosmolar conditions was significantly smaller in the presence of CBX compared to control conditions when the K^+ transient peak amplitudes showed no attenuation ('stable'; Figure 31C). This suggests that CBX might interfere with the release of K^+ during these conditions. Thus, it could be hypothesized that when the volume-regulatory mechanisms are ineffective and extracellular K^+ transients still augment, additional K^+ is released from the astrocytes to regulate the cellular volume. Since CBX also inhibits connexin hemichannels (Sáez et al., 2005), this additional K^+ release could be mediated by these hemichannels. Their inhibition would consequently reduce the amount of K^+ release under these conditions and limit basal extracellular K^+ elevation. If this mechanism then impacts delayed on the peak amplitudes of the evoked K^+ transients remains speculative, because the experiments were terminated after 30 minutes in the presence of hypoosmolar conditions.

In summary, these experiments investigated the role of gap junction coupling for the clearance of extracellular K^+ transients during conditions of a reduced ECS. Overall, gap junction uncoupling by the application of 50 µM CBX had no impact on the K^+ peak amplitudes of extracellular K^+ transient during hypoosmolar conditions (Figure 30). A simple explanation for this could be that gap junction coupling was inhibited by the hypoosmolar solution in both control and CBX-conditions. This could be the case when the induced cellular swelling would interfere with the intracellular pH and Ca^{2+} homeostasis that were shown to close gap junction channels (Bukauskas and Verselis, 2004; Obaid et al., 1983; Peracchia, 2004). Thus, the pharmacological inhibition by CBX would have no additional effect on the K^+ transients. However, in a subset of experiments the increase of the basal K^+ concentrations during hypoosmolar conditions was

significantly reduced. The underlying mechanism remains speculative, but it could point towards a role for connexin hemichannels during cellular volume regulation. This would, however, require open hemichannels during hypoosmolar conditions that were then closed by CBX. Such a scenario would, in turn, require distinct gating mechanism for unapposed hemichannels and hemichannels that form gap junction channels. Interestingly, both hemichannels and gap junction channels were reported to exhibit two molecular distinct gating mechanism (Bukauskas and Verselis, 2004) that could be differentially affected by the hypoosmolar conditions. It will be interesting to further reveal the role of hemichannels and gap junction channels for volume-regulatory mechanisms in future experiments.

4.1.9 Conclusions

Astrocytes contribute to the extracellular K^+ clearance via several mechanisms (Kofuji and Newman, 2004; Walz, 2000). Effective K^+ clearance is important for normal neuronal function, because an excess of extracellular K^+ results in neuronal hyperexcitability (Balestrino et al., 1986; Hablitz and Heinemann, 1987; Rausche et al., 1990; Voskuyl and ter Keurs, 1981) and has been associated with pathophysiological conditions such as epilepsy (Moody et al., 1974). The astrocytic gap junction coupling was postulated to facilitate K^+ clearance via K^+ redistribution from sites of elevated extracellular K^+ concentration to sites with a lower extracellular K^+ concentration. Previous studies found indications for this spatial K^+ buffering using mice that exhibit coupling-deficient astrocytes via an astrocyte-specific gene deletion of connexins (Pannasch et al., 2011; Wallraff et al., 2006). However, this was also accompanied by astrocyte morphology changes (Ghézali et al., 2018; Pannasch et al., 2014). Thus, it was not clear if the impaired K^+ clearance was a consequence of the absence of gap junction coupling or the morphology changes.

Therefore, pharmacological gap junction inhibitors were acutely applied in order to avoid long-term adaptions. The resulting disruption of the astrocyte network was then used to investigate the functional consequence on the clearance of extracellular K^+. For this purpose, extracellular K^+ transients were evoked by various stimuli and recorded with K^+-sensitive microelectrodes during intact and inhibited gap junction coupling. First, standard electrophysiological stimulation paradigms to probe hippocampal circuit function, i.e. the activation of CA3/1 Schaffer collaterals, were used to evoke K^+ transients. Such K^+ transients exhibited peak amplitudes in the sub to low millimolar range, but were largely unaffected by the inhibition of gap junction coupling in hippocampal slices obtained from juvenile rats. Next, K^+ transients with different peak amplitudes were evoked during silenced neuronal activity by a point-source K^+ application in hippocampal slices obtained

from adult rats. Such K^+ transients were also unaffected by acute gap junction uncoupling when they showed peak amplitudes in the low millimolar range. In contrast, extracellular K^+ transients with peak amplitudes exceeding ~10-15 mM were increased after gap junction uncoupling.

In conclusion, astrocytic gap junction coupling seem not to be involved in the clearance of extracellular small K^+ transients that are generally associated with physiological conditions (Heinemann et al., 1990; Rasmussen et al., 2019). Conversely, other K^+ clearance mechanisms, such as the Na^+/K^+-ATPase, could mediate K^+ clearance under these conditions (D'Ambrosio et al., 2002; Jauch et al., 2002; Ransom et al., 2000). In contrast, our results indicate that astrocytic gap junction coupling facilitates the clearance of large extracellular K^+ loads that are generally associated with pathophysiological conditions (de Curtis et al., 2018; Fisher et al., 1976; Moody et al., 1974). Thus, astrocytic gap junction coupling might act as a rescue mechanism when other K^+ clearance mechanisms are not able to cope with extensive extracellular K^+ loads. The acute gap junction uncoupling augmented the peak amplitude of the applied K^+ transients, but did not affect their decay. This suggests that astrocytic gap junction coupling facilitates K^+ clearance during the application phase of K^+ and is not involved in mediating the recovery of the extracellular K^+ concentration back to basal levels. Interestingly, similar was observed when the passive K^+ uptake via Kir4.1 channels, a proposed requirement for spatial K^+ buffering (Larsen and MacAulay, 2014; Orkand, 1986), was acutely inhibited (Larsen et al., 2014). This supports the conclusion that the coupling of astrocytic gap junction channels indeed mediates spatial K^+ buffering and thereby facilitates local K^+ uptake by the following mechanism. A local extracellular K^+ elevation will result in K^+ uptake and a depolarization of the astrocyte membrane. This K^+-induced astrocyte membrane depolarization will be limited by a fast K^+ redistribution within the astrocytic network or cytosol assisted by gap junction channels. As a consequence, the local membrane potential is kept below the K^+ equilibrium potential and K^+ enters constantly the astrocyte. In turn, this will limit the extracellular accumulation of the applied K^+. After the constant supply of K^+ into the ECS, K^+ is no longer redistributed and other mechanisms, such as the active K^+ uptake by the Na^+/K^+-ATPase (Larsen et al., 2014; Ransom et al., 2000), mediate the decay of the extracellular K^+ concentration back to basal levels. The conducted experiments further indicate that astrocytic gap junctions facilitate K^+ clearance specifically when a local extracellular K^+ concentration of around 10-15 mM was reached. These concentrations might represent the levels at which the other K^+ clearance mechanisms, such as the $Na^{+/}K^+$-ATPase, were saturated and cannot cope with the large amounts of extracellular K^+. As a consequence, K^+ redistribution assisted by astrocytic gap junction channels is required to sustain efficient extracellular K^+ clearance.

4.2 Proepileptiform mechanisms of rapid astrocyte morphology changes and uncoupling

Previous work from our lab (e.g. Anders, 2016) investigated astrocyte morphology and gap junction coupling in an *in vitro* epilepsy model. This model consisted of the induction of epileptiform activity by the suppression of inhibitory synaptic transmission through the application of the $GABA_AR$ antagonist penicillin for 30 minutes. It could be shown that epileptiform activity rapidly induced changes of the astrocyte morphology. This was manifested by a shrinkage of peripheral processes which was paralleled by a reduced intra- and intercellular diffusivity (Chapter 1.6.1). It was demonstrated that these morphology changes occurred within minutes after the onset of the epileptiform activity and persisted after the recovery of the inhibitory synaptic transmission. Importantly, also the epileptiform activity persisted after the inhibitory synaptic transmission was restored. Additionally, the frequency of the persistent epileptiform discharges was positively correlated with the degree of the astrocyte morphology changes. These morphology changes were prevented by inhibiting the Rho associated protein kinase (ROCK) pathway which suggests a role for the actin cytoskeleton. Importantly, the inhibition of ROCK also attenuated the epileptiform activity which indicates a proepileptiform effect of the rapid astrocyte morphology changes (Anders, 2016). However, the functional mechanism underlying the proepileptiform effect of the astrocyte morphology changes remained elusive. Therefore, the following experiments addressed the functional consequences of the astrocyte morphology changes in order to explain the observed proepileptiform effect.

4.2.1 Inhibitory input on CA1 pyramidal neurons after epileptiform activity

A first attempt to unravel the underlying mechanism of the persistent epileptiform activity after the removal of penicillin was to investigate a potential impact of astrocyte morphology changes on inhibitory input onto CA1 pyramidal neurons (Chapter 1.5.2 and 1.6). In the hippocampus, the major inhibitory input is mediated by the activation of $GABA_AR$ and the subsequent Cl^- influx that leads to a hyperpolarization or shunting of the neuronal membrane potential (Pelkey et al., 2017). In contrast, excitatory input is predominantly attributed to the activation of AMPARs and NMDARs associated with an influx of cations, such as Na^+ and Ca^{2+}, and a depolarization of the membrane. The integration of excitatory and inhibitory synaptic inputs determines the output of neurons, i.e. action potential firing (represented by the population spike of the field potential). Thus, a balanced integration is considered to be essential for normal brain function.

Since astrocytes, as a part of the tripartite synapse (Araque et al., 1999), are involved in regulating synaptic transmission, alteration of their morphology could impair this regulation

and, in turn, result in an imbalance of the synaptic integration. Thus, it was probed if alterations of the astrocyte morphology affected inhibitory input on CA1 pyramidal neurons and evoked a disinhibition that could explain the neuronal hyperexcitability, i.e. persistent epileptiform activity. As a measure for the inhibitory input, spontaneous inhibitory postsynaptic currents (sIPSC) were recorded from CA1 pyramidal neurons in hippocampal slices obtained from juvenile Wistar rats. These currents originate from spontaneous GABA release that activates postsynaptic $GABA_AR$. Previous experiments showed that the induction of epileptiform activity by penicillin for 30 minutes was able to evoke significant astrocyte morphology changes, therefore, the same approach was employed for the following experiments. Since the astrocyte morphology changes have been shown to occur rapidly after the onset of the epileptiform activity and persisted, it was hypothesized that the functional alterations were also already present during this period.

In order to monitor evoked and spontaneous neuronal activity in the hippocampal slices, a field potential electrode was placed in the CA1 str. oriens close to the pyramidal cell layer (Chapter 3.4.2 and 3.4.5). In addition, a bipolar stimulation electrode was placed in the str. radiatum at the CA3/1 border in order to stimulate Schaffer collaterals (SCs) and, in turn, evoke neuronal activity. The SCs were stimulated throughout the experiment with paired pulses (20Hz) at an interval of 30 seconds leading to two consecutive fEPSPs with a population spike each. First, the basal synaptic transmission and neuronal firing were monitored during a 10 minutes baseline period. Next, inhibitory GABAergic synaptic transmission was inhibited by the application of 4 mM penicillin to the aCSF. This resulted generally in the occurrence of multiple population spikes on top of the evoked fEPSPs (Figure 32A) and spontaneous epileptiform discharges (Figure 32B). In contrast, no spontaneous discharges were observed in control conditions. In line with previous experiments, the evoked synaptic transmission, quantified by the slope of the fEPSPs, was not affected by the inhibition of GABAergic transmission (Figure 32C). Epileptiform discharges occurred roughly 5-10 minutes after the application of penicillin and increased in frequency until a steady state discharge frequency of on average 2.56 ± 0.57 min^{-1} was reached (Figure 32D). After 30 minutes of penicillin treatment, penicillin was removed by the application of penicillin-free aCSF, also containing the NMDAR and AMPAR antagonists D-APV (50 µM) and NBQX (10 µM). This terminated the evoked and epileptiform activity. Importantly, previous experiments from our lab showed that the removal of penicillin recovered inhibitory input onto CA1 pyramidal neurons to control levels. Thus, potential effects on the GABAergic synaptic transmission after the wash-out of penicillin were likely mediated by the induced astrocyte morphology changes but not by residual penicillin in the tissue.

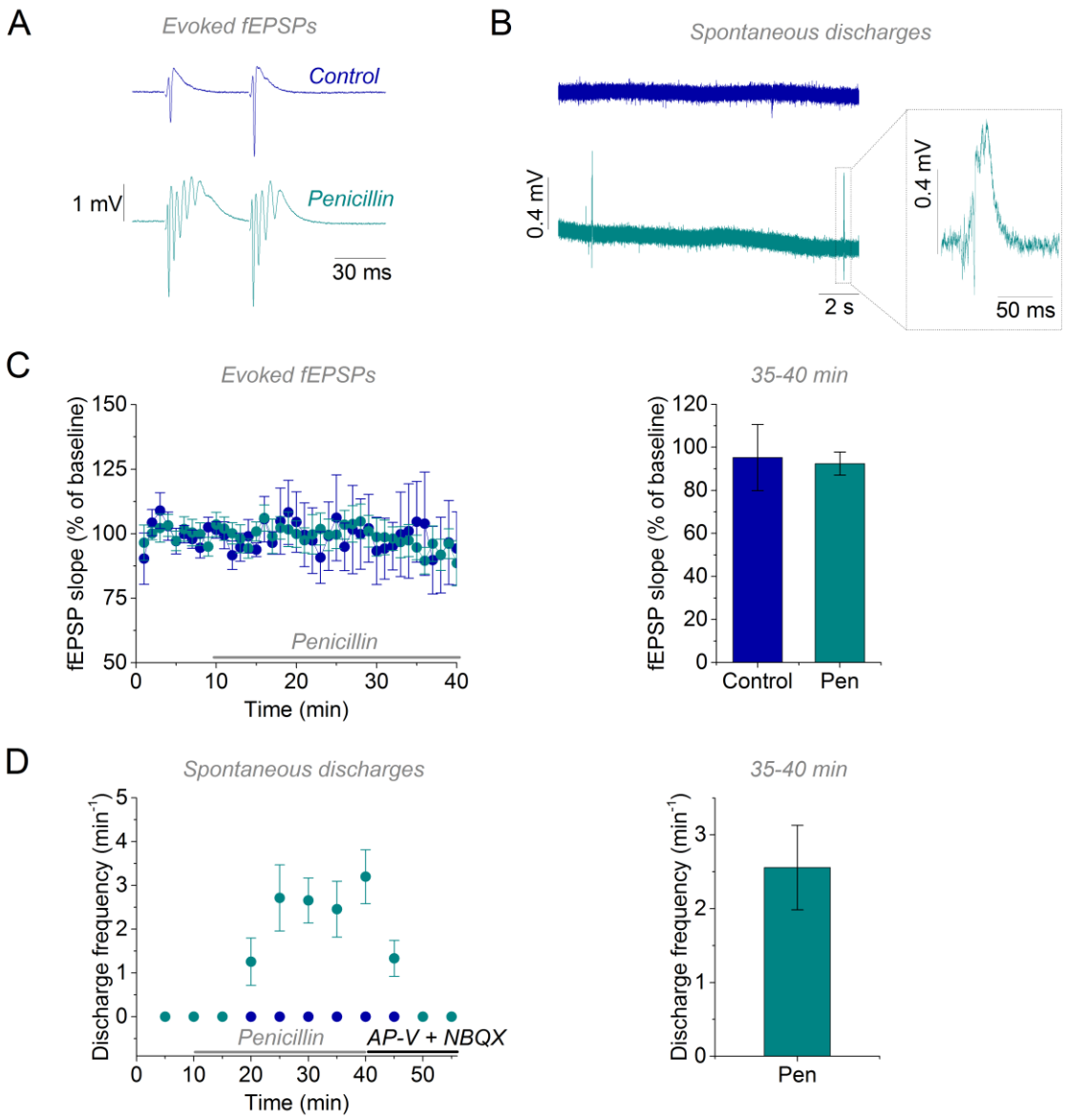

Figure 32 Induction of epileptiform activity by the application of 4 mM penicillin. A) Field potentials evoked by a paired-pulse SC stimulation were recorded in the CA1 str. pyramidale of hippocampal slices obtained from juvenile Wistar rats. Example traces of evoked field potentials recorded during control conditions (top) and in the presence of 4 mM penicillin (bottom). **B)** Spontaneous epileptiform discharges occurred during the application of penicillin (bottom), but not during control conditions (top). The inset on the right depicts a typical epileptiform discharge. **C)** The slope of the first evoked fEPSP was monitored throughout the experiment (Left panel) and was not different after penicillin treatment compared to control conditions (Right panel; Control, 95.26 ± 15.37%, n = 7; Penicillin, 92.75 ± 5.40%, n = 7; p = 0.609, Mann Whitney U test). **D)** The epileptiform discharges occurred shortly after the application of 4 mM penicillin and were terminated by the application of penicillin-free aCSF containing 50 µM D-APV and 10 µM NBQX (Left panel). The frequency of the epileptiform discharges increased within the first 10 minutes of penicillin treatment and reached on average 2.56 ± 0.57 min^{-1} (n = 7) after 30 minutes (Right panel). N indicates the number of hippocampal slices.

A CA1 pyramidal neuron was patched and kept in the voltage-clamp mode at a potential of -70 mV and filled with 40 µM Alexa Fluor 594 via the patch pipette (Chapter 3.4.4). Pyramidal neurons were identified by their typical morphology (large primary apical and multiple basal dendrites) visualized by the fluorescence signal of Alexa Fluor 594 and their location in the str. pyramidale of the hippocampal slice (Figure 33A-B). After 5 minutes of dialysis with the intracellular solution, sIPSCs were recorded over a period of 5 minutes (Figure 33C). Since the normal equilibrium potential for Cl^- is close to the neuronal membrane potential, opening of $GABA_AR$ would only lead to small inward currents. Thus, sIPSCs were recorded with an intracellular solution containing a high Cl^- concentration in order to render the equilibrium potential more positive. Consequently, $GABA_AR$ activation lead to larger, but outward-directed Cl^- currents (recorded as a negative deflection of the current signal). However, no significant difference was found for the frequency (Figure 33D) and amplitude (Figure 33E) of sIPSCs recorded in control condition compared to after epileptiform activity. Although not statistically significant, there was a tendency towards smaller width ($p = 0.0977$) of sIPSCs recorded in slices that experienced epileptiform activity (Figure 33G). This could indicate that the amount of extracellular GABA was unaffected but the GABA was present at the synapses for a shorter time period after epileptiform activity. This was further supported by the statistically significant shorter decay times when the sIPSCs decay was analyzed with a monoexponentially decaying function. The access resistance (Control, 12.37 ± 1.34 MΩ, n = 11; Penicillin, 12.75 ± 0.99 MΩ, n = 10; p = 0.307, Mann-Whitney U test) and the holding current (Control, -136.49 ± 18.04 pA, n =11; Penicillin, -141.94 ± 13.15 pA, n = 10; p = 0.812, two-sample Student's t-test) were also not different between the two conditions.

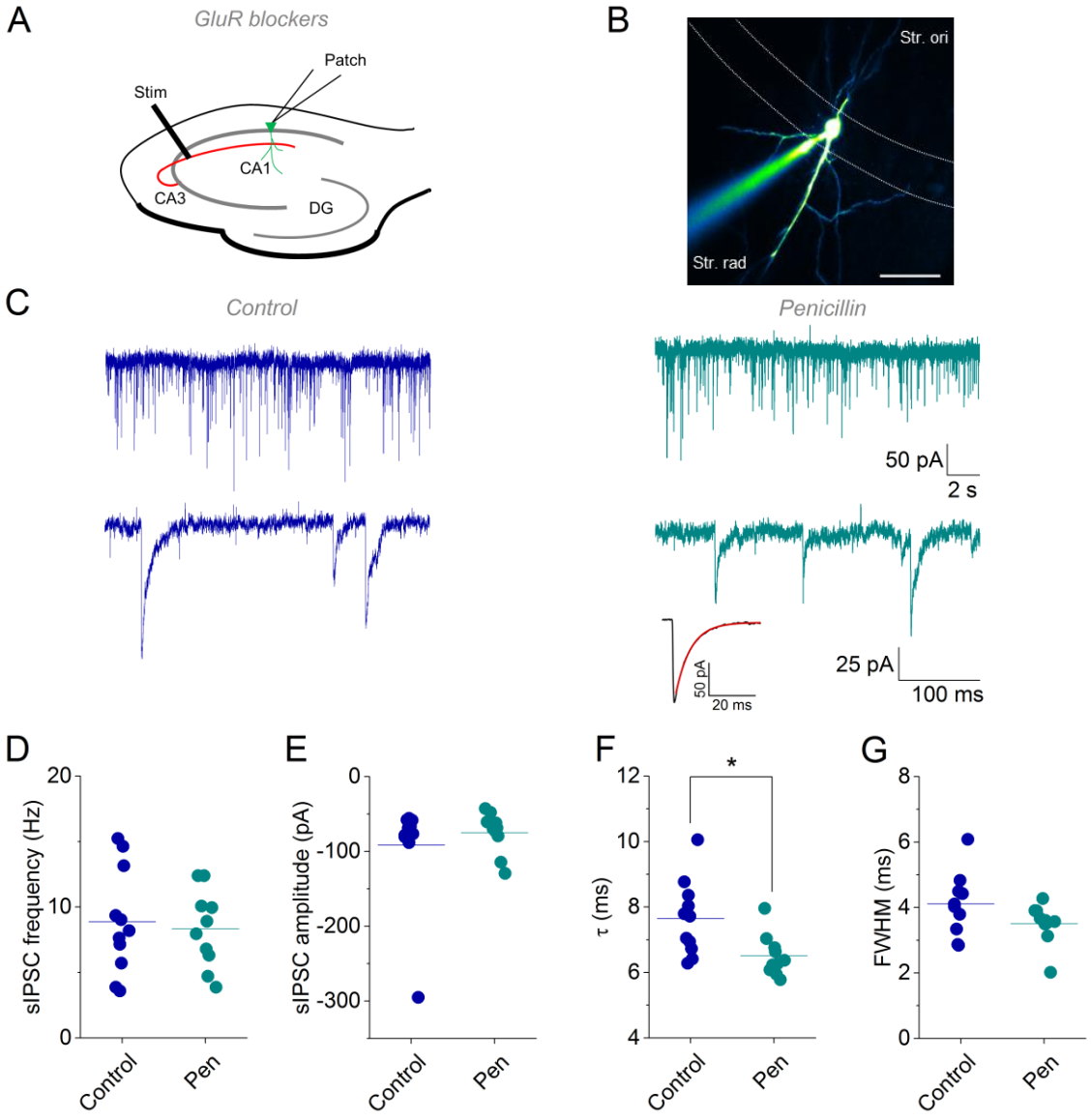

Figure 33 Spontaneous inhibitory input on CA1 pyramidal neurons was not affected by epileptiform activity. A) After the wash-out of penicillin and the application of glutamate receptor antagonists (50 µM D-APV & 10 µM NBQX), a CA1 pyramidal neuron (indicated in green) was patched in the whole-cell configuration and filled with Alexa Fluor 594 via the patch pipette. **B)** Example of a patched pyramidal neuron visualized by the Alexa Fluor 594 fluorescence. Scale bar: 50 µm. **C)** Example traces of spontaneous inhibitory postsynaptic currents (sIPSC) recorded from neurons in control conditions (Left panels) and after penicillin treatment (Right panels). Inset: The decay of the averaged sIPSCs was analyzed with a monoexponentially decaying function (red). **D-G)** No difference of the sIPSC frequency (Control, 8.88 ± 1.21 Hz; Penicillin, 8.34 ± 0.93 Hz; p = 0.734, two-sample Student's t-test), sIPSC amplitude (Control, -91.33 ± 20.62 pA; Penicillin, -74.74 ± 8.66 pA; p = 0.647, Mann Whitney U test) and the full-width at half maximum (FWHM) (Control, 4.11 ± 0.28 ms; Penicillin, 3.54 ± 0.19 ms; p = 0.0977, Mann Whitney U test) in control conditions was observed compared to after the induction of epileptiform activity. However, the decay time constant (τ) was significantly reduced after epileptiform activity (Control, 7.65 ± 0.34 ms, n = 11; Penicillin, 6.51 ± 0.20, n = 10; p = 0.0112, two-sample Student's t-test). Points represent the mean of the sIPSCs in a single recording. Lines represent the mean of the single recordings (Control, n = 11 neurons from 7 slices; Penicillin, n = 10 neurons from 7 slices).

Taken together, these results indicate that the frequency and amplitude of spontaneous inhibitory postsynaptic currents onto CA1 pyramidal neurons was largely unaffected by the induction of epileptiform activity and corresponding astrocyte morphology changes. However, there was tendency towards reduced width of the sIPCSs after epileptiform activity. Furthermore, the sIPSCs decay time constants were significantly decreased after epileptiform activity. This suggests that the presence of extracellular GABA at the synapses was shorter after epileptiform activity and therefore lead to an inefficient inhibitory synaptic input. If the faster sIPSC decay rates were a result of the astrocyte morphology changes, acute inhibition of the morphology changes should prevent the faster decay rates. Thus, further experiments and analysis might provide further insights about the impact of epileptiform activity on inhibitory synaptic transmission and, in turn, the neuronal hyperexcitability. On the other hand, neuronal hyperexcitability could not only be attributed to a disinhibition but also to increased extracellular K^+ or glutamate concentrations. This can be caused by an impaired clearance of K^+ or glutamate from the ECS or an increased release into the ECS. In addition, the structure of the ECS also impacts directly the extracellular concentration of K^+ and glutamate by determining the volume into K^+ and glutamate is released.

4.2.2 The ECS during epileptiform activity

Shrinkage of the ECS has been hypothesized to facilitate epileptiform activity by enhancing extracellular K^+ or glutamate accumulations (Kilb et al., 2006; Traynelis and Dingledine, 1989). However, also extracellular K^+ elevations itself, for instance evoked by neuronal activity, can induce cellular swelling and a reduction of the ECS. This results from water that enters the astrocyte during K^+ uptake in order to ensure isotonic conditions (MacAulay and Zeuthen, 2012; Syková et al., 1999). Interestingly, a pronounced activity-dependent ECS shrinkage was observed in hippocampal slices with coupling-deficient astrocytes. It was argued that this was a consequence of facilitated astrocytic swelling due to an impaired redistribution of K^+ within the astrocyte network (Pannasch et al., 2011).

This raised the question if the astrocyte morphology changes that were accompanied with a decreased intra- and intercellular diffusivity (Anders, 2016) would also lead to pronounced astrocyte swelling. A possible scenario how pronounced astrocyte swelling would facilitate the generation of epileptiform activity would be the following. Spontaneous excitatory synaptic activity that evokes under normal conditions sub-threshold postsynaptic activity results in small extracellular K^+ or glutamate accumulation. The astrocyte morphology changes would then lead to pronounced cellular swelling and

shrinkage of the ECS. As a consequence, K^+ or glutamate released by the spontaneous excitatory synaptic activity would induce higher extracellular concentrations and, in turn, above-threshold postsynaptic activity, i.e. epileptiform activity. On the other hand, the astrocyte morphology changes, i.e. the shrinkage of fine astrocyte processes (Anders, 2016), could also result in an increase of the ECS. Conversely to K^+ and glutamate, an increase of the ECS could also act proepileptiform by lowering the local extracellular concentration of inhibitory neurotransmitter, such as GABA.

In order to test this possibility, the real-time TMA^+-iontophoresis approach (Chapter 3.6.4) was employed in order to quantify the ECS structure. Briefly, TMA^+ was applied in the CA1 str. radiatum with a TMA^+ filled iontophoresis pipette and the corresponding extracellular TMA^+ transients were recorded in 100-200 µm distance. Simultaneously, field potentials were recorded in the CA1 str. oriens close to the str. pyramdiale. The application of 4 mM penicillin resulted in epileptiform discharges for 30 minutes (Figure 34A) that previously induced the astrocyte morphology changes. Considering that the epileptiform activity results in elevated extracellular K^+ levels (see Figure 35A in chapter 4.2.3), a decreased ECS fraction would be expected compared to control conditions if K^+-induced cellular swelling would be facilitated by the astrocyte morphology changes. Afterwards, epileptiform activity was terminated by the application of NMDAR, AMPAR and voltage-gated Na^+ channel inhibitors (Figure 34A). Conversely, if the shrinkage of the fine astrocyte processes would have increased the ECS, this should be most prominent in the absence of neuronal activity and the corresponding extracellular K^+ accumulations. However, the TMA^+ diffusion analysis revealed no alterations of the ECS fraction compared to control conditions (Figure 34B).

In summary, these experiments revealed that the ECS fraction was not affected during epileptiform activity. This indicates that the epileptiform discharges and the corresponding extracellular K^+ and glutamate accumulation were too small to induce ECS shrinkage or the shrinkage was too marginal to be detected. The unaltered ECS fraction during inhibited neuronal activity further suggests that the shrinkage of the fine astrocyte processes had also no impact on the ECS during resting conditions. As a consequence, the extracellular concentration of K^+ or glutamate is unlikely to be affected by the structure of the ECS. However, an impaired clearance of the extracellular K^+ or glutamate by the astrocyte morphology changes could promote the accumulation of K^+ or glutamate in the ECS and thereby increase neuronal excitability.

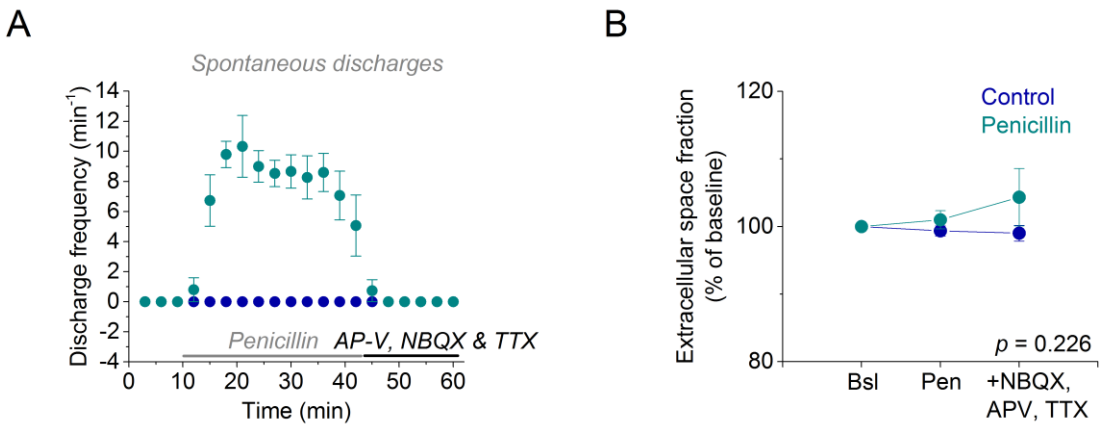

Figure 34 Induction of epileptiform activity had no impact on the ECS fraction. A) The application of 4 mM penicillin induced spontaneous epileptiform discharges, which were terminated after 30 minutes by 1 µM TTX, 10 µM NBQX and 50 µM D-APV (Control, n = 7; Penicillin, n = 6). **B)** The ECS fraction was unaffected by the induction of epileptiform activity (Control, n = 7, Penicillin, n = 6; p for Ctl vs. Pen = 0.226, two-way repeated measures ANOVA). Analysis done by Dr. C. Henneberger.

4.2.3 Extracellular K^+ clearance after epileptiform activity

Extracellular K^+ concentration elevations were shown to facilitate action potential firing and synaptic transmission (Balestrino et al., 1986; Hablitz and Lundervold, 1981; Rausche et al., 1990; Voskuyl and ter Keurs, 1981). Consequently, an impaired extracellular K^+ clearance and the corresponding excess of extracellular K^+ would increase neuronal excitability and, in turn, might contribute to the generation of epileptiform activity. Astrocytes contribute to the clearance of extracellular K^+ concentrations by several mechanisms (Kofuji and Newman, 2004; Walz, 2000). It was for instance shown that slowed K^+ uptake in hippocampal slices from Cx30 and 43 knock-out mice was associated with a reduced threshold for the generation of epileptiform activity (Wallraff et al., 2006). Therefore, we hypothesized that the induced astrocyte morphology changes and the corresponding decreased intra- and intercellular diffusivity (Anders, 2016) impaired the extracellular K^+ clearance. For instance, a reduced intra- and intercellular K^+ redistribution could impair spatial K^+ buffering and thereby lead to facilitated extracellular K^+ accumulations. Furthermore, the astrocyte morphology changes might alter the proximity of K^+ channels and transporters to the K^+ release sites and decrease their uptake efficiency. Thus, if astrocyte morphology changes impaired extracellular K^+ clearance, augmented peak amplitudes and/or a prolonged decay of extracellular K^+ transients would be expected after epileptiform activity.

In order to test this hypothesis, field potentials and the extracellular K^+ concentration were recorded in the CA1 stratum pyramidale and radiatum, respectively (Figure 35A). Next, 4

mM penicillin was applied for 30 minutes in order to induce epileptiform activity and, in turn, astrocyte morphology changes. The epileptiform discharges (Figure 35B) evoked extracellular K^+ transients with peak amplitudes of on average 0.23 ± 0.042 mM (n = 6). Simultaneously, axonal and synaptic activity was evoked by the stimulation of Schaffer collaterals with a paired-pulse (20 Hz, 30 s interstimulus interval, stimulation intensity was adjusted to obtain 80% of the maximal fiber volley amplitude). Next, it was tested if the epileptiform activity altered the extracellular K^+ clearance. Since the epileptiform activity and the increased postsynaptic activity would lead to more activity-dependent K^+ release compared to control conditions, NMDAR and AMPAR were acutely inhibited by 50 µM DAP-V and 10 µM NBQX, respectively, in order to terminate epileptiform activity and inhibit postsynaptic activity. As a consequence, the extracellular K^+ transients were solely induced by axonal activity, which allowed a better comparison of the evoked extracellular K^+ transients between the conditions. Schaffer collaterals were stimulated with 50 pulses at 100 Hz that resulted in axonal activity (represented by a train of 50 fiber volleys, FV) and extracellular K^+ transients with peak amplitudes (Control, 0.93 ± 0.20 mM, n = 6; Penicillin, 1.20 ± 0.24, n = 6; p = 0.409, two-sample Student's t-test) in the low millimolar range (Figure 35C). Impaired K^+ clearance after epileptiform activity is expected to result in larger extracellular K^+ accumulations compared to control conditions when evoked by similar neuronal activity. Since the number of activated axons can vary between the experiments and thereby the activity-dependent K^+ release, the K^+ peak amplitudes were normalized to their corresponding mean FV-amplitude. However, the normalized peak amplitudes of the extracellular K^+ transients after epileptiform activity were not different from control conditions (Figure 35D, left panel). This indicates that the epileptiform activity and the corresponding astrocyte morphology changes did not facilitate the accumulation of extracellular K^+. Since limiting the extracellular accumulation of K^+ and the recovery back to basal levels was previously suggested (Larsen and MacAulay, 2014; Larsen et al., 2014) and further supported in this study (Chapter 4.1 and Breithausen et al., 2020) to be mediated by different mechanisms also the decay of the extracellular K^+ transients was analyzed. A prolonged presence of K^+ in the ECS, represented by a prolonged decay of the K^+ transients, would also lead to neuronal hyperexcitability and could underlie the generation of epileptiform activity. However, also the decay of the extracellular K^+ transients after epileptiform activity was not different from control conditions (Figure 35D, right panel).

In summary, the conducted experiments show that the extracellular K^+ clearance was not affected by epileptiform activity during these conditions. This indicates the persistence of the epileptiform activity after the recovery of inhibitory synaptic transmission (Anders, 2016) was not mediated by augmented or prolonged extracellular K^+ accumulations. In

addition to extracellular K^+, increased and/or prolonged extracellular glutamate accumulations would lead to increased glutamate receptor actitation and, in turn, to increased postsynaptic activity.

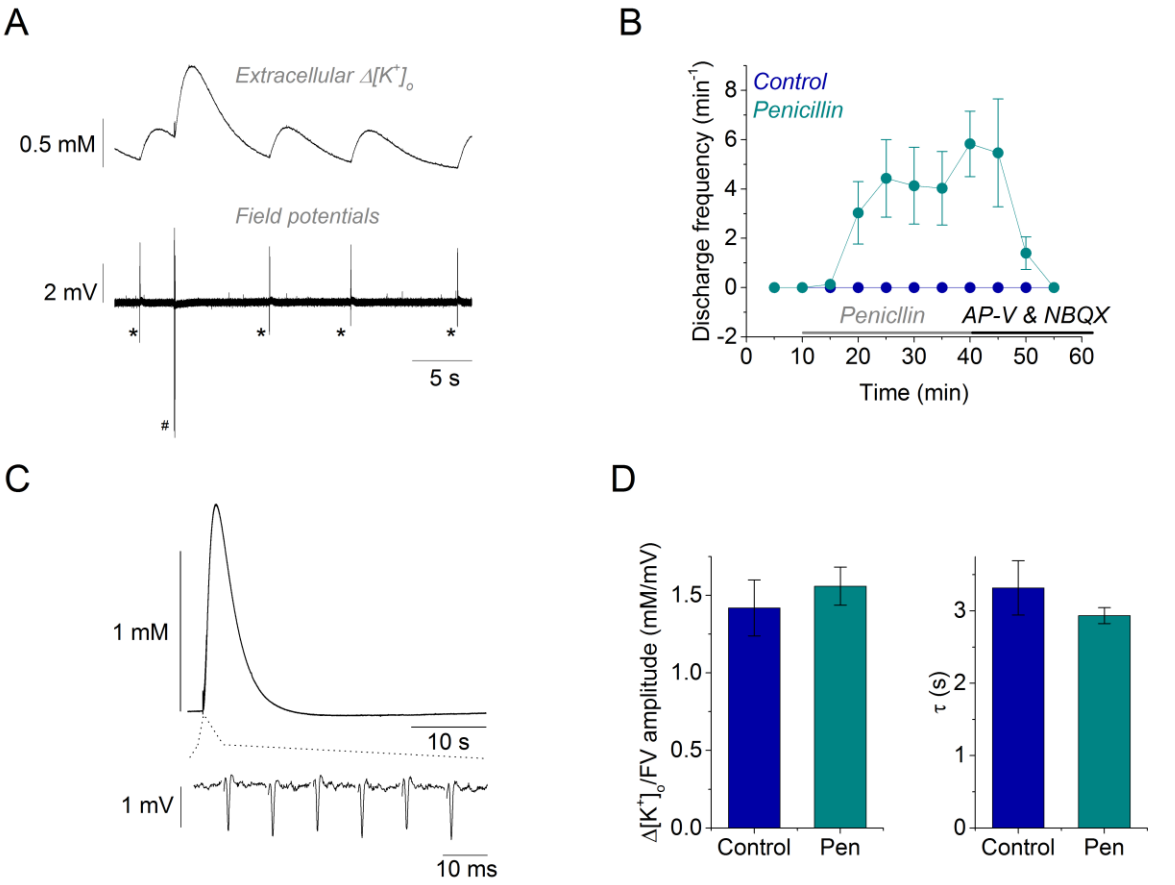

Figure 35 Extracellular K^+ clearance was unaffected by epileptiform activity. **A)** The extracellular K^+ concentration was recorded in the CA1 stratum radiatum with a K^+-sensitive microelectrode (top trace) in parallel to field potentials in the CA1 stratum pyramidale (bottom trace). Spontaneous epileptiform discharges are indicated by * and stimulation-evoked fEPSPs are indicated by #. **B)** The application of 4 mM penicillin evoked epileptiform discharges (max. rate; 5.83 ± 1.32 min^{-1}, n = 6), which were terminated by the inhibition of postsynaptic activity (50 µM DAP-V & 10 µM NBQX). **C)** After the inhibition of postsynaptic activity, extracellular K^+ transients (top trace) were evoked by the stimulation (50 pulses at 100 Hz) of Schaffer collaterals (bottom trace, 6/50 fiber volleys shown, recorded by the reference compartment of the K^+-sensitive microelectrode). **D)** Left panel: The peak amplitudes of the evoked extracellular K^+ transients that were normalized to the mean fiber volley (FV) amplitude were not affected by epileptiform activity (Control, 1.42 ± 0.18 mM/mV, n = 6; Penicillin, 1.56 ± 0.12 mM/mV, n = 6; p = 0.533, two-sample Student's t-test). Right panel: The decay rate (τ) of the extracellular K^+ transients (quantified by a monoexponentially decaying function) was also not affected by epileptiform activity (Control, 3.32 ± 0.37 s, n = 6; Penicillin, 2.93 ± 0.11 s, n = 6; p = 0.810, Mann–Whitney U test). A subset of the presented data belongs to my Master Thesis. This set of data was then completed during the time as a PhD student.

4.2.4 Glutamate clearance after epileptiform activity

Glutamate is the predominant excitatory neurotransmitter in the brain (Danbolt, 2001; Rose et al., 2018). Excitatory synapses release glutamate spontaneously or upon stimulation into the synaptic cleft, where it binds to glutamate receptors that mediate the synaptic transmission by the influx of cations into the postsynaptic compartment. An excess of extracellular glutamate, caused for example by an impaired extrasynaptic clearance, could therefore evoke increased postsynaptic activity and, in turn, facilitate epileptiform activity. Astrocytes have been shown to be involved in the regulation of glutamatergic transmission by the uptake of glutamate and by limiting glutamate spillover at the synapse (Asztely et al., 1997; Rose et al., 2018). For that reason, astrocytes are located at the extrasynaptic sites (Kikuchi et al., 2020; Medvedev et al., 2014; Ventura and Harris, 1999; Witcher et al., 2007) and express glutamate transporters that clear glutamate from the ECS.

This glutamate uptake was shown to depend on the cotransport of Na^+ and, in turn on the transmembrane concentration gradient for Na^+ (Levy et al., 1998; Nicholls and Attwell, 1990; Rose et al., 2018; Stallcup et al., 1979). It was further shown that increased intracellular Na^+ accumulations in astrocytes and, in turn, a reduced Na^+ transmembrane concentration gradient reduced glutamate uptake (Karus et al., 2015). This raised the question if the reduced astrocyte volume and the decreased intra- and intercellular diffusivity (Anders, 2016) would facilitate intracellular Na^+ accumulations, impair the glutamate clearance and, in turn, promote epileptiform activity. Furthermore, the glutamate transporter GLT-1 was shown to be highly motile in the membrane of hippocampal astrocytes and thus affect synaptic transmission (Murphy-Royal et al., 2015). As a consequence, the astrocytic morphology changes could impair this surface diffusion and impair glutamate clearance (Henneberger, 2017; Murphy-Royal et al., 2015). In order to probe if glutamate clearance was affected by astrocyte morphology changes, extracellular glutamate dynamics were visualized with the intensity-based glutamate sensor iGluSnFR (Marvin et al., 2013). For this purpose, the fluorescence glutamate sensor iGluSnFR was expressed specifically on the surface of astrocytes. .

As described above, basal synaptic transmission recorded in the CA1 str. oriens close to the pyramidal cell layer was monitored for 10 minutes during a baseline period in the absence of penicillin. Next, 4 mM penicillin was applied to evoke epileptiform activity. Again, the epileptiform discharges occurred after the application of penicillin and reached a frequency of 0.525 ± 0.38 min^{-1} after 30 minutes (Figure 36). Afterwards, penicillin was removed by the application of penicillin-free aCSF containing also 10 µM NBQX, 50 µM D-APV, 1 µM TTX and 100 µM Ly341495 in order to block AMPARs, NMDARs, action potential firing and mGluRs. Thus, epileptiform activity was terminated and the

subsequently applied glutamate was prevented from activating glutamate receptors. This allowed me to investigate extracellular glutamate clearance in isolation, because modulatory effects of glutamate on, for instance astrocytic Ca^{2+} signaling or presynaptic glutamate release, were largely reduced.

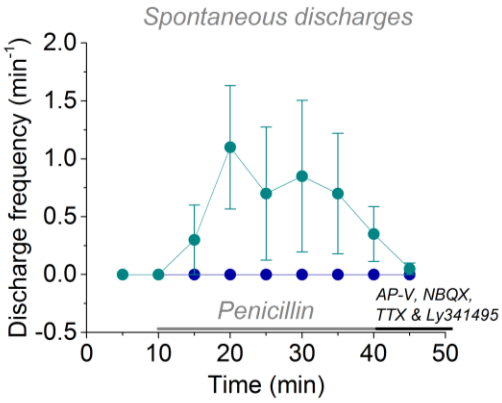

Figure 36 Low frequency of epileptiform discharges in slices obtained from FVB mice expressing iGluSnFR on astrocytes. Epileptiform discharges appeared shortly after the application of 4 mM penicillin and reached a frequency of 0.525 ± 0.38 min^{-1} after 30 minutes (Cyan, n = 4 slices). No discharges were observed during control conditions (Blue, n = 4 slices). After 30 minutes, penicillin-free aCSF containing 10 µM NBQX, 50 µM D-APV, 1µM TTX and 100 µM Ly341495 was applied to the hippocampal slices.

It was tested if glutamate clearance was influenced by astrocyte morphology changes that were induced during the period of epileptiform activity. To this end, iGluSnFR-expressing astrocytes were identified in the CA1 str. radiatum of hippocampal slices that experienced epileptiform activity or control conditions (Figure 37A). In order to inject glutamate into the hippocampal slice, an iontophoresis pipette filled with 150 mM glutamate was placed in the territory of an astrocyte expressing iGluSnFR (Chapter 3.5). The advantage of the iontophoresis approach was that the amount of applied glutamate was controlled by the application current and thus was kept constant between the experiments. Furthermore, it allowed investigating the spatial spread of glutamate into the ECS since the release site of glutamate was known. For visualizing the applied glutamate, the iGluSnFR-expressing astrocyte territory was imaged repetitively by a line scan close to the tip of the iontophoresis pipette (Figure 37B, left panel). This line scan provides information about the spatial profile of the extracellular glutamate transients along the imaged line. Also information about the tempotal profile of the extracellular glutamate transients is obtained by the repetitive scanning of the same line.

Next, glutamate was applied by a -5 nA current injection for 250 ms which resulted in a glutamate transient represented by a fluorescence increase in the line scan (Figure 37B,

right panel). The duration of the iontophoretic glutamate application (200 ms) resembled roughly the duration of interictal discharges that can be observed in an electroencephalogram of epilepsy patients (de Curtis and Avanzini, 2001). During the post-hoc analysis, the line scan was binned into 1 µm broad sections, which were normalized to their respective baseline fluorescence and converted into the actual glutamate concentration (Chapter 3.8.3).

If glutamate clearance would be impaired after epileptiform activity, an accelerated extracellular glutamate accumulation, augmented extracellular glutamate concentrations and/or a pronounced spread into the ECS would be expected. These scenarios could lead to increased glutamate receptor activation and thereby promote epileptiform activity. In order to test the accumulation rate (quantified by an exponential function) and the peak amplitude of the evoked extracellular glutamate transients, the temporal profile of the line scan was analyzed. Both parameters varied between the separate lines depending on their distance to the glutamate source (tip of the iontophoresis pipette). This was expected since the applied glutamate dissipates in the ECS with distance to its source and thus creates an extracellular gradient. Therefore, the temporal glutamate profiles were compared between different lines according to their lateral distance to the source. Since the fastest glutamate accumulation was expected to occur closest to the source, the line with the smallest accumulation constant (τ) was designated as such. As indicated above, the accumulation rate and peak amplitudes decreased with increasing distance of the respective line to the glutamate source (Figure 37C). Next, the glutamate accumulation rates were compared between control conditions and after epileptiform activity since a fastened accumulation could indicate an impaired glutamate clearance. The accumulation rates were, overall and independently of the lateral distance to the glutamate source, decreased after epileptiform activity compared to control condition (Figure 37E). However, no such effect was observed for the glutamate peak amplitude (Figure 37F). This indicates that the applied glutamate accumulates slightly slower after epileptiform activity but reaches similar concentrations compared to control conditions.

In addition to the analysis of the temporal glutamate profile, the spatial profile, i.e. the extent of the glutamate spread into the ECS, was quantified. To this end, the glutamate concentration along the line scan was approximated with a Gaussian fitting function at the end of the glutamate accumulation period. An impaired glutamate clearance could lead to a facilitated spread of glutamate into the ECS, which would be detected by an increased width of the spatial glutamate transient profiles. Although not statistically significant, the fitting functions of the glutamate transients showed a tendency towards an increased full width at the half maximal amplitude (FWHM) after epileptiform activity (Figure 37D, right panel). This could point towards an increased spread of glutamate into the ECS and

thereby to pronounced glutamate receptor actitation. In a subset of experiments, the glutamate transients showed ‘sag’ where the peak would be expected (Figure 37D, left panel). This ‘sag’ was then manually removed from the analysis. This sag might have originated from a small glutamate leakage out of the iontophoresis pipette tip that bound to the iGluSnFR before the actual glutamate application and in turn decreased the dynamic range of the sensor. Consequently, the fluorescence change to glutamate would be smaller compared to the naïve iGluSnFR at some distance from the pipette tip.

In summary, these experiments showed that the accumulation rates of the iontophoretically applied glutamate were slightly slowed after the induction of epileptiform activity compared to control conditions (Figure 37E). Additionally, it seemed that glutamate, although not statistically significant, tended to spread further into the ECS after the induction of epileptiform activity (Figure 37D). However, the number of epileptiform discharges was, surprisingly, reduced compared to previous experiments performed with slices obtained from non-transfected mice (Anders, 2016) and rats (Figure 34). We hypothesized that this was caused by the expression of iGluSnFR, which binds glutamate and thus might reduce epileptiform activity by attenuating extracellular glutamate accumulations. A reduced number of epileptiform discharges might also induce only small changes of the astrocyte morphology. In turn, this could lead to an underestimation of the impact of epileptiform activity on the glutamate clearance. Therefore, a stronger protocol to evoke epileptiform discharges at higher frequencies was used in the following experiments. Glutamate release during synaptic transmission is mainly restricted to the synaptic cleft. Thus, it can be assumed that extracellular glutamate transients occur at several sources more or less time-locked during epileptiform activity. The iontophoretic glutamate application in contrast creates a single glutamate point source randomly in the ECS. In order to probe glutamate clearance during more physiological scenarios, extracellular glutamate transients were evoked by synaptic activity in the following experiments.

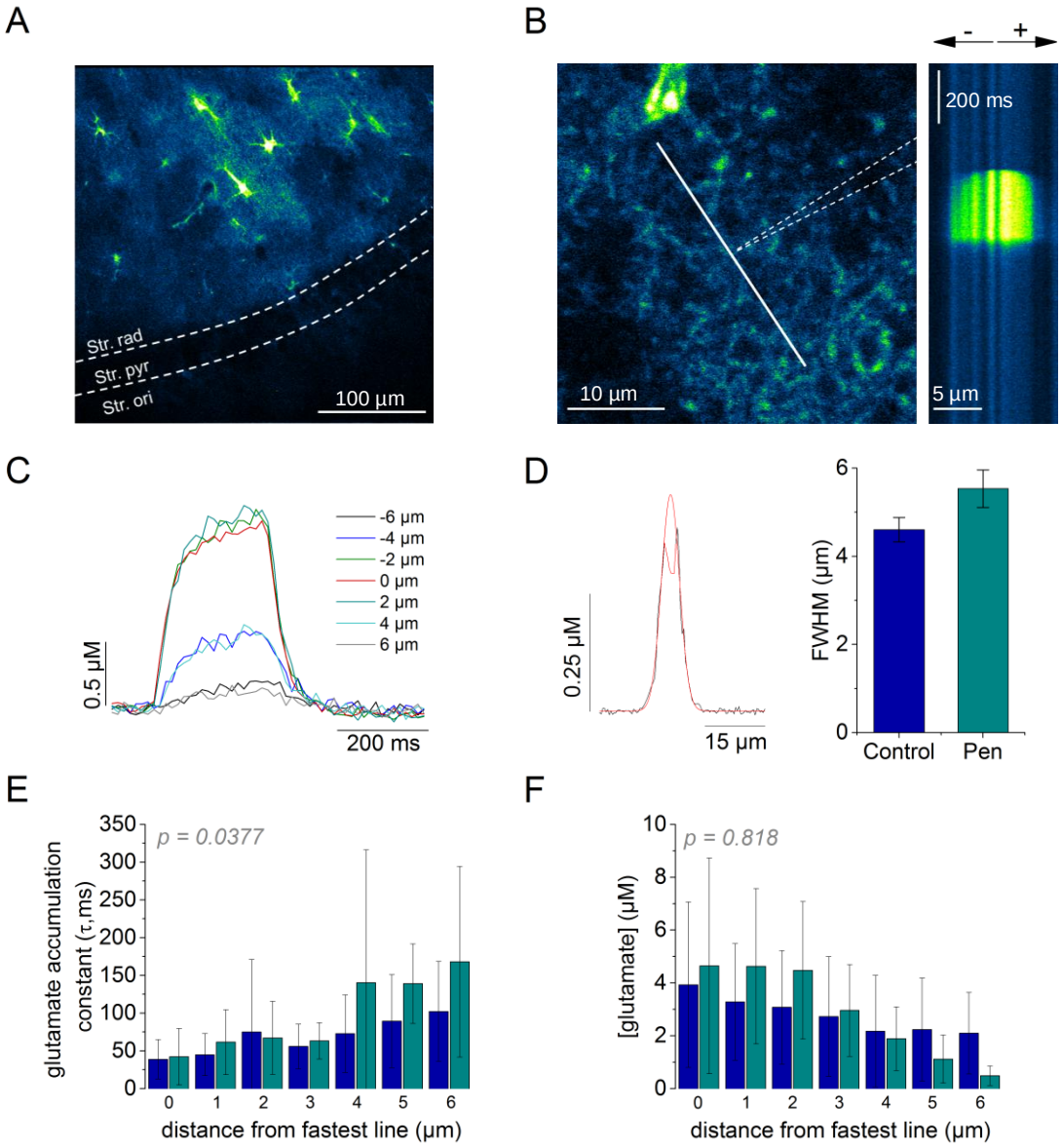

Figure 37 Clearance of iontophoretically applied glutamate was largely not affected by astrocyte morphology changes. A) Astrocytes expressing iGluSnFR were identified in the CA1 str. radiatum of the hippocampal slices. In each slice one to three astrocyte were randomly selected for imaging. **B)** For glutamate application, an iontophoresis pipette (represented by the dotted lines) was placed in the territory of an iGluSnFR-expressing astrocyte. Next, a line (represented by the solid line) was manually defined close to the tip of the iontophoresis pipette and scanned repetitively (Left panel). Glutamate was then injected by a -5 nA current injection which resulted in a fluorescence increase of iGluSnFR in the line scan (right panel). The fluorescence intensity was then converted into the actual glutamate concentration (see methods). **C)** The line scans were binned into 1 µm lines and the temporal glutamate profiles were analyzed separately for the glutamate accumulation rate (τ). The line with the fastest glutamate accumulation was defined as closest to the glutamate source (0 µm). As the example glutamate transients depicts, the amplitude and accumulation rate decreased with increasing distance ('-', left from source; '+', right from source) to the line with the fastest accumulation rate. **D)** The spatial spread of the applied glutamate was analyzed at the end of the glutamate injection with a Gaussian function along the spatial profile of the line scan. The full-width at the half maximal amplitude (FWHM) of the Gaussian functions was not different in control conditions from after epileptiform activity (Control, 4.60 ± 0.28 µm, n = 9 astrocytes from 4 slices; Penicillin, 5.54 ± 0.43 µm, n = 10 astrocytes

from 5 slices; p = 0.0910, two-sample Student's t-test). **E)** Overall, the accumulation constant (p = 0.0377 for treatment, p = 0.00274 for distance, two-way ANOVA; no significant interactions) of the applied glutamate was different in control conditions (Blue, n = 9 astrocytes from 4 slices) compared to after epileptiform activity (Cyan, n = 10 astrocytes from 5 slices) **F)** No difference was observed for the amplitude of the glutamate transients (p = 0.818 for treatment, p < 0.001 for distance, two-sample ANOVA; no significant interactions). These experiments were performed together with Dr. D. Minge.

The following experiments were again performed in hippocampal slices obtained from mice that underwent a stereotactic virus injection and expressed iGluSnFR specifically on astrocytes. In contrast to the previous experiments, a stronger protocol to induce epileptiform activity was used and extracellular K^+ transients were evoked by synaptic release. In addition, a third experimental condition was introduced in which Y27632, a selective inhibitor of the Rho-associated protein kinase (ROCK)-signaling pathway, was present throughout the experiments. It was previously shown that inhibiting the ROCK-signaling pathway prevents astrocyte morphology changes and decreased the number of persistent epileptiform discharges after the recovery of inhibitory transmission (Anders, 2016). If glutamate clearance was impaired by the astrocyte morphology changes, augmented extracellular glutamate transients or a prolonged decay back to basal levels would be expected after epileptiform activity. Conversely, extracellular glutamate transients would be unaffected in control conditions and after epileptiform activity in the presence of Y27632.

To investigate this, hippocampal slices were treated in a subset of experiments throughout the experimental time-course with 20 µM Y27632. As described above, Schaffer collaterals were then stimulated and the corresponding neuronal activity was monitored in the CA1 str. oriens close to the pyramidal cell layer via a field potential electrode. After a 10 minutes baseline, epileptiform activity was evoked for 30 minutes by the application of 4 mM penicillin in order to induce astrocyte morphology changes. In contrast to the previous experiments, the penicillin was applied together with a Mg^{2+}-free aCSF in order to relieve the Mg^{2+} block from the NMDAR pore. As a consequence, NMDAR mediated transmission was enhanced and facilitated neuronal excitability (Gloveli et al., 1995; Mody et al., 1987). During treatment of the hippocampal slices with Mg^{2+}-free aCSF containing 4 mM penicillin, the evoked fEPSPs were accompanied by multiple population spikes (Figure 38A) and epileptiform discharges occurred (Figure 38B). The extracellular K^+ concentration was 2.5 mM in a subset of experiments since one batch of hippocampal slices tended to show spontaneous discharges already during baseline condition at a extracellular K^+ concentration of 4 mM (Hippocampal slices measured at 2.5 mM extracellular K^+: Control (4/7), Penicillin (4/6), Penicillin + Y27632 (5/6)). Both sets of experiments were subsequently pooled.

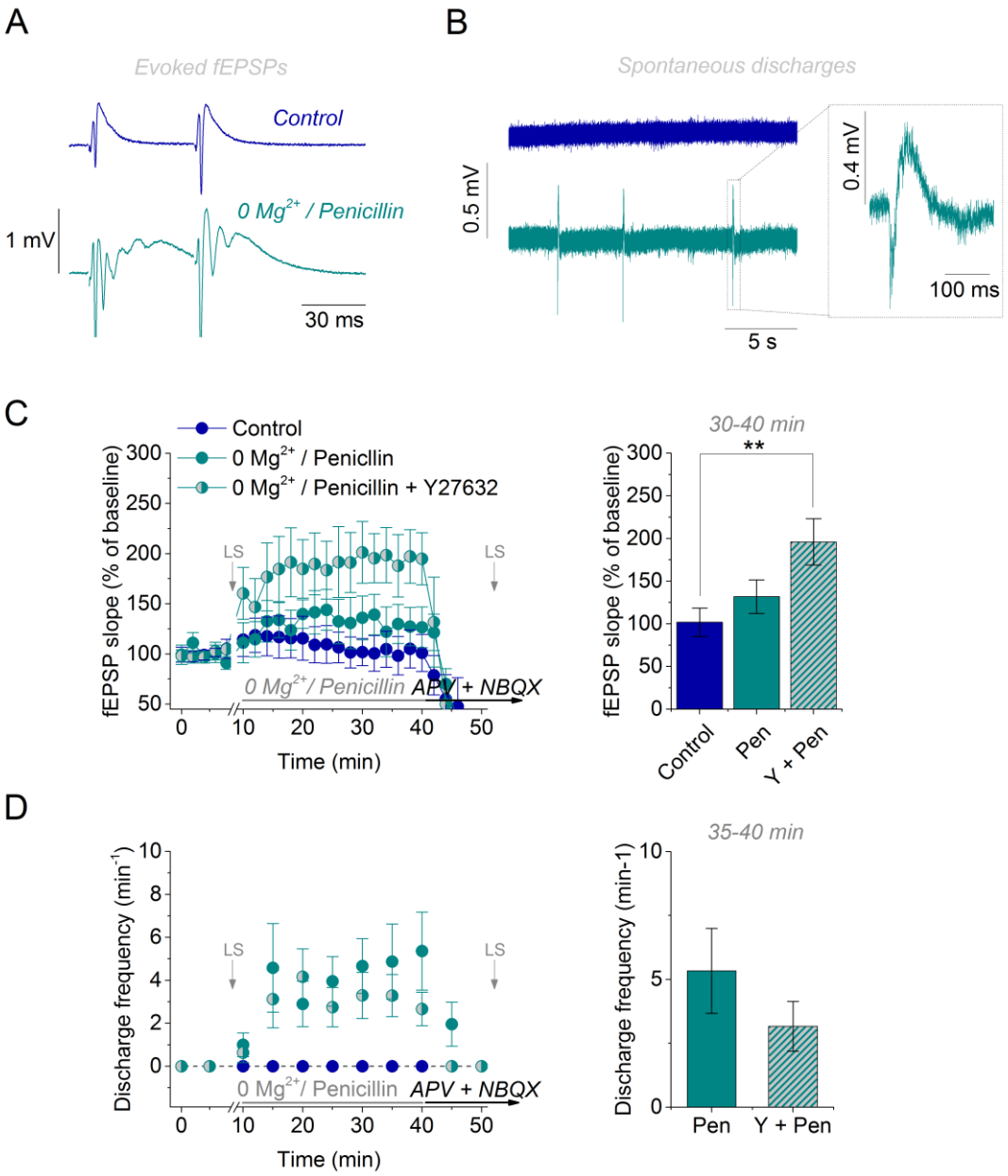

Figure 38 Application of 4 mM penicillin and Mg^{2+}-free aCSF increased the frequency of epileptiform discharges in slices obtained from mice expressing iGluSnFR on astrocytes. A) Example fEPSPs recorded in the CA1 str. oriens close to the str. pyramidale showed repetitive population spikes. **B)** Example epileptiform discharges during condition of 0 mM Mg^{2+} and 4 mM penicillin. The inset shows a typical epileptiform discharge. **C)** The slope of the fEPSP increased after the application of penicillin in Mg^{2+}-free aCSF in the presence of 20 µM of the ROCK-inhibitor Y27632. The fEPSP slope was not significantly affected in the absence of Y27632 (Control, 101.77 ± 16.65%, n = 6; Penicillin, 131.82 ± 19.54%, n = 5; Penicillin + Y, 196.02 ± 27.11%, n = 5; p = 0.0212, one-way ANOVA; p = 0.325 for Control vs. Pen, p = 0.00689 for Control vs. Pen + Y, p = 0.0568 for Pen vs. Pen + Y, Holm-Bonferroni post-hoc test). Line scans (LS) to image iGluSnFR were performed after the baseline period before the application of penicillin and after the wash-out of penicillin in the presence of D-APV and NBQX. **D)** Epileptiform discharges occurred rapidly after the application of penicillin and Mg^{2+}-free aCSF, but their frequency was not affected by Y27632 (Pen, 5.33 ± 1.66 min^{-1}, n = 6; Pen + Y, 3.17 ± 0.97 min^{-1}, n = 6; p = 0. 286, two-sample Student's t-test). N represents the number of hippocampal slices.

First, it was tested if the synaptic transmission, quantified by the fEPSP slope, was affected by Y27632 during the application of penicillin and Mg^{2+}-free aCSF. Compared to control conditions, the relative fEPSP slopes increased significantly in the presence of Y27632 during the treatment with 4 mM penicillin and Mg^{2+}-free aCSF. There was also a trend towards increased fEPSP slopes in the presence of Y27632 compared to 4 mM penicillin and Mg^{2+}-free aCSF without Y27632 (Figure 38C). In contrast to the previous experiments with iGluSnFR-transfected mice (Figure 36), Mg^{2+}-free aCSF in addition to penicillin reliably evoked epileptiform discharges. However, the inhibition of astrocyte morphology changes by Y27632 had no impact on the discharge frequency (Figure 38D). This observation was surprising since the inhibition of the (ROCK)-signaling pathway had previously reduced the frequency of epileptiform discharges (Anders, 2016). Since these experiments were conducted in the presence of extracellular Mg^{2+}, it is not unlikely that the facilitated NMDAR activation in our experiments determined the discharge frequency in both conditions independently of astrocyte morphology changes. However, we would still expect increased glutamate accumulations or a prolonged decay of glutamate transients after epileptiform activity compared to control conditions if astrocyte morphology changes impaired the glutamate clearance. Conversely, such differences were expected to be smaller or absent when the astrocyte morphology changes were inhibited by Y27632.

In order to probe the impact of this type of astrocyte morphology changes on glutamate clearance, glutamate transients were evoked after the baseline period (before penicillin and Mg^{2+}-free aCSF were applied) and after the inhibition of AMPARs and NMDARs (Figure 38C-D). At both time points, the periphery of three to four astrocyte expressing iGluSnFR for each brain slice were imaged by a line scan in the CA1 str. radiatum (Figure 39A, left panel). In order to evoke glutamate release from presynaptic terminals, axons were stimulated repetitively with a sequence of 5 pulses at 20 Hz. This resulted in glutamate transients that manifested in five consecutive fluorescence increases in the line scan. Since the morphology changes have been shown to predominantly affect the fine astrocyte processes (Anders, 2016), the analysis was intended to focus on these processes. It was assumed that the fine processes exhibit lower basal fluorescence intensities compared to thicker astrocyte branches. Therefore, only lines that showed a basal fluorescence (before the onset of the glutamate transient) below the average basal fluorescence of all lines (Figure 39A, right panel) were used for further analysis. These lines were then averaged and resulted in a temporal glutamate profile as shown in Figure 39B. The glutamate profiles recorded in the same slice during the baseline condition were then pooled and compared to the pooled glutamate profiles after the epileptiform activity was terminated at the end of the experiment.

In order to investigate if the glutamate clearance was affected by the induction of epileptiform activity, the glutamate decay from the last peak back to basal levels was quantified by a monoexponentially decaying function. This provided information about how long the glutamate was present in the ECS. A longer decay time would indicate an inefficient glutamate removal and a prolonged presence of glutamate in the ECS. In turn, this could result in increased glutamate receptor activation and neuronal hyperexcitability. During the baseline period, the glutamate decay constants were similar in the three conditions ($p = 0.573$, one-way ANOVA). Interestingly, the decay constants of the glutamate transients were significantly smaller, i.e. decayed faster, during control conditions compared to the respective baseline. A similar trend was observed for the decay after epileptiform activity in the presence of Y27632. No significant difference was observed after the induction of epileptiform activity in the absence of Y27632 (Figure 39C). However, the change of the decay constants relative to their baseline levels was not different among the three conditions (Figure 39D), as well as the absolute decay constants (Control, 34.50 ± 3.89 ms, n = 7; Penicillin, 35.31 ± 2.74 ms, n = 6; Penicillin + Y, 27.87 ± 3.68 ms, n = 6; $p = 0.304$, one-way ANOVA).

These findings indicate that the glutamate clearance was accelerated compared to baseline in control conditions and when the astrocyte morphology changes were inhibited by Y27632, whereas this was not the case in the absence of Y27632. However, the observed changes were rather small and the absolute decay constants at the end of the experiment were similar in all experimental groups. Consequently, the previously observed persistence of the epileptiform activity at this time point (Anders, 2016) cannot be explained by a prolonged presence of extracellular glutamate.

In addition to the decay of the last glutamate peak, the glutamate accumulation was investigated by comparing the peak amplitudes evoked by the individual stimulation pulses. This provided information about amount of glutamate that accumulated during the stimulation. Increased peak amplitudes would indicate an impaired glutamate clearance or an increased glutamate release. These glutamate peaks were similar during the baseline period among the conditions ($p = 0.484$, two-way repeated measures ANOVA). However, the glutamate peak amplitudes were also not significantly altered after the induction of epileptiform activity compared to their respective baseline amplitudes in all conditions (Figure 39E).

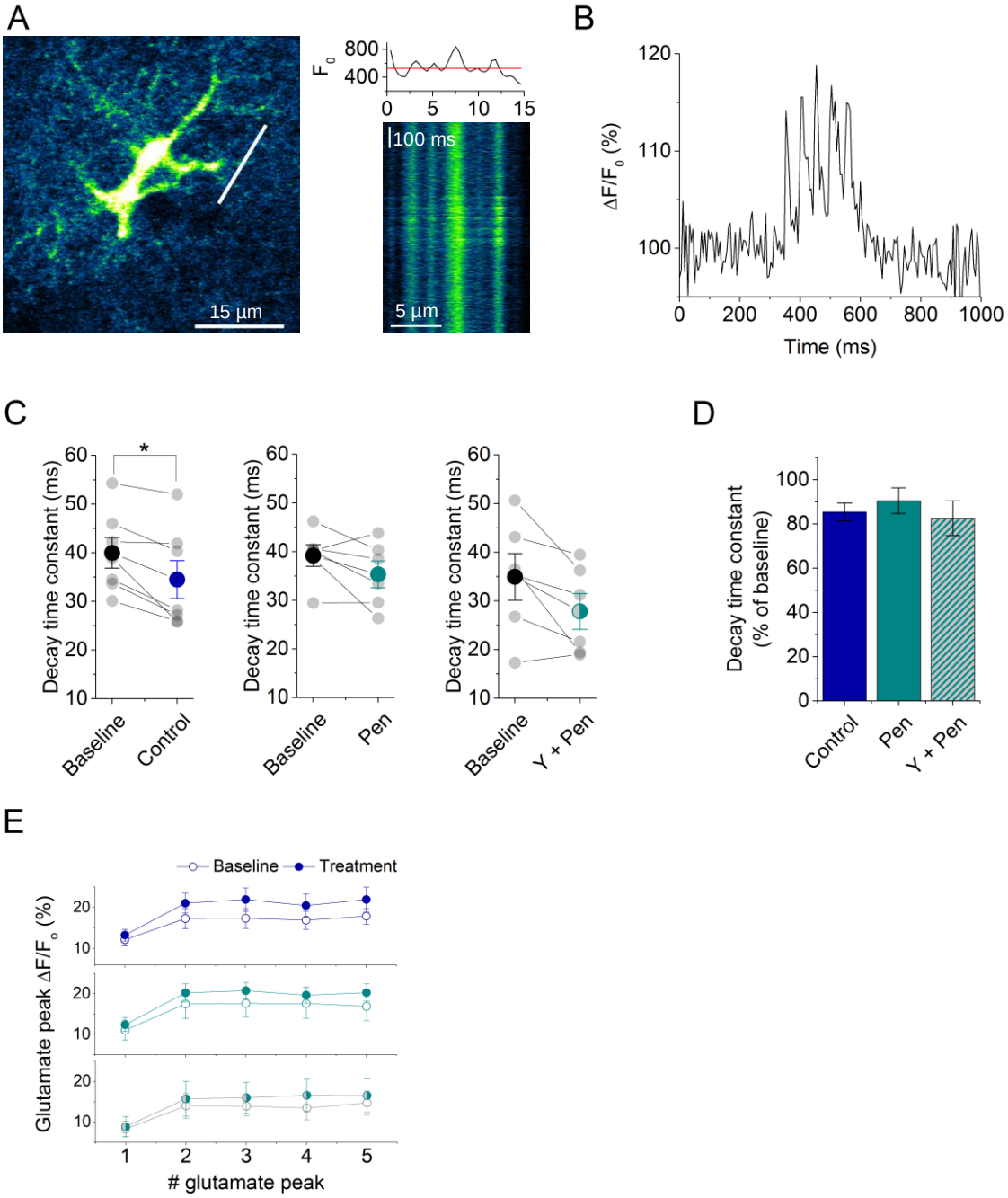

Figure 39 Astrocyte morphology changes had no impact on glutamate transients evoked by synaptic activity. A) Left panel: The periphery of an iGluSnFR-expressing astrocyte was imaged by a line scan (represented by the white line) and glutamate release was evoked by stimulating SCs with 5 pulses at 20 Hz. Right panel: The stimulation evoked glutamate transient that were represented by five fluorescence increases in the temporal line scan profile (Bottom). The top diagram depicts the basal fluorescence (before the onset of the stimulation) of each line (0.395 µm). For further analysis, only lines that exhibited a basal fluorescence intensity below the averaged basal fluorescence intensity of all line (represented by the red line) were used. **B)** Temporal glutamate profile of the averaged lines with a low basal fluorescence intensity. The glutamate profiles of the individual astrocytes in the same slice were then averaged for analysis. **C)** The decay of the glutamate transients was analyzed from their last peak back to basal levels by a monoexponentially decaying function. Compared to the respective transients imaged during baseline conditions, only glutamate transients during control conditions were significantly affected (Baseline, 39.98 ± 3.14 ms, Control, 34.50 ± 3.89 ms, n =

7, p = 0.0114; Baseline, 39.18 ± 2.22 ms, Penicillin, 35.31 ± 2.74 ms, n = 6, p = 0.152; Baseline, 34.97 ± 4.81 ms, Penicillin + Y, 27.87 ± 3.68 ms, n = 6, p = 0.0594, all tested with paired Student's t-test). **D)** The relative change of the decay constants compared to baseline was also not different among the conditions (Control, 85.39 ± 4.078 ms, n = 7; Penicillin, 90.49 ± 5.82 ms, n = 6; Penicillin + Y, 82.60 ± 7.84 ms, n = 6; p = 0.656, one-way ANOVA). **E)** The peak amplitudes of the evoked glutamate transients during the three conditions were not different compared to their respective baseline transients (Control, p = 0.293, n = 7; Penicillin, p = 0.511, n = 6; Penicillin + Y, p = 0.393, n = 6; all tested with two-way repeated measures ANOVA, no significant interaction). N represents the number of hippocampal slices.

In summary, extracellular glutamate clearance was investigated using two different approaches that employed either the artificial application of glutamate by an iontophoresis pipette or neuronal stimulation that led to synaptic glutamate release. Both experimental approaches, however, revealed no profound impairment of glutamate clearance after epileptiform activity. Actually, the glutamate accumulation rates of the iontophoretically evoked glutamate transients were slower after the epileptiform activity compared to control conditions (Figure 37E). However, this rather counterintuitive finding was accompanied by a large variability in the data set. In contrast, the analysis of the spatial glutamate profiles revealed a tendency towards a pronounced glutamate spread into the tissue after epileptiform activity (Figure 37D). Although the determination of the peak amplitude of the glutamate profiles was not possible in a subset of experiments (in both experimental conditions), this could point towards a facilitated glutamate spill-over and, in turn, contribute to the generation of epileptiform activity. On the other hand, epileptiform activity had also no impact on the peak amplitudes of extracellular glutamate transients evoked by synaptic activity. Their decay rate, however, seemed to accelerate compared to baseline in control conditions and when the astrocytic morphology changes were inhibited. Although this was not the case in when the astrocytic morphology changes were not inhibited, the absolute decay rates were similar among all conditions. Thus, an impaired glutamate clearance is not a major factor that can explain the persistence of epileptiform activity, which was observed previously at this time point. This is, however, in line with the previously observed stable fEPSP slopes (Figure 32C) since those indicated that the excitatory (glutamatergic) synaptic transmission was unaltered.

4.2.5 Conclusions

Previous experiments from our lab have revealed that the acute inhibition of inhibitory $GABA_AR$ and the concomitant epileptiform activity induced rapid astrocyte morphology changes. These resulted in a decreased intracellular volume and a reduced inter- and intracellular diffusivity. Interestingly, the altered astrocyte morphology and the epileptiform

activity persisted after the recovery of the inhibitory synaptic transmission. Preventing astrocyte morphology changes by inhibiting the Rho-associated protein kinase (ROCK)-signaling pathway resulted in attenuated epileptiform activity. This indicated that the rapid astrocyte morphology changes had a proepileptiform effect. However, the underlying mechanism of this effect remained to be investigated.

In the present study, we tested several possible candidates that could underlie the proepileptiform effect. As a part of the tripartite synapse (Araque et al., 1999), astrocytes modulate inhibitory synaptic transmission by the release of gliotransmitter (Mederos and Perea, 2019). This neuron-astrocyte interaction depends on the spatial arrangement of the fine astrocyte processes with the synapse. Therefore, we tested if the rapid astrocyte morphology changes, which were most prominent for the fine astrocyte processes (Anders, 2016), impaired inhibitory synaptic transmission. The experiments revealed that the frequency and amplitude of spontaneous inhibitory currents (sIPSCs) recorded in CA1 pyramidal neurons after epileptiform activity were not different from control conditions. However, the decay of the sIPSCs was significantly shorter after epileptiform activity. In addition, there was a trend towards smaller width of the sIPSCs after epileptiform activity. Both suggest a decreased inhibitory input onto CA1 pyramidal neurons, which might increase the neuronal excitability and promote the generation of epileptiform activity. Additional experiments are, however, required to provide further information about the inhibitory synaptic input after epileptiform activity.

The structure of the extracellular space has a direct impact on the extracellular accumulation and diffusion of ions and neurotransmitter. A shrinkage of the extracellular space was suggested to promote epileptiform activity by facilitating the extracellular accumulation of K^+ and glutamate (Kilb et al., 2006; Traynelis and Dingledine, 1989). On the other hand, also an increase of the ECS could promote epileptiform activity by attenuating the extracellular accumulation of inhibitory neuro- or gliotransmitter. Therefore, we tested by a TMA^+ diffusion analysis if the epileptiform activity had in impact on the extracellular space fraction. However, the extracellular space fraction during epileptiform activity was not different from control conditions. This indicates that the extracellular accumulation of K^+ or glutamate was not facilitated by an activity-dependent cellular swelling. Furthermore, the ECS was also not affected when the neuronal activity was inhibited. This suggests that also in the absence of potential activity-dependent cellular swelling, the shrinkage of the fine astrocyte processes had no significant impact on the ECS. This means that the proepileptiform effect of the astrocyte morphology changes cannot be explained by an altered ECS structure that affected the extracellular accumulation of neuroactive substances, such as K^+, glutamate or gliotransmitter.

We have further shown that the peak amplitude and the decay of extracellular K^+

transients were unaffected after epileptiform activity. These findings indicate that K^+ clearance was not impaired by the shrinkage of the fine astrocyte processes and the decreased intra- and intercellular diffusivity. This is in line with experiments that used the same experimental approach and revealed no impact on the extracellular K^+ clearance when the intracellular diffusivity was completely abolished (Breithausen et al., 2020).

Furthermore, the extracellular glutamate clearance was probed using two different experimental approaches. First, the iontophoretic application of glutamate as a point source revealed a slightly slower accumulation of glutamate after epileptiform activity. In contrast, the reached extracellular glutamate concentrations after epileptiform activity were not different from control conditions. Furthermore, we observed a tendency towards a pronounced spread of glutamate in to the ECS. Taken together, these findings could indicate that the local extracellular glutamate diffusion is facilitated after epileptiform activity and thus resulted in the pronounced spatial spread and the slowed accumulation. The increased extracellular glutamate spread could indicate a pronounced glutamate spillover that activates a larger number of synapses and thus facilitates neuronal activation. Although the TMA^+ diffusion analysis suggested unaltered extracellular molecule diffusion, alterations of the local and short-range diffusion in the micrometer range as it was the case for glutamate might be undetected (see chapter 5.2.2). The iontophoretic application of glutamate resulted in extracellular glutamate concentrations larger than 1 µM. Such concentrations were suggested to occur only when glutamate uptake is dramatically impaired (Zheng et al., 2008). Thus, it is possible that the glutamate transporters were already saturated in both experimental conditions by the large extracellular glutamate accumulations. As a consequence, the extracellular glutamate concentrations would be mainly determined by the amount of glutamate and thus would reach similar levels in both conditions.

The second approach employed synaptic activity to evoke extracellular glutamate transients. This had the advantage that the glutamate sources were directly at the synapses where glutamate would also be released during physiological conditions. Thus, the shrinkage of the fine astrocyte processes located at the synapses might have a more pronounced on the clearance of those glutamate transients. However, the peak amplitudes of the evoked glutamate transients were not affected by epileptiform activity. This indicates that the extracellular glutamate release and accumulation was not altered by epileptiform activity. This is in line with the unaltered fEPSP slopes during epileptiform activity, because they represent the excitatory (glutamatergic) synaptic transmission and would be affected by altered extracellular glutamate accumulations. In contrast, the decay rates of the extracellular glutamate transients were slightly reduced in control conditions compared to baseline. A similar trend was observed after epileptiform activity when the

astrocyte morphology changes were inhibited with Y27632 but not in the absence of Y27632. This indicates that the glutamate clearance was slightly accelerated in control conditions and when astrocyte morphology changes were inhibited over the experimental time course, but not in the presence of astrocyte morphology changes. However, the absolute decay rates were similar in the three tested conditions and thus cannot explain the persistent epileptiform activity that was previously observed at this time point.

In conclusion, the conducted experiments provided important information about different functions after epileptiform activity. Although most of the investigated parameters were not drastically impacted by the epileptiform activity, the experiments helped us to narrow down the list of possible candidates that could underlie the observed proepileptiform effect of astrocyte morphology changes. We revealed that spontaneous inhibitory currents decayed faster after epileptiform activity and thus could underlie the observed neuronal hyperexcitability. Therefore, further experiments on the inhibitory synaptic transmission might provide the missing link between the astrocyte morphology changes and their proepileptiform effect. In line with the largely unaffected extracellular K^+ and glutamate clearance, excitatory synaptic transmission quantified by the fEPSP slopes was unaltered by epileptiform activity. However, the action potential firing was amplified represented by an increased amplitude and number of population spikes. Therefore, it would also be interesting to investigate if the astrocyte morphology changes modulate the transformation of synaptic potential into neuronal activation.

5 Discussion

The knowledge about the role of astrocytes as an important regulator of many brain functions is continuously increasing (Sofroniew and Vinters, 2010). From being considered as just ‘nerve glue’ (Virchow, 1859), astrocytes emerged to be active contributors to neuronal communication as part of the ‘tripartite synapse’. This concept defines the fine astrocyte processes and pre- and postsynaptic terminal as a functional unit (Araque et al., 1999). By the expression of various ion channels, neurotransmitter receptors and transporters (Verkhratsky and Steinhäuser, 2000), astrocytes have been shown to be able to modulate synaptic transmission and plasticity. For instance, astrocytes are known to clear K^+ (Kofuji and Newman, 2004; MacAulay and Zeuthen, 2012; Walz, 2000) and glutamate (Danbolt, 2001; Rothstein et al., 1996) from the ECS and supply neurons with metabolites (Rouach et al., 2008). In addition, astrocytes release factors that influence the synapse formation or react directly to neuronal activity via intracellular Ca^{2+} signaling with the release of gliotransmitter (Halassa et al., 2007b; Perea et al., 2009; Volterra and Meldolesi, 2005). Another key feature of astrocytes is their formation of an extensive network via gap junction channels that allow intercellular trafficking of small molecules (Pannasch and Rouach, 2013). It has been proposed that this network supports the metabolite supply for neurons (Rouach et al., 2008), facilitates the clearance of extracellular K^+ and glutamate and limits cellular swelling (Pannasch et al., 2011, 2012; Wallraff et al., 2006). However, the majority of the studies investigating the functional role of the astrocyte network employed transgenic mice that were lacking the gap junction composing proteins Cx30 and 43. Indeed, gap junction coupling was absent in those mice, but it was also shown that astrocytes from mice deficient for Cx30 exhibit morphological changes. These include an increased synapse invasion of the fine astrocyte processes into the synaptic cleft and the polarization of astrocytes (Ghézali et al., 2018; Pannasch et al., 2014). This complicates statements about the pure channel function of astrocytic gap junctions and its significance of K^+ redistribution through the gap junction coupled astrocyte network or within a single astrocyte (Chapter 1.4.2), referred as ‘spatial K^+ buffering’ (Orkand, 1986; Orkand et al., 1966). Thus, the first part of this study investigated the impact of acute pharmacological gap junction uncoupling on the clearance of extracellular K^+ in order to avoid developmental adaptions and astrocyte morphology changes. The results of this part will be discussed in chapter 5.1.

Beside their role in physiological processes, astrocytes became also a target for investigating pathophysiological conditions, because there is raising evidence that malfunction of astrocytes is involved in neurodegenerative diseases, such as epilepsy (Bedner et al., 2015; Henneberger, 2017; Steinhäuser et al., 2015). Previous work by Dr.

S. Anders found a proepileptiform effect of astrocyte morphology changes in an acute epilepsy model (Chapter 1.6.1). However, the underlying mechanism of this proepileptiform effect remained unclear. Therefore, the second part of this study investigated the functional consequences of the rapid astrocyte morphology changes in the same model of epilepsy (Chapter 3.4.5). The results of the described experiments will be discussed in the chapter 5.2.

5.1 Contribution of gap junction coupling to the clearance of extracellular K^+

The concept that K^+ is carried from the site of elevated extracellular K^+ levels through electrically coupled cells to sites with a lower extracellular K^+ concentration was first introduced in a study that investigated the membrane potential of glial cells in the optic nerve of amphibians (Orkand et al., 1966). These findings were then later combined among others with those from experiments performed within the retina of the drone (Gardner-Medwin, 1983) and resulted in the concept of 'spatial K^+ buffering' (Orkand, 1986). It has been often hypothesized that 'spatial K^+ buffering' substantially facilitates the clearance of extracellular K^+ also in other brain regions, but the functional significance of this concept remains controversial (Kofuji and Newman, 2004; MacAulay and Zeuthen, 2012; Walz, 2000). However, there is evidence that the disruption of the astrocyte network mildly increased the amplitude of extracellular K^+ transients (Wallraff et al., 2006) and slowed astrocytic K^+ uptake currents (Pannasch et al., 2011) in the hippocampus. These studies were performed with mice exhibiting a genetic deletion of Cx30 and 43 and illustrate a common problem for investigating the functional role of astrocytic gap junction channels. In addition to the inhibited intercellular communication between those Cx-deficient astrocytes, a genetic deletion of Cx30 has been shown to affect the astrocyte polarity and the morphology of their fine processes in the hippocampus (Ghézali et al., 2018; Pannasch et al., 2014). Thus, it cannot be ruled out that these changes impacted on the K^+ clearance independently of the K^+ redistribution via gap junction channels.

In this study, the role of gap junctions as functional channels between astrocytes for the clearance of extracellular K^+ was explored using an approach to acutely uncouple the astrocyte network and exclude obstacles due to long-term adaptations induced by a gene knock-out (Chapter 4.1.1). For this purpose, the commonly used gap junction blockers, Meclofenamic acid (MFA) and Carbenoxolone (CBX), were employed in order to acutely inhibit the intercellular trafficking of molecules between astrocytes and within a single astrocyte via gap junction channels. For instance, MFA was shown to result in an almost

complete inhibition of the electrical and dye-coupling between Cx43 expressing cultured fibroblasts (Harks et al., 2001) as well as the dye-coupling of horizontal cells in the isolated retina (Pan et al., 2007). Also CBX was shown to inhibit the electrical and dye-coupling between cells, such as interneurons in the hippocampus (Zsiros and Maccaferri, 2005) and mitral cells of the olfactory bulb (Schoppa and Westbrook, 2002).

For probing the inhibition of the gap junction coupled astrocyte network, a dye-coupling approach was used in this study (Chapter 3.8.2), because it enables the quantification of several coupled astrocytes simultaneously and is less technically challenging compared to double patch-clamp recordings from two astrocytes. Furthermore, this technique has been considered as sensitive to changes in well coupled networks (Rozental et al., 2001). In line with the findings reported above, the treatment of hippocampal slices with MFA or CBX resulted in a significant reduction of the number of dye coupled astrocytes and strongly decreased the cumulative fluorescence intensity of the few remaining coupled cells (Figure 13).

In accordance to the 'spatial K^+ buffering concept', K^+ is redistributed in the astrocytic network by a net K^+ current that is conducted through the gap junction channels (Orkand, 1986). However, the analysis of the dye-diffusivity within the astrocytic network is only an indirect readout for the gap junction channel conductivity between single astrocytes. However, reproducing the dye-diffusion in the astrocyte network with a previously published model (Anders et al., 2014) revealed that our results can be explained by a near complete inhibition of coupling between individual astrocytes (Breithausen et al., 2020).

The dye-coupling approach also did not reveal the time course of the pharmacological gap junction uncoupling, i.e. it is not clear at which time point the observed decrease in coupling was achieved or if the uncoupling was still proceeding at the moment of imaging the dye-coupled network. No differences of the astrocytic resting membrane potential or resistance were found after 10 minutes of MFA or CBX treatment compared to control conditions (Figure 12). This indicates that the membrane properties of astrocytes were not affected by MFA or CBX. However, open gap junction channels are expected to increase the membrane conductivity and, in turn, decrease to the membrane resistance. Conversely, the inhibition of gap junction channels is expected to increase the membrane resistance, as it was revealed by biophysical modelling of astrocytes (Savtchenko et al., 2018) and by the genetic-deletion of connexin from astrocytes (Wallraff et al., 2006). In contrast, other studies found unaltered membrane resistances in coupling-deficient astrocytes (Pannasch et al., 2011; Wallraff et al., 2004).

These discrepancies might be explained by considering the following aspects. First, astrocytes gap junction coupling is likely to occur predominantly in the periphery and not at the soma. Second, astrocytes show a large resting K^+ conductance (Djukic et al., 2007;

Seifert et al., 2009) and thus cause an inefficient control over the membrane properties distant from the patch-pipette. Since the astrocytic membrane properties were determined by somatic recordings, the analysis provides rather information about the membrane properties close to the soma than about the periphery. As a consequence, the effect of acute gap junction uncoupling on the overall membrane resistance might be largely underestimated. Also the quality of the access to the cell cytoplasm via the patch-pipette influences the control over the astrocytic membrane properties and could underlie the discrepancies in the literature.

In summary, the presented inhibition of dye-coupling within the astrocyte network indicates that the treatment with 100 µM MFA or 50 µM CBX also reduced the electrical coupling, i.e. the trafficking of ions, such as K^+, between astrocytes within 10 minutes while minimizing developmental side effects. Importantly, there are, at least to my knowledge, virtually no reports about unspecific actions of MFA or CBX on astrocytes.

5.1.1 Clearance of K^+ transients that are associated with physiological neuronal activity

The next upcoming question was if the acute gap junction uncoupling affected the clearance of extracellular K^+ increases. Therefore, an experimental setup was employed that is commonly used to investigate hippocampal synaptic transmission (Chapter 4.1.2). A paired pulse stimulation of the SCs evoked axonal and synaptic activity that was accompanied by the release of K^+ into the ECS (Figure 14). This stimulation paradigm is commonly used to evoke neuronal activity that is assumed to represent physiological conditions. The corresponding extracellular K^+ transients had relatively small amplitudes (~0.1 mM). However, the gap junction uncoupling with 200 µM MFA in hippocampal slices from juvenile and adult animals did not affect the decay and peak amplitude of the evoked K^+ transients. These findings point towards an insignificant role of gap junction coupling for the clearance of extracellular K^+ in the CA1 str. radiatum during those experimental conditions.

This could be explained by the small K^+ transient peak amplitudes and the corresponding relatively small amount of released K^+. The basic idea of spatial K^+ buffering is a membrane depolarization-accompanying K^+ current that distributes the accumulated K^+ via the cytoplasm and, if so, through gap junctions to sites exhibiting a lower membrane potential (Orkand, 1986). Thus, a requirement for the involvement of gap junctions in this scenario would be a membrane area affected large enough to reach gap junction channels. If the extracellular amount of K^+ is not sufficient to evoke a substantial membrane depolarization that exhibits an adequate length constant (i.e. spatial spread),

inhibition of gap junction coupling would have no effect. It was reported that the average distance between astrocytic gap junction channels is 1-1.2 µm in the barrel cortex (Genoud et al., 2015). Considering the same for hippocampal astrocytes, spatially distributed local K^+ sources (e.g. induced by active single synapses) that dissipate within a micrometer range between astrocytic gap junction channels would be unaffected by acute uncoupling. Therefore, it has to be considered that for the clearance of these small extracellular K^+ transients other uptake mechanisms or simple extracellular diffusion were rather involved.

These experiments were performed in hippocampal slices obtained from juvenile and adult rats in order to probe if gap junction coupling differently affects K^+ clearance during aging. It is assumed that a reduction of ECS fraction observed during aging (Syková et al., 1998, 2002) impairs the extracellular diffusion and leads to a facilitated accumulation of neuroactive substances and ions, such as K^+ (Syková, 2004; Syková and Nicholson, 2008). Surprisingly, there was no difference of the evoked K^+ accumulations between hippocampal slices obtained from juvenile and adult animals. There are at least two possible explanations for this observation. First, the impact of the age-dependent reduction of the ECS on the extracellular accumulation of relatively small amount of K^+ might be too marginal to be detected. Second, the K^+ clearance mechanisms also adapt during aging to the reduced ECS fraction and, in turn, limit K^+ accumulation.

Since neuronal activity and extracellular K^+ are mutually affecting each other, it was also analyzed if the synaptic transmission was affected by the gap junction uncoupling or by potential side effects of MFA. Although there are a few side effects of MFA, such as opening KCNQ2/3 potassium channels (Peretz et al., 2005) and modulation of $GABA_AR$ (Woodward et al., 1994), reported in the literature, the synaptic transmission was not affected by the treatment with MFA, except for a small change of the paired-pulse ratio in hippocampal slices from juvenile animals. Also interneurons are coupled via gap junction channels (Connors and Long, 2004; Fukuda and Kosaka, 2000; Kosaka and Hama, 1985) and were, in turn, presumably also affected by MFA. A potential increased interneuron activity would, for instance, attenuate neuronal activity and, in turn, lead to a reduced activity-dependent K^+ release. This could counteract increased extracellular K^+ accumulation that were mediated by a potential impaired extracellular K^+ clearance and thereby mask an effect of acute uncoupling of astrocytic gap junctions. However, the unaffected fEPSP amplitudes indicate that the evoked neuronal activity was not altered upon MFA application. In summary, these experiments indicate that the gap junction coupling does not contribute to the clearance of extracellular K^+ transients in the low sub millimolar range in the CA1 str. radiatum during these conditions. Such extracellular K^+ elevations are generally observed during physiological activity, such as light-evoked

activity in the visual cortex (Connors et al., 1979) or activity in the spinal cord after skin-stimulation (Heinemann et al., 1990).

The next question emerging from these findings was if gap junction coupling is involved in the clearance of larger extracellular K^+ loads (Chapter 4.1.3). Considering that larger extracellular K^+ accumulations would also affect a larger membrane area, astrocytic gap junction coupling might have a more pronounced role in limiting the local membrane potential. Thus, a stronger stimulation protocol was used in the following experiments in order to evoke K^+ transients of larger peak amplitude. Interestingly, Wallraff and colleagues found in hippocampal slices obtained from mice lacking astrocytic Cx43 and Cx30 that K^+ transients evoked by strong alvear stimulation showed increased peak amplitudes in the CA1 str. pyramidale. This was found for K^+ transients with peak amplitudes of several millimolar and in the sub millimolar range evoked by paired pulses and a pulse train, respectively, but only when the maximal number of CA1 neurons was activated. The authors concluded that a sparse activation of CA1 neurons could evoke K^+ release distant from the recording site and that the following K^+ diffusion towards the recording site attenuates the increased K^+ transient peak amplitudes (Wallraff et al., 2006). Thus, Schaffer collaterals were stimulated with a HFS at a stimulation intensity that activated the maximal number of axonal fibers in order to evoke K^+ release close to the recording site. Since this kind of HFS (100 Hz for 500 ms) is commonly used to induce and investigate synaptic plasticity, AMPAR and NMDAR inhibitors were present in order to prevent uncontrolled changes of the stimulated cells and, in turn, K^+ release. Consequently, K^+ was only released from axons and presynaptic compartments, whereas the post synaptic compartments, which are considered as the main source of activity-evoked K^+ release (Poolos et al., 1987), were silenced. However, this stimulation was sufficient to evoke K^+ transients in the CA1 str. radiatum with peak amplitudes several times larger compared to the previous experiments (Figure 15). Although larger compared to the previous experiments, the extracellular K^+ elevations were similar to those observed during physiological conditions (Rasmussen et al., 2019).

Again, the experiments were performed in hippocampal slices obtained from juvenile and adult animals in order to test for an age-dependent effect of gap junction uncoupling. In contrast to the previous experiments using MFA, CBX was used in order to acutely inhibit gap junction coupling, because it was shown in previous experiment from our laboratory to increase stimulus-induced astrocyte depolarization (Bedner et al., 2015). Interestingly, axonal activity and the corresponding K^+ transients evoked in hippocampal slices obtained from the juvenile animals were unaffected by the CBX treatment, whereas FV amplitudes and the corresponding K^+ transient peak amplitudes were significantly increased in hippocampal slices from adult animals. This suggests that, at least in the CA1 str.

radiatum, the amount of activated fibers did not determine if an effect of gap junction uncoupling on K^+ clearance is observed, because the stimulation activated the same maximal number of fibers (similar FV amplitudes) in both age groups. However, it needs to be emphasized that the str. radiatum and pyramidale differ significantly in their structure. Whereas K^+ transients in the str. pyramidale are predominantly recorded close to the somata of pyramidal neurons, K^+ transients in the str. radiatum are recorded in the proximity of much smaller structures, such as axons, dendrites and astrocyte processes. If and to which degree the structure of the CNS influences K^+ clearance remains speculative.

Counterintuitively, the K^+ accumulations were smaller in hippocampal slices from adult compared to juvenile animals despite their reported reduced ECS fraction (Syková and Nicholson, 2008). This surprising finding might indicate that an age-dependent reduction of the ECS does not per se facilitate extracellular K^+ accumulation, but also other mechanism that shape extracellular K^+ transients, such as activity-dependent K^+ efflux, are affected during aging. Interestingly, similar was found for stimulation-induced K^+ rises in the CA1 str. pyramidale of rat hippocampal slices and was suggested to depend on the maturation state of astrocytes (Nixdorf-Bergweiler et al., 1994).

Nevertheless, the increased FV and K^+ peak amplitudes in hippocampal slices of adult animals after CBX-treatment could indicate that gap junction uncoupling under these conditions impaired K^+ clearance, facilitated extracellular K^+ accumulation and, in turn, increased axonal excitability. However, broadening of action potentials is a known gap junction-independent effect of CBX on neurons as shown in neuronal-astrocyte cocultures (Tovar et al., 2009). Consequently, the described scenario is not distinguishable from CBX directly increasing axonal excitability, facilitating the recruitment of axons and thereby evoking increased K^+ transients independently of gap junction uncoupling. In contrast, a different study on neurons cocultured with astrocytes indicated a CBX induced increase of their action potential threshold and a decreased spike rate (Rouach et al., 2003). It has also been shown that CBX had no impact on intrinsic membrane properties of CA3 and CA1 pyramidal neurons in acute rat hippocampal slices (Köhling et al., 2001; Schmitz et al., 2001) and interneurons of hippocampal slices prepared from guinea pig (Yang and Michelson, 2001). In summary, although there are many more studies (Connors, 2012; Rouach et al., 2003; Tovar et al., 2009; Travagli et al., 1995; Vessey et al., 2004) investigating the action of CBX with various approaches and arguing for and against gap junction-independent effects of CBX, it remains uncertain if the observed effects in the present study were gap junction independent. It is also not clear how a potential gap junction-independent action of CBX would affect axons in hippocampal slices from adult animals but not from juvenile. Interestingly, the FV amplitudes further increased in

hippocampal slices from adult rats after the treatment with CBX although the stimulation intensity was adjusted to elicit the maximal FV amplitude already during baseline conditions. One possible explanation is that the same number of axons might be activated more synchronously due to the K^+-induced increased excitability or a direct effect of CBX (e.g. on the action potential threshold) and thereby led to the increased FV amplitudes.

Taken together, peak amplitudes of K^+ transient in the sub millimolar range increased exclusively in hippocampal slices obtained from adult animals when evoked over a period of 500 ms by a HFS. However, the decay of the K^+ transient was unaffected by acute gap junction uncoupling. This is in agreement with studies that impaired spatial K^+ buffering by acute inhibition of the Kir4.1 channel, a proposed requirement for passive K^+ uptake during K^+ buffering. This resulted in augmented peak amplitudes of extracellular K^+ transients, but had no effect on their decay back to basal levels (Jauch et al., 2002; Larsen et al., 2014). Thus, our results support that astrocytic gap junction channels facilitate spatial K^+ buffering during the accumulation phase of extracellular K^+ and the decay is mainly mediated by the Na^+/K^+-ATPase (D'Ambrosio et al., 2002; Larsen and MacAulay, 2014; Larsen et al., 2014; Ransom et al., 2000).

Since the experiments performed so far revealed only a small impact of acute gap junction uncoupling on the K^+ peak amplitudes, an emerging question was if the experimental conditions itself would prevent the establishment of spatial K^+ redistribution. A postulated requirement for spatial K^+ redistribution is an extracellular concentration gradient of K^+ that evokes differences in the local membrane potential of the astrocyte and, in turn, creates a driving force for the electrotonic spread of K^+ from sites of elevated extracellular K^+ to distant sites with a lower extracellular K^+ concentration (Orkand, 1986). Thus, a homogenous elevation of the extracellular K^+ concentration could prevent such a driving force and consequently also the establishment of the required K^+ currents. Considering the highly collateralized axons of CA3 pyramidal cells (Schaffer collaterals) pervading the CA1 str. radiatum and their corresponding synapses on the elongated dendrites of pyramidal neurons (Andersen et al., 2007), it cannot be excluded that their synchronous activation led to a extracellular K^+ elevation over a large area in the str. radiatum. However, the exact spatial-temporal extracellular K^+ dynamics elicited by the used stimulations remain speculative since KSMs only record the K^+ concentration at a single point without providing any spatial resolution.

To summarize, the experiments described so far revealed that the clearance of small extracellular K^+ elevations were unaffected or only slightly affected by acute gap junction uncoupling. Since such extracellular K^+ elevations are commonly observed during physiological neuronal activity (Connors et al., 1979; Heinemann et al., 1990; Rasmussen et al., 2019), it can be concluded that astrocytic gap junction coupling play an insignificant

role during physiological conditions or experimental approaches commonly used for probing hippocampal physiology. These findings could be explained when the stimulation-induced synaptic activity in our experiments evoked small, local and spatially-distributed extracellular K^+ elevations that dissipate within a few micrometers in the ECS. Consequently, the extracellular K^+ concentration might return to basal levels within micrometers and only affects a small astrocyte membrane area without/only a few gap junction channels. In such a scenario, acute astrocytic gap junction inhibition would not affect the clearance of the extracellular K^+. Importantly, this does not exclude that K^+ is spatially redistributed along the extracellular K^+ concentration gradient, but very locally without gap junction channels involved. Other active K^+ uptake mechanism (e.g. Na^+/K^+-ATPase) might also be involved. On the other hand, when the employed strong axonal high-frequency stimulation evoked extracellular K^+ elevations over a large-area, an extracellular K^+ concentration gradient would be less prominent. Consequently, K^+ would be less efficiently redistributed via astrocytic gap junction channels and their acute uncoupling inhibition would have less effect on the K^+ clearance.

5.1.2 Iontophoretically evoked K^+ transients of different amplitudes

The previous experiments have found that acute inhibition of gap junction coupling slightly augment the peak amplitude of extracellular K^+ transients and the corresponding axonal activity. However, the two following aspects could have influenced these observations. First, unspecific side-effects of CBX might have increased neuronal excitability, led to the increased axonal activity and, in turn, to the augmented extracellular K^+ transients independently of astrocytic gap junction uncoupling. Second, the strong axonal stimulation might have evoked homogenous extracellular K^+ elevations in the tissue and thereby impaired the K^+ redistribution assisted by astrocytic gap junction channels. Consequently, the impact of acute gap junction coupling on the clearance of extracellular K^+ transients would be underestimated.

Thus, the next question was if the clearance of extracellular K^+ accumulations were controlled by a gap junction-dependent mechanism when simultaneous extracellular K^+ elevations over a large area were prevented. In order to investigate this, K^+ transients were no longer evoked by neuronal activity, but by the iontophoretic application of K^+ directly into the ECS. This approach also enabled the investigation of extracellular K^+ transients by drastically reducing potential side effects of CBX on neuronal activity and, in turn, on K^+ release since neuronal activity was virtually absent during these experiments (inhibition of AMPARs, NMDARs and voltage-gated Na^+ channels). In contrast to evoking K^+ transients by neuronal activity, the iontophoretic K^+ application allowed to control the

amount of applied K^+ as a point source at a known location and resulted reliably in a K^+ concentration gradient in the ECS. By adjusting the amplitude and length of the application current, the amount of applied K^+ and, in turn, the amplitude of the evoked K^+ transients was regulated. Before using this approach to test the impact of acute gap junction uncoupling on K^+ clearance, the two following issues were addressed.

First, the spatial spread of the applied K^+ in the ECS was determined (Chapter 4.1.4). This revealed that extracellular K^+ concentration in the CA1 str. radiatum declined on average by 63.2% (decay constant τ) over a distance of ~13 µm independently of the amount of applied K^+ (Figure 17). This provided an estimation about the potential number of astrocytes with direct contact to the applied K^+ considering the following. Astrocytes in the CA1 str. radiatum have been found to occupy exclusive territories with only a small overlap to neighboring astrocyte territories (Bushong et al., 2002) and show a polar orientation, i.e. astrocytes orientate their larger branches and territory parallel to the pyramidal cell apical dendrites. Accordingly, astrocyte span their larger branches over a distance of approximately 100 µm in perpendicular to the str. pyramidale, but much less in parallel as shown in rat hippocampal slices (Anders et al., 2014; Nixdorf-Bergweiler et al., 1994). Considering astrocyte territories as spherical with a mean area of ~3320 μm^2 as reported for hippocampal slices obtained from adult mice (Ogata and Kosaka, 2002), the maximal distance to the territory boundaries within such a territory from the K^+ source is ~32 µm. Incorporating the polar astrocyte orientation in the CA1 str. radiatum would even further reduce the minimal distance to the next astrocyte. Importantly, no difference in the territory area of mouse and rat hippocampal astrocytes were reported (Ogata and Kosaka, 2002). Therefore, it can be estimated that the iontophoretically applied K^+ spread across the territory boundaries into at least one neighboring astrocyte since the K^+ concentration is at least ~8.5% of its initial amplitude at a distance of 32 µm.

Second, it was tested if the spatial spread was direction-dependent, i.e. if the diffusion of the applied K^+ was facilitated in the perpendicular or parallel direction to the str. pyramidale, for the following reasons. The extracellular diffusion of ions has been shown to be anisotropic in the CA1 str. radiatum as shown with the real-time TMA^+-iontophoresis approach. It was argued that the orientation of the SCs in the CA1 str. radiatum favor the diffusion in parallel to the str. pyramidale (Mazel et al., 1998; Syková and Vargová, 2008). In addition, it was shown that astrocyte coupling is anisotropic in the CA1 str. radiatum, i.e. astrocytes located close to the str. pyramidale were coupled preferentially in parallel to the pyramidal cell layer, while astrocytes located more distal coupled preferentially perpendicular to the pyramidal cell layer (Anders et al., 2014). Accordingly, the extracellular K^+ diffusion could be shaped if gap junction were involved in the clearance of the extracellular K^+. However, no such anisotropic diffusion was observed for the

iontophoretic applied K^+ during these experimental conditions. Although this finding contrasts the observed diffusion anisotropy for TMA^+ in the CA1 str. radiatum, it has to be considered that TMA^+, in contrast to K^+, is almost not cleared from the ECS (Nicholson and Phillips, 1981; Nicholson and Syková, 1998) and, hence, might be more affected by the structure of the ECS. Furthermore, compared to the relatively long-lasting application of TMA^+ (1 minute) in these studies, K^+ was applied here over a much shorter duration and diffused not that far into the ECS. Thus, the local ECS structure (e.g. depending on the local cellular structures, such as blood vessels or dendrites, which are not necessarily anisotropic) close to the K^+ source might rather affect the local diffusion of K^+ than the general diffusion anisotropy of the CA1 stratum radiatum.

Taken together, the iontophoretic K^+ application provides an interesting approach to study the extracellular K^+ clearance with the following advantages. First, the amount of applied K^+ can be controlled by adjusting the amplitude and duration of the iontophoretic application current. Second, the initiation site of the corresponding K^+ transient is known. Finally, the K^+ application as a point-source resulted in a reliable K^+ concentration gradient in the ECS that is likely to spread over the territory border of a single astrocyte and, in turn, gap junction channels between adjacent astrocytes and reflexive gap junction channels.

In the following experiments, the impact of acute gap junction uncoupling was investigated using the just described approach (Chapter 4.1.5). First, K^+ transients of relatively small peak amplitude, similar to those evoked by the HFS of SCs, were evoked by the iontophoretic K^+ application (Figure 18). However, no significant impact of acute gap junction uncoupling on the peak amplitude of those evoked K^+ transients was found. Since the K^+ transients were recorded at varying distances to the K^+ source and, in turn, with different basal peak amplitudes, it was tested if one of these factors determined if gap junction coupling was involved in their clearance. For instance, it could be possible that an effect of gap junction uncoupling becomes more pronounced the more gap junction channels were located between K^+ source and the recording site, because the contribution to the recorded K^+ transient would be larger. Consequently, the impact of gap junction uncoupling on K^+ transients would be expected to increase with increasing distance to the K^+ source. In contrast, it could be argued that gap junction coupling only contributes to K^+ clearance by limiting substantial astrocytic membrane depolarization induced by large extracellular K^+ loads. Accordingly, gap junction uncoupling would have a larger impact on K^+ transients with larger peak amplitudes. Thus, an impact of gap junction uncoupling on K^+ transients would be positively correlated with their basal peak amplitude and, in turn, negatively with the distance to the K^+ source. However, no such correlations were found for the iontophoretically evoked small K^+ transients. This indicates

that gap junction coupling is not involved in the clearance of small iontophoretically-evoked K^+ transients. Consequently, these findings support the previous conclusion that astrocytic gap junction coupling does not facilitate the clearance of extracellular K^+ elevations with peak amplitudes in the low millimolar range.

The K^+ transients investigated so far exhibited peak amplitudes similar to those found in vivo during physiological conditions. For instance, extracellular K^+ increases in the sub to low millimolar range were observed in the motor and visual cortex of mice upon running onset (Rasmussen et al., 2019), the visual cortex of cats after light stimulation (Connors et al., 1979; Singer and Dieter Lux, 1975) and in the spinal cord of cats during an innocuous stimulation of the skin and movement of their leg (Heinemann et al., 1990). In contrast, extracellular K^+ elevations up to 10 mM were recorded during ictal activity in the cortex (Moody et al., 1974) and hippocampus (Fisher et al., 1976) of epileptic cats. It has often been argued that impaired K^+ clearance contributes to the accumulation of such large extracellular K^+ loads and thereby facilitates neuronal excitability during those pathophysiological conditions. Indeed, it was shown that Kir4.1-mediated K^+ clearance mechanisms were absent in sclerotic hippocampal slices obtained from epileptic rats and from patients suffering from epilepsy (Heinemann et al., 2000; Jauch et al., 2002; Kivi et al., 2000). Experiments with slices obtained from non-epileptic rodents further revealed that Kir4.1 is involved in the clearance of extracellular K^+, because the pharmacological inhibition and astrocyte-specific genetic deletion, respectively, of these channels facilitated extracellular K^+ accumulation (Jauch et al., 2002; Larsen et al., 2014). It was argued that the passive K^+ uptake via Kir4.1 channel is required for spatial K^+ buffering (Kofuji and Newman, 2004; Larsen and MacAulay, 2014). However, spatial K^+ buffering, i.e. the spatial redistribution of K^+ from sites with an elevated extracellular K^+ concentrations ('active') to those with a lower extracellular K^+ concentrations ('resting'), can also occur when active and resting astrocytic domains are efficiently connected without gap junction channels. Thus, the acute inhibition of Kir4.1 channel provide important information about the K^+ uptake important to establish spatial K^+ buffering, but do not provide information about the role of astrocytic gap junction channels. On the other hand, astrocytes in sclerotic hippocampi from epilepsy patents were found to be devoid of gap junction coupling and, thus, proposed to be proepileptiform through an ineffective clearance of extracellular K^+ (Bedner et al., 2015). Therefore, the next aim was to investigate if gap junction uncoupling affect K^+ transients that were generally associated with pathophysiological conditions.

For this purpose, the iontophoretic current amplitude and duration were increased in order to evoke K^+ transients with larger peak amplitudes of up to ~30 mM (Figure 20) (Chapter 4.1.5). Thus, the extracellular K^+ concentration partly exceeded the described ceiling level

of ~11 mM during seizure activity and prolonged electrical stimulation, respectively, in the cat cortex (Heinemann and Lux, 1977) and even reached concentrations that were recorded during spreading depression (Somjen, 2001; Theis et al., 2003). During conditions of inhibited gap junction coupling, the peak amplitudes of these K^+ transients then significantly increased compared to control conditions. This indicates that the clearance of large extracellular K^+ transients, in contrast to the small K^+ transients described before, was facilitated by gap junction coupling. Accompanying the increase of the K^+ peak amplitudes during acute gap junction uncoupling, K^+ transients recorded during control conditions tend to decrease their peak amplitudes. A simple explanation would be a clogging of the iontophoresis pipette by particles from the back-fill solutions or a slight decrease of K^+-sensitive microelectrodes sensitivity for K^+. Another potential explanation could be a K^+ clearance mechanism increasing its efficiency over time. For instance, elevations of the extracellular K^+ concentration have been shown to increase the coupling between astrocytes in culture (De Pina-Benabou et al., 2001; Enkvist and McCarthy, 1994) and in acute slices obtained from mouse olfactory glomeruli. Accordingly, it was argued that extracellular K^+ elevations could facilitate their clearance by mediating increased astrocytic coupling and, in turn, an increased spatial buffering efficiency (Roux et al., 2011). If this mechanism was also induced by the repetitive K^+ applications used in this study and caused the slight decrease of the K^+ peak amplitudes remains to be tested. This could be done by repeating the experiments in control conditions without the repetitive injection of K^+ via the iontophoresis. Instead, K^+ transients will be evoked only a few times at the beginning of experiment and after 15-20 minutes. As a consequence, gap junction coupling should not be affected and no reduction of the K^+ peak amplitudes should be observed. However, it was assumed that the underlying effect was also present in the experimental group treated with CBX and, in turn, attenuated the observed effect of acute gap junction uncoupling on the K^+ peak amplitudes. The comparison of the relative peak amplitude changes between CBX and control conditions was therefore considered to be the best for quantifying the effect of acute gap junction uncoupling.

Interestingly, the gap junction uncoupling mediated increase of K^+ peak amplitudes was most prominent for K^+ transients recorded close to the K^+ application site and for those with the largest initial peak amplitudes. Since the initial peak amplitude of K^+ transients was largely affected by the recording distance to the K^+ application site, it was investigated which of these parameters was critical to mediate gap junction dependent K^+ clearance. Further analysis revealed that small K^+ transients recorded close to the K^+ source (< 15µm) were virtually unaffected by gap junction uncoupling, whereas large K^+ transients showed significantly increased peak amplitudes (Figure 24). This suggests that

the amount of applied K^+ and, in turn, the K^+ peak amplitude of the corresponding K^+ transient determined if gap junctions were involved in their clearance. The causal role of gap junction uncoupling for the increased peak amplitudes of large K^+ transients was then further supported by reproducing this effect with MFA instead of CBX (Figure 23). Interestingly, the peak amplitudes of large and local K^+ transients were similarly increased (~30%) by the treatment with CBX and MFA. In contrast to the previous experiments (Chapter 4.1.1 & 4.1.2), the MFA stock solution was prepared with DMSO (final concentration in the aCSF: 0.2%) since the used MFA batch was not completely dissolving in H_20. However, it was reported that K^+ uptake of reactive astrocyte in rat hippocampal slices was not affected by even 1% DMSO in the aCSF (Walz and Wuttke, 1999). Since there are, at least to my knowledge, no reports about the direct action of DMSO on extracellular K^+ clearance, DMSO is not likely to cause of the observed effect. Taken together, this strongly suggests that astrocytic gap junction uncoupling, a shared effect of MFA and CBX, induced the increased peak amplitudes rather than a gap junction independent side effect of both drugs.

The experiments conducted indicate that larger K^+ transients were rather affected by acute gap junction uncoupling than smaller K^+ transients. The emerging question from this finding was then at which extracellular K^+ concentration gap junctions contribute to K^+ clearance. Therefore, K^+ transients with increasing peak amplitudes were evoked before and after acute gap junction uncoupling (Figure 25 & Figure 27) (Chapter 4.1.6). These experiments showed that the peak amplitudes of K^+ transients were significantly increased by gap junction uncoupling provided that their basal peak amplitudes exceeded ~10-15 mM. This indicates that gap junction coupling is involved in limiting the accumulation of extracellular K^+ loads that are generally associated with pathophysiological conditions. In contrast, K^+ transients that are observed during physiological conditions are not controlled by gap junction mediated spatial buffering. These findings suggest that K^+ clearance of small extracellular K^+ loads is mainly mediated by gap junction-independent mechanisms, such as the Na^+/K^+-ATPase. When these mechanisms are saturated and are unable to cope with the large extracellular K^+ loads, K^+ redistribution assisted by gap junction channels sustain K^+ uptake and thereby limit the extracellular K^+ accumulation. These considerations could explain the observed specific effect of acute gap junction uncoupling on extracellular K^+ transients with large peak amplitudes exceeding 10-15 mM.

5.1.3 Decay of iontophoretically evoked K^+ transients

In addition to the impact of gap junction uncoupling on the peak amplitudes, the decay of the K^+ transients was investigated. However, the decay of the K^+ transients was

unaffected by acute gap junction inhibition in all conducted experiments and supports the general idea that the return to basal extracellular K^+ levels is not mediated by spatial K^+ buffering. This idea is based on previous experiments employing the acute inhibition of Kir4.1 channels, the predominant astrocytic K^+ channel (Seifert et al., 2009) and proposed key contributor to spatial K^+ buffering currents by mediating the in- and efflux of K^+ (Ballanyi et al., 1987; Karwoski et al., 1989). For instance, the acute inhibition of Kir4.1 channels by Ba^{2+} had no effect on the decay of extracellular K^+ transients evoked by neuronal activity in the in the CA3 (D'Ambrosio et al., 2002) and CA1 region of the hippocampus (Larsen et al., 2014; Meeks and Mennerick, 2007), in the dentate gyrus (Xiong and Stringer, 2000) and in the rat optic nerve (Ransom et al., 2000). On the other hand, inhibition of Kir4.1 channels was shown to increase the peak amplitude of iontophoretically evoked extracellular K^+ transients (Jauch et al., 2002; Larsen et al., 2014). These findings together with the increased K^+ peak amplitudes after gap junction uncoupling observed in this study, indicate that spatial K^+ buffering limit the accumulation of K^+ in the ECS during the K^+ application phase. This has been already suggested by Larsen and MacAuly based on the observations made by Karwoski and colleagues in the amphibian retina. There, light-evoked extracellular K^+ elevations in the inner plexiform layer were redistributed into the vitreous humor through the Müller cell in a Ba^{2+}-sensitive manner ('K^+ siphoning') only during the light pulse, i.e. the phase of extracellular K^+ accumulation but not during the decay phase (Karwoski et al., 1989; Larsen and MacAulay, 2014). This is in line with previous studies that report the Na^+/K^+-ATPase as the predominant mediator for the decay of extracellular K^+ transients back to basal levels in the hippocampus (D'Ambrosio et al., 2002; Larsen et al., 2014) and optic nerve (Ransom et al., 2000).

In contrast, it needs to be mentioned that slowed K^+ decay rates in the brain stem and hippocampus of mice with a astrocyte specific Kir4.1 deletion were reported in vitro (Haj-Yasein et al., 2011; Neusch et al., 2006) and in vivo (Chever et al., 2010). However, it was argued that the side-effects induced by the Kir4.1 deletion such as smaller brains and stress-induced seizures (Djukic et al., 2007) complicate the interpretation of these findings (MacAulay and Zeuthen, 2012).

In summary, our findings strongly support that spatial K^+ redistribution assisted by astrocytic gap junction channels do not contribute the recovery of extracellular K^+ elevation back to basal concentration levels. On the other hand, astrocytic K^+ uptake currents and the decay of extracellular K^+ transients was slowed in hippocampal slices with an astrocyte-specific deletion of Cx30 and 43 (Pannasch et al., 2011; Wallraff et al., 2006). However, it is not clear if the altered polarization and fine process morphology reported for Cx30-deficient astrocytes (Ghézali et al., 2018; Pannasch et al., 2014) were

underlying the slowed decay rates rather than the gap junction uncoupling. Taken together, the absent effect of acute gap junction uncoupling on the K^+ transients' decay is in accordance with the emerging picture from the literature and the proposed minor role for (Kir4.1-mediated) spatial K^+ buffering (Larsen and MacAulay, 2014; MacAulay and Zeuthen, 2012).

Importantly, the decay characteristics observed for the extracellular K^+ transients in this study were similar to those found previously (Strohschein et al., 2011; Wallraff et al., 2006). For the iontophoretically evoked K^+ transients, three major characteristics were found. First, the decay of small K^+ transients was best fitted by a single exponential function whereas the decay of larger K^+ transients was best fitted by a biexponential function. Second, the fast component of the biexponential decay function became more prominent with increasing peak amplitude of the corresponding K^+ transient. Third, increasing K^+ transient peak amplitudes were accompanied by accelerated decay rates.

These findings are generally in line with previous studies that addressed extracellular K^+ clearance with different approaches in various conditions. For instance, K^+ transients in the str. pyramidale of mouse hippocampal slices evoked by an alveus stimulation exhibited decreased decay rates with increasing peak amplitudes (Strohschein et al., 2011; Wallraff et al., 2006). Indeed, the Na^+/K^+-ATPase of cultured astrocytes was shown to increase its activity with increasing extracellular K^+ concentrations until a steady state was reached at 12 mM (Rose and Ransom, 1996; Walz and Hertz, 1982). Thus, the observed negative correlation of the decay rates and the peak amplitude of K^+ transients (< 12 mM) evoked by weak K^+ injections (800 nA for 200 ms) could be explained by the increasing astrocytic Na^+/K^+-ATPase activity. Also, the fast decay rate of K^+ transients evoked by strong K^+ injections (900 nA for 500 ms). Interestingly, the amplitude dependent acceleration of the fast decay rate was most prominent in the amplitude range of <15 mM and seems to reached a steady state at even larger amplitudes (Figure 22). This is roughly in line with what would be expected when the astrocyte Na^+/K^+-ATPase was mediating the fast decay rate assuming the reported Na^+/K^+-ATPase characteristics are similar among astrocytes in culture and in acute hippocampal slices.

In addition to the fast decay rate, the slow decay rate of K^+ transients evoked by a strong K^+ injection was also accelerated with increasing peak amplitudes (Figure 22). Experiments with the rat optical nerve suggested that the slower decay phase of stimulation-evoked K^+ transients was mediated by the neuronal Na^+/K^+-ATPase (Ransom et al., 2000). However, it seems unlikely that the neuronal Na^+/K^+-ATPase was by itself responsible for the observed correlation due to the following reasons. Experiments with neuronal cultures indicated that the neuronal Na^+/K^+-ATPase increases its activity with increasing intracellular Na^+ concentrations but is less sensitive to extracellular K^+ levels

(Rose and Ransom, 1997). Since the used iontophoretic K^+ application in combination with inhibited voltage-gated Na^+ channels has been considered to minimize the accumulation of intracellular Na^+ (Jauch et al., 2002), the uptake rate of the neuronal Na^+/K^+-ATPase should be less affected by increasing K^+ peak amplitudes. This does not exclude that the neuronal Na^+/K^+-ATPase is involved in the clearance of K^+, but indicates that other clearance mechanism(s) contribute that adjust their activity to the extracellular K^+ concentration. A possible candidate would be the previously suggested NKCC1-mediated transmembrane Na^+ cycle. This cycle comprises K^+-dependent NKCC1-mediated uptake of Na^+ that is subsequently expelled by the Na^+/K^+-ATPase (MacAulay and Zeuthen, 2012). NKCC1 that was shown by Larsen and colleagues to increase its activity with increasing extracellular K^+ concentrations up to 30 mM in cultured rat astrocytes and when expressed on oocytes. In the same study, however, the decay of stimulation-induced K^+ transients in the CA1 str. radiatum of rat hippocampal slices was unaffected by acute inhibition of the NKCC1 (Larsen et al., 2014). Since the activity of NKCC1 depends on the transmembrane driving force for Na^+, intracellular Na^+ accumulations, for instance evoked by neuronal activity, could decrease the activity of NKCC1. In contrast, K^+ transients evoked by iontophoretic application of K^+ are expected to cause less intracellular Na^+ accumulations compared to those evoked by neuronal activity (Jauch et al., 2002) and would facilitate NKCC1-mediated Na^+ and K^+ uptake. Thus, the clearance of the iontophoretically evoked K^+ transients would be accelerated directly by the K^+ uptake via the NKCC1 and indirectly by the increased neuronal Na^+/K^+-ATPase activity induced by the NKCC1-mediated intracellular Na^+ accumulation. However, it has to be mentioned that the neuronal expression of NKCC1 during adolescence is debated (Blaesse et al., 2009). If this mechanism underlies the observed accelerated decay rates of the iontophoretically evoked K^+ transients in the present study remains speculative. In summary, the accelerated fast decay rates at higher extracellular K^+ concentration were likely mediated by an increased astrocytic Na^+/K^+-ATPase activity. The accelerated slow decay rates at higher extracellular K^+ concentration could be caused by an NKCC1-mediated transmembrane Na^+ cycle that indirectly increases the neuronal Na^+/K^+-ATPase activity. However, a more detailed exploration of the contribution of the different K^+ clearance mechanisms mediating the decay of extracellular K^+ transients were beyond the scope of this study.

Noteworthy, K^+ undershoots, i.e. decline of the extracellular K^+ concentration below basal levels, were not observed after the decay of iontophoretically evoked K^+ transient evoked in this study. It was only observed in a minority of experiments employing the high-frequency stimulation of axons to evoked extracellular K^+ transient. The K^+ undershoot was shown in different studies to be mediated by the Na^+/K^+-ATPase and supposed to

depend on the accumulation of intracellular Na^+ mediated by neuronal activity (D'Ambrosio et al., 2002; Förstl et al., 1982; Heinemann and Lux, 1975). Accordingly, it was shown that the K^+ undershoot after neuronal additivity was more pronounced with an increasing stimulation duration (Chever et al., 2010). Since a significant K^+ undershoot in the just mentioned study was only observed at stimulation duration longer than 10s, the stimulation durations used in this study to evoke neuronal activity and, in turn, K^+ transients were potentially too short. Consequently, less Na^+ accumulated intracellularly, no prolonged Na^+/K^+-ATPase activity was evoked and, in turn, no pronounced K^+ undershoot. The absence of a K^+ undershoot after the iontophoretically evoked K^+ transients can be explained by the inhibited neuronal activity during these experiments and the resulting reduced intracellular Na^+ accumulation, as suggested already previously (Jauch et al., 2002).

5.1.4 General and technical aspects concerning the experiments

Before the physiological relevance of the presented results will finally be discussed, a few technical aspects need to be mentioned. An unavoidable disadvantage of KSMs is the disruption of the ECS ('dead space') by inserting the electrode into the tissue. Since the electrode tip is several times larger than the ECS, it cannot be excluded that the actual extracellular K^+ concentrations would be different in an undisturbed tissue (Heinemann and Lux, 1977). Newly development optical sensors for extracellular K^+ imaging could overcome this problem (Bazzigaluppi et al., 2015; Bischof et al., 2017; Wellbourne-Wood et al., 2017). Furthermore, these sensors would allow investigating the extracellular K^+ landscape over larger areas. This is of particular interest because it could provide further information about the spatial spread of extracellular K^+ and if this is facilitated by gap junction closure. Furthermore, it could help to estimate how many coupled astrocytes are involved in spatial buffering since the re-release of K^+ from the astrocytes might result in the increase of the extracellular K^+ concentration distant from the K^+ source.

Another point to be considered is the absence of neuronal activity during the experiments employing the iontophoretic application of K^+. Although the inhibition of neuronal activity prevented an additional activity-dependent K^+ release, a neuronal depolarization and, in turn, a putative release of neuromodulators, such as endocannabinoids (Navarrete and Araque, 2010), was still possible. Therefore, a so far unreported side effect of CBX on postsynaptic depolarization, neuromodulator release or altered astrocytic Ca^{2+} signaling that, in turn, impacts on astrocytic K^+ clearance cannot be completely excluded. For instance, it was reported that astrocytic Ca^{2+} signaling via G-protein coupled receptor activation modulated astrocytic Na^+/K^+-ATPase activity (Wang et al., 2012). However, this

scenario is rather unlikely to underlie the increased peak amplitudes of the K^+ transients observed after CBX treatment in the present study. Although inhibition of the Na^+/K^+-ATPase was shown to augment the peak amplitude of iontophoretically evoked K^+ transients (Jauch et al., 2002), also slower decay rates are generally associated with Na^+/K^+-ATPase inhibition (D'Ambrosio et al., 2002; Larsen et al., 2014; Ransom et al., 2000). This was never observed after CBX treatment in our experiments and therefore indicates unaltered Na^+/K^+-ATPase activity.

Furthermore, the presented experiments were all conducted in hippocampal slice preparation that largely preserve the astrocyte network and neuronal microcircuits, but provide no blood flow pervading the tissue. Since an intact blood flow could act as a constant K^+ sink, similar to the vitreous humor during K^+ siphoning in the retina (Newman et al., 1984), the astrocytic contact to blood vessels via their highly Kir4.1-expressing endfeet (Higashi et al., 2001) could also be an important route for K^+ redistribution. Therefore, the significance of gap junction channels for K^+ redistribution in the slice preparation might be overestimated due to the absent K^+ sink of the blood flow.

Finally, the conducted experiments revealed a significant role of astrocytic gap junction channels for limiting large extracellular K^+ accumulations. In fact, astrocytes form gap junction channels with adjacent astrocytes, but also reflexive (or autocellular) gap junctions, i.e. gap junctions channel with themselves (Genoud et al., 2015; Giaume et al., 2010). MFA and CBX would presumably also affect those reflexive gap junctions and, in turn, do not allow a discrimination of their functions from intercellular gap junctions. It could be argued that the inhibition of reflexive gap junctions reduces the connectivity between depolarized and less depolarized regions in the same astrocyte territory. Consequently, the efficiency of K^+ redistribution would be impaired and, in turn, the extracellular K^+ clearance. However, the relative contribution of these gap junction populations to K^+ clearance remains unclear until the different populations of gap junction channels can be selectively inhibited.

5.1.5 Relevance of spatial K^+ buffering assisted by astrocytic gap junction channels

In summary, the experiments of this study indicate that gap junction coupling contributes to the clearance of extracellular K^+ accumulations when high concentrations of around ~10 mM are reached. I suggest that this mechanism requires a steep extracellular K^+ concentration gradient as, for instance, generated by a single K^+ point source or several, but temporally or spatially separated K^+ sources. The (patho-) physiological relevance of these findings shall be discussed in the following section. Previous in vivo studies

reported that during maximal brain stimulation or epileptic activity the extracellular K^+ concentration reached a ceiling level of ~10-12 mM (Heinemann and Lux, 1977; Sypert and Ward, 1974). Even higher concentration were only reported during spreading depression (Somjen, 2001; Theis et al., 2003). Based on these finding, the question emerges if gap junction coupling limits the severity of those pathophysiological conditions and if gap junction uncoupling even facilitates their induction. According to Bedner and colleagues, dissected sclerotic hippocampi from pharmaco-resistant mesial temporal lobe epilepsy (MTLE) patients were devoid of gap junction coupling between astrocytes. The same study reported that astrocyte uncoupling preceded the occurrence of spontaneous seizures in an epilepsy mouse model that reproduced the features of the human MTLE. The authors conclude that astrocytic dysfunction including their uncoupling might be causal to the development of epilepsy by, for instance, impaired K^+ clearance (Bedner et al., 2015). The concentration-dependent effect of gap junction uncoupling found in the present study suggests that gap junction mediated K^+ clearance might be particular involved in attenuating epileptic activity through limiting the corresponding extracellular K^+ accumulations. Since an extracellular K^+ concentration gradient is a proposed requirement for spatial K^+ buffering (Orkand, 1986), gap junction mediated K^+ redistribution might be of special importance at the seizure initiation site and propagation front. Indeed, a recent study reported that focal cortical seizures in mice originate within a spatially confined area comprising hyperactive neuronal ensembles followed by a traveling wave of neuronal activity (Wenzel et al., 2019). Such initial 'microseizures' were also found to occur in human and precede the seizure onset (Schevon et al., 2008; Stead et al., 2010). Thus, gap junction-mediated K^+ clearance might be involved in limiting the spread of epileptic activity into non-excited areas by attenuating the activity-induced K^+ accumulation and, in turn, the neuronal excitability. Another potential phenomenon that involves gap junction-mediated K^+ clearance is spreading depression, which is characterized by a depolarization wave followed by a phase of neuronal inactivation (Somjen, 2001). A common feature of this depolarization wave is the excessive accumulation of extracellular K^+ at the propagation front (Somjen, 2001), however, the exact mechanism and role for gap junctions during its propagation is not fully understood. Interestingly, the uncoupling of astrocytes by a genetic deletion of Cx43 increased the propagation velocity in the hippocampus. It was therefore suggested that astrocytic gap junction uncoupling impaired the redistribution of K^+, which led to a more abrupt local K^+ rise and, in turn, to a fast propagation of spreading depression (Theis et al., 2003). This is in line with the observations of this study and points further towards an important role for gap junctions during conditions comprising large extracellular K^+ accumulations in combination with an extracellular K^+ concentration gradient.

Another interesting question to be addressed is if the limited contribution of gap junction coupling to extracellular K^+ clearance can be observed also in other brain region. This study focused on the K^+ clearance in the CA1 str. radiatum. In this subregion of the hippocampus, astrocytes reveal an elongated morphology and thus might favor spatial K^+ redistribution. However, astrocytes in other brain regions exhibit different cellular morphologies (Anders et al., 2014; Nixdorf-Bergweiler et al., 1994; Wallraff et al., 2006). In order to investigate if the conclusions drawn from the present study also apply for other brain regions than the hippocampal CA1 str. radiatum, it would be interesting to perform additional experiment in other brain regions.

5.1.6 Impact of gap junction uncoupling during conditions of a reduced ECS fraction

The experiments discussed above have shown that gap junction coupling facilitate the clearance of large extracellular K^+ loads that are commonly associated with pathophysiological conditions. In contrast, smaller extracellular K^+ loads found during physiological conditions seem to not rely on gap junction coupling. The corresponding experiments were performed with hippocampal slices bathed in an isomolar (~300 mOsm/kg) aCSF, which was shown to maintain the ECS fraction similar to those found in vivo (Hrabětová, 2005; Mazel et al., 1998; Syková et al., 2002). However, large extracellular K^+ elevations, either during epileptic activity (Slais et al., 2008) or by artificially raising the extracellular K^+ concentration (Syková et al., 1999), can lead to cellular swelling, a substantial reduction of the ECS fraction and constrained extracellular diffusion. In turn, further extracellular K^+ accumulation would be facilitated and could amplify neuronal activity. In order to test if gap junction coupling is involved in the attenuation of extracellular K^+ accumulation during those conditions, extracellular K^+ transients were monitored during the induction of cellular swelling in the presence or absence of gap junctions coupling (Chapter 4.1.7 & 4.1.8). This was of particular interest, because spatial K^+ redistribution was proposed to clear extracellular K^+ without an intracellular accumulation of K^+ and, in turn, astrocyte swelling (MacAulay and Zeuthen, 2012; Orkand, 1986). Consequently, gap junction mediated spatial buffering could provide the astrocyte with an efficient mechanism to maintain K^+ clearance particularly when the ECS is already narrowed.

A commonly used method to induce the shrinkage of the ECS is the application of a hypoosmolar solution to the brain slices (Kilb et al., 2006; Kume-Kick et al., 2002). It is assumed that such a hypoosmolar challenge causes a water influx from the ECS into the cells by altering the osmotic pressure without changing the total tissue water content

(Syková and Nicholson, 2008). Similar as reported for slice preparations of the spinal cord and the cortex (Kilb et al., 2006; Kume-Kick et al., 2002), reducing the osmolarity of the aCSF by 100-120 mOsm/kg resulted in a significant reduction of the ECS fraction to ~50% compared to isomolar conditions (Figure 28). However, the reduced osmolarity was achieved by reducing the NaCl concentration of the aCSF and would therefore alter the cellular transmembrane gradient for Na^+ and Cl^- during the experimental time course. Astrocytes express various different pumps and transporter proteins that mediate important homeostatic functions and rely on the Na^+ transmembrane gradient (Verkhratsky and Rose, 2020). The altered Na^+ transmembrane gradient could have, for instance, impacted directly on the clearance of extracellular K^+ transients by altering the transport rate of NKCC1. Other indirect effects via Na^+-dependent mechanisms, such as altered activity of the Na^+/Ca^{2+}- and Na^+/HCO_3^--exchanger resulting in distorted Ca^{2+} and pH homeostasis, respectively, are also conceivable. Thus, the osmolarity of the aCSF was instead modified by adding and withdrawing sucrose from the aCSF while maintaining the extracellular ionic composition throughout the experiment. Sucrose is not metabolized by cells in the CNS and therefore should only affect the osmolarity of the aCSF. This resulted in a similar reduction of the ECS fraction as seen before (Figure 29) but bypassed potential side effects induced by the acute change of the extracellular Na^+ concentrations. This approach was also in parallel to the iontophoretic application of K^+ into the ECS (Chapter 4.1.8). As expected during shrinkage of the ECS, the peak amplitude of the evoked extracellular K^+ transients increased rapidly after the application of the hypoosmolar solution. Simultaneously, the basal extracellular K^+ concentration started to increase (Figure 29). In order to probe if gap junction coupling facilitates extracellular K^+ clearance and, in turn, attenuates the accumulation of extracellular K^+, the gap junction inhibitor CBX was applied together with the hypoosmolar aCSF. However, gap junction uncoupling had no effect on the peak amplitude of the evoked extracellular K^+ transients or on the basal K^+ concentrations during hypoosmolar conditions. Surprisingly, the extracellular K^+ transients that augmented for several minutes during the application of the hypoosmolar aCSF began to attenuate in subset of experiments (Figure 31).

An often-reported observation when cellular, in particular astrocytic, swelling was induced is the rapid shrinkage of the ECS that is followed with a delay of a few minutes by a normalization of the cellular volume and subsequent ECS widening. This can be observed in astrocytic cell cultures (Kimelberg and Frangakis, 1985; Olson et al., 1986) as well as in the acutely isolated spinal cord (Syková et al., 1999). The proposed corresponding mechanism was termed ‘regulatory volume decrease’ (Cala, 1977) and involves the release of various ions, such as K^+ and Cl^-, and other organic osmolytes in order to normalize the cellular volume as shown for cultured astrocytes (Bender and Norenberg,

1994; Morales and Schousboe, 1988; Vitarella et al., 1994). This could principally underlie the observed decreasing K^+ transient peak amplitudes after they had initially increased, however, the required ECS widening during the hypoosmolar conditions was not observed by the previous TMA^+ diffusion analysis (Figure 28). This is puzzling, however, it needs to be kept in mind that no additional K^+ was iontophoretically applied during the TMA^+ diffusion experiments. Thus, additional extracellular K^+ might be involved in initiating the regulatory volume decrease. Interestingly, such a normalization of the ECS fraction was observed when ECS shrinkage was initially evoked by the application of a high extracellular K^+ concentration in the isolated spinal cord, but was nearly absent when the tissue was instead treated with a hypoosmolar extracellular solution that maintained the extracellular K^+ concentration at basal levels (Syková et al., 1999). Consequently, the observed delayed decrease of the K^+ transients could be caused by a local regulatory volume decrease that was induced by the iontophoretic application of K^+ into the ECS without being observed during TMA^+ diffusion experiments.

If this was the case, how it was mediated and why it was only observed in a subset of recordings remains, however, speculative. The cellular structures, such as fine astrocytic processes or their main branches, might exhibit a differently efficient regulatory volume decrease. Thus, the local composition of cellular structures at the K^+ recording site might have influenced if and to what extend a regulatory volume decrease was initiated. This could then explain why the extracellular K^+ transients normalized only in a subset of experiments since it would depend on the cellular structures close to the K^+ recording site that vary between experiments.

More importantly, the acute inhibition gap junction coupling had no effect on the fate of the K^+ transients and the basal K^+ concentration in this subset of experiments (Figure 31B). Similar was observed for the peak amplitude of the K^+ transients that showed no delayed attenuation during the hypoosmolar conditions (Figure 31C). Taken together, these experiments could not reveal a significant impact of gap junction coupling on the peak amplitude of evoked K^+ transients during conditions of a reduced ECS. This observation would be explained if the astrocyte swelling would induce gap junction closure. Consequently, the pharmacological inhibition of gap junction channels would have on further impact on the extracellular K^+ transients. Increasing intracellular Ca^{2+} concentration in astrocytes were found to reduce the coupling between astrocytes (Enkvist and McCarthy, 1994; Peracchia, 2004). Interestingly, astrocyte swelling was also shown to be associated with increased intracellular Ca^{2+} concentrations (O'Connor and Kimelberg, 1993). To test this hypothesis, the astrocyte coupling analysis as shown in chapter 4.1.1 could be performed during hypoosmolar conditions. However, also other factors could have affected the K^+ clearance and, in turn, prevent gap junctions from participating. For

instance, increased GFAP labeling (indicating astrogliosis) and morphology changes were observed for astrocytes in the spinal cord after prolonged treatment with an hypoosmolar solution or a high extracellular K^+ concentration (Syková et al., 1999). Furthermore, the induction of cellular swelling by hypoosmolar conditions were associated with a membrane depolarizing of cultured astrocytes (Kimelberg and O'Connor, 1988). These scenarios could, principally, have already impaired spatial K^+ buffering und, in turn, occluded the effect of CBX on the K^+ peak amplitudes.

In contrast, the increase of the basal K^+ concentration during the hypoosmolar treatment was more pronounced in control conditions compared to CBX when the evoked K^+ transients showed no delayed attenuation (Figure 31C, bottom). If gap junction uncoupling interfered in this subset of experiments with the potential K^+ release in order to normalize the cellular volume remains speculative. However, CBX might also inhibit the opening of connexin hemichannels. This could suggest that when a regulatory volume decrease is inefficient (e.g. observed by the absent attenuation of the extracellular K^+ transients), K^+ is released via hemichannels to support the regulatory volume decrease. In this scenario, one would expect a delayed attenuation of the extracellular K^+ transients, which was not captured by the conducted experiments since the recording was terminated after 30 minutes. However, these considerations require distinct gating mechanism for unapposed hemichannels and hemichannels that form gap junction channels. Interestingly, both hemichannels and gap junction channels were reported to exhibit two molecular distinct gating mechanism (Bukauskas and Verselis, 2004) that could be differentially affected by the hypoosmolar conditions. It would be of particular interest to further investigate the role for gap junction channel and hemichannels in cellular volume regulation, because cellular swelling and ECS shrinkage is observed in many pathophysiological conditions including epilepsy and ischemia (Slais et al., 2008; Syková and Nicholson, 2008; Voříšek and Syková, 1997). Consequently, active modulation of these channels might be a future target to interfere with pathophysiological cellular volume changes.

5.2 Mechanism underlying the proepileptiform effect of astrocyte morphology changes and uncoupling

Physiological brain function relies on the balance between excitatory and inhibitory neuronal activity that is integrated in a meaningful way. In the hippocampus, excitatory synaptic transmission is mainly mediated by glutamate released from pyramidal neurons (Rose et al., 2018), whereas inhibitory synaptic transmission is based on the release of GABA by interneurons (Pelkey et al., 2017). Astrocytes are known to closely contact both types of neurons and modulate their activity by several mechanisms (Mederos and Perea, 2019; Perea and Araque, 2010). Consequently, a dysfunction of astrocytes could lead to a distortion of proper neuronal function (Henneberger, 2017; Steinhäuser et al., 2015) and, in turn, to neuronal hyperexcitability (Chapter 1.2 & 1.6).

The experiments discussed in the following chapter were based on previous work from Dr. S. Anders that investigated the role of astrocyte morphology changes in an acute model of epilepsy. It could be shown that the induction of epileptiform activity by the inhibition of $GABA_A$-receptors in acute hippocampal slices rapidly induced shrinkage of the fine and medium astrocytic processes. This was paralleled by a significant decrease of the intracellular diffusion in astrocytes and the diffusion between astrocytes via gap junctions. Inhibiting the ROCK-pathway and, in turn, the modulation of the actin cytoskeleton prevented these morphology changes. Importantly, this resulted in a significant attenuation of the epileptiform activity and points towards a proepileptiform action of astrocyte morphology changes. Furthermore, the epileptiform discharges persisted after the reestablishment of $GABA_A$R-mediated inhibitory transmission at a frequency which was correlated with the degree of astrocyte morphology changes (Anders, 2016). However, the mechanism underlying the persistent epileptiform activity remained not fully understood and was therefore the objective of the present study.

In order to replicate the observed astrocyte morphology changes, epileptiform discharges were induced similar as in the previous work by the application of the $GABA_A$R antagonist penicillin (Chapter 3.4.5). Since the morphology changes were observed within minutes after the onset of epileptiform activity, it was assumed that the corresponding proepileptiform effect had been already established during this induction period. Next, the penicillin was removed from the aCSF and the glutamate receptor antagonists D-APV and NBQX were applied in order to reestablish the $GABA_A$R-mediated inhibitory synaptic transmission and to terminate the ongoing epileptiform activity, respectively. The emerging question was then which parameter was altered by the evoked astrocyte morphology changes compared to control conditions (no inhibition of $GABA_A$R and, in turn, no epileptiform activity and morphology changes) and could have a proepileptiform effect.

5.2.1 Inhibitory synaptic transmission after epileptiform activity

In the hippocampus, interneurons represent 10-15% of the neuronal population and provide the major GABAergic synaptic input. This involves the activation of $GABA_AR$, the concomitant influx of Cl^- and a transient membrane hyperpolarization or shunting of the postsynaptic neuron. Thus, GABAergic synaptic input regulates neuronal excitability and can impact on circuit functions (Pelkey et al., 2017). Astrocytes are known to react to inhibitory synaptic activity by intracellular Ca^{2+} signaling and, in turn, with the release of neuroactive substances ('gliotransmitter') (Chapter 1.5.2). Consequently, the previously observed decreased intracellular diffusion (Anders, 2016) might distort Ca^{2+}-mediated gliotransmission and, in turn, synaptic transmission. It was shown in several studies that inhibitory transmission is modulated by astrocytes via gliotransmission (Losi et al., 2014; Mederos and Perea, 2019; Roux and Buzsáki, 2015) or the glutamine synthetase activity (Ortinski et al., 2010) and thus was the first candidate to be investigated (Chapter 4.2.1). In line with the previous work (Anders, 2016), the inhibition of $GABA_AR$ had no effect on the slope of the evoked fEPSPs but led to multiple population spikes (Figure 32). This is in line with the assumption that the fEPSP slope mainly represents excitatory synaptic transmission, because glutamatergic presynaptic terminals are directly activated by axonal stimulation. In contrast, GABAergic synapses are activated with a temporal delay, because the axonal stimulation activates first the interneuron, which then leads to the activation of the GABAergic synapses. As a consequence, $GABA_AR$ inhibition impacts on the later phase of the neuronal activity, i.e. fEPSP amplitude and population spike. Importantly, the frequency of epileptiform discharges in the presence of penicillin was similar as previously observed by Dr. S. Anders. Accordingly, it was assumed that also the astrocyte morphology changes were occurred in a similar fashion.

However, the frequency and amplitude of the spontaneous sIPSCs were not affected by epileptiform activity (Figure 33A-B). On the other hand, the sIPSCs recorded in slices that experienced epileptiform activity showed faster decay rates and a tendency towards smaller width (Figure 33C-D). This could point towards a shortened presence of extracellular GABA at the synapses and thus facilitate neuronal excitability by an inefficient inhibitory input. In order to further support that the decreased decay times were indeed caused by the astrocyte morphology changes, we would need to repeat the experiments and induce epileptiform activity in the presence of Y27632. In these conditions, the astrocyte morphology changes would be inhibited and the decay and width of the sIPSCs are expected to be similar to control conditions. Another experimental approach could also provide more details about the inhibitory input onto pyramidal neurons after epileptiform activity. In the presented experiments, the inhibitory input was recorded by patch-clamp recordings from the neuronal soma. Thus, inhibitory synaptic

input at the distal dendrites might not be efficiently sampled due to space-clamp problems. As a consequence, changes of the inhibitory synaptic transmission by the astrocyte morphology changes might be underestimated by the employed approach. The usage of fluorescent sensors in future experiments could overcome this problem by directly assessing the extracellular GABA dynamics (Marvin et al., 2019). The decay rates of the recorded sIPSCs (~7 ms) were shorter than what is reported in the literature. Previous studies recorded sIPSCs in rat CA1 pyramidal neurons at room temperature and found average decay rates of ~8-11 ms (Collingridge et al., 1984; Gage and Robertson, 1985). Another study recorded sIPCSs at 34°C in CA1 pyramidal neurons in hippocampal slices obtained from mice and revealed decay rates of on average ~15 ms (Matos et al., 2018). However, experimental differences in temperature, recording solutions, used species or the age of the used animals could explain the different sIPSC kinetics.

Although the frequency and amplitude of the sIPSCs was unaffected, the faster decay after epileptiform activity could indicate a less efficient inhibition and thus an increased neuronal excitability. However, the recordings of sIPSCs were performed in the presence of glutamate receptor inhibitors in order to isolate the inhibitory inputs and to avoid a bias by ongoing neuronal activity. Consequently, altered modulatory effects on the inhibitory synaptic transmission mediated by glutamate receptors were also prevented under these conditions. For instance, a previous study found that interneuron activity evoked $GABA_BR$-mediated Ca^{2+} elevations in astrocytes. This resulted in the release of glutamate which potentiated inhibitory transmission on CA1 pyramidal neurons (Kang et al., 1998). Accordingly, an impaired astrocytic Ca^{2+} signaling due to the astrocyte morphology changes might prevent potentiation of inhibitory transmission and led to increased neuronal excitability. However, the inhibitory effect on synaptic transmission observed by Kang and colleagues (1998) was absent in the presence of glutamate receptor antagonists and would consequently be undetectable in the presented experiments. Consequently, the effect of the astrocyte morphology changes on inhibitory synaptic transmission might be underestimated in our experiments.

In conclusion, spontaneous inhibitory currents in CA1 pyramidale neurons were reduced after epileptiform activity and could underlie the proepileptiform activity of astrocyte morphology changes. Thus, inhibitory synaptic transmission is an interesting candidate for further experiments that will help to validate our conclusions.

5.2.2 The extracellular space during and after epileptiform activity

The concentration of ions, neurotransmitter and gliotransmitter depend on the released amount and the volume into they are released. This volume is the extracellular space and

its structure can, thus, impact on the extracellular concentration and diffusion of neuroactive substances. Shrinkage of the ECS was observed during evoked neuronal activity (Larsen et al., 2014; Pannasch et al., 2011) and epileptic activity (Slais et al., 2008). Furthermore, those reductions of the ECS were also shown to augment epileptiform activity, presumably by facilitated accumulation of extracellular K^+ and glutamate (Kilb et al., 2006; Traynelis and Dingledine, 1989). On the other hand, reduced accumulations of inhibitory neurotransmitter, such as GABA, by an increase of the ECS could also promote epileptiform activity.

Thus, the observed astrocyte morphology changes could affect the ECS structure and, in turn, increase neuronal excitability by two different scenarios. First, the decreased intra- and intercellular diffusivity (Anders, 2016) could lead to a more pronounced astrocyte swelling during neuronal activity. The concomitant reduction of the ECS would then lead to facilitated K^+ or glutamate accumulations that, in turn, increased neuronal excitability. Second, the shrinkage of the fine astrocyte processes could increase locally the ECS and, in turn, reduce the accumulation of inhibitory neuro- or gliotransmitter, such as GABA or adenosine. In both scenarios, an altered ECS could have a proepileptiform effect.

In order to test if the induced astrocyte morphology changes facilitated an activity-dependent ECS shrinkage or itself modulated the ECS structure, the ECS fraction was monitored throughout the experiments, i.e. during baseline conditions, control conditions/ induced epileptiform activity and inhibited postsynaptic activity (Chapter 4.2.2). However, the ECS fraction during epileptiform activity was not different from control conditions. In addition, also the inhibition of postsynaptic activity in both conditions did not impact the ECS fraction (Figure 34). This suggests that the astrocytic morphology changes observed for the fine and medium-large processes were not capable to significantly affect the ECS fraction. Interestingly, the ECS fraction was also not affected during epileptiform activity compared to baseline conditions as it would be expected from an increased neuronal activity. However, the previous studies that showed an ECS shrinkage during neuronal activity employed a continuous stimulation over several seconds (Larsen et al., 2014; Pannasch et al., 2011). Thus, the rather short epileptiform discharges occurring every few seconds might not be sufficient to elicit a detectable impact on the extracellular TMA^+ diffusion. It also has to be kept in mind that the employed technique provides an average value of the ECS structure over several hundred micrometers. Since astrocytes occupy only ~5% of the volume of their territories (excluding the soma) and the shrinkage was predominantly observed for fine and medium-large processes (Anders, 2016), the impact on the ECS fraction might not be detectable with the employed technique. However, this does not exclude that the shrinkage of the fine processes located close to the synapses

had a greater functional impact than it would be predicted from the employed TMA^+ diffusion analysis.

5.2.3 Extracellular K^+ clearance after epileptiform activity

Impaired K^+ clearance has often been associated with epilepsy. Impaired extracellular K^+ clearance could result in an excess of extracellular K^+ and, in turn, an increased neuronal excitability (Balestrino et al., 1986; Hablitz and Lundervold, 1981; Rausche et al., 1990; Voskuyl and ter Keurs, 1981). As a consequence, this could facilitate the generation of epileptic activity. It was for instance shown that the expression of Kir4.1 channels was reduced in sclerotic hippocampi of MTLE patients (Das et al., 2012; Heuser et al., 2012). Further studies reported that the Kir4.1-mediated K^+ clearance was impaired in sclerotic tissue of humans and rats after epileptic activity (Heinemann et al., 2000; Jauch et al., 2002; Kivi et al., 2000). In addition, hippocampal astrocytes lost their ability to limit K^+-induced membrane depolarization via gap junction channels after epileptic activity (Bedner et al., 2015). The experiments of these studies were performed several hours to weeks after epileptic activity and thus provide important information about later stages of epilepsy. However, the involvement of K^+ clearance during early epileptogenesis remained largely unexplored. Thus, we investigated if K^+ clearance was also impaired by the rapid astrocyte morphology changes that were observed shortly after the onset of epileptiform activity.

Epileptiform activity induced a rapid shrinkage of the fine astrocyte process and resulted in a smaller intracellular volume and reduced intra- and intercellular diffusivity (Anders, 2016). A decreased diffusivity could lead to an impaired spatial K^+ redistribution and thereby lead to more pronounced K^+-induced membrane depolarizations. The resulting impaired K^+ uptake via, for instance, Kir4.1 channels would then lead to augmented peak amplitudes of extracellular K^+ transients as it was suggested previously (Larsen and MacAulay, 2014; Larsen et al., 2014) and further supported in the this study (Breithausen et al., 2020). However, the K^+ peak amplitudes were unaffected by epileptiform activity indicating that the decreased intra- and intercellular diffusivity had no significant effect on the spatial K^+ redistribution. This is in line with our findings on the extracellular K^+ clearance after acute gap junction uncoupling. We showed that the inhibition of intercellular and presumably also the intracellular diffusivity impacted only on the K^+ peak amplitudes when concentrations of 8-10 mM were exceeded (Breithausen et al., 2020). In contrast, the extracellular K^+ transients that were evoked by the epileptiform discharges and the axonal stimulation exhibited peak amplitudes in the submillimolar range. Thus, it unlikely that the reduced intra- and intercellular diffusivity impacted on the extracellular K^+

clearance by impairing the K^+ redistribution under these conditions.

On the other hand, other mechanisms are also involved in the clearance of extracellular K^+ accumulations and could be impaired by the rapid astrocyte morphology changes. For instance the Na^+/K^+-ATPase was shown to largely mediate the decay of extracellular K^+ transients back to basal levels (D'Ambrosio et al., 2002; Larsen et al., 2014; Ransom et al., 2000). A slowed K^+ decay rate would indicate a prolonged extracellular accumulation of K^+ that, in turn, could promote epileptiform activity by increasing the neuronal excitability. However, also the decay of the evoked extracellular K^+ transients was not affected by the epileptiform activity. Taken together, these experiments indicate that the rapid astrocyte morphology changes had no effect on the K^+ accumulation during the neuronal activity and the decay back to basal levels. Thus, an impaired K^+ clearance cannot explain the proepileptiform effect of the rapid astrocyte morphology changes.

Although the evoked K^+ transients had similar peak amplitudes as the K^+ transients observed during epileptiform discharges, probing the impact of morphology change on K^+ clearance with other experimental approaches could be interesting. Since the used K^+-sensitive microelectrodes provide no information about the spatial profile of the extracellular K^+ during epileptiform activity, new developed optical sensors for extracellular K^+ could be useful tools for additional experiments (Bazzigaluppi et al., 2015; Bischof et al., 2017; Wellbourne-Wood et al., 2017). These sensors might provide new information about the location and size of local K^+ release sites during epileptiform activity. This could help us to design new experimental conditions that better mimic the neuronal and synaptic activation during epileptiform activity.

5.2.4 Glutamate clearance

Excitatory synaptic transmission in the hippocampus is mediated by glutamate and its clearance from the ECS is mainly mediated by astrocytes that express high efficient glutamate transporters (Rose et al., 2018). The importance of glutamate clearance for synaptic function was revealed when glutamate transporters were acutely inhibited. This resulted in facilitated glutamate spill-over and the concomitant activation of extrasynaptic NMDARs (Asztely et al., 1997). Thus, impaired astrocytic glutamate clearance could facilitate the activation of NMDARs on neighboring neurons and, in turn, promote neuronal synchronization which might contribute to epileptiform activity. Interestingly, the genetic deletion of the glutamate transporter GLT-1 or the acute infusion of a broad-spectrum glutamate transporter inhibitor into the hippocampus evoked spontaneous seizures in mice (Demarque et al., 2004; Tanaka et al., 1997). In particular the exposed position of the astrocyte processes close to the synapses was found to be an important factor for

efficient glutamate clearance. This was supported by a study that revealed that a decreased synaptic coverage by astrocytes was associated with an impaired glutamate clearance (Oliet et al., 2001). Thus, it was investigated if the observed astrocyte morphology changes (Anders, 2016) might impair glutamate clearance and thereby facilitate epileptiform activity. For instance, glutamate uptake was shown to depend on the cotransport with Na^+ (Nicholls and Attwell, 1990; Rose et al., 2018). Accordingly, a reduced transmembrane Na^+ gradient by intracellular accumulations of Na^+ was suggested to impair extracellular glutamate clearance (Karus et al., 2015). Since the observed morphology changes were accompanied by an decreased intra- and intercellular diffusion (Anders, 2016), facilitated intracellular Na^+ accumulations could hypothetically underlie an impaired glutamate clearance. Another potential mechanism that was found to impair extracellular glutamate clearance is an impaired motility of glutamate transporters in the astrocyte membrane (Murphy-Royal et al., 2015). If the observed shrinkage of the fine astrocytic processes interfere with the membrane diffusion of glutamate transporters is, however, not clear but it could in theory interfere with the spatial positioning of glutamate receptors at the synapses and, in turn, impair their efficiency (Henneberger, 2017).

In order to probe if impaired glutamate clearance is causal for the observed persistent epileptiform discharges, the fluorescent glutamate sensor iGluSnFR (Marvin et al., 2013) was virally expressed in the hippocampus of mice (Chapter 4.2.4). After two to three weeks, astrocytes in the hippocampal slices obtained from these mice showed reliable iGluSnFR expression (Figure 37A). Similar to the previously described experiments, 4 mM penicillin evoked epileptiform discharges that were terminated after 30 minutes by inhibiting glutamatergic synaptic transmission, action potential firing and metabotropic glutamate receptors (Figure 36). Surprisingly, the discharges frequency was relatively low compared to the previous experiments from this study (Figure 32D) and from the previous study (Anders, 2016). Since it was shown that the frequency of penicillin-induced epileptiform discharges in rat hippocampal slices was similar compared to hippocampal slices of mice (Anders, 2016), the expression of iGluSnFR might have reduced the susceptibility to generate epileptiform discharges. A potential explanation for that observation could be the expressed iGluSnFR that binds extracellular glutamate and thus might act as an additional glutamate buffering mechanism.

Nevertheless, the extracellular glutamate homeostasis was then investigated by applying glutamate via an iontophoresis pipette. The iontophoretic glutamate application resulted in a local glutamate transient that spread over a distance of roughly 10 µm (Figure 37D). The analysis of the corresponding spatial glutamate profile revealed a trend towards a pronounced extracellular glutamate spread after epileptiform activity. This could point

towards a facilitated glutamate spill-over that activates more synapses and thus could promote the generation of epileptiform activity. The fluorescence ‘sag’ in the glutamate line profile that was observed in a subset of experiments might complicate the interpretation of the data. However, this was observed in both experimental conditions and thus allows a comparison. Nevertheless, additional experiments are required to further validate if the extracellular glutamate spread was facilitated after epileptiform activity.

The duration of the iontophoretic glutamate application (200 ms) resembled roughly the duration of interictal discharges that can be observed in an electroencephalogram of epilepsy patients (de Curtis and Avanzini, 2001). Since effective glutamate clearance might attenuate the build-up of extracellular glutamate during such activity and, in turn, tones down epileptiform epileptic activity, the accumulation of glutamate during the glutamate application phase was investigated (Figure 37C). Intuitively, the glutamate accumulation was the largest close to the glutamate application point and decreased with distance from this point (Figure 37F). As expected, the glutamate accumulation rate decreased with distance from the glutamate application point due to its diffusion in the ECS and the concomitant dilution (Figure 37E). Surprisingly, there was a slight but significant trend towards a faster glutamate accumulation in control conditions compared to after epileptiform activity which was independent of the distance from the glutamate source. However, this trend was rather small and accompanied with large data variability that was potentially due to small variations of the distance between line scan and the glutamate source. In addition, the concentrations of the glutamate accumulations were overall not affected by epileptiform activity. This observation was also independent of the distance from the glutamate source, i.e. was independent of the local glutamate concentration. This local glutamate concentration ranged from several micromoles close at the pipette tip to sub micromolar levels distant from the glutamate source. These concentrations were previously suggested to roughly reflect what is expected during the activity of a pool of synapses. This assumption was based on a study that simulated how extracellular glutamate accumulations are affected by the number of functional glutamate transporters. It was revealed that synaptic activity that is sufficient to excite CA1 pyramidal neurons evoked local glutamate elevations of ~1 µM when glutamate uptake mechanisms are fully intact. Extracellular glutamate accumulations exceeding ~1 µM were only observed when glutamate transporter activity was almost completely switched off (Zheng et al., 2008). This could indicate that the glutamate transporters are not able to cope with the large extracellular glutamate accumulations under our experimental conditions. Although it was reported that astrocytic glutamate transporters in the hippocampus were not overwhelmed by the amount of glutamate that was released even by a high-frequency stimulation (Diamond and Jahr, 2000), the iontophoresis might have released even larger

amount of glutamate that saturated the astrocytic glutamate transporters. Thus, glutamate clearance would have less impact on the accumulation of the applied glutamate in the ECS. As a consequence, an impaired glutamate uptake mediated by astrocyte morphology changes would also have less impact and, in turn, was not detectable under these conditions. In order to test this hypothesis, the glutamate application period or the application current could be decreased in further experiments in order to evoked extracellular glutamate accumulations in the submillimolar range.

It also has to be kept in mind that during synaptic transmission glutamate release is mainly restricted to the synaptic clefts and thus extracellular glutamate transients might originate more or less time-locked from several sources. In contrast, the employed iontophoretic glutamate application creates a single point source randomly in the ECS. Consequently, it can be assumed that not only the fine perisynaptic astrocyte processes get in contact with the extracellular glutamate and but also other parts of the astrocytes, such as thicker branches and soma. Since the astrocytic morphology changes were predominantly observed for the fine astrocyte processes (Anders, 2016), the effect of these changes on glutamate clearance might be underestimated by employing the iontophoretic application of glutamate.

Thus, extracellular glutamate transients were evoked in the following experiments by an axonal stimulation and the subsequent glutamate release from the presynaptic terminals. Since the frequency of epileptiform discharges was relatively low in hippocampal slices from iGluSnFR-expressing slices during the previous experiments, Mg^{2+} was removed from the aCSF during the application period of the penicillin. This was shown to release the Mg^{2+} block from the pore of the NMDAR which results in facilitated neuronal excitability and epileptiform activity (Gloveli et al., 1995; Mody et al., 1987). Indeed, this resulted in an increased frequency of epileptiform discharge similar as observed previously (Figure 38D) and led to the assumption that the astrocyte morphology changes had occurred as reliably as in the previous study (Anders, 2016) (Chapter 1.6.1). Inhibition of the ROCK-pathway by the application of its inhibitor Y27632 prevented astrocyte morphology changes and reduced the frequency of epileptiform discharges (Anders, 2016). Surprisingly, the application of Y27632 did not significantly reduce the frequency of epileptiform discharges. However, the effect of Y27632 was previously only tested when epileptiform activity was induced by the application of penicillin in the presence of Mg^{2+} (Anders, 2016). Thus, it cannot be ruled out that the facilitated NMDAR activation by the removal of the Mg^{2+} block was a too strong stimulus and, in turn, redundantized the proepileptiform astrocyte morphology changes. Nonetheless, if the astrocyte morphology changes impacted on the clearance of glutamate released from synapses, this effect should still be observable and sensitive to the ROCK inhibition by Y27632. Interestingly,

the decay rate of the glutamate evoked fluorescence transients (also designated as ‘glutamate transients’) in control conditions were slightly but significantly accelerated compared to baseline values. Also, the glutamate transients after epileptiform activity in the presence of Y27632 revealed a trend towards faster decay rates. On the other hand, this effect was less pronounced for glutamate transients after epileptiform activity in the absence of Y27632 (Figure 39C). It is not clear if just an unspecific time-dependent effect or the inhibition of AMPARs and NMDARs were underlying the observed accelerated decay rates. Inhibition of these receptors was found to reduce the surface motility of astrocytic glutamate transporter that was suggested to facilitate extracellular glutamate clearance (Murphy-Royal et al., 2015). Consequently, glutamate receptor inhibition would decrease the decay rates of the extracellular glutamate transients, i.e. slow glutamate uptake. Since the opposite effect was observed (Figure 39C), it is unlikely that an impaired glutamate transporter motility mediated the observed effect.

On the other hand, the inhibition of excitatory synaptic transmission and the concomitant reduced activity-dependent K^+ release could have affected the glutamate uptake. Since glutamate uptake is electrogenic and depends additionally to the cotransport of Na^+ on the export of K^+, an extracellular K^+ accumulation was suggested to attenuate extracellular glutamate uptake (Barbour et al., 1988; Rose et al., 2018). Thus, the observed accelerated glutamate clearance might be a consequence of the inhibited postsynaptic activity since this could reduce activity-dependent extracellular K^+ accumulations. This could result in less depolarized astrocytes and a K^+ membrane gradient that favored glutamate uptake. As already mentioned, the accelerated decay rates were less pronounced in hippocampal slices that experienced epileptiform activity in the absence of Y27632. Hypothetically, the reduced intracellular diffusivity accompanying the astrocyte morphology changes could have enhanced intracellular Na^+ accumulations during glutamate uptake and, in turn, counteracted the facilitation of glutamate uptake during inhibited neuronal activity. However, the observed changes of the extracellular glutamate decay rates were relatively small and the absolute decay rates were not statistically different among the three experimental groups. The peak amplitudes of the glutamate-evoked fluorescence signals after induction of epileptiform activity further indicate that also the activity-dependent glutamate release was unaffected (Figure 39E). This is in line with the stable fEPSP slopes since they represent the glutamatergic synaptic transmission. In turn, altered glutamate release would directly affect the fEPSP slopes.

In summary, these experiments could not reveal that the clearance of iontophoretically and synaptically evoked glutamate accumulations was substantially affected by the induction of epileptiform activity. This suggests that changes of the glutamate clearance do not explain the proepileptiform effect of the astrocyte morphology changes. However,

additional experiments that further investigate the extracellular diffusion of glutamate might validate the observed trend towards an increased glutamate spread after epileptiform activity. Interestingly, the inhibition of glutamate clearance was shown to induce epileptic activity in mice (Demarque et al., 2004; Tanaka et al., 1997) and increased glutamate concentrations were found in the human epileptic hippocampus (During and Spencer, 1993). Although this indicated that impaired glutamate clearance is involved in epilepsy, impaired glutamate homeostasis could be a characteristic of later stages of epilepsy rather than early epileptogenesis. It was for instance shown that even high-frequency synaptic activation over 100 ms did not overwhelm astrocytic glutamate transporters in the hippocampus (Diamond and Jahr, 2000) and that those transporters seem to clear extracellular glutamate 20 to 50 times faster than the rate that glutamate is released from synapses during moderate activity (Zheng et al., 2008). These findings indicate that glutamate clearance in the brain is highly efficient. Consequently, the observed rapid shrinkage of the fine astrocyte processes might not be sufficient to drastically impair glutamate clearance at the investigated time point. However, further progression of the astrocyte morphology changes and their long-term effects might lead to a pronounced impairment of glutamate clearance and thus a proepileptiform effect at later time points.

Glutamate clearance is modulated by the neuronal activity and can differ between brain regions. For instance, it was revealed that glutamate clearance in the cortex is slowed by specific presynaptic activity (Armbruster et al., 2016). Another study showed that glutamate clearance in the somatosensory cortex was faster during high frequency neuronal stimulation compared to lower stimulation frequencies. The opposite was observed in the barrel cortex. Although the underlying mechanisms remain to be explored, these findings suggested that the astrocyte machinery for glutamate clearance is preferentially tuned to a specific neuronal activity (Romanos et al., 2019). As a consequence, the astrocyte morphology changes in the hippocampus might also only impact on glutamate clearance under specific neuronal activity. Therefore, future experiments could investigate the specific presynaptic activity pattern during epileptiform discharges using fluorescent Ca^{2+}-indicators expressed specifically in presynaptic terminals as previously used to study stimulation-evoked Ca^{2+}-signals in the hippocampus (Al-Osta et al., 2018). Afterwards, glutamate clearance can be investigated with a stimulation paradigm that mimics the neuronal activity during epileptiform activity. These experiments will then reveal if the astrocyte morphology changes impact on glutamate clearance specifically during epileptiform activity.

6 Summary & Conclusions

The present study addressed the contribution of astrocytic gap junction channels to extracellular K^+ clearance. Astrocyte form large networks through gap junction coupling that enables intercellular communication and trafficking of ions. The contribution of this network was proposed to facilitate extracellular K^+ clearance by the spatial redistribution of K^+ via the gap junction coupled network. However, the quantitative contribution of this mechanism to K^+ clearance was not fully clear. In order to obtain further insights, the extracellular K^+ concentration in the CA1 str. radiatum of hippocampal slices was recorded with K^+-sensitive microelectrodes in parallel to the inhibition of intercellular molecule trafficking. For this purpose, a pharmacological approach to acutely uncouple gap junction channels was employed. This allowed the fast disruption of the gap junction coupled astrocyte network and prevented potential cellular alterations induced by a long-term absence of gap junction coupling. Next, different experimental approaches were used to evoke extracellular K^+ transients before and after the acute inhibition of gap junction coupling. A commonly used stimulation paradigm to probe hippocampal circuit functions evoked neuronal activity and extracellular K^+ transients with relatively small K^+ peak amplitudes. However, acute gap junction uncoupling had no effect on these K^+ transients. Also, extracellular K^+ transients with larger K^+ peak amplitudes evoked by more intense neuronal stimulation were largely unaffected by gap junction uncoupling. Next, the iontophoretic application of K^+ was introduced in order to evoke extracellular K^+ transients in the absence of neuronal activity. This allowed the application of K^+ as a point source and the control of the K^+ transient's peak amplitudes by adjusting the amount of injected K^+. Interestingly, iontophoretically evoked K^+ transients with peak amplitudes in the low millimolar range were also unaffected, but large K^+ transients with peak amplitudes that exceeded ~10 mM showed further augmentation after gap junction uncoupling. These results demonstrate that the contribution of gap junction coupling to buffering of extracellular K^+ gradients is limited to large and localized K^+ increases. Since such large extracellular K^+ accumulations are commonly observed in association with pathophysiological conditions, astrocytic gap junction coupling might act as a rescue mechanism when other K^+ clearance mechanisms are not able to cope with extensive extracellular K^+ loads. Thus, the astrocyte network might not play a pivotal role for K^+ clearance during physiological conditions but rather in pathophysiological scenarios. In particular the attenuation of spatially confined epileptic activity or the dampening of spreading depression could be an important function of astrocyte gap junction coupling since these conditions could provide a steep extracellular K^+ gradient as observed in the present experiments.

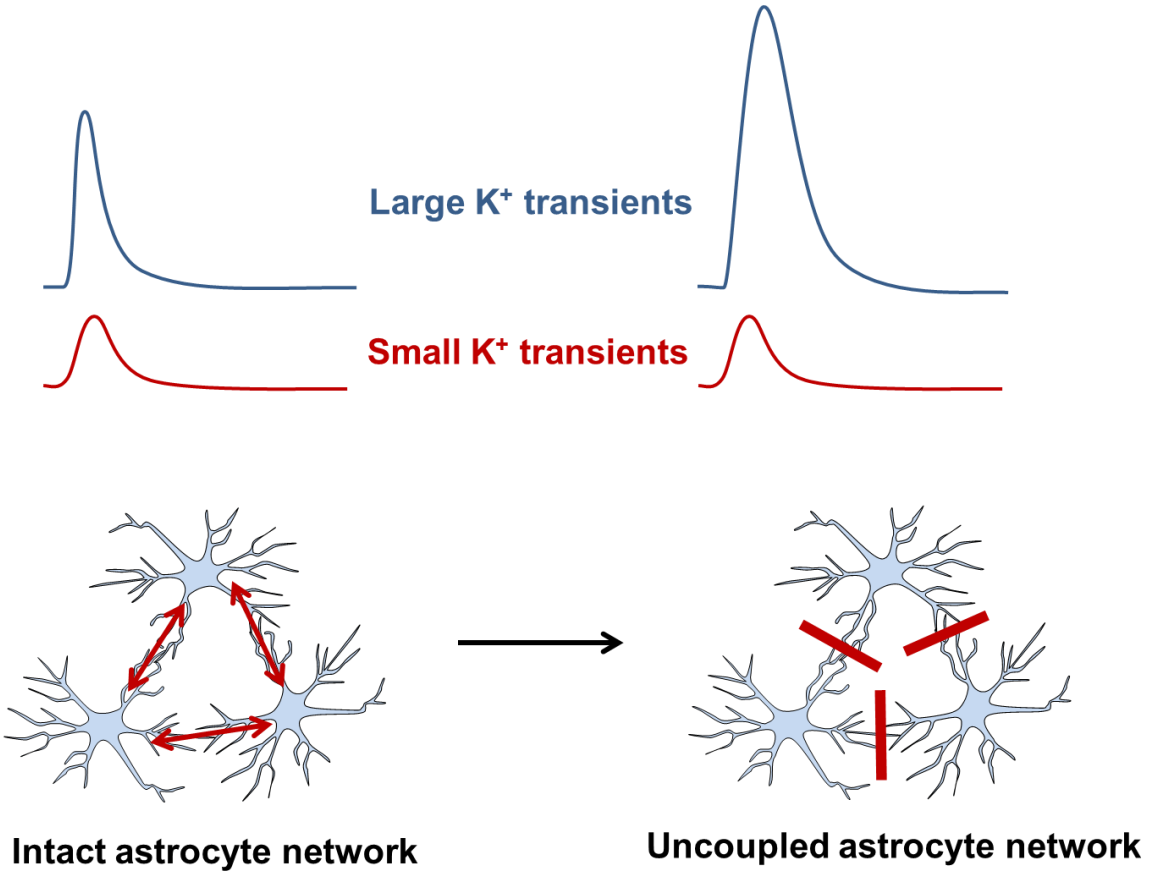

Figure 40 Summary of the experiments investigating the impact of acute gap junction uncoupling on K^+ clearance. The acute inhibition gap junction coupling had no effect on small extracellular K^+ transients. In contrast, large extracellular K^+ transients with peak amplitudes exceeding ~10 mM further increased after the acute gap junction inhibition.

The second aspect addressed by this study was the impact of rapidly occurring astrocyte morphology changes in the CA1 str. radiatum that were triggered by epileptiform activity. Previous experiments have shown that this morphology changes were accompanied by an impaired intra- and intercellular diffusion and had a proepileptiform effect (Anders, 2016). However, the underlying mechanism that mediated this proepileptiform effect remained uncertain. Thus, in the present study several approaches investigated the link between astrocyte morphology and the increased epileptiform activity.

First, it was tested if the induction of epileptiform activity and the concomitant morphology changes modulated inhibitory synaptic input on CA1 pyramidal neurons. This was quantified by recording spontaneous inhibitory currents from CA1 pyramidal neurons after epileptiform activity. We found that the frequency and amplitude of the spontaneous inhibitory currents were unaffected by epileptiform activity, but their decay was shorter compared to control conditions. This suggests that the astrocyte morphology changes decreased the inhibitory synaptic input onto CA1 pyramidale neurons and thereby might

induced neuronal hyperexcitability. In order to validate this, further experiments that employ the acute inhibition of the astrocyte morphology changes will be performed.

Second, it was analyzed if the extracellular space fraction was affected by the induction of epileptiform activity using a diffusion analysis of TMA^+. This analysis revealed that the epileptiform activity and astrocyte morphology changes had no influence on the extracellular space fraction.

Third, we employed K^+-sensitive microelectrodes to measure extracellular K^+ transients after epileptiform activity. The peak amplitude and decay of these K^+ transients were not different compared to control conditions. This indicates that the astrocyte morphology changes did not impair extracellular K^+ clearance and thus is unlikely to underlie the proepileptiform effect.

Finally, the extracellular glutamate clearance was investigated using the fluorescent glutamate sensor iGluSnFR. Extracellular glutamate elevations were either evoked by an iontophoretic application or by synaptic activity. We found that also glutamate clearance was largely unaffected by the epileptiform activity and thus cannot explain the observed proepileptiform effect of the astrocyte morphology changes. However, there was a tendency toward an increased spatial spread of glutamate into the extracellular space. This could contribute to a facilitated activation of glutamate receptors and, in turn, to an increased neuronal activity. Again, additional experiments are required to validate this observation.

In conclusion, this study provided further information about the functional consequences of rapid astrocyte morphology changes. Although, the mechanism underlying the proepileptiform effect of the morphology changes is still not finally clear, the conducted experiments helped to narrow down the list of possible candidates. Moreover, the experiments investigating the inhibitory synaptic transmission and glutamate clearance provided good starting points for further experiments.

7 Perspectives

My study revealed that astrocytic gap junction coupling facilitates the clearance of large and localized extracellular K^+ elevations. Since these K^+ elevations are generally associated with pathophysiological conditions, future experiments could investigate if the opening of astrocytic gap junction channels can be used to attenuate pathophysiological conditions. For this purpose, pharmacological agents that acutely open gap junction channels would be required. For instance, those gap junction openers could be used in combination with an animal model that was shown to mimic human MTLE (Bedner et al., 2015). In accordance to our hypothesis, the acute application of the gap junction openers before or during the induction of epileptic activity would attenuate the excessive accumulation of extracellular K^+. Consequently, a reduced severity or number of epileptic seizures would be expected. These experiments could provide new information about gap junction channels as a therapeutic target to treat epilepsy.

The mechanisms underlying the proepileptiform effect of rapid astrocyte morphology changes were also investigated in this study by several experimental approaches. These morphology changes resulted in a decreased intracellular volume and a reduced intra- and intercellular diffusivity (Anders, 2016). Astrocytes integrate neuronal activity with intracellular Ca^{2+} signals (Araque et al., 1999). Thus, further experiments employing Ca^{2+} sensitive indicators could reveal if the astrocytic Ca^{2+} signaling is affected by the astrocyte morphology changes. The corresponding results could then serve as a starting point for further experiments.

It was for instance shown that astrocytes release D-serine depending on intracellular Ca^{2+}-signaling and thereby control synaptic plasticity (Henneberger et al., 2010). An altered intracellular Ca^{2+}-signaling could, in turn, alter the D-serine release and modulate postsynaptic activity. Novel fluorescent sensors for D-serine that are currently developed in collaboration with the lab of Colin Jackson could provide new insights about D-serine release during and after epileptiform activity. In addition to D-serine, glycine is also a coagonist of the NMDAR (Johnson and Ascher, 1987). Thus, glycine release might also be of interests for following experiments that could employ a novel fluorescent sensor for glycine (Zhang et al., 2018).

Another aspect to be investigated could be slow NMDAR-mediated inward currents of CA1 pyramidal neurons. These currents were shown to depend on activation of extrasynaptic NMDARs and occur spontaneously or can be evoked by evoking astrocytic Ca^{2+} signaling. (Angulo et al., 2004; Fellin et al., 2004). The induction of astrocytic Ca^{2+} signaling during enhanced neuronal excitability was also associated with slow NMDAR-

mediated inward currents in the entorhinal cortex and promoted ictal discharges (Gómez-Gonzalo et al., 2010). Interestingly, it was further shown by Fellin and colleagues that the slow inward currents can occur highly synchronized in neighboring CA1 pyramidal neurons. These findings were then suggested to serve as an astrocytic feedback mechanism that can modulate neuronal excitation and synchronicity (Fellin et al., 2004). This was further supported by a study that revealed synchronized NMDAR-mediated slow inward currents in CA1 pyramidal neurons when an astrocyte was mechanically stimulated (Angulo et al., 2004). Thus, rapid astrocyte morphology changes might promote slow inward currents, promote neuronal synchronization and thereby facilitate the generation of epileptiform discharges.

Our experiments indicated that the clearance of fast glutamate accumulation evoked by synaptic activity or iontophoretic glutamate application was largely unaffected by epileptiform activity. However, this does not exclude that the resting glutamate levels were affected by the astrocyte morphology changes. Increased resting glutamate levels could be a result of a decreased sensitivity of glutamate transporters or an increased glutamate release from astrocytes. Both scenarios would facilitate neuronal excitability by facilitating glutamate receptor activation. Therefore, additional experiments that probe the time-course of the basal glutamate concentration over the complete experimental time course could reveal important insights about the proepileptiform effect.

We also observed that the excitatory synaptic transmission (fEPSP slopes) was unaffected by inhibiting the inhibitory GABAergic synaptic transmission and, in turn, by the astrocyte morphology changes. In contrast, action potential firing was drastically increased represented by the increased amplitude and number of population spikes. Thus, it could be interesting to probe if the transformation of the synaptic potentials into action potential firing is facilitated by the astrocyte morphology changes. To test this possibility, the ratio of the fEPSP slope and the population spike amplitude will be monitored over the complete experimental time course. After the inhibition of the GABAergic synaptic transmission and the induction of epileptiform activity, the ratio should increase. Conversely, if astrocyte morphology changes facilitate action potential firing, the acute inhibition of the morphology changes is expected to attenuate the ratio increase.

Taken together, my study provided new insights about the role of astrocytic gap junction channels for extracellular K^+ clearance. In addition, I revealed possible candidates that underlie the proepileptiform effect of rapid astrocyte morphology changes. Furthermore, my work provides interesting aspects that could serve as the basis for future studies.

8 Appendix

In addition to the two main aspects that were already addressed in this thesis, I participated on a few side projects that will be briefly introduced in the following chapters. First, the consequences of astrocyte hyperactivity on synaptic transmission and plasticity in an Alzheimer's disease model was investigated by electrophysiological tests of acute hippocampal slices (Reichenbach et al., 2018). Second, the impact of the genetic deletion of the chemokine CCL17 was also tested by probing synaptic transmission and plasticity in acute hippocampal slices (Fülle et al., 2018). Finally, I participated in collaboration with Dr. D. Minge in the development of a novel fluorescent sensor for glycine (Zhang et al., 2018).

8.1 Consequences of astrocyte hyperactivity on hippocampal synaptic transmission and plasticity in an Alzheimer's disease model

These experiments were part of a study that addressed the consequences of P_2Y1 receptor mediated astrocyte hyperactivity in the APP/PS1 Alzheimer's disease mouse model. This mouse model comprises a mutation of the amyloid precursor protein (APP) and presenilin 1 (PS1) which results in the formation of amyloid-β plaques, a characteristic of Alzheimer's disease. A previous study found that astrocytes in these APP/PS1 mice exhibit hyperactive Ca^{2+} activity. This hyperactivity was most prominent close to the amyloid-β plaques and was mediated by P_2Y1 receptor activation (Delekate et al., 2014). Thus, the effect of a P_2Y1 receptor inhibition on the cellular and behavioral level was investigated. Interestingly, it was revealed in the present study by Reichenbach and colleagues that the P_2Y1 receptor expression increased with age significantly in the cortex and hippocampus of APP/PS1 mice. As previously reported (Delekate et al., 2014), this was accompanied by hyperactive cortical and hippocampal astrocytes. Furthermore, the hyperactivity of cortical astrocytes in APP/PS1 mice was diminished after the chronic intracerebroventricularly application of the P_2Y1 receptor inhibitor MRS2179 for 6 weeks. This was also accompanied by an improved performance in a spatial learning task compared to untreated mice (Reichenbach et al., 2018). Since an impaired LTP (Chapter1.5.3) was already previously observed in the hippocampus of APP/PS1 mice (Gengler et al., 2010), it was probed if this was also present here and if the acute inhibition of P_2Y1 receptors could restore this impairment.

For this purpose, 300 µM thick hippocampal slices from 8-10-month-old wild-type (WT) and APP/PS1 mice were obtained. Field recordings in the CA1 str. radiatum were then performed in the interface-type chamber as described above (Chapter 3.4.2). In order to probe the basal synaptic transmission, fEPSPs were evoked by single stimulations of SCs (15 s interval) for 10 minutes with a stimulation intensity that was adjusted to obtain a half maximum fEPSP amplitude (Figure 41A). Interestingly, the basal synaptic transmission, quantified by the average slope of the fEPSPs during the baseline period, was significantly reduced in hippocampal slices of APP/PS1 mice compared to WT mice (Figure 41E, Left panel). Importantly, the stimulation intensities used for WT were not different from those used for hippocampal slices of APP/PS1 mice (WT, 66.16 ± 3.40 µA, n = 12; APP/PS1, 69.38 ± 7.64 µA, n = 8, p = 0.689, two-sample Student's t-test). Next, LTP was induced by stimulating SCs three times at an interval of one minute with a theta-burst stimulation (TBS). During TBS, eight stimulation trains consisting of four stimuli (100 Hz) were applied at a frequency of 5 Hz. Afterwards, single stimulations were again applied for 30 minutes to monitor the potentiated synaptic transmission (Figure 41C). As the examples in Figure 41A depict, the TBS led to potentiated fEPSPs in hippocampal slices from WT and APP/PS1 mice. However, this potentiation of the fEPSP slope was less pronounced in hippocampal slices of APP/PS1 compared to WT (Figure 41E, right panel). These experiments were then repeated in the presence of 30 µM of the P_2YR1 antagonist MRS2179. Again, fEPSPs were evoked during baseline conditions and after the potentiation by the TBS (Figure 41B). In contrast to the experiments in the absence of MRS2179, the basal synaptic transmission in hippocampal slices of WT mice was not different from APP/PS1 mice (Figure 41F, left panel). Again, the used stimulation intensities were similar in both groups (WT, 39.71 ± 10.35 µA, n = 7; APP/PS1, 46.82 ± 5.85 µM, n = 11, p = 0.527, two-sample Student's t-test). Even more importantly, the potentiation of the synaptic transmission by the TBS was no longer different between hippocampal slices of WT and APP/PS1 mice (Figure 41D&F, right panel). In summary, these experiments indicate that the impaired synaptic transmission and plasticity in APP/PS1 mice could be restored by the acute inhibition of P_2YR1. Since LTP is considered as the cellular correlate of learning and memory, the observed effect in vitro and the diminished astrocyte hyperactivity in vivo might explain the improved cognitive performance after long-term P_2YR1 inhibition (Reichenbach et al., 2018). It will be interesting to reveal the underlying mechanism that linked the astrocyte hyperactivity and impaired synaptic plasticity. Astrocytes are known to release several gliotransmitter in a Ca^{2+}-dependent manner (Sahlender et al., 2014) including D-serine, which was shown to underly LTP in the hippocampus (Henneberger et al., 2010). Thus, probing astrocytic D-serine release in APP/PS1 mice could be the first target for future studies.

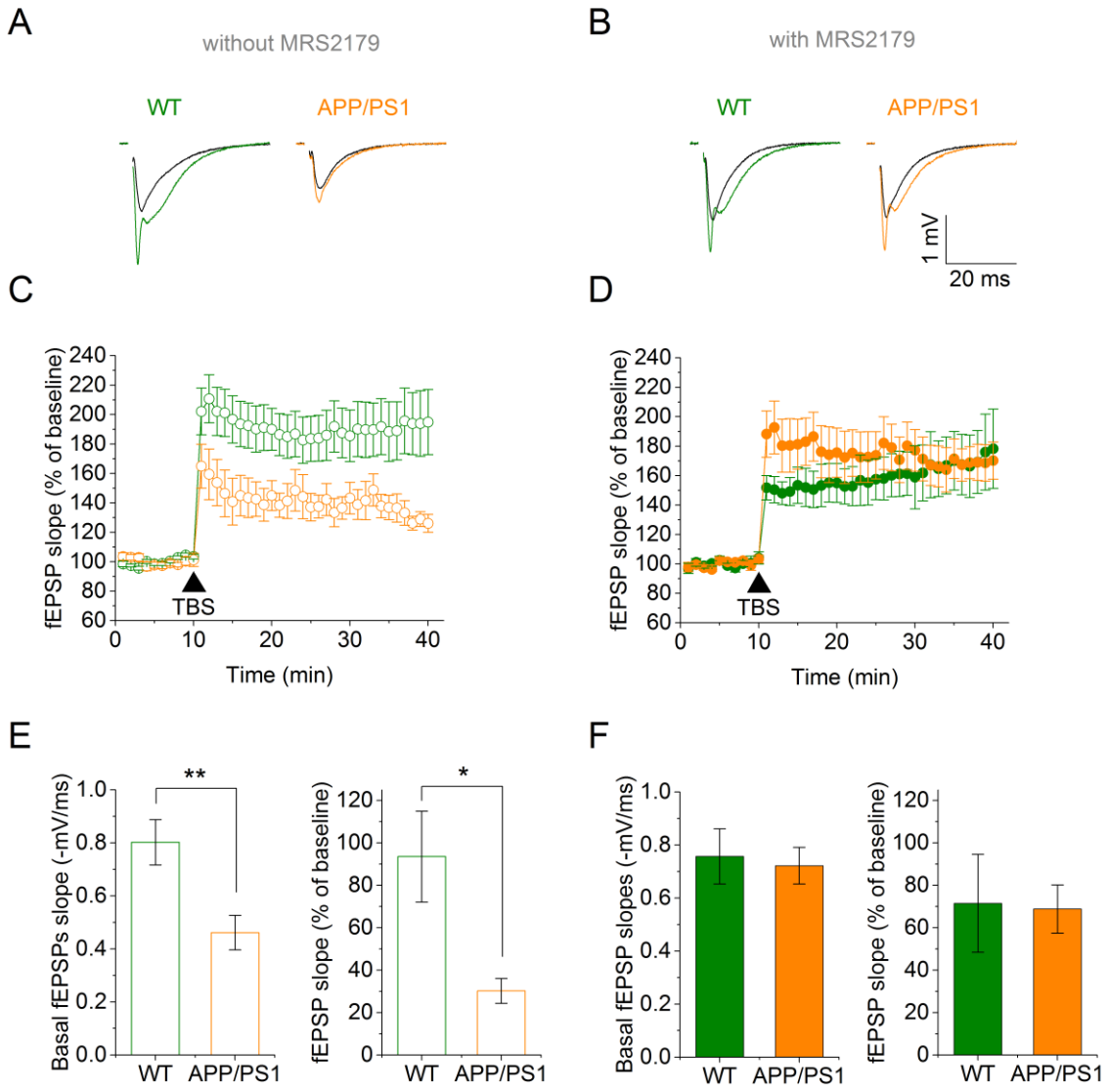

Figure 41 Synaptic transmission and plasticity in hippocampal slices of APP/PS1 mice was restored by the inhibition of P_2Y1 receptors. A) Field EPSPs evoked by Schaffer collateral stimulation were recorded in the CA1 str. radiatum in the absence or **B)** presence of 30 µM of the P_2Y1 receptor antagonist MRS2179. Field potentials were evoked during a baseline period (black) and after the induction of synaptic plasticity by a theta burst stimulation (TBS) in hippocampal slices of wild-type (WT, green) and APP/PS1 mice (orange). **C&D)** The fEPSP slopes were monitored over time and normalized to their respective baseline values (first 10 minutes) in the absence (**C**) or presence of MRS2179 (**D**). After the baseline period, synaptic plasticity was induced by the TBS that resulted in a potentiation of the fEPSP slopes. **E)** The basal fEPSP slopes (Left panel; WT, -0.802 ± 0.085 mV/ms n = 12, APP/PS1, -0.461 ± 0.065 mV/ms, n = 8, p = 0.00958, two-sample Student's t-test) and the fEPSP slope potentiation (Right panel; WT, 93.49 ± 21.93%, n = 12, APP/PS1, 30.18 ± 5.81%, n = 8, p = 0.0121, Mann–Whitney U test) were significantly reduced in hippocampal slices of APP/PS1 mice compared to WT in the absence of MRS2179. **F)** In the presence of MRS2179, no significant differences between the basal fEPSP slopes (Left panel; WT, -0.757 ± 0.104 mV/ms, n = 8, APP/PS1, -0.722 ± 0.069 mV/ms, n = 11, p = 0.776, two-sample Student's t-test) and the fEPSP slope potentiation (Right panel; WT, 71.46 ± 23.06%, n =8 12, APP/PS1, 68.78 ± 11.39%, n = 11, p = 0.911, two-sample Student's t-test) were observed between hippocampal slices of WT and APP/PS1 mice.

8.2 Impact of the chemokine CCL17 deficiency on hippocampal synaptic transmission and plasticity

Chemokines belong to the family of cytokines and control the migration and positioning of immune cells (Zlotnik and Yoshie, 2012). In the CNS, chemokines and their receptors were found to be expressed by several cell types including microglia, astrocytes and neurons (Rostène et al., 2011). The present study was interested in the chemokine-dependent interaction of neurons and microglia (Fülle et al., 2018). Microglia represent the resident immune cell of the CNS that exhibit highly ramified processes in order to monitor their microenvironment for damage or injury. They are known to be involved in controlling neuronal survival and synapse elimination. When microglia become activated by proinflammatory cytokines that are released during tissue damage or infection, microglia change their morphology, migrate towards the inflammatory site and remove dying cells or protein aggregates (Nayak et al., 2014). During those conditions, neurons were shown to upregulate specific chemokines in order to communicate with the activated microglia. The present study addressed the role of the chemokine CCL17 that is known to promote inflammation in skin allergy. Interestingly, the genetic deletion of the receptor for CCL17 induced behavioral abnormalities of mice indicating a function for CCL17 also in the brain (Ambrée et al., 2016). Indeed, CCL17 in the murine CNS was predominantly found in a subset of CA1 pyramidal neurons in the hippocampus. The genetic deletion of CCL17 resulted in a reduced number of hippocampal microglia with an altered morphology that resembled the morphology of activated microglia (Fülle et al., 2018). Since the depletion of microglia was shown to impact learning and synaptic functions (Parkhurst et al., 2013), it was tested if synaptic transmission and plasticity was affected in the CCL17-deficient mice. For this purpose, similar experiments as described in the previous chapter were performed with hippocampal slices obtained from 8-12-weeks-old wild-type (WT) and CCL17-deficient mice (CCL17KO). SCs were stimulated with paired pulses (20 Hz) in order to probe the presynaptic release probability. Interestingly, the basal synaptic transmission in hippocampal slices from CCL17KO mice was significantly increased compared to WT mice (Figure 42A). However, the PPR, an indirect determinant for the presynaptic release probability, and LTP in hippocampal slices of WT mice were not different from CCL17KO mice (Figure 42B&C). Since it was shown that synaptic transmission was facilitated during systemic inflammatory conditions, it was further tested if the CCL17 deficiency also has an impact during those conditions (Galic et al., 2008; Shen et al., 2016). Thus, WT and CCL17KO mice were injected i.p. 16h before the experiments with lipopolysaccharides (LPS) that are known to evoke a systemic inflammation, the production of inflammatory cytokines and also the activation of microglia (Dantzer et al., 2008; Hoogland et al., 2015). Indeed, microglia in hippocampal slices of

WT mice exhibited an altered morphology after LPS treatment that resembled the morphology of microglia in hippocampal slices of untreated CCL17KO mice. In contrast, the microglia morphology in hippocampal slices from LPS-treated CCL17KO mice was not altered compared to the untreated CCL17KO mice (Fülle et al., 2018). Similar to the untreated hippocampal slices (Figure 42A-C), PPR and LTP in hippocampal slices of LPS-treated WT mice were not significantly different from LPS-treated CCL17KO mice (Figure 42E&F). Interestingly, the previously observed facilitated basal synaptic transmission in CCL17KO mice compared to WT mice was not observed when the mice were treated with LPS (Figure 42D). Taken together, these results indicate that during homeostatic conditions (no systemic inflammation) CCL17 deficiency facilitated synaptic transmission. This was presumably mediated by a postsynaptic mechanism like an increased synapse number, since presynaptic neurotransmitter release probability seemed to be unaffected. Thus, it was suggested that CCL17 expression is required to maintain the typical 'resting' state of microglia during homeostatic conditions. On the other hand, microglia of WT mice acquired an activated phenotype in systemic inflammatory conditions while microglia of CCL17 deficient mice showed no further morphological modifications. In addition, no difference of the basal synaptic transmission in hippocampal slices of WT and CCL17KO mice was observed indicating that the basal synaptic transmission in WT mice was upregulated and CCL17 had no additional inhibitory effect during these inflammatory conditions. Further studies will be required to uncover the mechanism how CCL17 attenuated the synaptic transmission during homeostatic conditions.

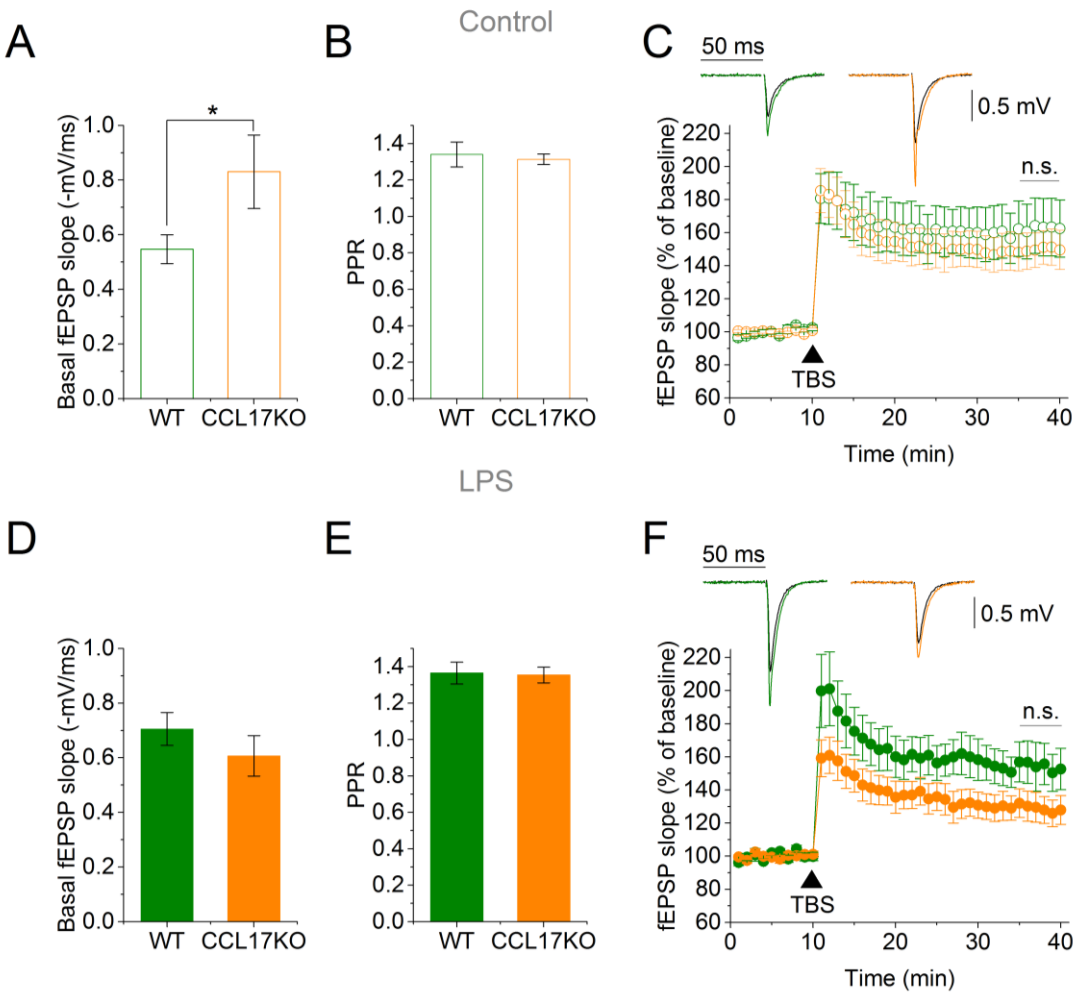

Figure 42 CCL17 deficiency and synaptic transmission and plasticity. A-C) Field EPSPs evoked by Schaffer collateral stimulation were recorded in the CA1 str. radiatum of hippocampal slices from WT or CCL17-deficient mice injected i.p. with phosphate buffered saline. **A)** The basal fEPSP slopes recorded in hippocampal slices from CCL17-deficient mice were significantly increased compared to WT mice (WT, -0.54 ± 0.83 mV/ms, n = 11, CCL17KO, -0.83 ± 0.13 mV/ms, n = 10, p = 0.0221, Mann–Whitney U test). **B)** The paired-pulse ratio (PPR) was not affected by the CCL17 deficiency (WT, 1.34 ± 0.69, n = 11; CCL17KO, 1.31 ± 0.03, n = 10, p = 0.729, two-sample Student's t-test). **C)** After a baseline period, synaptic plasticity was induced by a theta-burst stimulation (TBS) that resulted in the potentiation of the fEPSP slopes. Example fEPSP are depicted in the inset (black, baseline; green, WT after TBS; orange, CCL17KO after TBS). The potentiation of the fEPSP slopes 30 minutes after the TBS in hippocampal slices of WT mice were not different from CCL17KO mice (WT, 162.9 ± 16.93%, n = 11; CCL17KO, 150.1 ± 10.8%, n = 10; p = 0.699, Mann–Whitney U test). **D-F**) When the mice were injected i.p with LPS, the **(D)** basal fEPSP slopes (WT, -0.71 ± 0.06, n = 10; CCL17KO, -0.61 ± 0.07 mV/ms, n = 12; p = 0.315, Mann–Whitney U test), **(E)** the PPR (WT, 1.36 ± 0.06, n = 10; CCL17KO, 1.35 ± 0.04, n = 12, p = 0.921, Mann–Whitney U test) and the **(F)** TBS-induced potentiation (149.76 ± 12.02%, n = 10; CCL17KO, 128.31 ± 8.48%, n = 12; p = 0.151, two-sample Student's t-test) in hippocampal slices from WT mice were not different from CCL17KO mice. Inset as in C).

8.3 Characterization of a novel optical sensor for glycine

The experiments presented in this chapter were conducted in collaboration with Dr. D. Minge and were part of a study that described a novel fluorescence sensor for glycine (Zhang et al., 2018). Glycine is an important neurotransmitter in the CNS that can activate inhibitory glycine receptors or act as a co-agonist on NMDARs (Betz, 1991; Johnson and Ascher, 1987; Schell, 2004). So far, studying extracellular glycine dynamics is limited by the experimental approaches. Electrophysiological recordings of the NMDAR activity provided a lot of insights in the co-agonist signaling, but it remains an indirect readout that lacks any spatial resolution and discrimination between different co-agonists. In contrast, microdialysis approaches allow a discrimination between the different co-agonists but also have little spatial resolution. Thus, this study aimed to develop a novel fluorescence sensor that allows direct monitoring of the spatial and temporal glycine dynamics in brain tissue. This sensor (GlyFS) is composed of two fluorophores attached to a glycine-binding domain that induces a conformational change upon glycine binding. The used fluorophores were the enhanced cyan fluorescent protein (ECFP) and Venus-fluorescent protein (Venus), a fluorophore-pair that can undergo Förster resonance energy transfer (FRET) (Zhang et al., 2018). FRET is a physical phenomenon in which an excited donor fluorophore transfers its excitation energy to an adjacent acceptor fluorophore that, in turn, emits its specific fluorescence. The efficiency of FRET is highly dependent on the distance between donor and acceptor and, thus, can be modulated by a conformational change of the sensor (Bajar et al., 2016). It was shown that the ratio of the fluorescence intensities (R) of ECFP and Venus increased with increasing glycine concentrations with a K_D and a dynamic range of ~20µM and ~20%, respectively. This feature was then used to measure the extracellular glycine levels during resting conditions and after the stimulation of CA3/1 SC synapses with a HFS in hippocampal slices. This stimulation evoked a significant increase of the glycine concentration as indicated by an increased fluorescence intensity ratio (Zhang et al., 2018). Since changes of the extracellular K^+ and Ca^{2+} concentration as well as pH changes were observed previously during neuronal activity (Sinning and Hübner, 2013), it was tested if those changes can impact on the fluorescence intensity ratio independently of glycine.

For this purpose, GlyFS diluted in phosphate- buffered saline (PBS) or HEPES-buffer was imaged at room temperature with an excitation wavelength of 800 nm at the FV10MP two-photon microscope system (Olympus, Japan) using the photon-count function in order to determine the fluorescence intensities of the two fluorophores. First, the ratio of the two fluorophore fluorescence intensities (R) was determined in the presence of different K^+ and Ca^{2+} concentrations or pH values, respectively, but in the absence of glycine.

Finally, glycine was added (5 mM) to saturate GlyFS and to obtain the maximal fluorescence ratio (R_{max}). The fluorescence intensity ratios (R) in the absence of glycine were then normalized to the maximal fluorescence ratio (R_{max}) in order to account for differences of the absolute fluorescence intensities between the single experiments. In order to test if GlyFS was affected by extracellular K^+, the GlyFS ratio (R/R_{max}) was determined (in PBS, pH 7.4) in the presence of a physiological K^+ concentration (2.7 mM) and a concentration that was described as the 'ceiling K^+ concentration' reached during neuronal activity (Heinemann and Lux, 1977). However, the GlyFS ratio was not affected by increasing the K^+ concentration (Figure 43A). In the next set of experiments, the Ca^{2+} concentration was reduced from 2.0 to 1.8 mM which represents the decrease of the extracellular Ca^{2+} concentration that is expected during a 100-pulse HFS of SCs (Zhang et al., 2018). For this purpose, the concentration of the in PBS-diluted GlyFS was increased using centricons (Vivaspin 500, 10 kDa cutoff, Sartorius Stedim Biotech) in order to resuspend the GlyFS in a HEPES buffer. The HEPES buffer contained 2mM Ca^{2+} and 1.8 mM Mg^{2+} (similar to the aCSF in the slice experiments, the free Ca^{2+} and Mg^{2+} concentrations were estimated using the WebMax Chelator[2]). In order to reduce the Ca^{2+} concentration from 2.0 to 1.8 mM, Ca^{2+}-free HEPES buffer was added to the GlyFS containing buffer. Again, the GlyFS ratio was not affected (Figure 43B). Finally, it was tested if GlyFS reacts to changes of the pH since neuronal stimulation can led to an extracellular acidification with following alkalization (Sinning and Hübner, 2013). This was for example observed for mouse motor nerve terminals (Zhang et al., 2010) and the hippocampus. In the hippocampus, a single pulse SC stimulation evoked an initial and fast acidification in the str. radiatum of <0.005 pH units. This was followed by longer lasting alkalization of ~0.01 pH units (Krishtal et al., 1987). Furthermore, prolonged SC stimulation at 2 Hz for several seconds led to an alkalization of ~0.1 pH units (Tong et al., 2006) and a HFS with 10 pulses at 100 Hz resulted in a alkalization of roughly 0.04-0.05 ΔpH (Makani and Chesler, 2007). Thus, the pH-sensitivity of GlyFS was tested by changing the pH from 7.4 to 7.2 to 7.0 (in PBS by adding HCl) but no significant ratio change was observed (Figure 43C).

In summary, these experiments indicate that the observed GlyFS ratio increase during the HFS of Schaffer collateral was indeed evoked by an increase of extracellular glycine levels and not by other mechanism.

[2]https://somapp.ucdmc.ucdavis.edu/pharmacology/bers/maxchelator/webmaxc/webmaxcS.htm

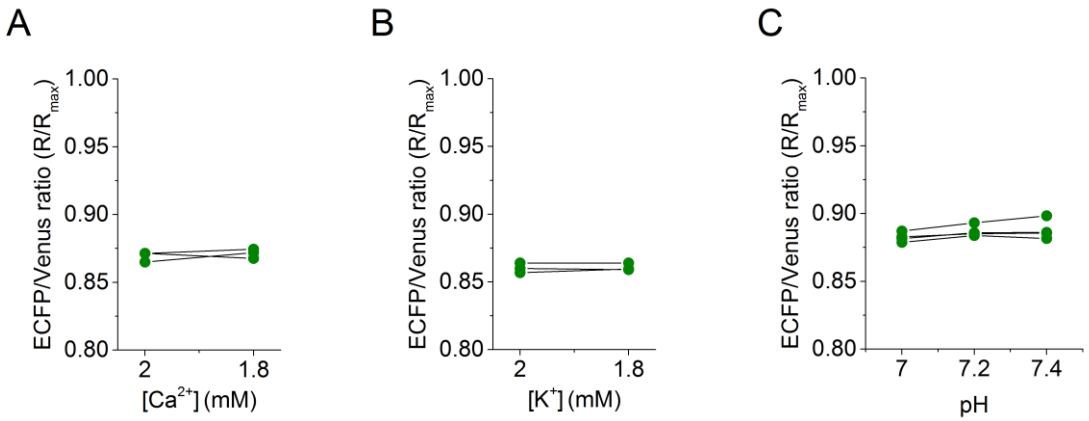

Figure 43 GlyFS ratio in response to different K^+ and Ca^{2+} concentrations and pH changes. A) Increasing the K^+ concentration by 10 mM did not significantly affect the GlyFS ratio (R/R_{max}) (n = 3, p = 0.61, paired Student's t-test). **B)** Lowering the Ca^{2+} concentration by 0.2 mM had no effect on the GlyFS ratio (n = 3, p = 0.57, paired Student's t-test). **C)** The GlyFS ratio was also not affected by pH changes from 7.4 to 7.0 (n = 4, p = 0.13, one-way repeated measures ANOVA). Analysis performed by Dr. C. Henneberger.

9 References

Al-Osta, I., Mucha, M., Pereda, D., Piqué-Gili, M., Okorocha, A.E., Thomas, R., and Hartell, N.A. (2018). Imaging Calcium in Hippocampal Presynaptic Terminals With a Ratiometric Calcium Sensor in a Novel Transgenic Mouse. Front. Cell. Neurosci. *12*, 209.

Amano, M., Nakayama, M., and Kaibuchi, K. (2010). Rho-Kinase/ROCK: A Key Regulator of the Cytoskeleton and Cell Polarity. Cytoskelet. Hoboken Nj *67*, 545–554.

Ambrée, O., Klassen, I., Förster, I., Arolt, V., Scheu, S., and Alferink, J. (2016). Reduced locomotor activity and exploratory behavior in CC chemokine receptor 4 deficient mice. Behav. Brain Res. *314*, 87–95.

Anders, S. (2016). Rapid astrocyte morphology changes during epileptogenesis in the rodent hippocampus. Rheinische Friedrich-Wilhelms-Universität Bonn.

Anders, S., Minge, D., Griemsmann, S., Herde, M.K., Steinhäuser, C., and Henneberger, C. (2014). Spatial properties of astrocyte gap junction coupling in the rat hippocampus. Philos. Trans. R. Soc. Lond. B. Biol. Sci. *369*, 20130600.

Andersen, P., Sundberg, S.H., Sveen, O., and Wigström, H. (1977). Specific long-lasting potentiation of synaptic transmission in hippocampal slices. Nature *266*, 736–737.

Andersen, P., Morris, R., Amaral, D., O'Keefe, J., Bliss, D. of N.T., and Bliss, T. (2007). The Hippocampus Book (Oxford University Press, USA).

Angulo, M.C., Kozlov, A.S., Charpak, S., and Audinat, E. (2004). Glutamate Released from Glial Cells Synchronizes Neuronal Activity in the Hippocampus. J. Neurosci. *24*, 6920–6927.

Araque, A., Parpura, V., Sanzgiri, R.P., and Haydon, P.G. (1999). Tripartite synapses: glia, the unacknowledged partner. Trends Neurosci. *22*, 208–215.

Armbruster, M., Hanson, E., and Dulla, C.G. (2016). Glutamate Clearance Is Locally Modulated by Presynaptic Neuronal Activity in the Cerebral Cortex. J. Neurosci. Off. J. Soc. Neurosci. *36*, 10404–10415.

Aronica, E., Vliet, E.A.V., Mayboroda, O.A., Troost, D., Silva, F.H.L.D., and Gorter, J.A. (2000). Upregulation of metabotropic glutamate receptor subtype mGluR3 and mGluR5 in reactive astrocytes in a rat model of mesial temporal lobe epilepsy. Eur. J. Neurosci. *12*, 2333–2344.

Ascher, P., and Nowak, L. (1988). The role of divalent cations in the N-methyl-D-aspartate responses of mouse central neurones in culture. J. Physiol. *399*, 247–266.

Asztely, F., Erdemli, G., and Kullmann, D.M. (1997). Extrasynaptic Glutamate Spillover in the Hippocampus: Dependence on Temperature and the Role of Active Glutamate Uptake. Neuron *18*, 281–293.

Bajar, B.T., Wang, E.S., Zhang, S., Lin, M.Z., and Chu, J. (2016). A Guide to Fluorescent Protein FRET Pairs. Sensors *16*, 1488.

Bak, L.K., Schousboe, A., and Waagepetersen, H.S. (2006). The glutamate/GABA-glutamine cycle: aspects of transport, neurotransmitter homeostasis and ammonia transfer. J. Neurochem. *98*, 641–653.

Balestrino, M., Aitken, P.G., and Somjen, G.G. (1986). The effects of moderate changes of extracellular K+ and Ca2+ on synaptic and neural function in the CA1 region of the hippocampal slice. Brain Res. *377*, 229–239.

Ballanyi, K., Grafe, P., and ten Bruggencate, G. (1987). Ion activities and potassium uptake mechanisms of glial cells in guinea-pig olfactory cortex slices. J. Physiol. *382*, 159–174.

Barbour, B., Brew, H., and Attwell, D. (1988). Electrogenic glutamate uptake in glial cells is activated by intracellular potassium. Nature *335*, 433–435.

Bazargani, N., and Attwell, D. (2016). Astrocyte calcium signaling: the third wave. Nat. Neurosci. *19*, 182–189.

Bazzigaluppi, P., Dufour, S., and Carlen, P.L. (2015). Wide field fluorescent imaging of extracellular spatiotemporal potassium dynamics in vivo. NeuroImage *104*, 110–116.

Bazzigaluppi, P., Weisspapir, I., Stefanovic, B., Leybaert, L., and Carlen, P.L. (2017). Astrocytic gap junction blockade markedly increases extracellular potassium without causing seizures in the mouse neocortex. Neurobiol. Dis. *101*, 1–7.

Bedner, P., Dupper, A., Hüttmann, K., Müller, J., Herde, M.K., Dublin, P., Deshpande, T., Schramm, J., Häussler, U., Haas, C.A., et al. (2015). Astrocyte uncoupling as a cause of human temporal lobe epilepsy. Brain *138*, 1208–1222.

Bender, A.S., and Norenberg, M.D. (1994). Calcium dependence of hypoosmotically induced potassium release in cultured astrocytes. J. Neurosci. *14*, 4237–4243.

Bernardinelli, Y., Randall, J., Janett, E., Nikonenko, I., König, S., Jones, E.V., Flores, C.E., Murai, K.K., Bochet, C.G., Holtmaat, A., et al. (2014). Activity-Dependent Structural Plasticity of Perisynaptic Astrocytic Domains Promotes Excitatory Synapse Stability. Curr. Biol. *24*, 1679–1688.

Betz, H. (1991). Glycine receptors: heterogeneous and widespread in the mammalian brain. Trends Neurosci. *14*, 458–461.

Bischof, H., Rehberg, M., Stryeck, S., Artinger, K., Eroglu, E., Waldeck-Weiermair, M., Gottschalk, B., Rost, R., Deak, A.T., Niedrist, T., et al. (2017). Novel genetically encoded fluorescent probes enable real-time detection of potassium in vitro and in vivo. Nat. Commun. *8*, 1422.

Blaesse, P., Airaksinen, M.S., Rivera, C., and Kaila, K. (2009). Cation-Chloride Cotransporters and Neuronal Function. Neuron *61*, 820–838.

Bliss, T.V.P., and Lømo, T. (1973). Long-lasting potentiation of synaptic transmission in the dentate area of the anaesthetized rabbit following stimulation of the perforant path. J. Physiol. *232*, 331–356.

Boddum, K., Jensen, T.P., Magloire, V., Kristiansen, U., Rusakov, D.A., Pavlov, I., and Walker, M.C. (2016). Astrocytic GABA transporter activity modulates excitatory neurotransmission. Nat. Commun. *7*, 1–10.

Bowser, D.N., and Khakh, B.S. (2004). ATP Excites Interneurons and Astrocytes to Increase Synaptic Inhibition in Neuronal Networks. J. Neurosci. *24*, 8606–8620.

Bradbury, M., and Kleeman, C. (1967). Stability of the potassium content of cerebrospinal fluid and brain. Am. J. Physiol.-Leg. Content *213*, 519–528.

Breithausen, B., Kautzmann, S., Boehlen, A., Steinhäuser, C., and Henneberger, C. (2020). Limited contribution of astroglial gap junction coupling to buffering of extracellular K+ in CA1 stratum radiatum. Glia *68*, 918–931.

Bukauskas, F.F., and Verselis, V.K. (2004). Gap junction channel gating. Biochim. Biophys. Acta BBA - Biomembr. *1662*, 42–60.

Bushong, E.A., Martone, M.E., Jones, Y.Z., and Ellisman, M.H. (2002). Protoplasmic astrocytes in CA1 stratum radiatum occupy separate anatomical domains. J. Neurosci. Off. J. Soc. Neurosci. *22*, 183–192.

Cala, P.M. (1977). Volume regulation by flounder red blood cells in anisotonic media. J. Gen. Physiol. *69*, 537–552.

Carmignoto, G., and Haydon, P.G. (2012). Astrocyte calcium signaling and epilepsy. Glia *60*, 1227–1233.

Cavelier, P., and Attwell, D. (2005). Tonic release of glutamate by a DIDS-sensitive mechanism in rat hippocampal slices. J. Physiol. *564*, 397–410.

Chang, B.S., and Lowenstein, D.H. (2003). Epilepsy. N. Engl. J. Med. *349*, 1257–1266.

Chen, R.-C., Huang, Y.-H., and How, S.-W. (1986). Systemic penicillin as an experimental model of epilepsy. Exp. Neurol. *92*, 533–540.

Chever, O., Djukic, B., McCarthy, K.D., and Amzica, F. (2010). Implication of Kir4.1 Channel in Excess Potassium Clearance: An In Vivo Study on Anesthetized Glial-Conditional Kir4.1 Knock-Out Mice. J. Neurosci. *30*, 15769–15777.

Chever, O., Pannasch, U., Ezan, P., and Rouach, N. (2014a). Astroglial connexin 43 sustains glutamatergic synaptic efficacy. Philos. Trans. R. Soc. Lond. B. Biol. Sci. *369*, 20130596.

Chever, O., Lee, C.-Y., and Rouach, N. (2014b). Astroglial connexin43 hemichannels tune basal excitatory synaptic transmission. J. Neurosci. Off. J. Soc. Neurosci. *34*, 11228–11232.

Chever, O., Dossi, E., Pannasch, U., Derangeon, M., and Rouach, N. (2016). Astroglial networks promote neuronal coordination. Sci Signal *9*, ra6–ra6.

Clasadonte, J., Dong, J., Hines, D.J., and Haydon, P.G. (2013). Astrocyte control of synaptic NMDA receptors contributes to the progressive development of temporal lobe epilepsy. Proc. Natl. Acad. Sci. *110*, 17540–17545.

Coles, J.A., and Orkand, R.K. (1983). Modification of potassium movement through the retina of the drone (Apis mellifera male) by glial uptake. J. Physiol. *340*, 157–174.

Collingridge, G.L., Kehl, S.J., and McLennan, H. (1983). Excitatory amino acids in synaptic transmission in the Schaffer collateral-commissural pathway of the rat hippocampus. J. Physiol. *334*, 33–46.

Collingridge, G.L., Gage, P.W., and Robertson, B. (1984). Inhibitory post-synaptic currents in rat hippocampal CA1 neurones. J. Physiol. *356*, 551–564.

Connors, B.W. (2012). Tales of a Dirty Drug: Carbenoxolone, Gap Junctions, and Seizures. Epilepsy Curr. *12*, 66–68.

Connors, B.W., and Long, M.A. (2004). Electrical synapses in the mammalian brain. Annu. Rev. Neurosci. *27*, 393–418.

Connors, B., Dray, A., Fox, P., Hilmy, M., and Somjen, G. (1979). LSD's effect on neuron populations in visual cortex gauged by transient responses of extracellular potassium evoked by optical stimuli. Neurosci. Lett. *13*, 147–150.

Cornell-Bell, A.H., and Finkbeiner, S.M. (1991). Ca2+ waves in astrocytes. Cell Calcium *12*, 185–204.

Cornell-Bell, A.H., Finkbeiner, S.M., Cooper, M.S., and Smith, S.J. (1990). Glutamate induces calcium waves in cultured astrocytes: long-range glial signaling. Science *247*, 470–473.

Curia, G., Longo, D., Biagini, G., Jones, R.S.G., and Avoli, M. (2008). The pilocarpine model of temporal lobe epilepsy. J. Neurosci. Methods *172*, 143–157.

de Curtis, M., and Avanzini, G. (2001). Interictal spikes in focal epileptogenesis. Prog. Neurobiol. *63*, 541–567.

de Curtis, M., Uva, L., Gnatkovsky, V., and Librizzi, L. (2018). Potassium dynamics and seizures: Why is potassium ictogenic? Epilepsy Res. *143*, 50–59.

Dahl, E., Manthey, D., Chen, Y., Schwarz, H.-J., Chang, Y.S., Lalley, P.A., Nicholson, B.J., and Willecke, K. (1996). Molecular Cloning and Functional Expression of Mouse Connexin-30,a Gap Junction Gene Highly Expressed in Adult Brain and Skin. J. Biol. Chem. *271*, 17903–17910.

D'Ambrosio, R., Gordon, D.S., and Winn, H.R. (2002). Differential Role of KIR Channel and Na+/K+-Pump in the Regulation of Extracellular K+ in Rat Hippocampus. J. Neurophysiol. *87*, 87–102.

Danbolt, N.C. (2001). Glutamate uptake. Prog. Neurobiol. *65*, 1–105.

Dantzer, R., O'Connor, J.C., Freund, G.G., Johnson, R.W., and Kelley, K.W. (2008). From inflammation to sickness and depression: when the immune system subjugates the brain. Nat. Rev. Neurosci. *9*, 46–56.

Das, A., Wallace, G.C., Holmes, C., McDowell, M.L., Smith, J.A., Marshall, J.D., Bonilha, L., Edwards, J.C., Glazier, S.S., Ray, S.K., et al. (2012). Hippocampal tissue of patients with refractory temporal lobe epilepsy is associated with astrocyte activation, inflammation, and altered expression of channels and receptors. Neuroscience *220*, 237–246.

De Pina-Benabou, M.H., Srinivas, M., Spray, D.C., and Scemes, E. (2001). Calmodulin kinase pathway mediates the K+-induced increase in Gap junctional communication between mouse spinal cord astrocytes. J. Neurosci. Off. J. Soc. Neurosci. *21*, 6635–6643.

Debanne, D., Guérineau, N.C., Gähwiler, B.H., and Thompson, S.M. (1996). Paired-pulse facilitation and depression at unitary synapses in rat hippocampus: quantal fluctuation affects subsequent release. J. Physiol. *491*, 163–176.

Delekate, A., Füchtemeier, M., Schumacher, T., Ulbrich, C., Foddis, M., and Petzold, G.C. (2014). Metabotropic P2Y1 receptor signalling mediates astrocytic hyperactivity in vivo in an Alzheimer's disease mouse model. Nat. Commun. *5*, 1–14.

Demarque, M., Villeneuve, N., Manent, J.-B., Becq, H., Represa, A., Ben-Ari, Y., and Aniksztejn, L. (2004). Glutamate Transporters Prevent the Generation of Seizures in the Developing Rat Neocortex. J. Neurosci. *24*, 3289–3294.

Deng, W., Aimone, J.B., and Gage, F.H. (2010). New neurons and new memories: how does adult hippocampal neurogenesis affect learning and memory? Nat. Rev. Neurosci. *11*, 339–350.

Dermietzel, R., Traub, O., Hwang, T.K., Beyer, E., Bennett, M.V., Spray, D.C., and Willecke, K. (1989). Differential expression of three gap junction proteins in developing and mature brain tissues. Proc. Natl. Acad. Sci. U. S. A. *86*, 10148–10152.

Diamond, J.S., and Jahr, C.E. (2000). Synaptically Released Glutamate Does Not Overwhelm Transporters on Hippocampal Astrocytes During High-Frequency Stimulation. J. Neurophysiol. *83*, 2835–2843.

Dichter, M., and Spencer, W.A. (1969). Penicillin-induced interictal discharges from the cat hippocampus. I. Characteristics and topographical features. J. Neurophysiol. *32*, 649–662.

Djukic, B., Casper, K.B., Philpot, B.D., Chin, L.-S., and McCarthy, K.D. (2007). Conditional Knock-Out of Kir4.1 Leads to Glial Membrane Depolarization, Inhibition of Potassium and Glutamate Uptake, and Enhanced Short-Term Synaptic Potentiation. J. Neurosci. *27*, 11354–11365.

During, M.J., and Spencer, D.D. (1993). Extracellular hippocampal glutamate and spontaneous seizure in the conscious human brain. The Lancet *341*, 1607–1610.

Egawa, K., Yamada, J., Furukawa, T., Yanagawa, Y., and Fukuda, A. (2013). Cl− homeodynamics in gap junction-coupled astrocytic networks on activation of GABAergic synapses. J. Physiol. *591*, 3901–3917.

Eid, T., Thomas, M.J., Spencer, D.D., Rundén-Pran, E., Lai, J.C.K., Malthankar, G.V., Kim, J.H., Danbolt, N.C., Ottersen, O.P., and de Lanerolle, N.C. (2004). Loss of glutamine synthetase in the human epileptogenic hippocampus: possible mechanism for raised extracellular glutamate in mesial temporal lobe epilepsy. Lancet Lond. Engl. *363*, 28–37.

Eid, T., Ghosh, A., Wang, Y., Beckström, H., Zaveri, H.P., Lee, T.-S.W., Lai, J.C.K., Malthankar-Phatak, G.H., and de Lanerolle, N.C. (2008). Recurrent seizures and brain pathology after inhibition of glutamine synthetase in the hippocampus in rats. Brain *131*, 2061–2070.

Enkvist, M.O.K., and McCarthy, K.D. (1994). Astroglial Gap Junction Communication Is Increased by Treatment with Either Glutamate or High K+ Concentration. J. Neurochem. *62*, 489–495.

Fellin, T., Pascual, O., Gobbo, S., Pozzan, T., Haydon, P.G., and Carmignoto, G. (2004). Neuronal Synchrony Mediated by Astrocytic Glutamate through Activation of Extrasynaptic NMDA Receptors. Neuron *43*, 729–743.

Fellin, T., Gomez-Gonzalo, M., Gobbo, S., Carmignoto, G., and Haydon, P.G. (2006). Astrocytic Glutamate Is Not Necessary for the Generation of Epileptiform Neuronal Activity in Hippocampal Slices. J. Neurosci. *26*, 9312–9322.

Fisher, R.S., Pedley, T.A., Moody, W.J., and Prince, D.A. (1976). The Role of Extracellular Potassium in Hippocampal Epilepsy. Arch. Neurol. *33*, 76–83.

Förstl, J., Galvan, M., and ten Bruggencate, G. (1982). Extracellular K+ concentration during electrical stimulation of rat isolated sympathetic ganglia, vagus and optic nerves. Neuroscience *7*, 3221–3229.

Freund, T.F., and Buzsáki, G. (1996). Interneurons of the hippocampus. Hippocampus *6*, 347–470.

Fukuda, T., and Kosaka, T. (2000). Gap Junctions Linking the Dendritic Network of GABAergic Interneurons in the Hippocampus. J. Neurosci. *20*, 1519–1528.

Fülle, L., Offermann, N., Hansen, J.N., Breithausen, B., Erazo, A.B., Schanz, O., Radau, L., Gondorf, F., Knöpper, K., Alferink, J., et al. (2018). CCL17 exerts a neuroimmune modulatory function and is expressed in hippocampal neurons. Glia *66*, 2246–2261.

Gage, P.W., and Robertson, B. (1985). Prolongation of inhibitory postsynaptic currents by pentobarbitone, halothane and ketamine in CA1 pyramidal cells in rat hippocampus. Br. J. Pharmacol. *85*, 675–681.

Galic, M.A., Riazi, K., Heida, J.G., Mouihate, A., Fournier, N.M., Spencer, S.J., Kalynchuk, L.E., Teskey, G.C., and Pittman, Q.J. (2008). Postnatal Inflammation Increases Seizure Susceptibility in Adult Rats. J. Neurosci. *28*, 6904–6913.

Gardner-Medwin, A.R. (1983). A study of the mechanisms by which potassium moves through brain tissue in the rat. J. Physiol. *335*, 353–374.

Gengler, S., Hamilton, A., and Hölscher, C. (2010). Synaptic Plasticity in the Hippocampus of a APP/PS1 Mouse Model of Alzheimer's Disease Is Impaired in Old but Not Young Mice. PLOS ONE *5*, e9764.

Genoud, C., Houades, V., Kraftsik, R., Welker, E., and Giaume, C. (2015). Proximity of excitatory synapses and astroglial gap junctions in layer IV of the mouse barrel cortex. Neuroscience *291*, 241–249.

Ghézali, G., Calvo, C.-F., Pillet, L.-E., Llense, F., Ezan, P., Pannasch, U., Bemelmans, A.-P., Manneville, S.E., and Rouach, N. (2018). Connexin 30 controls astroglial polarization during postnatal brain development. Development *145*, dev155275.

Giaume, C., Koulakoff, A., Roux, L., Holcman, D., and Rouach, N. (2010). Astroglial networks: a step further in neuroglial and gliovascular interactions. Nat. Rev. Neurosci. *11*, 87–99.

Gloveli, T., Albrecht, D., and Heinemann, U. (1995). Properties of low Mg2+ induced epileptiform activity in rat hippocampal and entorhinal cortex slices during adolescence. Dev. Brain Res. *87*, 145–152.

Gómez-Gonzalo, M., Losi, G., Chiavegato, A., Zonta, M., Cammarota, M., Brondi, M., Vetri, F., Uva, L., Pozzan, T., Curtis, M. de, et al. (2010). An Excitatory Loop with Astrocytes Contributes to Drive Neurons to Seizure Threshold. PLOS Biol. *8*, e1000352.

Gordon, G.R.J., Baimoukhametova, D.V., Hewitt, S.A., Rajapaksha, W.R.A.K.J.S., Fisher, T.E., and Bains, J.S. (2005). Norepinephrine triggers release of glial ATP to increase postsynaptic efficacy. Nat. Neurosci. *8*, 1078–1086.

Haber, M., Zhou, L., and Murai, K.K. (2006). Cooperative astrocyte and dendritic spine dynamics at hippocampal excitatory synapses. J. Neurosci. Off. J. Soc. Neurosci. *26*, 8881–8891.

Hablitz, J.J., and Heinemann, U. (1987). Extracellular K+ and Ca2+ changes during epileptiform discharges in the immature rat neocortex. Dev. Brain Res. *36*, 299–303.

Hablitz, J.J., and Lundervold, A. (1981). Hippocampal excitability and changes in extracellular potassium. Exp. Neurol. *71*, 410–420.

Haj-Yasein, N.N., Jensen, V., Vindedal, G.F., Gundersen, G.A., Klungland, A., Ottersen, O.P., Hvalby, O., and Nagelhus, E.A. (2011). Evidence that compromised K+ spatial buffering contributes to the epileptogenic effect of mutations in the human Kir4.1 gene (KCNJ10). Glia *59*, 1635–1642.

Halassa, M.M., Fellin, T., Takano, H., Dong, J.-H., and Haydon, P.G. (2007a). Synaptic Islands Defined by the Territory of a Single Astrocyte. J. Neurosci. *27*, 6473–6477.

Halassa, M.M., Fellin, T., and Haydon, P.G. (2007b). The tripartite synapse: roles for gliotransmission in health and disease. Trends Mol. Med. *13*, 54–63.

Harks, E.G.A., Roos, A.D.G. de, Peters, P.H.J., Haan, L.H. de, Brouwer, A., Ypey, D.L., Zoelen, E.J.J. van, and Theuvenet, A.P.R. (2001). Fenamates: A Novel Class of Reversible Gap Junction Blockers. J. Pharmacol. Exp. Ther. *298*, 1033–1041.

Hebb, D.O. (1949). The Organization of Behavior (Wiley).

Heinemann, U., and Lux, H.D. (1975). Undershoots following stimulus-induced rises of extracellular potassium concentration in cerebral cortex of cat. Brain Res. *93*, 63–76.

Heinemann, U., and Lux, H.D. (1977). Ceiling of stimulus induced rises in extracellular potassium concentration in the cerebral cortex of cat. Brain Res. *120*, 231–249.

Heinemann, U., Schaible, H.G., and Schmidt, R.F. (1990). Changes in extracellular potassium concentration in cat spinal cord in response to innocuous and noxious stimulation of legs with healthy and inflamed knee joints. Exp. Brain Res. *79*, 283–292.

Heinemann, U., Gabriel, S., Jauch, R., Schulze, K., Kivi, A., Eilers, A., Kovacs, R., and Lehmann, T.-N. (2000). Alterations of Glial Cell Function in Temporal Lobe Epilepsy. Epilepsia *41*, S185–S189.

Henneberger, C. (2017). Does rapid and physiological astrocyte–neuron signalling amplify epileptic activity? J. Physiol. *595*, 1917–1927.

Henneberger, C., Papouin, T., Oliet, S.H.R., and Rusakov, D.A. (2010). Long-term potentiation depends on release of D-serine from astrocytes. Nature *463*, 232–236.

Herman, M.A., and Jahr, C.E. (2007). Extracellular Glutamate Concentration in Hippocampal Slice. J. Neurosci. *27*, 9736–9741.

Herring, B.E., and Nicoll, R.A. (2016). Long-Term Potentiation: From CaMKII to AMPA Receptor Trafficking. Annu. Rev. Physiol. *78*, 351–365.

Hertz, L. (1965). Possible Role of Neuroglia: A Potassium-Mediated Neuronal – Neuroglial – Neuronal Impulse Transmission System. Nature *206*, 1091–1094.

Heuser, K., Eid, T., Lauritzen, F., Thoren, A.E., Vindedal, G.F., Taubøll, E., Gjerstad, L., Spencer, D.D., Ottersen, O.P., Nagelhus, E.A., et al. (2012). Loss of perivascular Kir4.1 potassium channels in the sclerotic hippocampus of patients with mesial temporal lobe epilepsy. J. Neuropathol. Exp. Neurol. *71*, 814–825.

Higashi, K., Fujita, A., Inanobe, A., Tanemoto, M., Doi, K., Kubo, T., and Kurachi, Y. (2001). An inwardly rectifying K+ channel, Kir4.1, expressed in astrocytes surrounds synapses and blood vessels in brain. Am. J. Physiol.-Cell Physiol. *281*, C922–C931.

Höltje, M., Hoffmann, A., Hofmann, F., Mucke, C., Große, G., Rooijen, N.V., Kettenmann, H., Just, I., and Ahnert-Hilger, G. (2005). Role of Rho GTPase in astrocyte morphology and migratory response during in vitro wound healing. J. Neurochem. *95*, 1237–1248.

Hoogland, I.C.M., Houbolt, C., van Westerloo, D.J., van Gool, W.A., and van de Beek, D. (2015). Systemic inflammation and microglial activation: systematic review of animal experiments. J. Neuroinflammation *12*, 114.

Hrabětová, S. (2005). Extracellular diffusion is fast and isotropic in the stratum radiatum of hippocampal CA1 region in rat brain slices. Hippocampus *15*, 441–450.

Hrabětová, S., and Nicholson, C. (2007). Biophysical Properties of Brain Extracellular Space Explored with Ion-Selective Microelectrodes, Integrative Optical Imaging and Related Techniques. In Electrochemical Methods for Neuroscience, A.C. Michael, and L.M. Borland, eds. (Boca Raton (FL): CRC Press/Taylor & Francis), p.

Isaac, J.T.R., Nicoll, R.A., and Malenka, R.C. (1995). Evidence for silent synapses: Implications for the expression of LTP. Neuron *15*, 427–434.

Ishizuka, N., Cowan, W.M., and Amaral, D.G. (1995). A quantitative analysis of the dendritic organization of pyramidal cells in the rat hippocampus. J. Comp. Neurol. *362*, 17–45.

Jäkel, S., and Dimou, L. (2017). Glial Cells and Their Function in the Adult Brain: A Journey through the History of Their Ablation. Front. Cell. Neurosci. *11*.

Jauch, R., Windmüller, O., Lehmann, T.-N., Heinemann, U., and Gabriel, S. (2002). Effects of barium, furosemide, ouabaine and 4,4′-diisothiocyanatostilbene-2,2′-disulfonic acid (DIDS) on ionophoretically-induced changes in extracellular potassium concentration in hippocampal slices from rats and from patients with epilepsy. Brain Res. *925*, 18–27.

Jefferys, J.G. (1990). Basic mechanisms of focal epilepsies. Exp. Physiol. *75*, 127–162.

Johnson, J.W., and Ascher, P. (1987). Glycine potentiates the NMDA response in cultured mouse brain neurons. Nature *325*, 529–531.

Kandel, E.R., Schwartz, J.H., Jessell, T.M., Siegelbaum, S.A., Hudspeth, A.J., and Mack, S. (2013). Principles of Neural Science (McGraw-Hill Companies).

Kang, J., Jiang, L., Goldman, S.A., and Nedergaard, M. (1998). Astrocyte-mediated potentiation of inhibitory synaptic transmission. Nat. Neurosci. *1*, 683–692.

Karus, C., Mondragão, M.A., Ziemens, D., and Rose, C.R. (2015). Astrocytes restrict discharge duration and neuronal sodium loads during recurrent network activity. Glia *63*, 936–957.

Karwoski, C.J., Lu, H.-K., and Newman, E.A. (1989). Spatial Buffering of Light-Evoked Potassium Increases by Retinal Müller (Glial) Cells. Science *244*, 578–580.

Kikuchi, T., Gonzalez-Soriano, J., Kastanauskaite, A., Benavides-Piccione, R., Merchan-Perez, A., DeFelipe, J., and Blazquez-Llorca, L. (2020). Volume Electron Microscopy Study of the Relationship Between Synapses and Astrocytes in the Developing Rat Somatosensory Cortex. Cereb. Cortex *30*, 3800-3819.

Kilb, W., Dierkes, P.W., Syková, E., Vargová, L., and Luhmann, H.J. (2006). Hypoosmolar conditions reduce extracellular volume fraction and enhance epileptiform activity in the CA3 region of the immature rat hippocampus. J. Neurosci. Res. *84*, 119–129.

Kimelberg, H.K., and Frangakis, M.V. (1985). Furosemide- and bumetanide-sensitive ion transport and volume control in primary astrocyte cultures from rat brain. Brain Res. *361*, 125–134.

Kimelberg, H.K., and O'Connor, E. (1988). Swelling of astrocytes causes membrane potential depolarization. Glia *1*, 219–224.

King, D., and Spencer, S. (1995). Invasive electroencephalography in mesial temporal lobe epilepsy. J. Clin. Neurophysiol. Off. Publ. Am. Electroencephalogr. Soc. *12*, 32–45.

Kivi, A., Lehmann, T.-N., Kovács, R., Eilers, A., Jauch, R., Meencke, H.J., Deimling, A.V., Heinemann, U., and Gabriel, S. (2000). Effects of barium on stimulus-induced rises of [K+]o in human epileptic non-sclerotic and sclerotic hippocampal area CA1. Eur. J. Neurosci. *12*, 2039–2048.

Kofuji, P., and Newman, E.A. (2004). Potassium buffering in the central nervous system. Neuroscience *129*, 1045–1056.

Köhling, R., Gladwell, S.J., Bracci, E., Vreugdenhil, M., and Jefferys, J.G.R. (2001). Prolonged epileptiform bursting induced by 0-Mg2+ in rat hippocampal slices depends on gap junctional coupling. Neuroscience *105*, 579–587.

Kosaka, T., and Hama, K. (1985). Gap junctions between non-pyramidal cell dendrites in the rat hippocampus (CA1 and CA3 regions): A combined Golgi-electron microscopy study. J. Comp. Neurol. *231*, 150–161.

Krishtal, O.A., Osipchuk, Yu.V., Shelest, T.N., and Smirnoff, S.V. (1987). Rapid extracellular pH transients related to synaptic transmission in rat hippocampal slices. Brain Res. *436*, 352–356.

Kuffler, S.W., Nicholls, J.G., and Orkand, R.K. (1966). Physiological properties of glial cells in the central nervous system of amphibia. J. Neurophysiol. *29*, 768–787.

Kullmann, D.M., Erdemli, G., and Asztély, F. (1996). LTP of AMPA and NMDA Receptor–Mediated Signals: Evidence for Presynaptic Expression and Extrasynaptic Glutamate Spill-Over. Neuron *17*, 461–474.

Kume-Kick, J., Mazel, T., Vořišek, I., Hrabětová, S., Tao, L., and Nicholson, C. (2002). Independence of extracellular tortuosity and volume fraction during osmotic challenge in rat neocortex. J. Physiol. *542*, 515–527.

Larsen, B.R., and MacAulay, N. (2014). Kir4.1-mediated spatial buffering of K+: Experimental challenges in determination of its temporal and quantitative contribution to K+ clearance in the brain. Channels *8*, 544–550.

Larsen, B.R., Assentoft, M., Cotrina, M.L., Hua, S.Z., Nedergaard, M., Kaila, K., Voipio, J., and MacAulay, N. (2014). Contributions of the Na+/K+-ATPase, NKCC1, and Kir4.1 to hippocampal K+ clearance and volume responses. Glia *62*, 608–622.

Lehmenkühler, A., Syková, E., Svoboda, J., Zilles, K., and Nicholson, C. (1993). Extracellular space parameters in the rat neocortex and subcortical white matter during postnatal development determined by diffusion analysis. Neuroscience *55*, 339–351.

Lévesque, M., and Avoli, M. (2013). The kainic acid model of temporal lobe epilepsy. Neurosci. Biobehav. Rev. *37*, 2887–2899.

Levy, L.M., Warr, O., and Attwell, D. (1998). Stoichiometry of the Glial Glutamate Transporter GLT-1 Expressed Inducibly in a Chinese Hamster Ovary Cell Line Selected for Low Endogenous Na+-Dependent Glutamate Uptake. J. Neurosci. *18*, 9620–9628.

Liao, D., Hessler, N.A., and Malinow, R. (1995). Activation of postsynaptically silent synapses during pairing-induced LTP in CA1 region of hippocampal slice. Nature *375*, 400–404.

Liu, Q., Xu, Q., Arcuino, G., Kang, J., and Nedergaard, M. (2004a). Astrocyte-mediated activation of neuronal kainate receptors. Proc. Natl. Acad. Sci. U. S. A. *101*, 3172–3177.

Liu, Q.-S., Xu, Q., Kang, J., and Nedergaard, M. (2004b). Astrocyte activation of presynaptic metabotropic glutamate receptors modulates hippocampal inhibitory synaptic transmission. Neuron Glia Biol. *1*, 307–316.

Löscher, W., and Schmidt, D. (2011). Modern antiepileptic drug development has failed to deliver: Ways out of the current dilemma. Epilepsia *52*, 657–678.

Losi, G., Mariotti, L., and Carmignoto, G. (2014). GABAergic interneuron to astrocyte signalling: a neglected form of cell communication in the brain. Philos. Trans. R. Soc. B Biol. Sci. *369*.

Lux, H.D., and Neher, E. (1973). The equilibration time course of [K+]0 in cat cortex. Exp. Brain Res. *17*, 190–205.

Lynch, G., Larson, J., Kelso, S., Barrionuevo, G., and Schottler, F. (1983). Intracellular injections of EGTA block induction of hippocampal long-term potentiation. Nature *305*, 719–721.

MacAulay, N., and Zeuthen, T. (2012). Glial K+ Clearance and Cell Swelling: Key Roles for Cotransporters and Pumps. Neurochem. Res. *37*, 2299–2309.

MacDermott, A.B., Mayer, M.L., Westbrook, G.L., Smith, S.J., and Barker, J.L. (1986). NMDA-receptor activation increases cytoplasmic calcium concentration in cultured spinal cord neurones. Nature *321*, 519–522.

Maekawa, M., Ishizaki, T., Boku, S., Watanabe, N., Fujita, A., Iwamatsu, A., Obinata, T., Ohashi, K., Mizuno, K., and Narumiya, S. (1999). Signaling from Rho to the Actin Cytoskeleton Through Protein Kinases ROCK and LIM-kinase. Science *285*, 895–898.

Makani, S., and Chesler, M. (2007). Endogenous Alkaline Transients Boost Postsynaptic NMDA Receptor Responses in Hippocampal CA1 Pyramidal Neurons. J. Neurosci. *27*, 7438–7446.

Malenka, R.C., and Bear, M.F. (2004). LTP and LTD: An Embarrassment of Riches. Neuron *44*, 5–21.

Mariotti, L., Losi, G., Sessolo, M., Marcon, I., and Carmignoto, G. (2016). The inhibitory neurotransmitter GABA evokes long-lasting Ca2+ oscillations in cortical astrocytes. Glia *64*, 363–373.

Marvin, J.S., Borghuis, B.G., Tian, L., Cichon, J., Harnett, M.T., Akerboom, J., Gordus, A., Renninger, S.L., Chen, T.-W., Bargmann, C.I., et al. (2013). An optimized fluorescent probe for visualizing glutamate neurotransmission. Nat. Methods *10*, 162–170.

Marvin, J.S., Shimoda, Y., Magloire, V., Leite, M., Kawashima, T., Jensen, T.P., Kolb, I., Knott, E.L., Novak, O., Podgorski, K., et al. (2019). A genetically encoded fluorescent sensor for in vivo imaging of GABA. Nat. Methods *16*, 763–770.

Matos, M., Bosson, A., Riebe, I., Reynell, C., Vallée, J., Laplante, I., Panatier, A., Robitaille, R., and Lacaille, J.-C. (2018). Astrocytes detect and upregulate transmission at inhibitory synapses of somatostatin interneurons onto pyramidal cells. Nat. Commun. *9*, 4254.

Mayer, M.L., Westbrook, G.L., and Guthrie, P.B. (1984). Voltage-dependent block by Mg 2+ of NMDA responses in spinal cord neurones. Nature *309*, 261–263.

Mazel, T., Šimonová, Z., and Syková, E. (1998). Diffusion heterogeneity and anisotropy in rat hippocampus. Neuroreport *9*, 1299–1304.

Mederos, S., and Perea, G. (2019). GABAergic-astrocyte signaling: A refinement of inhibitory brain networks. Glia *67*, 1842–1851.

Medvedev, N., Popov, V., Henneberger, C., Kraev, I., Rusakov, D.A., and Stewart, M.G. (2014). Glia selectively approach synapses on thin dendritic spines. Philos. Trans. R. Soc. B Biol. Sci. *369*.

Meeks, J.P., and Mennerick, S. (2007). Astrocyte membrane responses and potassium accumulation during neuronal activity. Hippocampus *17*, 1100–1108.

Meier, S.D., Kafitz, K.W., and Rose, C.R. (2008). Developmental profile and mechanisms of GABA-induced calcium signaling in hippocampal astrocytes. Glia *56*, 1127–1137.

Meur, K.L., Galante, M., Angulo, M.C., and Audinat, E. (2007). Tonic activation of NMDA receptors by ambient glutamate of non-synaptic origin in the rat hippocampus. J. Physiol. *580*, 373–383.

Mody, I., Lambert, J.D., and Heinemann, U. (1987). Low extracellular magnesium induces epileptiform activity and spreading depression in rat hippocampal slices. J. Neurophysiol. *57*, 869–888.

Moody, W.J., Futamachi, K.J., and Prince, D.A. (1974). Extracellular potassium activity during epileptogenesis. Exp. Neurol. *42*, 248–263.

Morales, H.P., and Schousboe, A. (1988). Volume regulation in astrocytes: A role for taurine as an osmoeffector. J. Neurosci. Res. *20*, 505–509.

Mothet, J.-P., Parent, A.T., Wolosker, H., Brady, R.O., Linden, D.J., Ferris, C.D., Rogawski, M.A., and Snyder, S.H. (2000). d-Serine is an endogenous ligand for the glycine site of the N-methyl-d-aspartate receptor. Proc. Natl. Acad. Sci. *97*, 4926–4931.

Mothet, J.-P., Pollegioni, L., Ouanounou, G., Martineau, M., Fossier, P., and Baux, G. (2005). Glutamate receptor activation triggers a calcium-dependent and SNARE protein-dependent release of the gliotransmitter D-serine. Proc. Natl. Acad. Sci. *102*, 5606–5611.

Murphy-Royal, C., Dupuis, J.P., Varela, J.A., Panatier, A., Pinson, B., Baufreton, J., Groc, L., and Oliet, S.H.R. (2015). Surface diffusion of astrocytic glutamate transporters shapes synaptic transmission. Nat. Neurosci. *18*, 219–226.

Nagelhus, E.A., Mathiisen, T.M., and Ottersen, O.P. (2004). Aquaporin-4 in the central nervous system: Cellular and subcellular distribution and coexpression with KIR4.1. Neuroscience *129*, 905–913.

Nagy, J.I., and Dermietzel, R. (2000). Gap junctions and connexins in the mammalian central nervous system. In Advances in Molecular and Cell Biology, (Elsevier), pp. 323–396.

Navarrete, M., and Araque, A. (2010). Endocannabinoids Potentiate Synaptic Transmission through Stimulation of Astrocytes. Neuron *68*, 113–126.

Nayak, D., Roth, T.L., and McGavern, D.B. (2014). Microglia Development and Function. Annu. Rev. Immunol. *32*, 367–402.

Neher, E., and Sakmann, B. (1976). Single-channel currents recorded from membrane of denervated frog muscle fibres. Nature *260*, 799–801.

Neusch, C., Papadopoulos, N., Müller, M., Maletzki, I., Winter, S.M., Hirrlinger, J., Handschuh, M., Bähr, M., Richter, D.W., Kirchhoff, F., et al. (2006). Lack of the Kir4.1 Channel Subunit Abolishes K+ Buffering Properties of Astrocytes in the Ventral Respiratory Group: Impact on Extracellular K+ Regulation. J. Neurophysiol. *95*, 1843–1852.

Newman, E.A. (1984). Regional specialization of retinal glial cell membrane. Nature *309*, 155–157.

Newman, E.A., Frambach, D.A., and Odette, L.L. (1984). Control of Extracellular Potassium Levels by Retinal Glial Cell K+ Siphoning. Science *225*, 1174–1175.

Nicholls, D., and Attwell, D. (1990). The release and uptake of excitatory amino acids. Trends Pharmacol. Sci. *11*, 462–468.

Nicholson, C. (1993). Ion-selective microelectrodes and diffusion measurements as tools to explore the brain cell microenvironment. J. Neurosci. Methods *48*, 199–213.

Nicholson, C., and Phillips, J.M. (1981). Ion diffusion modified by tortuosity and volume fraction in the extracellular microenvironment of the rat cerebellum. J. Physiol. *321*, 225–257.

Nicholson, C., and Syková, E. (1998). Extracellular space structure revealed by diffusion analysis. Trends Neurosci. *21*, 207–215.

Nicoll, R.A. (2017). A Brief History of Long-Term Potentiation. Neuron *93*, 281–290.

Nixdorf-Bergweiler, B.E., Albrecht, D., and Heinemann, U. (1994). Developmental changes in the number, size, and orientation of GFAP-positive cells in the CA1 region of rat hippocampus. Glia *12*, 180–195.

Numberger, M., and Draguhn, A. (1996). Patch-Clamp-Technik (Spektrum Akademischer Verlag).

Obaid, A.L., Socolar, S.J., and Rose, B. (1983). Cell-to-cell channels with two independently regulated gates in series: Analysis of junctional conductance modulation by membrane potential, calcium, and pH. J. Membr. Biol. *73*, 69–89.

Oberheim, N.A., Tian, G.-F., Han, X., Peng, W., Takano, T., Ransom, B., and Nedergaard, M. (2008). Loss of Astrocytic Domain Organization in the Epileptic Brain. J. Neurosci. *28*, 3264–3276.

O'Connor, E.R., and Kimelberg, H.K. (1993). Role of calcium in astrocyte volume regulation and in the release of ions and amino acids. J. Neurosci. *13*, 2638–2650.

Ogata, K., and Kosaka, T. (2002). Structural and quantitative analysis of astrocytes in the mouse hippocampus. Neuroscience *113*, 221–233.

Oliet, S.H., Piet, R., and Poulain, D.A. (2001). Control of glutamate clearance and synaptic efficacy by glial coverage of neurons. Science *292*, 923–926.

Olson, J.E., Sankar, R., Holtzman, D., James, A., and Fleischhacker, D. (1986). Energy-dependent volume regulation in primary cultured cerebral astrocytes. J. Cell. Physiol. *128*, 209–215.

Orkand, R.K. (1986). Glial-interstitial fluid exchange. Ann. N. Y. Acad. Sci. *481*, 269–272.

Orkand, R.K., Nicholls, J.G., and Kuffler, S.W. (1966). Effect of nerve impulses on the membrane potential of glial cells in the central nervous system of amphibia. J. Neurophysiol. *29*, 788–806.

Ortinski, P.I., Dong, J., Mungenast, A., Yue, C., Takano, H., Watson, D.J., Haydon, P.G., and Coulter, D.A. (2010). Selective induction of astrocytic gliosis generates deficits in neuronal inhibition. Nat. Neurosci. *13*, 584–591.

Otis, T.S., and Jahr, C.E. (1998). Anion Currents and Predicted Glutamate Flux through a Neuronal Glutamate Transporter. J. Neurosci. *18*, 7099–7110.

Pan, F., Mills, S.L., and Massey, S.C. (2007). Screening of gap junction antagonists on dye coupling in the rabbit retina. Vis. Neurosci. *24*, 609–618.

Panatier, A., Theodosis, D.T., Mothet, J.-P., Touquet, B., Pollegioni, L., Poulain, D.A., and Oliet, S.H.R. (2006). Glia-Derived d-Serine Controls NMDA Receptor Activity and Synaptic Memory. Cell *125*, 775–784.

Pannasch, U., and Rouach, N. (2013). Emerging role for astroglial networks in information processing: from synapse to behavior. Trends Neurosci. *36*, 405–417.

Pannasch, U., Vargová, L., Reingruber, J., Ezan, P., Holcman, D., Giaume, C., Syková, E., and Rouach, N. (2011). Astroglial networks scale synaptic activity and plasticity. Proc. Natl. Acad. Sci. U. S. A. *108*, 8467–8472.

Pannasch, U., Derangeon, M., Chever, O., and Rouach, N. (2012). Astroglial gap junctions shape neuronal network activity. Commun. Integr. Biol. *5*, 248–254.

Pannasch, U., Freche, D., Dallérac, G., Ghézali, G., Escartin, C., Ezan, P., Cohen-Salmon, M., Benchenane, K., Abudara, V., Dufour, A., et al. (2014). Connexin 30 sets synaptic strength by controlling astroglial synapse invasion. Nat. Neurosci. *17*, 549–558.

Parkhurst, C.N., Yang, G., Ninan, I., Savas, J.N., Yates, J.R., Lafaille, J.J., Hempstead, B.L., Littman, D.R., and Gan, W.-B. (2013). Microglia Promote Learning-Dependent Synapse Formation through Brain-Derived Neurotrophic Factor. Cell *155*, 1596–1609.

Pascual, O., Casper, K.B., Kubera, C., Zhang, J., Revilla-Sanchez, R., Sul, J.-Y., Takano, H., Moss, S.J., McCarthy, K., and Haydon, P.G. (2005). Astrocytic Purinergic Signaling Coordinates Synaptic Networks. Science *310*, 113–116.

Pekny, M., and Pekna, M. (2014). Astrocyte Reactivity and Reactive Astrogliosis: Costs and Benefits. Physiol. Rev. *94*, 1077–1098.

Pelkey, K.A., Chittajallu, R., Craig, M.T., Tricoire, L., Wester, J.C., and McBain, C.J. (2017). Hippocampal GABAergic Inhibitory Interneurons. Physiol. Rev. *97*, 1619–1747.

Peracchia, C. (2004). Chemical gating of gap junction channels: Roles of calcium, pH and calmodulin. Biochim. Biophys. Acta BBA - Biomembr. *1662*, 61–80.

Perea, G., and Araque, A. (2007). Astrocytes potentiate transmitter release at single hippocampal synapses. Science *317*, 1083–1086.

Perea, G., and Araque, A. (2010). GLIA modulates synaptic transmission. Brain Res. Rev. *63*, 93–102.

Perea, G., Navarrete, M., and Araque, A. (2009). Tripartite synapses: astrocytes process and control synaptic information. Trends Neurosci. *32*, 421–431.

Perea, G., Gómez, R., Mederos, S., Covelo, A., Ballesteros, J.J., Schlosser, L., Hernández-Vivanco, A., Martín-Fernández, M., Quintana, R., Rayan, A., et al. (2016). Activity-dependent switch of GABAergic inhibition into glutamatergic excitation in astrocyte-neuron networks. ELife *5*, e20362.

Peretz, A., Degani, N., Nachman, R., Uziyel, Y., Gibor, G., Shabat, D., and Attali, B. (2005). Meclofenamic Acid and Diclofenac, Novel Templates of KCNQ2/Q3 Potassium Channel Openers, Depress Cortical Neuron Activity and Exhibit Anticonvulsant Properties. Mol. Pharmacol. *67*, 1053–1066.

Poolos, N.P., Mauk, M.D., and Kocsis, J.D. (1987). Activity-evoked increases in extracellular potassium modulate presynaptic excitability in the CA1 region of the hippocampus. J. Neurophysiol. *58*, 404–416.

Priestley, T., Laughton, P., Myers, J., Bourdellés, B.L., Kerby, J., and Whiting, P.J. (1995). Pharmacological properties of recombinant human N-methyl-D-aspartate receptors comprising NR1a/NR2A and NR1a/NR2B subunit assemblies expressed in permanently transfected mouse fibroblast cells. Mol. Pharmacol. *48*, 841–848.

Racchetti, G., D'Alessandro, R., and Meldolesi, J. (2012). Astrocyte stellation, a process dependent on Rac1 is sustained by the regulated exocytosis of enlargeosomes. Glia *60*, 465–475.

Ramón y Cajal, S. (1909). Histologie du système nerveux de l'homme & des vertébrés (Paris : Maloine).

Ransom, C.B., Ransom, B.R., and Sontheimer, H. (2000). Activity-dependent extracellular K+ accumulation in rat optic nerve: the role of glial and axonal Na+ pumps. J. Physiol. *522*, 427–442.

Rasmussen, R., Nicholas, E., Petersen, N.C., Dietz, A.G., Xu, Q., Sun, Q., and Nedergaard, M. (2019). Cortex-wide Changes in Extracellular Potassium Ions Parallel Brain State Transitions in Awake Behaving Mice. Cell Rep. *28*, 1182-1194.e4.

Rausche, G., Igelmund, P., and Heinemann, U. (1990). Effects of changes in extracellular potassium, magnesium and calcium concentration on synaptic transmission in area CA1 and the dentate gyrus of rat hippocampal slices. Pflüg. Arch. *415*, 588–593.

Reichenbach, N., Delekate, A., Breithausen, B., Keppler, K., Poll, S., Schulte, T., Peter, J., Plescher, M., Hansen, J.N., Blank, N., et al. (2018). P2Y1 receptor blockade normalizes network dysfunction and cognition in an Alzheimer's disease model. J. Exp. Med. *215*, 1649–1663.

Ribak, C.E., Tong, W.M.Y., and Brecha, N.C. (1996). GABA plasma membrane transporters, GAT-1 and GAT-3, display different distributions in the rat hippocampus. J. Comp. Neurol. *367*, 595–606.

Romanos, J., Benke, D., Saab, A.S., Zeilhofer, H.U., and Santello, M. (2019). Differences in glutamate uptake between cortical regions impact neuronal NMDA receptor activation. Commun. Biol. *2*, 1–15.

Rose, C.R., and Ransom, B.R. (1996). Intracellular sodium homeostasis in rat hippocampal astrocytes. J. Physiol. *491 (Pt 2)*, 291–305.

Rose, C.R., and Ransom, B.R. (1997). Regulation of intracellular sodium in cultured rat hippocampal neurones. J. Physiol. *499*, 573–587.

Rose, C.R., Felix, L., Zeug, A., Dietrich, D., Reiner, A., and Henneberger, C. (2018). Astroglial Glutamate Signaling and Uptake in the Hippocampus. Front. Mol. Neurosci. *10*, 451.

Rostène, W., Dansereau, M.-A., Godefroy, D., Steenwinckel, J.V., Goazigo, A.R.-L., Mélik-Parsadaniantz, S., Apartis, E., Hunot, S., Beaudet, N., and Sarret, P. (2011). Neurochemokines: a menage a trois providing new insights on the functions of chemokines in the central nervous system. J. Neurochem. *118*, 680–694.

Rothstein, J.D., Dykes-Hoberg, M., Pardo, C.A., Bristol, L.A., Jin, L., Kuncl, R.W., Kanai, Y., Hediger, M.A., Wang, Y., Schielke, J.P., et al. (1996). Knockout of Glutamate Transporters Reveals a Major Role for Astroglial Transport in Excitotoxicity and Clearance of Glutamate. Neuron *16*, 675–686.

Rouach, N., Segal, M., Koulakoff, A., Giaume, C., and Avignone, E. (2003). Carbenoxolone Blockade of Neuronal Network Activity in Culture is not Mediated by an Action on Gap Junctions. J. Physiol. *553*, 729–745.

Rouach, N., Koulakoff, A., Abudara, V., Willecke, K., and Giaume, C. (2008). Astroglial Metabolic Networks Sustain Hippocampal Synaptic Transmission. Science *322*, 1551–1555.

Roux, L., and Buzsáki, G. (2015). Tasks for inhibitory interneurons in intact brain circuits. Neuropharmacology *88*, 10–23.

Roux, L., Benchenane, K., Rothstein, J.D., Bonvento, G., and Giaume, C. (2011). Plasticity of astroglial networks in olfactory glomeruli. Proc. Natl. Acad. Sci. *108*, 18442–18446.

Rozental, R., Srinivas, M., and Spray, D.C. (2001). How to close a gap junction channel. Efficacies and potencies of uncoupling agents. Methods Mol. Biol. Clifton NJ *154*, 447–476.

Sáez, J.C., Retamal, M.A., Basilio, D., Bukauskas, F.F., and Bennett, M.V.L. (2005). Connexin-based gap junction hemichannels: Gating mechanisms. Biochim. Biophys. Acta BBA - Biomembr. *1711*, 215–224.

Sahlender, D.A., Savtchouk, I., and Volterra, A. (2014). What do we know about gliotransmitter release from astrocytes? Philos. Trans. R. Soc. B Biol. Sci. *369*.

Sander, J.W., and Shorvon, S.D. (1996). Epidemiology of the epilepsies. J. Neurol. Neurosurg. Psychiatry *61*, 433–443.

Savtchenko, L.P., Bard, L., Jensen, T.P., Reynolds, J.P., Kraev, I., Medvedev, N., Stewart, M.G., Henneberger, C., and Rusakov, D.A. (2018). Disentangling astroglial physiology with a realistic cell model in silico. Nat. Commun. *9*, 3554.

Schell, M.J. (2004). The N–methyl D–aspartate receptor glycine site and D–serine metabolism: an evolutionary perspective. Philos. Trans. R. Soc. Lond. B. Biol. Sci. *359*, 943–964.

Schell, M.J., Molliver, M.E., and Snyder, S.H. (1995). D-serine, an endogenous synaptic modulator: localization to astrocytes and glutamate-stimulated release. Proc. Natl. Acad. Sci. *92*, 3948–3952.

Schevon, C.A., Ng, S.K., Cappell, J., Goodman, R.R., McKhann, G.J., Waziri, A., Branner, A., Sosunov, A., Schroeder, C.E., and Emerson, R.G. (2008). Microphysiology of Epileptiform Activity in Human Neocortex. J. Clin. Neurophysiol. *25*, 321–330.

Schiller, J., Schiller, Y., and Clapham, D.E. (1998). NMDA receptors amplify calcium influx into dendritic spines during associative pre- and postsynaptic activation. Nat. Neurosci. *1*, 114–118.

Schmitz, D., Schuchmann, S., Fisahn, A., Draguhn, A., Buhl, E.H., Petrasch-Parwez, E., Dermietzel, R., Heinemann, U., and Traub, R.D. (2001). Axo-Axonal Coupling: A Novel Mechanism for Ultrafast Neuronal Communication. Neuron *31*, 831–840.

Schoppa, N.E., and Westbrook, G.L. (2002). AMPA autoreceptors drive correlated spiking in olfactory bulb glomeruli. Nat. Neurosci. *5*, 1194–1202.

Schwartzkroin, P.A., and Prince, D.A. (1977). Penicillin-induced epileptiform activity in the hippocampal in vitro preparation. Ann. Neurol. *1*, 463–469.

Seifert, G., and Steinhäuser, C. (2013). Neuron-astrocyte signaling and epilepsy. Exp. Neurol. *244*, 4–10.

Seifert, G., Schilling, K., and Steinhäuser, C. (2006). Astrocyte dysfunction in neurological disorders: a molecular perspective. Nat. Rev. Neurosci. *7*, 194–206.

Seifert, G., Hüttmann, K., Binder, D.K., Hartmann, C., Wyczynski, A., Neusch, C., and Steinhäuser, C. (2009). Analysis of Astroglial K+ Channel Expression in the Developing Hippocampus Reveals a Predominant Role of the Kir4.1 Subunit. J. Neurosci. *29*, 7474–7488.

Seifert, G., Carmignoto, G., and Steinhäuser, C. (2010). Astrocyte dysfunction in epilepsy. Brain Res. Rev. *63*, 212–221.

Seifert, G., Henneberger, C., and Steinhäuser, C. (2016). Diversity of astrocyte potassium channels: An update. Brain Res. Bull.

Shen, Y., Qin, H., Chen, J., Mou, L., He, Y., Yan, Y., Zhou, H., Lv, Y., Chen, Z., Wang, J., et al. (2016). Postnatal activation of TLR4 in astrocytes promotes excitatory synaptogenesis in hippocampal neurons. J. Cell Biol. *215*, 719–734.

Shi, S.-H., Hayashi, Y., Petralia, R.S., Zaman, S.H., Wenthold, R.J., Svoboda, K., and Malinow, R. (1999). Rapid Spine Delivery and Redistribution of AMPA Receptors After Synaptic NMDA Receptor Activation. Science *284*, 1811–1816.

Singer, W., and Dieter Lux, H. (1975). Extracellular potassium gradients and visual receptive fields in the cat striate cortex. Brain Res. *96*, 378–383.

Sinning, A., and Hübner, C.A. (2013). Minireview: pH and synaptic transmission. FEBS Lett. *587*, 1923–1928.

Slais, K., Vorisek, I., Zoremba, N., Homola, A., Dmytrenko, L., and Sykova, E. (2008). Brain metabolism and diffusion in the rat cerebral cortex during pilocarpine-induced status epilepticus. Exp. Neurol. *209*, 145–154.

Soderling, T.R., and Derkach, V.A. (2000). Postsynaptic protein phosphorylation and LTP. Trends Neurosci. *23*, 75–80.

Sofroniew, M.V., and Vinters, H.V. (2010). Astrocytes: biology and pathology. Acta Neuropathol. (Berl.) *119*, 7–35.

Somjen, G.G. (2001). Mechanisms of spreading depression and hypoxic spreading depression-like depolarization. Physiol. Rev. *81*, 1065–1096.

Stallcup, W.B., Bulloch, K., and Baetge, E.E. (1979). Coupled Transport of Glutamate and Sodium in a Cerebellar Nerve Cell Line. J. Neurochem. *32*, 57–65.

Stead, M., Bower, M., Brinkmann, B.H., Lee, K., Marsh, W.R., Meyer, F.B., Litt, B., Van Gompel, J., and Worrell, G.A. (2010). Microseizures and the spatiotemporal scales of human partial epilepsy. Brain *133*, 2789–2797.

Steinhäuser, C., Grunnet, M., and Carmignoto, G. (2015). Crucial role of astrocytes in temporal lobe epilepsy. Neuroscience *323*, 157–169.

Stenovec, M., Kreft, M., Grilc, S., Pangršič, T., and Zorec, R. (2008). EAAT2 density at the astrocyte plasma membrane and Ca2 + -regulated exocytosis. Mol. Membr. Biol. *25*, 203–215.

Strohschein, S., Hüttmann, K., Gabriel, S., Binder, D.K., Heinemann, U., and Steinhäuser, C. (2011). Impact of aquaporin-4 channels on K+ buffering and gap junction coupling in the hippocampus. Glia *59*, 973–980.

Syková, E. (2004). Diffusion properties of the brain in health and disease. Neurochem. Int. *45*, 453–466.

Syková, E., and Nicholson, C. (2008). Diffusion in Brain Extracellular Space. Physiol. Rev. *88*, 1277–1340.

Syková, E., and Vargová, L. (2008). Extrasynaptic transmission and the diffusion parameters of the extracellular space. Neurochem. Int. *52*, 5–13.

Syková, E., Mazel, Tomáš., and Šimonová, Z. (1998). Diffusion constraints and neuron–glia interaction during aging. Exp. Gerontol. *33*, 837–851.

Syková, E., Vargová, L., Prokopová, Š., and Šimonová, Z. (1999). Glial swelling and astrogliosis produce diffusion barriers in the rat spinal cord. Glia *25*, 56–70.

Syková, E., Mazel, T., Hasenöhrl, R.U., Harvey, A.R., Simonová, Z., Mulders, W.H. a. M., and Huston, J.P. (2002). Learning deficits in aged rats related to decrease in extracellular volume and loss of diffusion anisotropy in hippocampus. Hippocampus *12*, 269–279.

Sypert, G.W., and Ward, A.A. (1974). Changes in extracellular potassium activity during neocortical propagated seizures. Exp. Neurol. *45*, 19–41.

Tanaka, K., Watase, K., Manabe, T., Yamada, K., Watanabe, M., Takahashi, K., Iwama, H., Nishikawa, T., Ichihara, N., Kikuchi, T., et al. (1997). Epilepsy and Exacerbation of Brain Injury in Mice Lacking the Glutamate Transporter GLT-1. Science *276*, 1699–1702.

Theis, M., Jauch, R., Zhuo, L., Speidel, D., Wallraff, A., Döring, B., Frisch, C., Söhl, G., Teubner, B., Euwens, C., et al. (2003). Accelerated Hippocampal Spreading Depression and Enhanced Locomotory Activity in Mice with Astrocyte-Directed Inactivation of Connexin43. J. Neurosci. *23*, 766–776.

Thom, M. (2014). Review: Hippocampal sclerosis in epilepsy: a neuropathology review. Neuropathol. Appl. Neurobiol. *40*, 520–543.

Tian, G.-F., Azmi, H., Takano, T., Xu, Q., Peng, W., Lin, J., Oberheim, N., Lou, N., Wang, X., Zielke, H.R., et al. (2005). An astrocytic basis of epilepsy. Nat. Med. *11*, 973–981.

Tong, C.-K., Chen, K., and Chesler, M. (2006). Kinetics of Activity-Evoked pH Transients and Extracellular pH Buffering in Rat Hippocampal Slices. J. Neurophysiol. *95*, 3686–3697.

Tovar, K.R., Maher, B.J., and Westbrook, G.L. (2009). Direct Actions of Carbenoxolone on Synaptic Transmission and Neuronal Membrane Properties. J. Neurophysiol. *102*, 974–978.

Travagli, R.A., Dunwiddie, T.V., and Williams, J.T. (1995). Opioid Inhibition in Locus Coeruleus. J. Neurophysiol. *74*, 519–528.

Traynelis, S.F., and Dingledine, R. (1989). Role of extracellular space in hyperosmotic suppression of potassium-induced electrographic seizures. J. Neurophysiol. *61*, 927–938.

Tsuda, A., Ito, M., Kishi, K., Shiraishi, H., Tsuda, H., and Mori, C. (1994). Effect of penicillin on GABA-gated chloride ion influx. Neurochem. Res. *19*, 1–4.

Turski, W.A., Cavalheiro, E.A., Bortolotto, Z.A., Mello, L.M., Schwarz, M., and Turski, L. (1984). Seizures produced by pilocarpine in mice: A behavioral, electroencephalographic and morphological analysis. Brain Res. *321*, 237–253.

Uhlmann, E.J., Wong, M., Baldwin, R.L., Bajenaru, M.L., Onda, H., Kwiatkowski, D.J., Yamada, K., and Gutmann, D.H. (2002). Astrocyte-specific TSC1 conditional knockout mice exhibit abnormal neuronal organization and seizures. Ann. Neurol. *52*, 285–296.

Ulas, J., Satou, T., Ivins, K.J., Kesslak, J.P., Cotman, C.W., and Balázs, R. (2000). Expression of metabotropic glutamate receptor 5 is increased in astrocytes after kainate-induced epileptic seizures. Glia *30*, 352–361.

Ventura, R., and Harris, K.M. (1999). Three-Dimensional Relationships between Hippocampal Synapses and Astrocytes. J. Neurosci. *19*, 6897–6906.

Verkhratsky, A., and Rose, C.R. (2020). Na+-dependent transporters: The backbone of astroglial homeostatic function. Cell Calcium *85*, 102136.

Verkhratsky, A., and Steinhäuser, C. (2000). Ion channels in glial cells. Brain Res. Rev. *32*, 380–412.

Vessey, J.P., Lalonde, M.R., Mizan, H.A., Welch, N.C., Kelly, M.E.M., and Barnes, S. (2004). Carbenoxolone inhibition of voltage-gated Ca channels and synaptic transmission in the retina. J. Neurophysiol. *92*, 1252–1256.

Virchow, R. (1859). Die Cellularpathologie in ihrer Begründung auf physiologische und pathologische Gewebelehre (Berlin : Verlag von August Hirschwald).

Vitarella, D., DiRisio, D.J., Kimelberg, H.K., and Aschner, M. (1994). Potassium and Taurine Release Are Highly Correlated with Regulatory Volume Decrease in Neonatal Primary Rat Astrocyte Cultures. J. Neurochem. *63*, 1143–1149.

Volterra, A., and Meldolesi, J. (2005). Astrocytes, from brain glue to communication elements: the revolution continues. Nat. Rev. Neurosci. *6*, 626–640.

Voříšek, I., and Syková, E. (1997). Ischemia-Induced Changes in the Extracellular Space Diffusion Parameters, K+, and pH in the Developing Rat Cortex and Corpus Callosum. J. Cereb. Blood Flow Metab. *17*, 191–203.

Voskuyl, R.A., and ter Keurs, H.E.D.J. (1981). Modification of neuronal activity in olfactory cortex slices by extracellular K+. Brain Res. *230*, 372–377.

Vossler, D.G., Weingarten, M., and Gidal, B.E. (2018). Summary of Antiepileptic Drugs Available in the United States of America. Epilepsy Curr. *18*, 1–26.

Walker, A.E., Johnson, H.C., and Kollros, J.J. (1945). Penicillin convulsions; the convulsive effects of penicillin applied to the cerebral cortex of monkey and man. Surg. Gynecol. Obstet. *81*, 692–701.

Wallraff, A., Odermatt, B., Willecke, K., and Steinhäuser, C. (2004). Distinct types of astroglial cells in the hippocampus differ in gap junction coupling. Glia *48*, 36–43.

Wallraff, A., Köhling, R., Heinemann, U., Theis, M., Willecke, K., and Steinhäuser, C. (2006). The Impact of Astrocytic Gap Junctional Coupling on Potassium Buffering in the Hippocampus. J. Neurosci. *26*, 5438–5447.

Walz, W. (2000). Role of astrocytes in the clearance of excess extracellular potassium. Neurochem. Int. *36*, 291–300.

Walz, W., and Hertz, L. (1982). Ouabain-Sensitive and Ouabain-Resistant Net Uptake of Potassium into Astrocytes and Neurons in Primary Cultures. J. Neurochem. *39*, 70–77.

Walz, W., and Hertz, L. (1984). Intense Furosemide-Sensitive Potassium Accumulation in Astrocytes in the Presence of Pathologically High Extracellular Potassium Levels. J. Cereb. Blood Flow Metab. *4*, 301–304.

Walz, W., and Wuttke, W.A. (1999). Independent mechanisms of potassium clearance by astrocytes in gliotic tissue. J. Neurosci. Res. *56*, 595–603.

Wang, F., Smith, N.A., Xu, Q., Fujita, T., Baba, A., Matsuda, T., Takano, T., Bekar, L., and Nedergaard, M. (2012). Astrocytes Modulate Neural Network Activity by Ca2+-Dependent Uptake of Extracellular K+. Sci Signal *5*, ra26–ra26.

Wellbourne-Wood, J., Rimmele, T.S., and Chatton, J.-Y. (2017). Imaging extracellular potassium dynamics in brain tissue using a potassium-sensitive nanosensor. Neurophotonics *4*, 015002.

Wenzel, M., Hamm, J.P., Peterka, D.S., and Yuste, R. (2019). Acute Focal Seizures Start As Local Synchronizations of Neuronal Ensembles. J. Neurosci. *39*, 8562–8575.

Witcher, M.R., Kirov, S.A., and Harris, K.M. (2007). Plasticity of perisynaptic astroglia during synaptogenesis in the mature rat hippocampus. Glia *55*, 13–23.

Woodward, R.M., Polenzani, L., and Miledi, R. (1994). Effects of fenamates and other nonsteroidal anti-inflammatory drugs on rat brain GABAA receptors expressed in Xenopus oocytes. J. Pharmacol. Exp. Ther. *268*, 806–817.

Xiong, Z.-Q., and Stringer, J.L. (2000). Sodium Pump Activity, Not Glial Spatial Buffering, Clears Potassium After Epileptiform Activity Induced in the Dentate Gyrus. J. Neurophysiol. *83*, 1443–1451.

Xu, L., Zeng, L.-H., and Wong, M. (2009). Impaired astrocytic gap junction coupling and potassium buffering in a mouse model of tuberous sclerosis complex. Neurobiol. Dis. *34*, 291–299.

Yang, Q., and Michelson, H.B. (2001). Gap junctions synchronize the firing of inhibitory interneurons in guinea pig hippocampus. Brain Res. *907*, 139–143.

Yao, X., Hrabětová, S., Nicholson, C., and Manley, G.T. (2008). Aquaporin-4-Deficient Mice Have Increased Extracellular Space without Tortuosity Change. J. Neurosci. *28*, 5460–5464.

Zhang, W.H., Herde, M.K., Mitchell, J.A., Whitfield, J.H., Wulff, A.B., Vongsouthi, V., Sanchez-Romero, I., Gulakova, P.E., Minge, D., Breithausen, B., et al. (2018). Monitoring hippocampal glycine with the computationally designed optical sensor GlyFS. Nat. Chem. Biol. *14*, 861–869.

Zhang, Z., Nguyen, K.T., Barrett, E.F., and David, G. (2010). Vesicular ATPase Inserted into the Plasma Membrane of Motor Terminals by Exocytosis Alkalinizes Cytosolic pH and Facilitates Endocytosis. Neuron *68*, 1097–1108.

Zheng, K., Scimemi, A., and Rusakov, D.A. (2008). Receptor Actions of Synaptically Released Glutamate: The Role of Transporters on the Scale from Nanometers to Microns. Biophys. J. *95*, 4584–4596.

Zhou, X., Chen, Z., Yun, W., Ren, J., Li, C., and Wang, H. (2015). Extrasynaptic NMDA Receptor in Excitotoxicity: Function Revisited. The Neuroscientist *21*, 337–344.

Zlotnik, A., and Yoshie, O. (2012). The Chemokine Superfamily Revisited. Immunity *36*, 705–716.

Zsiros, V., and Maccaferri, G. (2005). Electrical Coupling between Interneurons with Different Excitable Properties in the Stratum Lacunosum-Moleculare of the Juvenile CA1 Rat Hippocampus. J. Neurosci. *25*, 8686–8695.

Abbreviations

$[Glu]_o$	extracellular glutamate concentration
$[K^+]_o$	extracellular K^+ concentration
$[TMA^+]_o$	extracellular Tetramethylammonium concentration
AAV	adeno-associated virus
AC	alternating current
aCSF	artificial cerebrospinal fluid
AMPA	α-amino-3-hydroxy-5-methyl-4-isoxazolepropionic acid
AMPAR	α-amino-3-hydroxy-5-methyl-4-isoxazolepropionic acid receptor
ANOVA	analysis of variance
APP	amyloid precursor protein
ATP	adenosine triphosphate
bw	bodyweight
CA	cornu ammonsis
CBX	carbenoxolone
CC	current-clamp
CCL17	chemokine (C-C motif) ligand17
CNS	central nervous system
Cx	connexin
D-APV	D-2-amino-5-phosphonovalerate
DC	direct-current
DG	dentate gyrus
DMSO	dimethylsulfoxid
EC	entorhinal cortex
ECFP	enhanced cyan fluorescent protein
ECS	extracellular space
E_{ion}	potential of the ion-sensitive compartment
E_K	equilibrium potential for potassium
EPSC	excitatory postsynaptic current
EPSP	excitatory postsynaptic potential
E_{ref}	potential of the reference compartment
F	Faraday constant/ fluorescence intensity
F_0	basal fluorescence intensity
fEPSP	field excitatory postsynaptic potential
FRET	Förster resonance energy transfer
FV	fiber volley

FVB	friend leukemia virus B
GABA	γ-aminobutyric acid
$GABA_AR$	γ-aminobutyric acid receptor type A
$GABA_BR$	γ-aminobutyric acid receptor type B
GAT-3	GABA-transporter 3
GFAP	glial fibrillary acidic protein
g_K	membrane conductance for potassium
GLAST	glutamate/aspartate transporter
GLT-1	glutamate transporter 1
GluR	glutamate receptor
GlyFS	optical glycine FRET sensor
GTP	guanosine-5'-triphosphate
HCl	hydrogen chloride
HEPES	4-(2-hydroxyethyl)-1-piperazineethanesulfonic acid
HFS	high-frequency stimulation
i.p.	intraperitoneal
IC	intracellular solution
iGluSnFR	intensity-based glutamate-sensing fluorescent reporter
I_K	potassium current
IPSC	inhibitory postsynaptic current
K_d	dissociation constant
Kir4.1	inwardly-rectifying potassium channel 4.1
KMS	potassium methanesulfonate
KO	genetic knock-out
KSM	K^+-sensitive microelectrode
LPS	lipopolysaccharides
LTP	long-term potentiation
Ly341495	(2*S*)-2-Amino-2-[(1*S*,2*S*)-2-carboxycycloprop-1-yl]-3-(xanth-9-yl) propanoic acid
MFA	meclofenamic acid
mGluR	metabotropic glutamate receptor
mIPSC	miniature inhibitory postsynaptic current
MP	membrane potential
MRS2179	2'-Deoxy-N^6-methyladenosine 3',5'-bisphosphate tetrasodium salt
MTLE	mesial temporal lobe epilepsy
n	number of experiments/ transport number
NBQX	2,3-dihydroxy-6-nitro-7-sulfamoyl-benzo[f]quinoxaline-2,3-dione

NCX	Na^+/Ca^{2+} exchanger
NKCC1	$Na^+/K^+/2Cl^-$-cotransporter 1
NMDA	N-methyl-D-aspartate
NMDAR	N-methyl-D-aspartate receptor
PBS	phosphate-buffered saline
PMT	photomultiplier tubes
PPR	paired-pulse ratio
PS1	presenilin 1
QX314	*N*-(2,6-Dimethylphenylcarbamoylmethyl) triethylammonium bromide
R	ratio
R_a	access resistance
R_m	membrane resistance
ROCK	rho associated protein kinase
SC	Schaffer collaterals
sIPSC	spontaneous inhibitory postsynaptic current
Str. ori	stratum oriens
Str. pyr.	stratum pyramidale
Str. rad.	stratum radiatum
TBS	theta-burst stimulation
TEA^+	tetraethylammonium
TMA^+	tetramethylammonium
TMACl	tetramethylammonium chloride
TRD	Texas Red Dextran 3 kDa
TSM	TMA^+-sensitive microelectrode
TTX	tetrodotoxin
VC	voltage-clamp
Venus	Venus-fluorescent protein
V_m	membrane potential
WT	wild-type
z	valence electrons
α	extracellular space fraction
Ω	Ohm
$\Delta[K^+]_o$	increase of the extracellular K^+ concentration
$\Delta[TMA^+]_o$	increase of the extracellular TMA^+ concentration
τ	accumulation/ decay constant

List of Figures

List of Tables

Danksagung

Als erstes möchte ich mich herzlichst bei **Prof. Dr. Christian Henneberger** für die Möglichkeit diese Arbeit in seiner Arbeitsgruppe anzufertigen und die hervorragende Betreuung in den letzten Jahren bedanken. Er nahm sich immer Zeit für Fragen und Belange aller Art und zeigte immer Interesse an meiner Arbeit. Durch ihn lernte ich nicht nur das Meiste, was ich über die Neurowissenschaften zu verstehen glaube, sondern schärfte er auch in vielen wissenschaftlichen und nichtwissenschaftlichen Diskussionen meinen Verstand für logisches Denken, Schlussfolgerungen und Zusammenhänge. Außerdem tolerierte er über Jahre meinen schlechten Humor. Darüber hinaus möchte ich mich auch bei **Prof. Dr. Christian Steinhäuser** bedanken, der mich während meiner Zeit als Student in seinem Institut auf dieses Projekt aufmerksam machte und daher maßgeblich zu dessen Bearbeitung beitrug. Auch sein stetiges Interesse an meiner Arbeit soll hier nicht unerwähnt bleiben. Des Weiteren ist **Prof. Dr. Walter Witke** zu nennen, dem ich sehr dafür danken möchte, dass er die Rolle des Zweitgutachters dieser Arbeit übernommen hat. **Prof. Dr. Gerhard von der Emde** und **Prof. Dr. Christa Müller** möchte ich auch meinen Dank aussprechen für ihre Zeit und Mühen diese Arbeit zu begutachten. Es sei auch nicht **PD Dr. Gerald Seifert** vergessen, der mich als Student während meines ersten Kurses in diesem Institut betreut hat und über die Jahre immer eine sehr große Hilfe and ein Ansprechpartner für alle möglichen Dinge war, seien es die unzähligen Genotypisierungen oder nur sein reines Interesse an meiner Arbeit. Auch **PD Dr. Ronald Jabs** sei gedankt für sein immer konstruktives Interesse an diesem Projekt während unserer Seminare und sein offenes Ohr für alle, besonders physikalische, Fragen meinerseits.

Nun möchte ich zu einigen Menschen kommen, die mich in den letzten Jahren begleitet haben und ohne die diese Arbeit nicht möglich gewesen wäre. **Dr. Stefanie Anders** (jetzt Hoffmeister) ist hierbei zuerst zu nennen. Sie zeigte mir nicht nur alles Wichtige als ich neu in der Arbeitsgruppe war, sondern war über all die Jahre immer mein erster Ansprechpartner für Belange aller Art. Nicht nur wissenschaftlich, sondern auch zwischenmenschlich habe ich eine Menge von ihr gelernt. Dafür möchte ich mich herzlich bedanken und hoffe, dass wir auch noch länger befreundet bleiben. Bei **Dr. Daniel Minge** möchte ich mich für seine stetige Hilfe in allen Belangen bedanken. Er nahm sich nicht nur immer Zeit, mir alles Denkbare zu erklären und gab mir dabei nie das Gefühl, dass ich ihn störe, sondern war auch immer interessiert an jeglichen Aspekten meiner Arbeit. Neben unserer gemeinsamen Arbeit im Institut habe ich auch die zahlreichen Abende vor unseren jeweiligen Plattenspielern sehr genossen. Nun möchte ich mich bei **Dr. Anne Boehlen** für die Hilfe bei der Etablierung der Kalium-sensitiven Elektroden und für die

Einführung an die Interface-Kammer bedanken. Als nächstes muss ich **Dr. Stefan Paßlick** nennen, der noch rechtzeitig seinen Weg aus New York zurück in unser Institut gefunden hat. Durch ihn habe ich einen weiteren Menschen kennen gelernt, der meinen schlechten Humor zu schätzen weiß. Darüber hinaus möchte ich mich bei ihm für sein Interesse an meiner Arbeit und den regen wissenschaftlichen und nichtwissenschaftlichen Austausch bedanken. **Dr. Michel Herde** sei an dieser Stelle auch nicht vergessen. Besonders unsere Zusammenarbeit bezüglich des D-Serin Sensors hat mir eine Menge beigebracht und Spaß bereitet. **Dr. Petr Unichenko** möchte ich dafür danken, dass er mich durch seinen stetigen Enthusiasmus für die Forschung immer wieder aufs Neue motiviert hat, eine gute Arbeit zu leisten. Eine weitere Person, die ich hier nicht vergessen möchte, ist **Kirsten Bohmbach**. Ich könnte nun mehrere Dinge nennen, für die ich mich bei ihr bedanken möchte, aber es ist wohl ausreichend, wenn ich folgendes erwähne: „Iontophorese Pipetten“ und „geteiltes Leid ist halbes Leid“. Bei **Catia Domingos** und **Alberto Pauletti** möchte ich mich einfach für die tolle gemeinsame Zeit bedanken. Unsere Projekte hatten zwar nicht allzu große Überschneidungen, doch möchte ich unsere gemeinsame Zeit nicht missen. Besonders unsere diversen Diskussionen abseits der Wissenschaft haben mir eine Menge Freude bereitet. Auch **Charlotte Behringer** verdient hier ihre Nennung. Ich möchte mich bei ihr für die mir entgegengebrachte Wertschätzung bedanken. **Steffen Kautzmann** möchte ich sehr für die Mitarbeit an meinem Projekt und die spaßige gemeinsame Zeit bedanken. Zudem möchte ich mich auch bei allen Weiteren bedanken, die mich im Laufe der Jahre unterstützt haben: **Katharina Hill, Dr. Peter Bedner, Aline Timmermann, Dr. Camille Philippot, Dr. Julia Müller, Dr. Tushar Deshpande, Dr. Magda Skubal, Dr. Silke Künzel, Thomas Erdmann, Dr. Ines Heuer, Paula Baum, Nehal Gebril, Dario Tascio, Dr. Zhou Wu, Dimitry Fedorov** und **Lukas Henning**. Auch alle **meine Freunde**, die mich abseits der Wissenschaft begleitet haben und mir eine tolle Studentenzeit bereiteten, sei an dieser Stelle herzlichst gedankt.

Schlussendlich möchte ich auch meiner Freundin **Eva** danken, die trotz meiner vielen Marotten all die ganzen Jahre nie versuchte mich zu verändern, sondern mich unterstützt und ausgehalten hat. **Meinen Eltern** widme ich die letzten Worte dieser Arbeit. Sie haben mich in allen Lebenslagen und all meinen Entscheidungen stets unterstützt, ohne zu versuchen diese zu beeinflussen. Dafür gilt ihnen mein unbegrenzter Dank!

Ausgewählte Konferenzpräsentationen

B. Breithausen, S. Anders & C. Henneberger (2015). Role of astrocyte uncoupling for potassium buffering and synaptic transmission in acute brain slices. BIGS Neuroscience Student Retreat, Diez, Germany.

S. Anders, M. K. Herde, D. Minge, T. Deshpande, **B. Breithausen**, A. Boehlen, P. Bedner, C. Steinhäuser & C. Henneberger (2017). Rapid astrocyte morphology changes support epileptic activity. XIII European Meeting on Glial Cells in Health and Disease, Edinburgh, Schottland.

B. Breithausen, S. Kautzmann, A. Boehlen, C. Steinhäuser & C. Henneberger (2018). The impact of acute astroglial uncoupling on hippocampal potassium buffering. Meeting of the Federation of European Neuroscience Societies (FENS), Berlin, Deutschland.

B. Breithausen, S. Kautzmann, A. Boehlen, C. Steinhäuser & C. Henneberger (2019). The impact of acute astroglial uncoupling on hippocampal potassium buffering. Meeting des Bonner Forum Biomedizin, Hennef, Deutschland.

B. Breithausen, S. Kautzmann, A. Boehlen, C. Steinhäuser & C. Henneberger (2019). The impact of acute astroglial uncoupling on hippocampal potassium buffering. Bonn Brain Meeting, Bonn, Germany.

B. Breithausen, S. Kautzmann, A. Boehlen, C. Steinhäuser & C. Henneberger (2019). The impact of acute astroglial uncoupling on hippocampal potassium buffering. XIV European Meeting on Glial Cells in Health and Disease, Porto, Portugal.

Publikationen

Breithausen, B., Kautzmann, S., Boehlen, A., Steinhäuser, C., and Henneberger, C. (2020). Limited contribution of astroglial gap junction coupling to buffering of extracellular K+ in CA1 stratum radiatum. Glia 68, 918–931.

Fülle, L., Offermann, N., Hansen, J.N., **Breithausen, B.**, Erazo, A.B., Schanz, O., Radau, L., Gondorf, F., Knöpper, K., Alferink, J., et al. (2018). CCL17 exerts a neuroimmune modulatory function and is expressed in hippocampal neurons. Glia 66, 2246–2261.

Reichenbach, N., Delekate, A., **Breithausen, B.**, Keppler, K., Poll, S., Schulte, T., Peter, J., Plescher, M., Hansen, J.N., Blank, N., et al. (2018). P2Y1 receptor blockade normalizes network dysfunction and cognition in an Alzheimer's disease model. J. Exp. Med. 215, 1649–1663.

Zhang, W.H., Herde, M.K., Mitchell, J.A., Whitfield, J.H., Wulff, A.B., Vongsouthi, V., Sanchez-Romero, I., Gulakova, P.E., Minge, D., **Breithausen, B.**, et al. (2018). Monitoring hippocampal glycine with the computationally designed optical sensor GlyFS. Nat. Chem. Biol. 14, 861–869.

Müller, F.E., Schade, S.K., Cherkas, V., Stopper, L., **Breithausen, B.**, Minge, D., Domingos, C., Compan, V., Kirchhoff, F., Henneberger, C., Ponimaskin, E., Zeug A. Serotonin receptor 4 regulates hippocampal astrocyte morphology and Function. In preparation.

Graduiertenprogramm

Bonn International Graduate School of Neuroscience (BIGS)